Title

Small Molecule Activation at Transition Metal Complexes of a Sterically-Encumbered Multidentate Phosphinimide Ligand

Author

Winslow, Charles

Publication Date

2022

Small Molecule Activation at Transition Metal Complexes of a Sterically-Encumbered Multidentate Phosphinimide Ligand

By

Charles Winslow

A dissertation submitted in partial satisfaction of the
requirements for the degree of
Doctor of Philosophy
in
Chemistry
in the
Graduate Division
of the
University of California, Berkeley

Committee in charge:
Professor Jonathan Rittle, Chair
Professor T. Don Tilley
Professor Alexis T. Bell

Spring 2022

To my mentors, friends, and family

Table of Contents

Acknowledgements

As with most PhD trajectories, my path in getting a PhD in Chemistry from Berkeley had its share of extreme highs and lows. Taking a non-traditional route in going from a chemical engineer with little air-free synthetic experience to becoming someone who's entire graduate career depended upon it took a lot of great mentorship and training as well as a great group of people to support me when it was a struggle and I needed to get my mind off of chemistry for a bit. The following list is just a fraction of the people that helped me get to this point, and without whom I would not be getting this degree.

First of all, I would like to thank my family, specifically my parents. Though I was a bit of a problem child early on, they were constant in encouraging me and helping me to believe that I could accomplish anything I put my mind to as long as I stayed focused and worked hard. Although chemistry was far from your favorite subject growing up, you were always supportive and attentive as I first went into chemical engineering and then took the deep dive into a PhD in chemistry, always asking how things were going with classes and research at every opportunity. Without this support and always having a home to come back to, I wouldn't have made it this far.

Second, I owe a debt of gratitude to the people who made me fall in love with chemistry and who inspired me to take up this career path. First, I have to thank my high school chemistry teacher, Mrs. Donna Malkmus, who first introduced me to the world of chemistry and encouraged my passion for it throughout the rest of high school and beyond. From allowing me to organize and set up labs to sponsoring our Battle of the Burets team and everything in between, she nurtured a love for chemistry that gave me no choice but to follow it throughout my academic career. Secondly, I have to thank the person who introduced me to chemical research, Dr. Charles Liotta. He took on a sophomore chemical engineer with little to no experience outside of general chemistry labs into his research group, and alongside a team of great senior grad students and postdocs helped me develop a passion for fundamental research. His relentless passion for physical organic chemistry and applying it to solve both fundamental and applied problems is what made me see how exciting and stimulating a life of chemical research could be, and is what made up my mind in both applying to and attending graduate school.

Next, I have to thank the people in my research group for being such great supporters, coworkers, and friends. First, I have to thank JR, who took a chance on a second-year graduate student switching research groups and took me on as his first student, even though I still had a ton to learn before becoming a competent synthetic inorganic chemist. His patience and direct mentorship during those first couple of years were what helped me develop into the chemist I am today and further instilled a passion for bioinorganic and organometallic chemistry into me. I have no doubt that switching into this research group was the best decision of my PhD. I would also be remiss with thanking Dr. Heui Beom Lee, a postdoc mentor and friend, who worked alongside me during most of my time in the Rittle lab and was always there to teach me everything I needed to learn about being an inorganic chemist. Lastly, I have to thank the great set of friends that I've made in the Rittle lab, especially Magan Powell, Nick Ciolkowski, and Paul Rathke. Though

COVID sometimes made it hard, I can’t be happier with the group social culture that we’ve developed. I am truly proud to be part of a group of people that enjoys both working and hanging out together, and that has made these past few years so much more fun. I’m going to miss all of our shenanigans and going to every Emo Night together to scream our lungs out and dance the night away. I have to particularly thank Magan for always putting up with me and for being one of my best friends; I leave feeling comfortable that the “cult” is in good hands.

Finally, I have to thank the vast friend network I’ve made outside of lab. I won’t be able to list all of them here, but they are what truly what made Berkeley feel like home from day one. First, I have to thank my weekly board game night crew (Mark Babin, Blake Erickson, Eugene Kim, Nathan Odendahl, Katherine Oosterbaan, and Carlos Mejuto Zaera, among others). Having that consistent night every weekend where we could hang out, take our mind off chemistry for a while, and enjoy each other’s’ company was definitely one of the things that kept me together these past years. It was also one of the events, during the COVID lockdown, that helped me keep a sane schedule. I’m so glad that we moved to a virtual game night and continued that tradition even as some of us have moved away. I also have to thank my beer bois, specifically Mark, Blake, Eugene, and Zachary Heim, for all the nights out, bottle shares, and trips to places all across California. I will miss having us all in the same city, and can’t wait for y’all to come visit in the years to come and vice versa. I have to thank Katherine for being a close friend and someone who I could always go to for anything, especially talking about baseball, the Midwest, music, and beverages. These people and many more were such a great support system who were often involved in the ups of grad school and made the downs feel minor in comparison.

Abstract

Small Molecule Activation at Transition Metal Complexes of a Sterically-Encumbered Multidentate Phosphinimide Ligand

By

Charles Christopher Winslow

Doctor of Philosophy in Chemistry

University of California, Berkeley

Professor Jonathan Rittle, Chair

Chapter 1. Introduction to Phosphinimide Ligands and the Development of a Generable Methodology for Their Synthesis

High-valent late transition metals are invoked in myriad synthetic and biological processes but are often highly unstable, precluding their full characterization. Phosphinimides are strongly π-basic ligands that have been primarily utilized to stabilize electron-deficient early metals and lanthanides. The oxidative robustness and high level of tunability of these platforms should, in principle, allow access to high-valent late first row transition metals. A general and scalable electrophilic amination methodology giving access to rationally designed multi-dentate phosphinimide frameworks was developed.

Chapter 2. 1,2-Addition at a Phosphinimide Supported Zirconium Complex Highlights Isolobality to Imido Ligands

Early transition metal imido complexes have been shown to activate X-H type bonds across a metal ligand multiple bonds. Phosphinimide (PN) moieties are isolobal to imidos and have been shown to have metal-ligand π-bonding character. To highlight the multiple bonding character of the PN-Metal bond, a trisphosphinimide zirconium platform was synthesized. Reaction of the trisphosphinimide zirconium arene complex with phenylacetylene and aniline resulted in the formation of the corresponding bisphosphinimide, phosphinimine zirconium acetylide and anilide, respectively. Addition of acetophenone and nitromethane resulted in the oxygen bound products upon activation of the C-H bond across the PN-Zr bond. This reactivity showcases the ability of the isolobal analogy to predict the reactivity of ligand fragments that are analogous to each other.

Chapter 3. Multi-Electron Processes Mediated by a Phosphinimide Supported Chromium(II) Complex

The activation of small molecules via multi-electron transfer processes has drawn vast interest in the organometallic field due to its diverse application in performing difficult transformations by enzymatic systems. To that end, an electron rich and multi-dentate phosphinimide platform was designed to stabilize a low-coordinate, reducing chromium(II) complex capable of performing a series of net 4-electron processes, including the reduction of dioxygen, nitrosoarenes, and aryl azides to the corresponding chromium (VI) dioxo, imido/oxo, and bisimido complexes, respectively. Additionally, the chromium(VI) imido/oxo complexes are capable of performing oxo/imido heterometathesis to an additional equivalent of nitrosobenzene to form the corresponding azobenzene and chromium(VI) dioxo. The structural and spectroscopic characterization of these compounds highlights the flexibility of phosphinimides to support both low- and high- valent transition metal complexes.

Chapter 4. Structure and Reactivity of a High-Spin, Nonheme Iron(III)- Superoxo Complex Supported by Phosphinimide Ligands

Nonheme iron oxygenases utilize dioxygen to accomplish challenging chemical oxidations. A further understanding of the Fe-O_2 intermediates implicated in these processes is challenged by their highly transient nature. To that end, we have developed a ligand platform featuring phosphinimide donors intended to stabilize oxidized, high-spin iron complexes. O_2 exposure of single crystals of a three-coordinate Fe(II) complex of this framework allowed for *in crystallo* trapping of a terminally bound Fe-O_2 complex suitable for XRD characterization. Spectroscopic and computational studies of this species support a high-spin Fe(III) center antiferromagnetically coupled to a superoxide ligand, similar to that proposed for numerous nonheme iron oxygenases. In addition to the apparent stability of this synthetic Fe-O_2 complex, its ability to engage in a range of stoichiometric and catalytic oxidation processes demonstrates that this iron-phosphinimide system is primed for development in modelling oxidizing bioinorganic intermediates and green oxidation chemistry.

Chapter 1

Introduction to Phosphinimide Ligands and the Development of a Generable Methodology for Their Synthesis

Portions of this work is based upon previously published work with permissions from all authors:

Lee H.B.; Ciolkowski , N.; Winslow, C.;Rittle, J. *Inorg. Chem.* **2021**, *60*(16), 11830-11837.

1.1 Introduction

High-valent states of late first-row transition metals are invoked as reactive intermediates in various synthetic and biological processes; their importance in these transformations has lead bioinorganic and organometallic chemists alike to isolate and characterize these intermediates directly or through synthetic model complexes.[1–8] The stabilization of such species remains of great interest to the field. The application of highly electron-donating ligands that are robust to highly oxidative conditions and provide the ability to sterically tune the environment around the metal should enable access to such species.

Phosphinimides (PN), also known as imidophosphoranes and phosphoraniminatos, are a class of ligands that has sporadically garnered the attention of various organometallic chemists.[9-28] Their electron-donating properties merit further exploration in the stabilization of inorganic fragments. The two canonical resonance structures of PNs (Figure 1.1) highlight their ability to act as 1, 3, or 5 electron donors, attendant with the ability to bind anywhere from one to three metals (Figure 1.2).[19] In the case of a terminally bound PN where the ∠(P-N-M) angle approaches 180°, the PN moiety can serve as a 5 electron donor engaging in π-bonding with the metal center in two orthogonal planes, akin to imido ligands (Fig 1.2B).

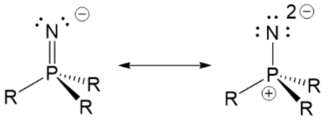

Figure 1.1. Canonical resonance structures of a phosphinimide (PN) functional group

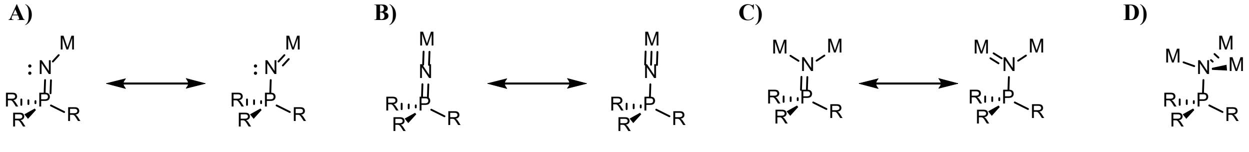

Figure 1.2. Possible binding modes for phosphinimides to metal center(s)

The ability of phosphinimides to effectively donate electrons has been utilized by organometallic chemists to stabilize a variety of inorganic fragments, primarily focusing on architectures utilizing monodentate PN's. Various groups have utilized these ligands as surrogates to isolobal cyclopentadienyls in olefin polymerization (Fig 1.3A).[13] The Stryker group has utilized the ability of PN's to support low coordination metal centers to develop Ni- and Co- promoted hydrogenation catalysts via tetrametallic molecular squares (Figure 1.3B).[14] More recently, the La Pierre group has been utilizing the donating properties of PN's to stabilize tetravalent, homoleptic lanthanide complexes (Figure 1.3C).[18]

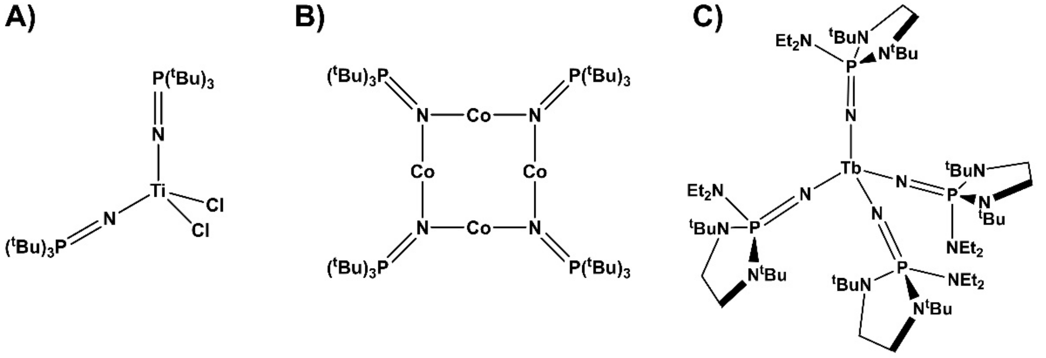

Figure 1.3. Selection of metal PN complexes

Despite their effectiveness in releasing electrons to metal ions, very few monometallic late transition metal PN-complexes have been reported. Among these are an iron(II) spin cross-over complexes both from the Smith[19,25] (Figure 1.4A) and Peters[24] (Figure 1.4B) groups as well as several ruthenium and osmium complexes from a variety of groups[20–23] (Figure 1.4C), all generated via the reaction of PR_3 with a transition metal nitride rather than the reaction with a preconstructed PN ligand. These complexes often require the presence of sterically-demanding co-ligands to prevent oligomerization, which can be partially explained by significant dπ-pπ repulsive effects which are expected to impede the ability of PN ligands to serve as 3- or 5-electron donors. Furthermore, there has been no exploration into the effect of having multiple PN's on a single late transition metal ion, likely due to the problems with oligomerization when even sterically encumbering monodentate PN's are utilized. The combination of this lack of precedent as well as the fact that preconstructed PN's are derived from their parent phosphines, for which there is vast synthetic precedent for tuning both sterically and electronically, showcases that vast space for exploration using rationally designed multidentate PN platforms.

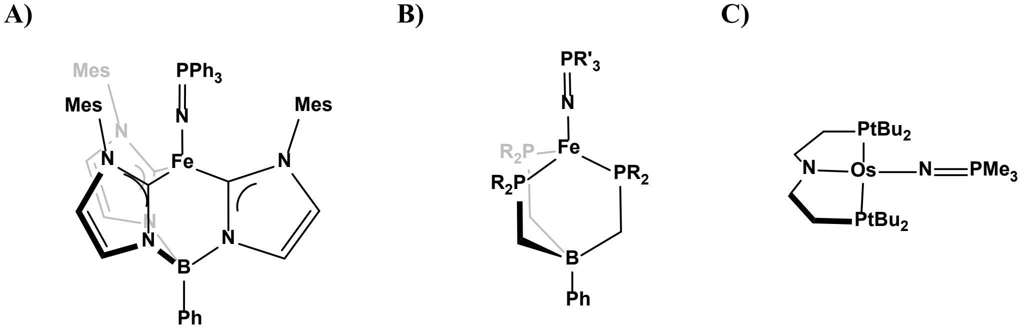

Figure 1.4. Selected mononuclear examples of late-transition metal phosphinimides derived from parent metal nitrides

1.2 Development of a General and Scalable Methodology to Synthesize Phosphinimines

We reasoned that terminal PN coordination to kinetically labile, late first row transition metals would be enforced via the incorporation of such ligands into a rigid, multidentate framework. To date, however, very few multidentate PN scaffolds have been prepared, and these suffer from pronounced flexibility and concomitant ambiguity in their metal coordination chemistry.[29–33] However, initial attempts to convert rigid, multidentate platforms via traditional routes, including the usage of Me_3SiN_3 via a Staudinger reaction or aminolysis of R_3PCl_2[34] derivatives proved unsuccessful, likely owing to the pronounced steric encumbrance and rigid nature of these platforms (Scheme 1.1, Figure S1.1). This observation underscores that the general application of PNs as ligands is limited by existing synthetic procedures for their preparation.

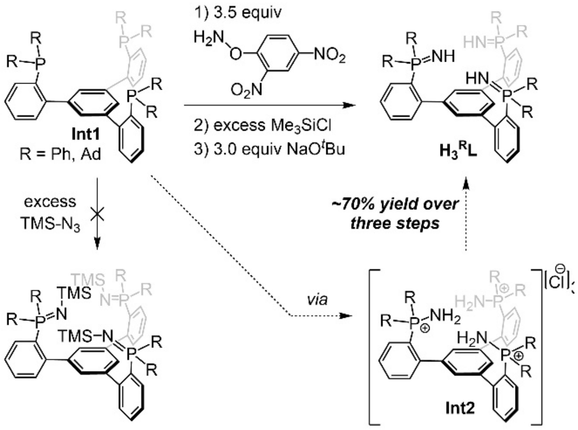

Scheme 1.1. Novel electrophilic amination strategy for the synthesis of phosphinimine ligands

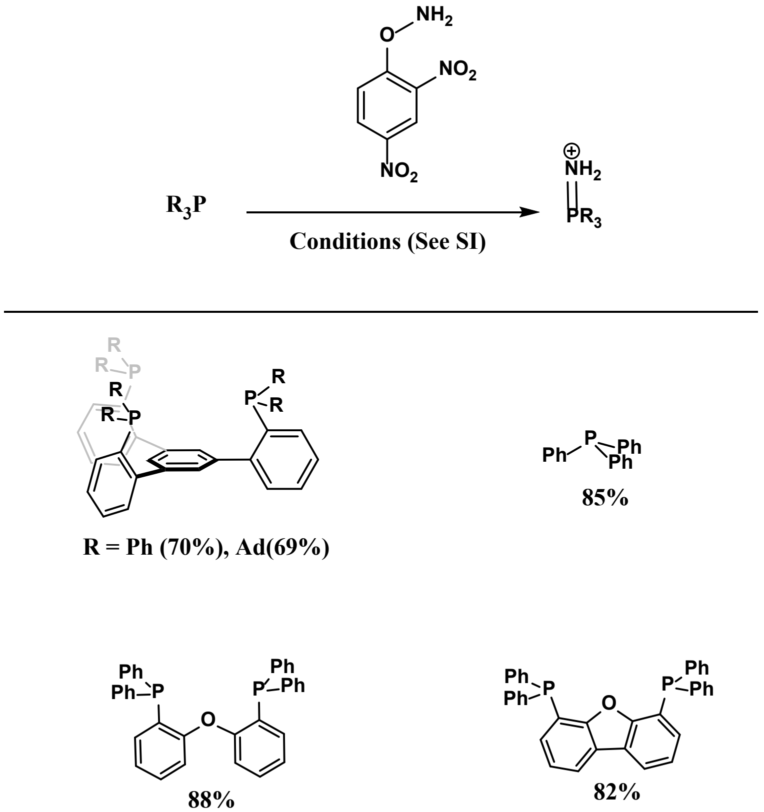

Scheme 1.2. Substrate scope of phosphine electrophilic amination

We canvassed alternative methods for transferring a nitrogen atom to a neutral phosphine and decided upon electrophilic amination as a viable strategy at transferring a NH_2^+ equivalent to the phosphine resulting in a compound that only requires deprotonation to obtain the ligand; we hypothesized that the substituting the transfer of $-NSiMe_3$ for $-NH_2$ would relieve the steric strain of transferring multiple nitrogen atoms to a rigid, bulky framework. We identified *O*-(2,4-dinitrophenyl)-hydroxylamine as a non-hygroscopic, stable, and easily scalable reagent that is capable of the amination a wide variety of unactivated nucleophiles.[35–37] The combination of this reagent with diverse mono- and diphosphines at room temperature results in quantitative conversion to the corresponding phospiniminium ions ($R_3PNH_2^+$) as observed by ^{31}P-NMR within 15 minutes, with isolated yields of 80-90% on gram scales (Scheme 1.2). Importantly, this reagent also quantitatively aminates all three phosphorus atoms of a rigid, tridentate phosphine as conveniently monitored by ^{31}P NMR spectroscopy. To facilitate isolation and remove unwanted phenoxide impurities, anion exchange by treatment with excess Me_3SiCl afforded the phosphiniminium chlorides as insoluble solids, which could be further deprotonated using NaOtBu to give the neutral phosphinimines as proligands.

1.3 Conclusions

In summary, the characterization of reactive high-valent late transition metal species is of great interest to the synthetic inorganic field due to such intermediates being often invoked in important biological processes. Phosphinimides are highly π-basic ligands that have primarily been used to stabilize early transition metal olefin polymerization catalysts and electron-deficient lanthanides. The electron donating ability and high degree of tunability of PN's allows for rational design of rigid, multidentate frameworks which maximize the ability of PN's to donate electrons to a single transition metal ion, which should allow for the stabilization of high-valent inorganic fragments. To access such frameworks, a novel, general, and scalable synthetic methodology based on electrophilic amination of the parent phosphines was developed. This methodology was essential to our groups ability to rationally explore rigid, multi-dentate phosphinimides and was instrumental to the accomplishments described in this thesis.

1.4 Acknowledgements

This research was supported by the University of California Berkeley. We thank Dr. Eugene Kim for assistance with TGA measurements. We thank Drs. Hasan Celik and Alicia Lund and UC Berkeley's NMR facility in the College of Chemistry (CoC-NMR) for spectroscopic assistance. Instruments in the CoC-NMR are supported in part by NIH S10OD024998.

1.5 Supporting Information

General Considerations. All reactions were performed at room temperature in an N_2-filled glovebox or by using standard Schlenk techniques unless otherwise specified. Glassware was oven dried at 150 ºC for at least 2h prior to use, and allowed to cool under vacuum. All reagents were used as received unless otherwise stated. Anhydrous pentane, CH_3CN, diethyl ether, benzene, toluene and THF were purified by sparging with nitrogen for 30 minutes and then passing under nitrogen pressure through a column of activated A2 alumina. NMR solvents were purchased from Cambridge Isotope Laboratories. C_6D_6 was degassed by three freeze-pump-thaw cycles and dried over freshly activated 4 Å molecular sieves for 24 hours prior to use. ^{1}H-, ^{13}C-, and ^{31}P-NMR spectra were recorded on Bruker 400 MHz or 600 MHz instruments, with shifts reported relative to the residual solvent peak.

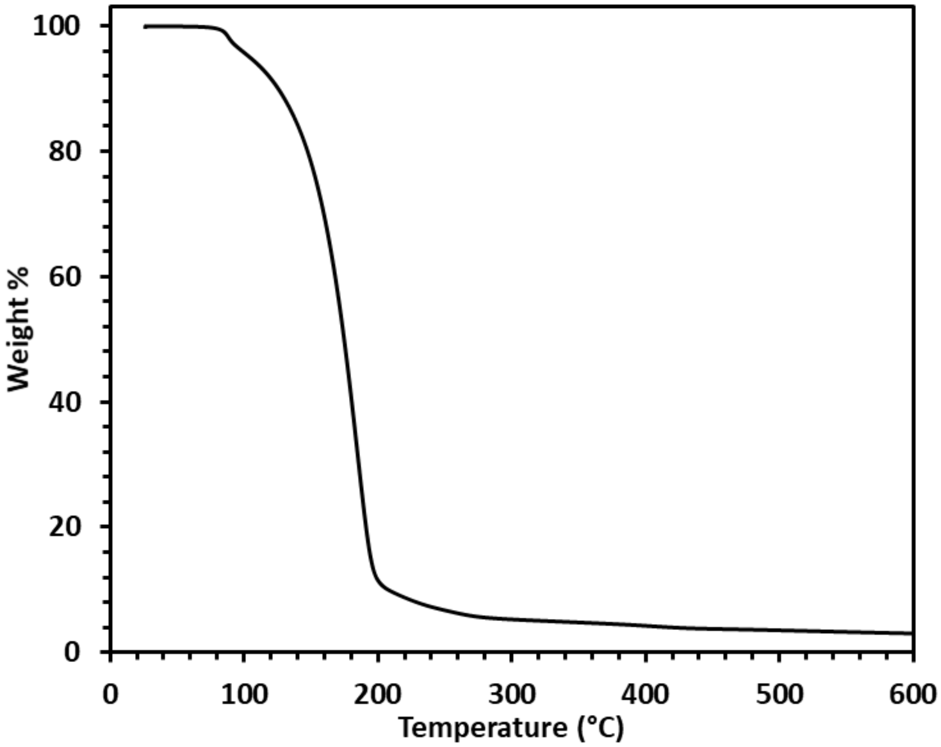

Figure S1.1. Thermogravimetric analysis (TGA) of the aminating agent O-(2,4-dinitrophenyl)-hydroxylamine collected from 26 °C to 600 °C with a 2 °C/min ramp on a TA Instruments Discovery TGA. The TGA shows no mass loss below 90 °C. Above 90 °C, a gradual mass loss is observed with increasing temperature. An abrupt change of mass (i.e. a vertical line) is not observed throughout the entire temperature range, indicating that the aminating agent and its decomposition products are not thermally activated explosives.

Synthetic Procedures:

Electrophilic amination of phosphines:

Standard Procedure A: To a round-bottom flask equipped with a magnetic stir bar was added a 0.1 M solution of the phosphine of choice in CH_2Cl_2. After cooling to 0 °C in an ice bath, solid *O*-(2,4-dinitrophenyl)-hydroxylamine (1 equivalent per phosphorus atom) was added in one portion. The ice bath was removed and the mixture was allowed to stir at room temperature for 1 hour. The mixture was poured into hexanes (twice the volume of DCM) to precipitate a yellow solid. The solid was collected on a fritted funnel, washed with hexanes, and dried under reduced pressure.

Standard Procedure B: To a round-bottom flask equipped with a magnetic stir bar was added a 0.1 M solution of the phosphine of choice in CH_3CN in a dinitrogen glovebox. Solid *O*-(2,4-dinitrophenyl)-hydroxylamine (1.1 equivalent per phosphorus atom) was added in one portion. The mixture was allowed to stir until aliquots showed complete conversion by ^{31}P NMR. Neat Me_3SiCl (excess, 10 equivalents) was added in one portion and the mixture was allowed to stir for 24 hours at room temperature, resulting in the precipitation of a colorless solid. The solid was collected via filtration on a fritted funnel. The precipitate was washed subsequently with MeCN, THF, and Et_2O and dried under reduced pressure.

Triphenylphosphine:

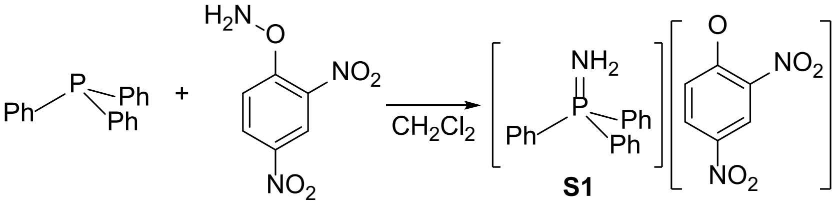

Synthesized via Standard Procedure A. PPh_3 (5.25 g, 20 mmol) was reacted with *O*-(2,4-dinitrophenyl)-hydroxylamine (3.98 g, 20 mmol, 1 equiv) in CH_2Cl_2 (200 mL) to give **S1** as a yellow powder in 85% isolated yield (7.84 g). ^1H NMR (400 MHz, $CDCl_3$) δ 8.70 (d, *J* = 3.1 Hz, 1H), 7.78 (dd, *J* = 9.6, 3.1 Hz, 1H), 7.74 – 7.50 (m, 9H), 7.58 – 7.48 (m, 6H), 6.25 (d, *J* = 9.6 Hz, 1H). ^{31}P NMR (162 MHz, $CDCl_3$) δ 35.76. HRMS (ESI): calcd. for $[C_{18}H_{17}PN]^+$: 278.1098; found: 278.1145.

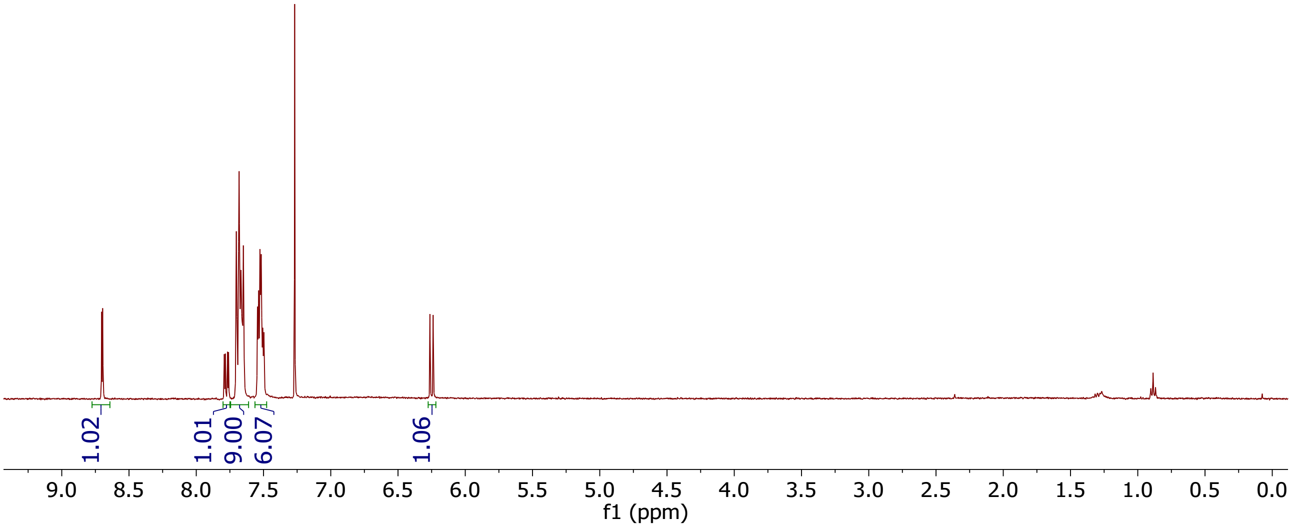

Figure S1.2. ^1H NMR(400 MHz, 298K) of **S1** recorded in $CDCl_3$.

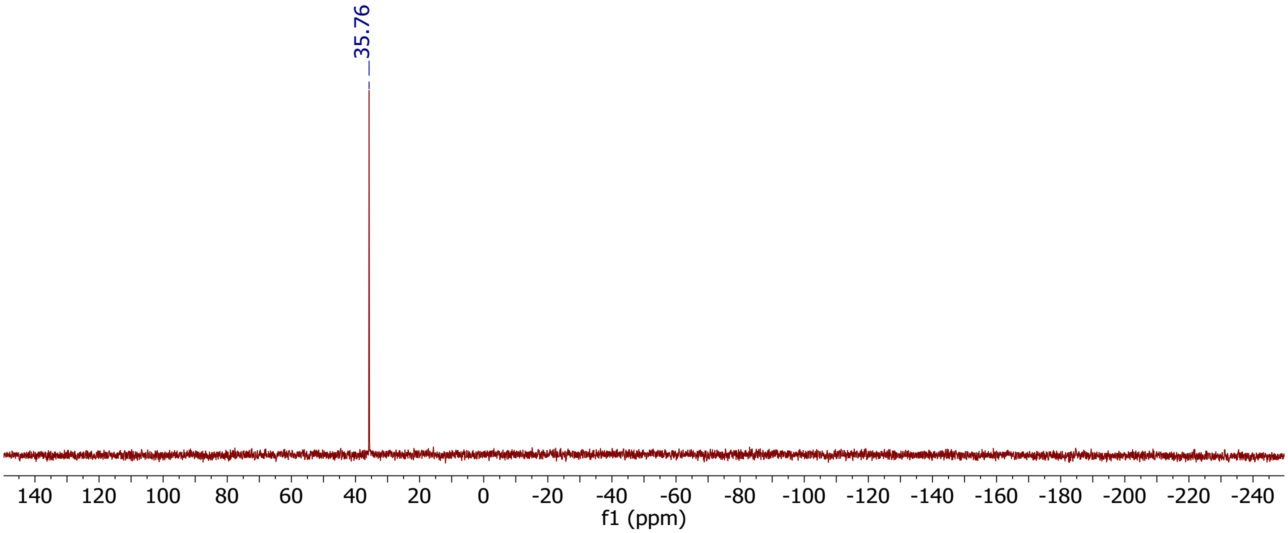

Figure S1.3. ^{31}P NMR (162 MHz, 298K) of **S1** recorded in $CDCl_3$.

Bis[(2-diphenylphosphino)phenyl] ether (DPEphos):

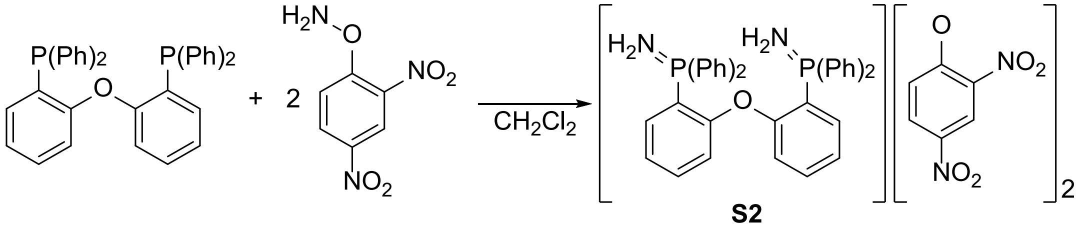

S2

Synthesized via Standard Procedure A. DPEPhos (267 mg, 0.5 mmol) was reacted with *O*-(2,4-dinitrophenyl)-hydroxylamine (199 mg, 1 mmol, 2 equiv) in CH_2Cl_2 (25 mL) to give **S2** as a yellow powder in 88% isolated yield (323 mg). ^1H NMR (400 MHz, $CDCl_3$) δ 8.77 (d, *J* = 3.1 Hz, 2H), 7.83 (dd, *J* = 9.6, 3.1 Hz, 2H), 7.81 – 7.50 (m, 20H), 7.46 (t, *J* = 7.9 Hz, 2H), 7.14 (t, *J* = 7.2 Hz, 2H), 6.97 (dd, *J* = 14.7, 7.8 Hz, 2H), 6.69 (dd, *J* = 8.3, 5.2 Hz, 2H), 6.26 (d, *J* = 9.6 Hz, 2H). ^{31}P NMR (162 MHz, $CDCl_3$) δ 32.88. HRMS (ESI): calcd. for $[C_{36}H_{32}N_2OP_2]^{2+}$: 285.0995; found: 285.0815.

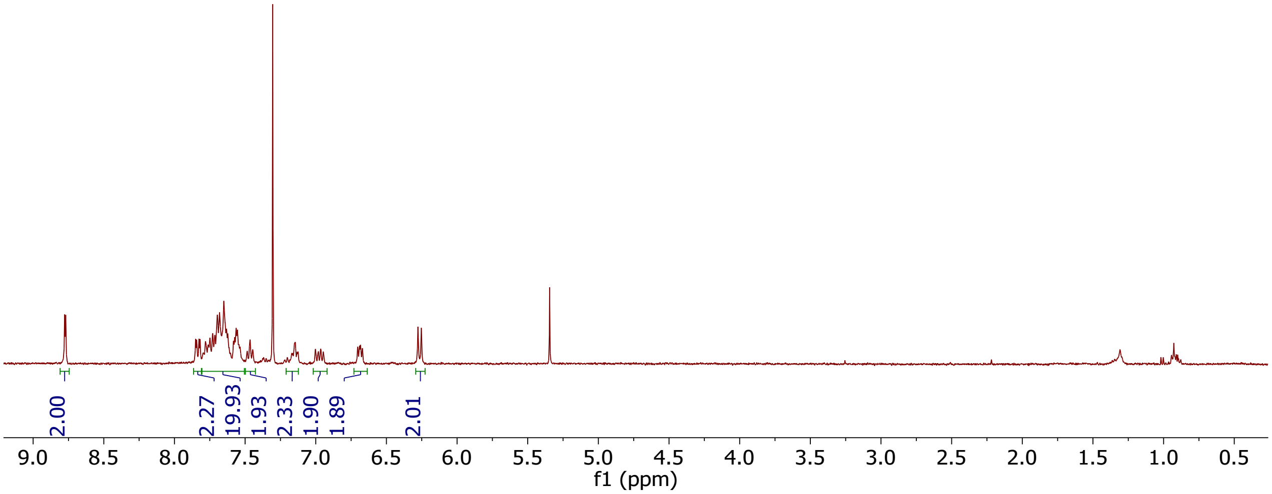

Figure S1.4. ^1H NMR (400 MHz, 298K) of **S2** recorded in $CDCl_3$.

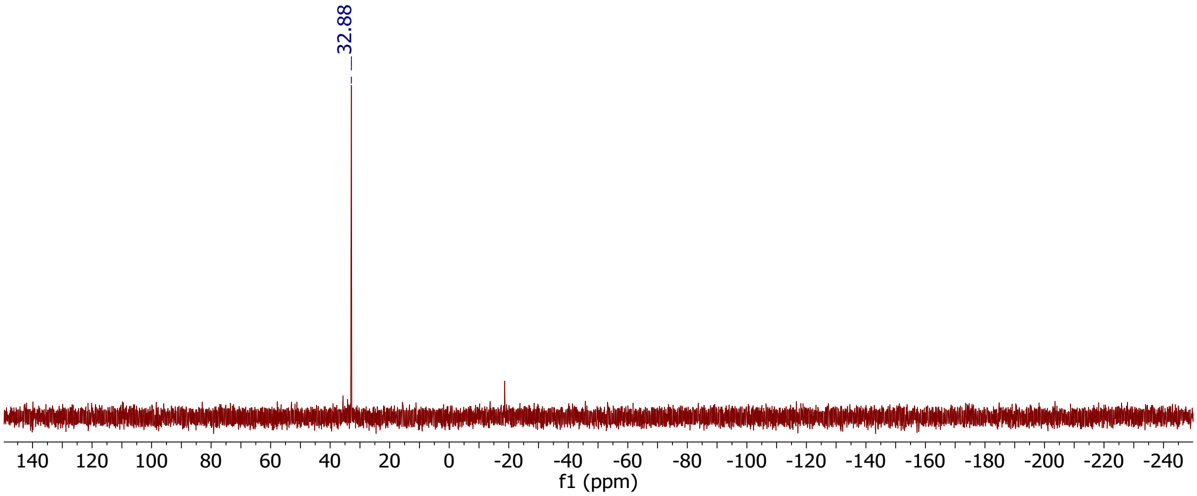

Figure S1.5. ^{31}P NMR (162 MHz, 298K) of **S2** recorded in CDCl$_3$.

4,6-bis(diphenylphosphino) dibenzofuran (DBFPhos):

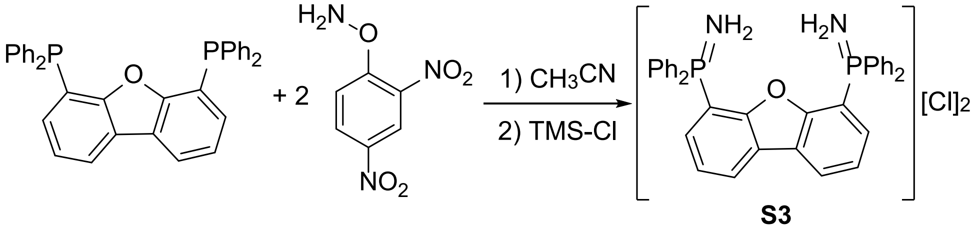

Synthesized via Standard Procedure B. DBFPhos (5 g, 9.3 mmol) was reacted with *O*-(2,4-dinitrophenyl)-hydroxylamine (4.08 g, 20.5 mmol, 2.2 equiv) in CH_3CN (100 mL) for 3 hours. Subsequently, TMS−Cl (12 mL, 10 equiv) was added and stirred for 18 hours. The precipitate was collected to give **S3** as a white solid in 82% isolated yield (4.88 g). ^{1}H NMR (400 MHz, DMSO-*d*$_6$) δ 8.86 (d, *J* = 7.7 Hz, 2H), 7.84 (t, *J* = 7.7 Hz, 2H), 7.76 (dd, *J* = 14.9, 7.6 Hz, 2H), 7.67 (tt, *J* = 5.6, 2.7 Hz, 4H), 7.57 – 7.47 (m, 16H), 6.88 (t, *J* = 3.7 Hz, 2H). ^{31}P NMR (162 MHz, DMSO) δ 31.74.

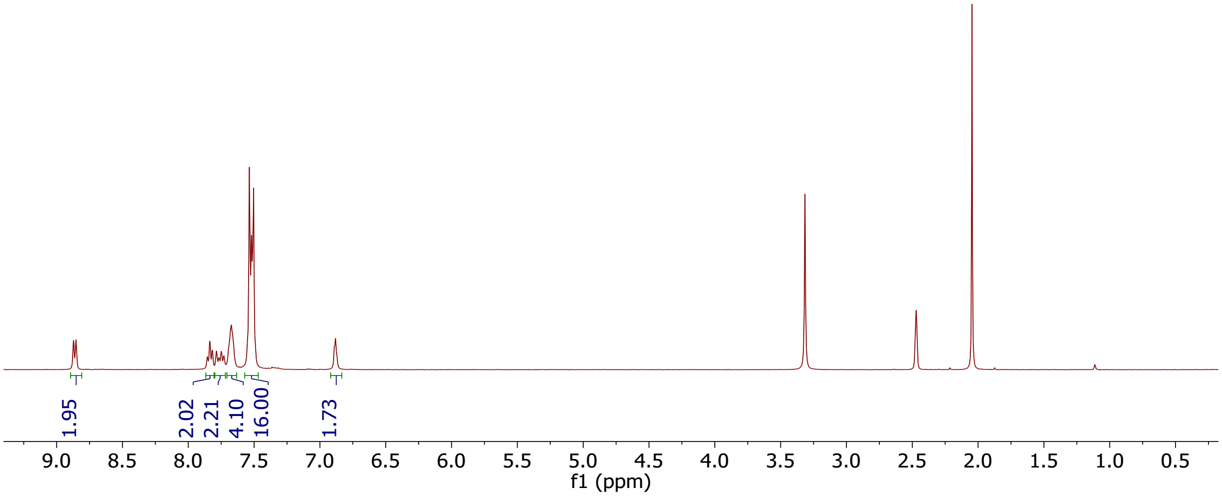

Figure S1.6. ^{1}H NMR (400 MHz, 298K) of **S3** recorded in d$_6$-DMSO.

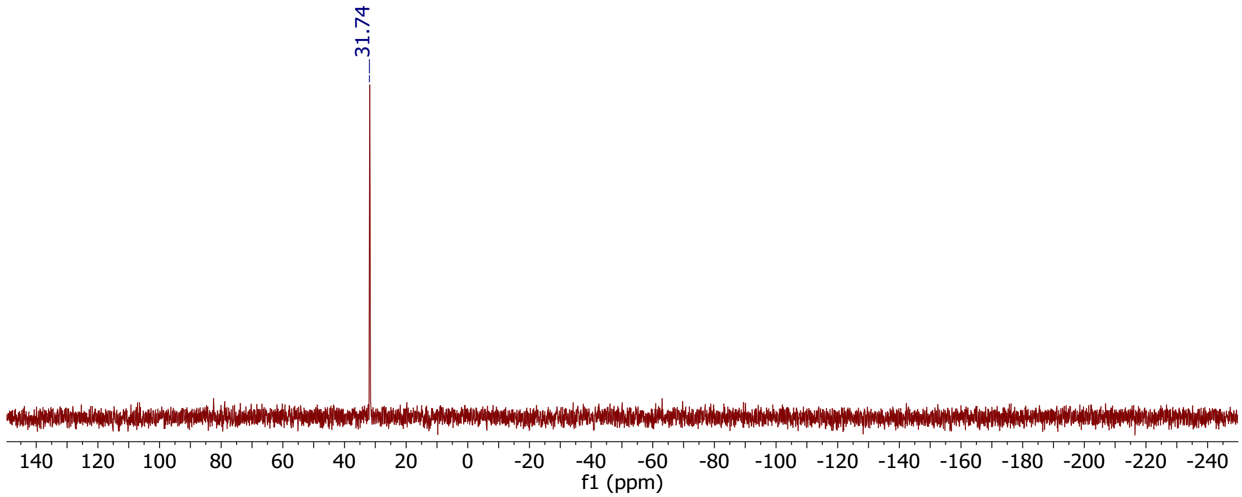

Figure S1.7. ^{31}P NMR (162 MHz, 298K) of **S3** recorded in d_6-DMSO.

Synthesis of tris-phosphine $^{\mathbf{Ph}}$**Int1**

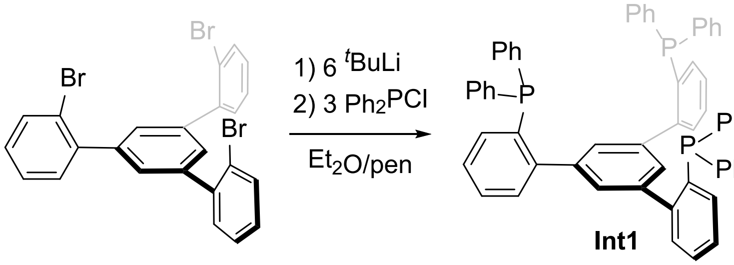

Int1

A 1 L round-bottom flask equipped with a stir bar was charged with 1,3,5-tris(2-bromophenyl)-benzene (31 g, 57 mmol, 1 equiv) and Et_2O (600 mL). The flask was cooled in a liquid nitrogen-chilled cold well. A solution of *t*BuLi (23 g, 359 mmol, 6.3 equiv) in pentane (60 mL) was added slowly in 1 mL portions with stirring. The mixture was allowed to warm up to room temperature, resulting in the formation of a deep red solution containing the tris-aryllithium intermediate. After stirring for 2 hours at room temperature, the flask was cooled again in a liquid nitrogen-chilled cold well. Neat Ph_2PCl (42 g, 190 mmol, 3.3 equiv) that had been previously purified by short-path vacuum distillation was added in small portions with stirring. The mixture was allowed to warm up to room temperature, resulting in the formation of a white suspension. The mixture was further stirred at room temperature for 24 hours before water was added. The white precipitate was collected, washed with MeOH, and dried under reduced pressure. The tris-phosphine intermediate $^{\mathbf{Ph}}$**Int1** was isolated as a white solid (27 g, 55 %). ^{1}H NMR (400 MHz, $CDCl_3$): 7.37 (s, 3H), 7.35 – 7.31 (m, 12 H), 7.22 (dd, *J* = 7.2, 2.8 Hz, 3 H), 7.17 – 7.12 (m, 6 H), 7.09 (td, *J* = 7.4, 1.3 Hz, 3 H), 7.01 – 6.96 (m, 18 H). ^{31}P NMR (162 MHz, $CDCl_3$): −13.45 ppm.

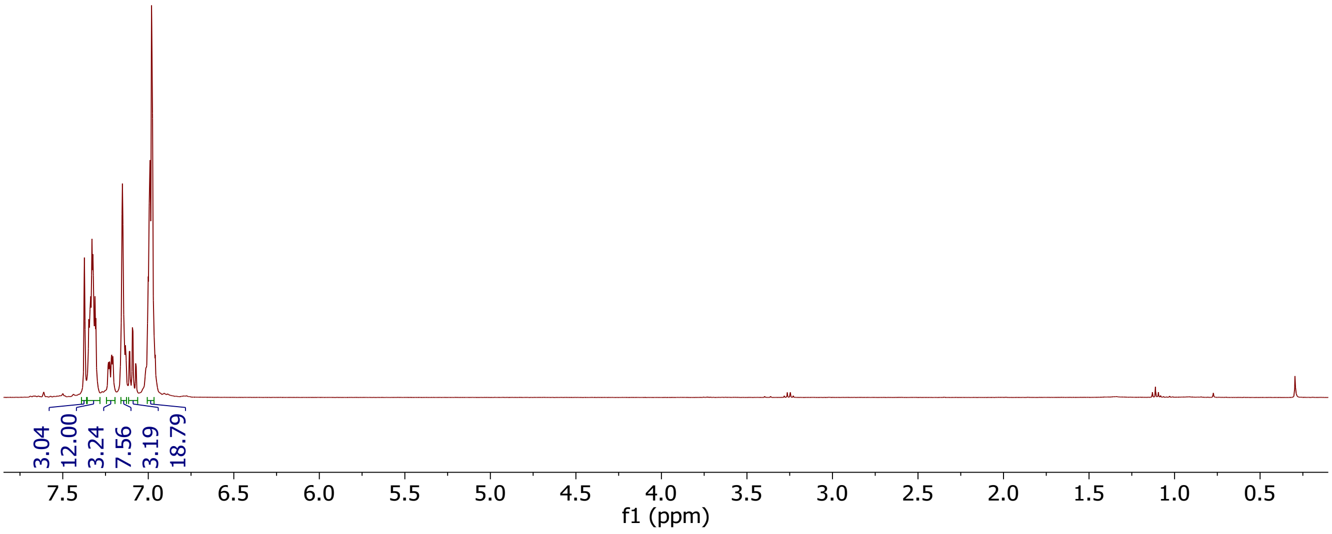

Figure S1.8. ^{1}H NMR of $^{\mathbf{Ph}}$**Int1**.

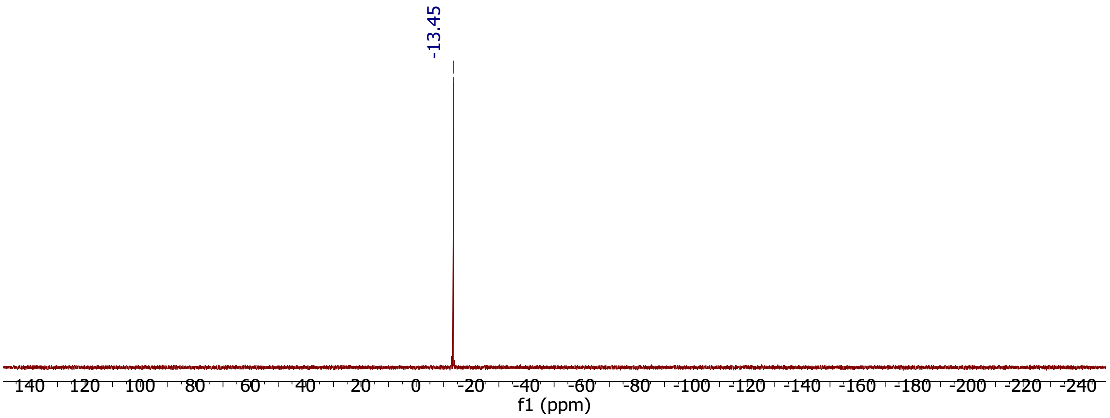

Figure S1.9. ^{31}P NMR of **Int1**.

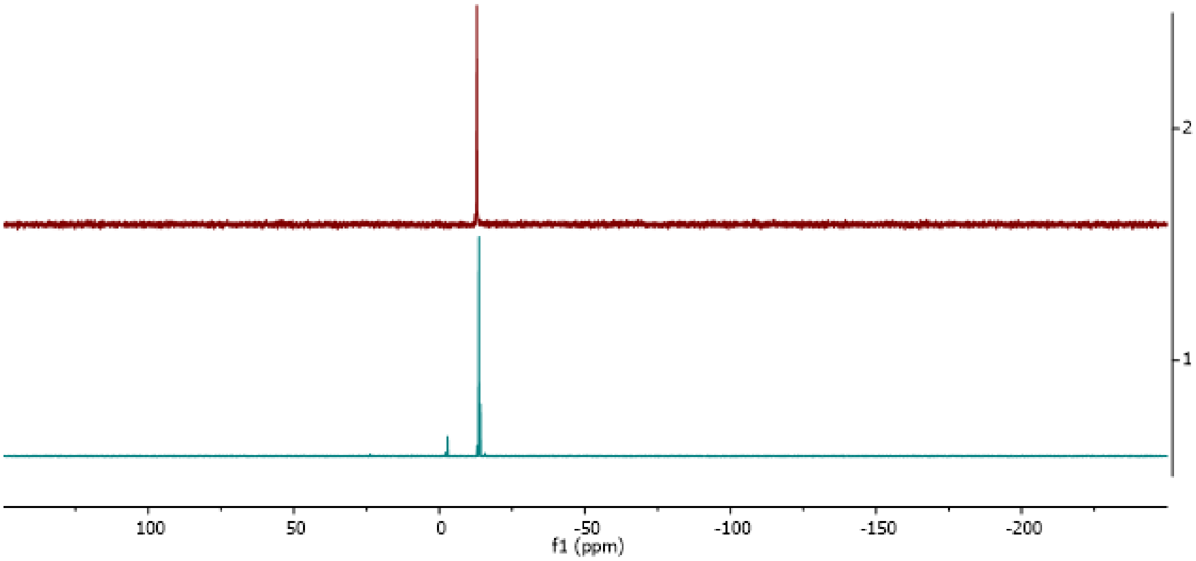

Figure S1.10. (Top) ^{31}P NMR spectrum of $^{\mathbf{Ph}}$**Int1** in toluene. (Bottom) ^{31}P NMR of the reaction mixture of $^{\mathbf{Ph}}$**Int1** and Me_3SiN_3 after refluxing in toluene overnight. The majority of the tri-phosphine remains unreacted, with formation of small amounts of unidentified side products.

Synthesis of tris-phosphinimine $H_3{}^{Ph}L$

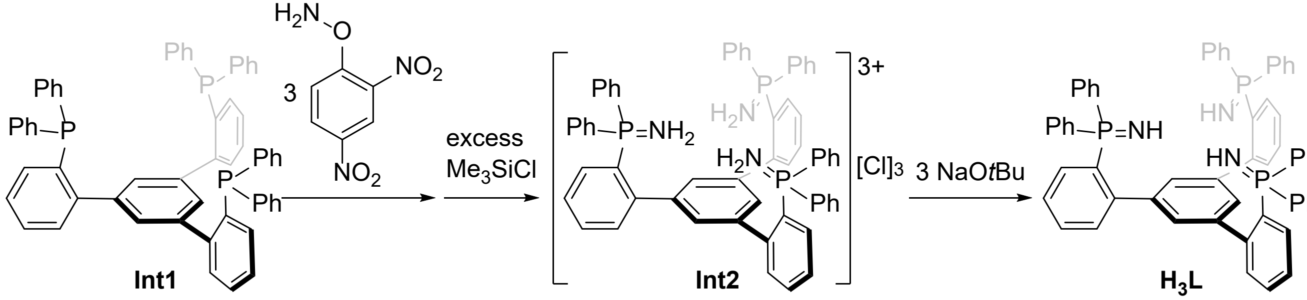

A 500 mL round-bottom flask equipped with a stir bar was charged with **^{Ph}Int1** (27 g, 31 mmol, 1 equiv) and MeCN (300 mL). The flask was cooled in a liquid nitrogen-chilled cold well. Solid *O*-(2,4-dinitrophenyl)-hydroxylamine (22 g, 110 mmol, 3.5 equiv) was added in small portions with stirring. The mixture was allowed to warm up to room temperature, resulting in the formation of a deep red solution with a yellow precipitate. The ^{31}P NMR of this red solution shows a single peak at 35 ppm, which corresponds to the chemical shift of the $[Ph_3PNH_2]^+$ moiety (Figure S9). After stirring for 3 hours at room temperature, the flask was cooled again in a liquid nitrogen-chilled cold well. Neat Me_3SiCl (35 g, 322 mmol, 10 equiv) that had been previously purified by short-path vacuum distillation was added in small portions with stirring. The mixture was allowed to warm up to room temperature, resulting in the formation of a yellow suspension. The mixture was further stirred at room temperature for 24 hours before the yellow precipitate was collected in a fritted funnel. The yellow solid was repeatedly washed with MeCN until the filtrate was colorless, subsequently washed with Et_2O, and thoroughly dried under reduced pressure. This insoluble yellow solid is assigned to the tris-phosphiniminium intermediate **^{Ph}Int2** with chloride counter-anions and was used without further purification. A 500 mL round-bottom flask equipped with a stir bar was charged with **^{Ph}Int2** (25 g, 25 mmol, 1 equiv) and THF (300 mL). The flask was cooled in a liquid nitrogen-chilled cold well. Solid NaO^{t}Bu (7.14 g, 74 mmol, 3 equiv) was added in small portions with stirring. The mixture was allowed to warm up to room temperature, resulting in the formation of a slightly beige solution over a brown precipitate. The mixture was further stirred at room temperature for 18 hours before being filtered through a pad of Celite. All volatiles were thoroughly removed from the filtrate. The beige residue was treated with Et_2O and stirred until a fine suspension was obtained. The solid was collected in a fritted funnel, and washed with Et_2O repeatedly. The collected solid was washed with small amounts of cold THF to remove colored impurities. The white solid was washed with pentane and dried under reduced pressure. **$H_3{}^{Ph}L$** was obtained as a white solid (20 g, 70 % from **^{Ph}Int1**). ^{1}H NMR (400 MHz, $CDCl_3$): 7.66 – 7.53 (dd, *J* = 11.9, 7.2 Hz, 12 H), 7.42 – 7.28 (m, 21 H), 7.19 (t, *J* = 7.7 Hz, 3H), 7.05 – 6.93 (m, 6 H), 6.60 (s, 3H), 1.50 (bs, 3H, N*H*). ^{31}P NMR (162 MHz, $CDCl_3$): 20.6 ppm. HRMS (ESI): calcd. for $C_{60}H_{50}N_3P_3$: 905.3218; found: 905.3267.

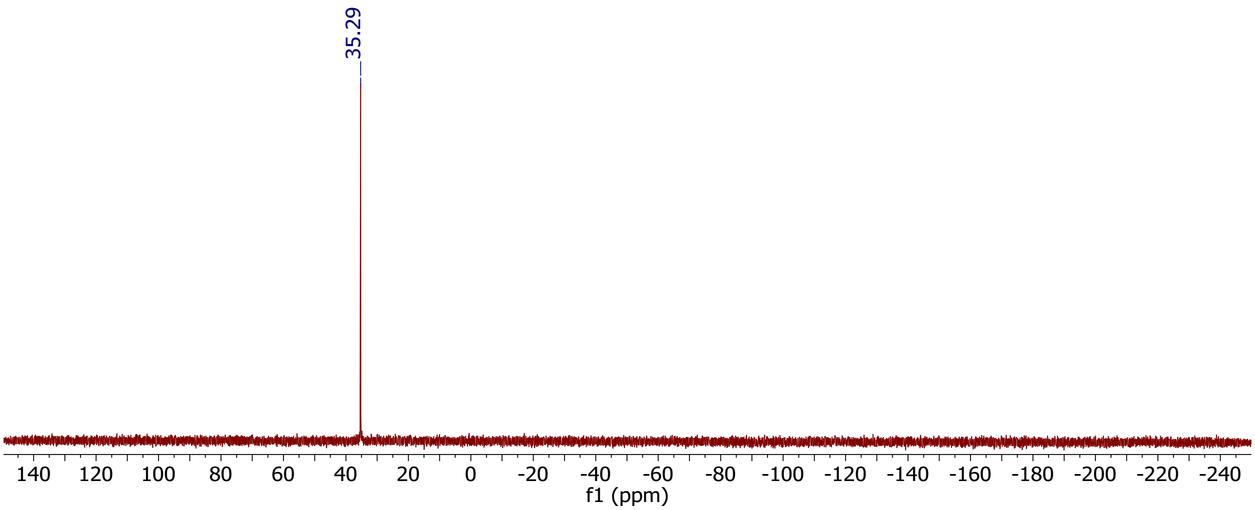

Figure S1.11. ^{31}P NMR of **^{Ph}Int2**.

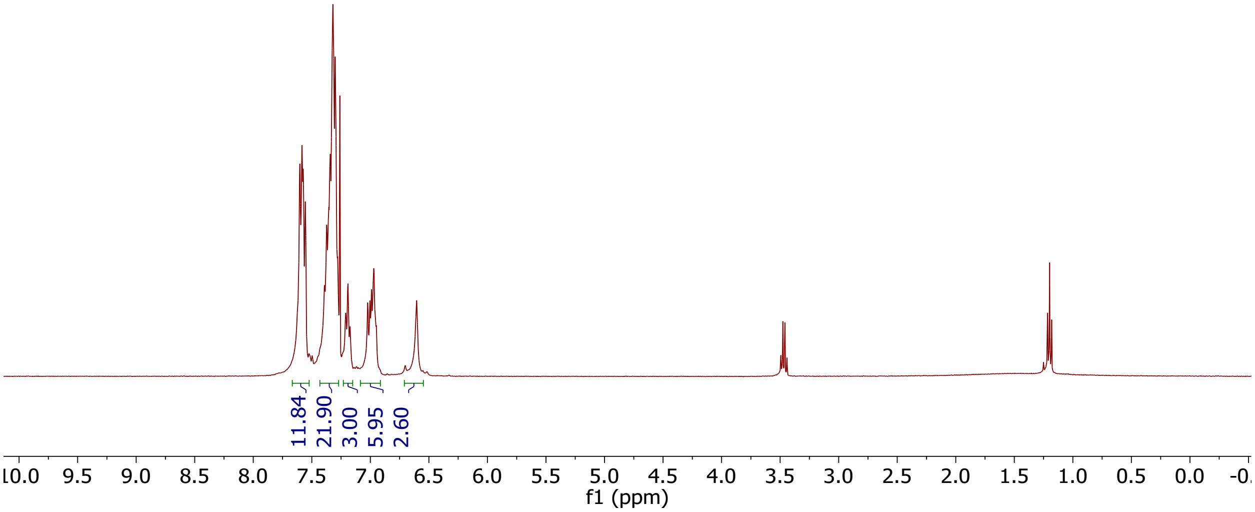

Figure S1.12. ^{1}H NMR of **H$_3$^{Ph}L**.

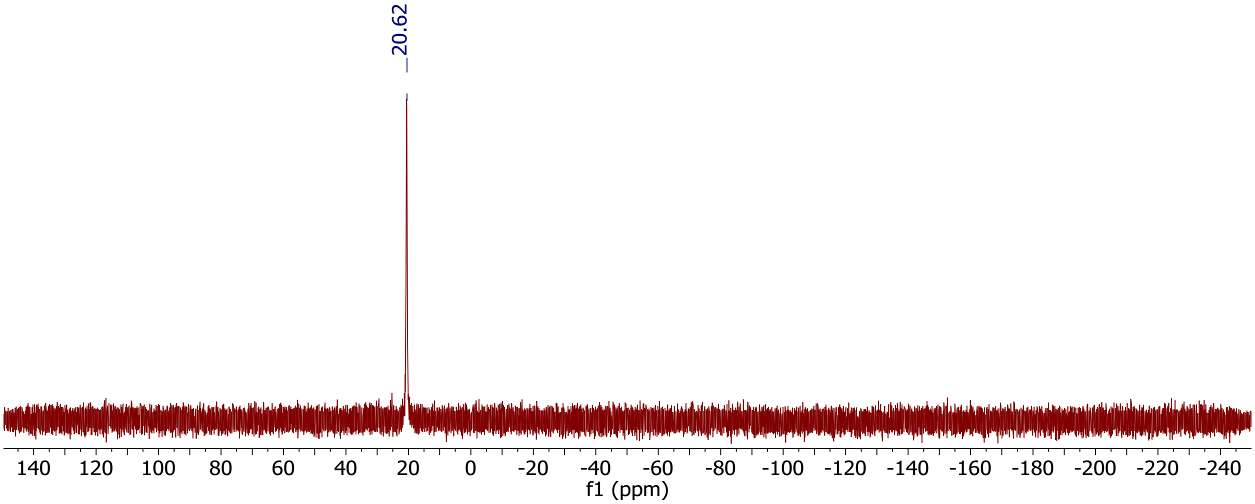

Figure S1.13. ^{31}P NMR of **H$_3$^{Ph}L**.

1.6 References

(1) Jasniewski, A. J.; Que, L. *Chem. Rev.* **2018**, *118* (5), 2554–2592.

(2) Larson, V. A.; Battistella, B.; Ray, K.; Lehnert, N.; Nam, W. *Nat. Rev. Chem. 2020 48* **2020**, *4* (8), 404–419.

(3) Fukuzumi, S.; Lee, Y. M.; Nam, W. *Dalton Transactions*. Royal Society of Chemistry July 3, 2019, pp 9469–9489.

(4) Chen, M. S.; White, M. C. *Science (80-.).* **2010**, *327* (5965), 533–571.

(5) Rittle, J.; Green, M. T. *Science (80-.).* **2010**, *330* (6006), 933–937.

(6) Costas, M.; Mehn, M. P.; Jensen, M. P.; Que, L. *Chem. Rev.* **2004**, *104* (2), 939–986.

(7) Oloo, W. N.; Que, L. *Acc. Chem. Res.* **2015**, *48* (9), 2612–2621.

(8) De Oliveira, F. T.; Chanda, A.; Banerjee, D.; Shan, X.; Mondal, S.; Que, L.; Bominaar, E. L.; Münck, E.; Collins, T. J. *Science (80-.).* **2007**, *315* (5813), 835–838.

(9) Dehnicke, K.; Krieger, M.; Massa, W. *Coord. Chem. Rev.* **1999**, *182* (1), 19–65.

(10) Dehnicke, K.; Weller, F. *Coord. Chem. Rev.* **1997**, *158*, 103–169.

(11) Guérin, F.; Stewart, J. C.; Beddie, C.; Stephan, D. W. *Organometallics* **2000**, *19* (16), 2994–3000.

(12) Stephan†, D. W. *Organometallics* **2005**, *24* (11), 2548–2560.

(13) Stephan, D. W. *Organometallics*. American Chemical Society May 23, 2005, pp 2548–2560.

(14) Camacho-Bunquin, J.; Ferguson, M. J.; Stryker, J. M. *J. Am. Chem. Soc.* **2013**, *135* (15), 5537–5540.

(15) Bai, T.; Janes, T.; Song, D. *Dalt. Trans.* **2017**, *46* (37), 12408–12412.

(16) Aguirre Quintana, L. M.; Yang, Y.; Ramanathan, A.; Jiang, N.; Bacsa, J.; Maron, L.; La Pierre, H. S. *Chem. Commun.* **2021**, *57* (54), 6664–6667.

(17) Rice, N. T.; Popov, I. A.; Russo, D. R.; Bacsa, J.; Batista, E. R.; Yang, P.; Telser, J.; La Pierre, H. S. *J. Am. Chem. Soc.* **2019**, *141* (33), 13222–13233.

(18) Gompa, T. P.; Ramanathan, A.; Rice, N. T.; La Pierre, H. S. *Dalt. Trans.* **2020**, *49* (45), 15945–15987.

(19) Scepaniak, J. J.; Harris, T. D.; Vogel, C. S.; Sutter, J.; Meyer, K.; Smith, J. M. *J. Am. Chem. Soc.* **2011**, *133* (11), 3824–3827.

(20) Fang, G. S.; Huang, J. S.; Zhu, N.; Che, C. M. *Eur. J. Inorg. Chem.* **2004**, *2004* (6), 1341–1348.

(21) Schendzielorz, F. S.; Finger, M.; Volkmann, C.; Würtele, C.; Schneider, S. *Angew. Chemie Int. Ed.* **2016**, *55* (38), 11417–11420.

(22) Wong, T. W.; Lau, T. C.; Wong, W. T. *Inorg. Chem.* **1999**, *38* (26), 6181–6186.

(23) Yi, X. Y.; Lam, T. C. H.; Sau, Y. K.; Zhang, Q. F.; Williams, I. D.; Leung, W. H. *Inorg. Chem.* **2007**, *46* (17), 7193–7198.

(24) Creutz, S. E.; Peters, J. C. *Inorg. Chem.* **2016**, *55* (8), 3894–3906.

(25) Lin, H. J.; Siretanu, D.; Dickie, D. A.; Subedi, D.; Scepaniak, J. J.; Mitcov, D.; Clérac, R.; Smith, J. M. *J. Am. Chem. Soc.* **2014**, *136* (38), 13326–13332.

(26) Chakarawet, K.; Bunting, P. C.; Long, J. R. *J. Am. Chem. Soc.* **2018**, *140* (6), 2058–2061.

(27) Chakarawet, K.; Atanasov, M.; Marbey, J.; Bunting, P. C.; Neese, F.; Hill, S.; Long, J. R. *J. Am. Chem. Soc.* **2020**, *142* (45), 19161–19169.

(28) Shoshani, M. M.; Agapie, T.; Li, R.; Chemcomm, /; Communication, C. *Chem. Commun.* **2020**, *56* (76), 11279–11282.

(29) Alhomaidan, O.; Bai, G.; Stephan, D. W. *Organometallics* **2008**, *27* (23), 6343–6352.
(30) Hollink, E.; Stewart, J. C.; Wei, P.; Stephan, D. W. *Dalt. Trans.* **2003**, *20* (20), 3968–3974.
(31) Ramos, A.; Stephan, D. W. *Dalt. Trans.* **2010**, *39* (5), 1328–1338.
(32) Siemeling, U.; Neumann, B.; Stammler, H.-G.; Kuhnert, O. *Zeitschrift für Anorg. und Allg. Chemie* **2000**, *626* (4), 825–826.
(33) Siemeling, U.; Kölling, L.; Stammler, A.; Stammler, H. G. *J. Chem. Soc. Dalt. Trans.* **2002**, No. 17, 3277–3279.
(34) Appel, R.; Kleinstück, R.; Ziehn, K. D.; Knoll, F. *Chem. Ber.* **1970**, *103* (11), 3631–3639.
(35) Legault, C.; Charette, A. B. *J. Org. Chem.* **2003**, *68* (18), 7119–7122.
(36) TAMURA, Y.; MINAMIKAWA, J.; IKEDA, M. *Synthesis (Stuttg).* **1977**, *1977* (01), 1–17.
(37) Tamura, Y.; Minamikawa, J.; Sumoto, K.; Fujii, S.; Ikeda, M. *J. Org. Chem.* **1973**, *38* (6), 1239–1241.

Chapter 2

1,2-Addition at a Phosphinimide Supported Zirconium Complex Highlights Isolobality to Imido Ligands

2.1 Introduction

Early transition metal complexes have been shown to activate a variety of X-H bonds across metal-ligand bonds with significant π-bonding character via 1,2-addition.[1] Since the seminal work from Wolczanski[2] and Bergman[3] (Figure 2.1) showcased the activation of strong C-H bonds across the metal-nitrogen multiple bond in low coordinate zirconium imido complexes, other groups have shown the activation of bonds across an array of metal-nitrogen and metal-carbon bonds.[4–9] The mechanism often invoked in these transformations is the combined interactions of the metal-ligand π-bond donating into the σ* of the X-H bond and the X-H σ-bond donating into an empty d-orbital on the transition metal center via a concerted four center transition state (Figure 2.3A).[1]

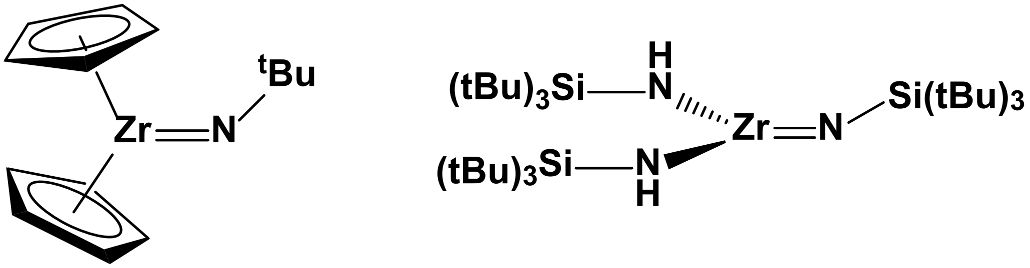

Figure 2.1. Literature precedent for 3-coordinate Zr Imidos for 1,2-Addition

The isolobal analogy predicts that two fragments which possess similar frontier molecular orbitals should have similar reactivity trends, even if they are not isostructural or isoelectronic.[10] Phosphinimide (PN) (Figure 2.2) ligands have been discussed due to their isolobality to cyclopentadienyl ligands in their application in olefin polymerization catalysts.[11,12] In their zwitterionic resonance form, these ligands are also isolobal to imido ligand as they contain a doubly anionic nitrogen capable of forming a sigma bond with a transition metal while maintaining cylindrical π-density . Indeed, these ligand fragments have been shown to have significant multiple bonding character with transition metal centers[13–18] and computational evidence has invoked the involvement of a transient nickel PN in the 1,2-activation of unactivated C-H bonds.[19]

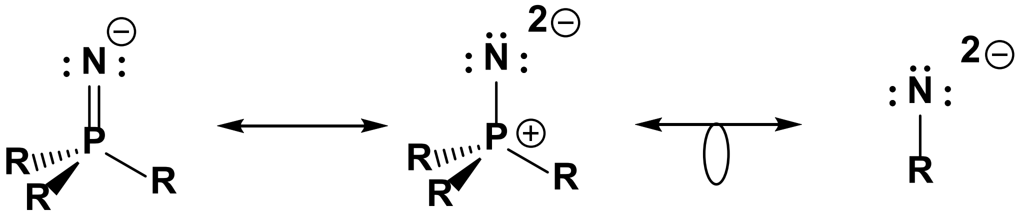

Figure 2.2. Phosphinimide resonance structures and isolobality to imidos

We hypothesized that the synthesis of a tris(phosphinimide) zirconium, analogous to the early Group(IV) complexes in 1,2-addition chemistry, would allow for the rational exploration of the ability of PN's to activate X-H type bonds via 1,2-addition (Figure 2.3B). We chose a rigid, tridentate platform to enforce quasi-linear PN-Zr bonds to maximize the π-interactions between the metal and the PN. Synthesis of a tris(PN) zirconium benzyl complex and the subsequent abstraction of the benzyl complex by a Lewis acid resulted in a tris(PN) zirconium cationic species capable of activating a variety of X-H type bonds including the N-H bonds of anilines and the C-H bonds of phenylacetylene, acetophenone, and nitromethane. These results highlight the isolobality of phosphinimides to imidos as well as their ability to not just be ancillary ligands but also participate in bond activation.

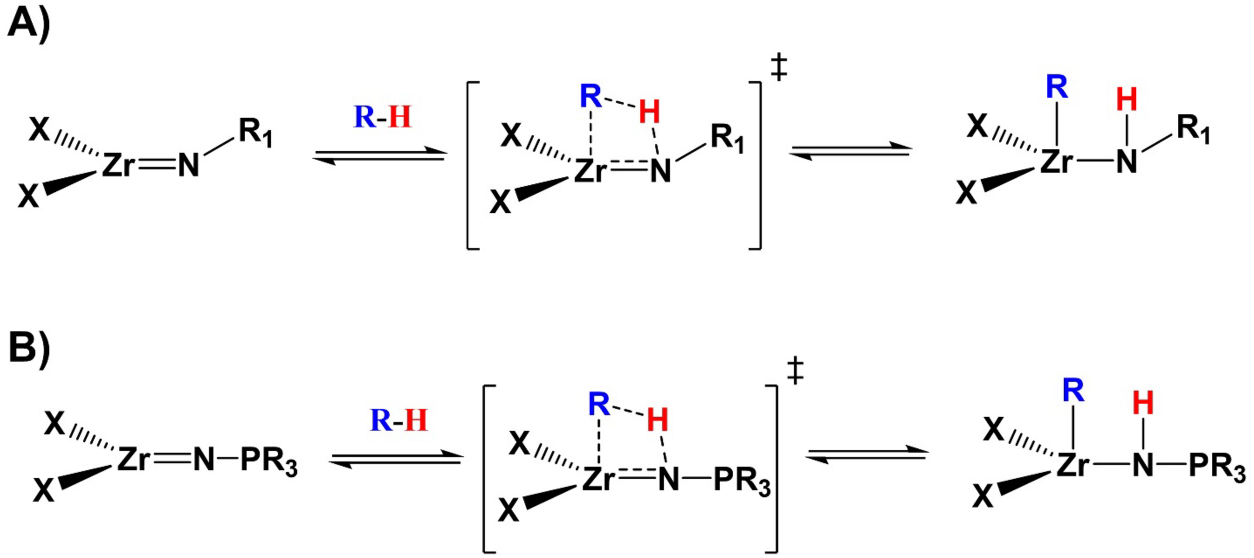

Figure 2.3. (A) Established mechanism for 1,2-RH addition to Zr imidos (B) Proposed analogous mechanism for 1,2-RH addition to Zr PN's (this work)

2.2 Results and Discussion

Terminally-bound phosphinimides are capable of being 5-electron donors.[11,20] Their usage has primarily been applied to using monodentate platforms to stabilize early transition metal olefin polymerization catalysts[21] and high-valent lanthanides[22]. The framework utilized here is a trisPN ligand with sterically crowded substituents to enforce monometallic complexes and allow for the PN's to maximize their donation to a single metal center. Additionally, the usage of PN's as imido surrogates allows for tracking of reactivity using ^{31}P-NMR as a convenient spectroscopic handle.

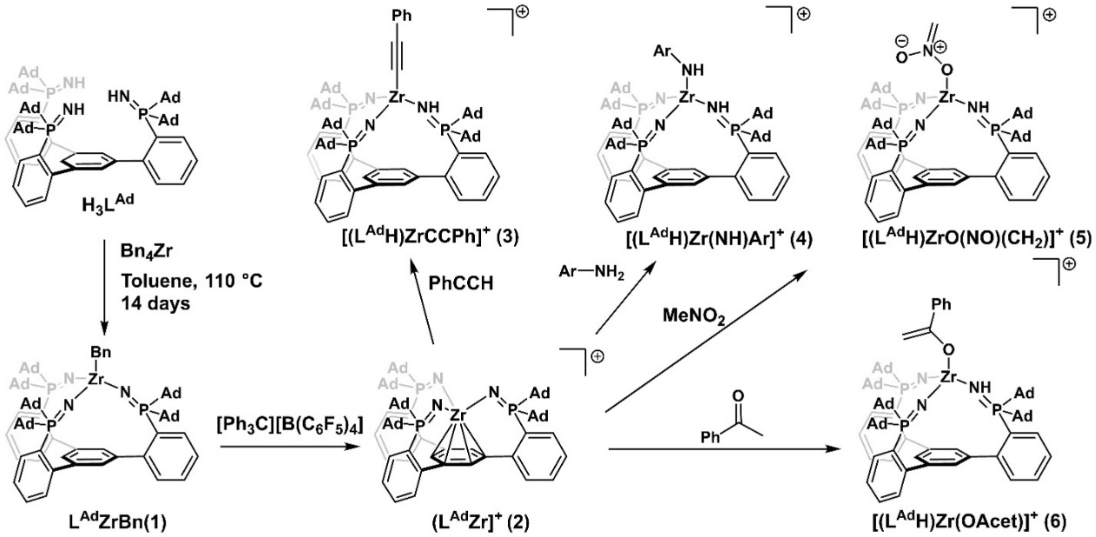

Scheme 2.3. Synthesis of the described complexes

To access a metal center with an open coordinate site to perform 1,2-addition, we sought to synthesize an L^{Ad}ZrX complex where the X-type ligand could be removed via Lewis acid abstraction. Upon combining the proligand **L^{Ad}H$_3$** with 1 equivalent of Bn$_4$Zr at room temperature, ^{31}P-NMR aliquots showed that two PN's were metalated via protonolysis where as one PN remained as an unbound phosphinimine (Figure S2.1). Upon toluene reflux, the formation of a new species with only a ^{31}P-NMR resonance consistent with all the PN's bound to a Zr center could be seen slowly growing in at 6 ppm (Figure S2.1), with complete conversion observed after 14 days of heating at reflux. The requirement of extended periods of heating is a testament to both the sterically encumbering nature of this platform as well as its thermal stability and that of **1**. ^{1}H-NMR analysis indicated that the resulting product is a three-fold symmetric product consistent with **L^{Ad}ZrBn (1)** (Scheme 2.1). The structure of this compound was confirmed with single crystal XRD (Figure 2.4). The Zr-NP bond distances are roughly identical with an average of 2.022 Å, consistent with previously published Zr-NP bond metrics[23], and has an average PNZr bond angle of 165.5°, indicating a significant contribution of the zwitterionic resonance structure due to being closer to a linear geometry than trigonal. The Zr-NP distance of **1** is shorter than the typical Zr-N(primary amido) bond (~2.1 Å) and longer than typical Zr-N(imido) bonds (~1.85-1.9 Å)[24], indicating that the degree of π-bonding between the Zr and the phosphinimide nitrogen is less than an imido but more than an amido.

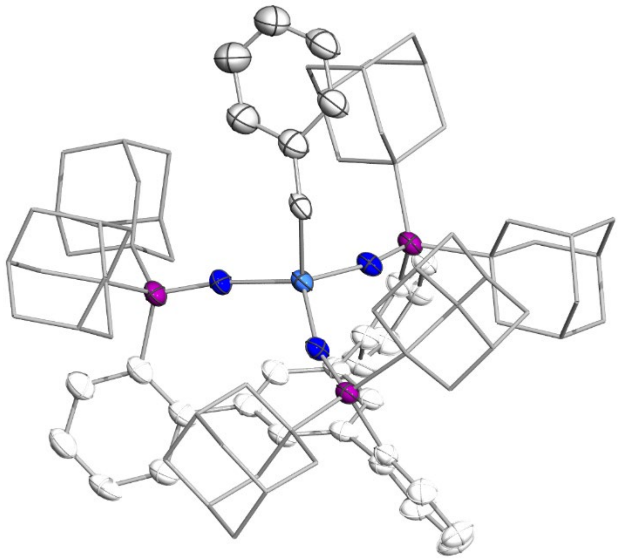

Figure 2.4. XRD structure of **1**. Thermal ellipsoids are drawn at 50% probability. Solvent molecules and C-H bonds have been removed. Portions of the ligand framework are hidden for clarity.

The reaction of **1** with Lewis acid $[Ph_3C][B(C_6F_5)_4]$, which is known to abstract benzyl groups from Group(IV) metal centers[25], resulted in full consumption of **1** by ^{31}P NMR within minutes at ambient temperature(Figure 2.5) concurrent with the formation of a new, three-fold symmetric species with a ^{31}P resonance at 18 ppm. Comparison of the ^{1}H-NMR features of the spectra show consumption of the benzylic protons of **1** and a 0.2ppm downfield shift of the proton of the central arene of the ligand (Figure S2.2), which is consistent with the formation of a cationic 18-electron Zr-arene complex (**2**, Scheme 2.1).[26]

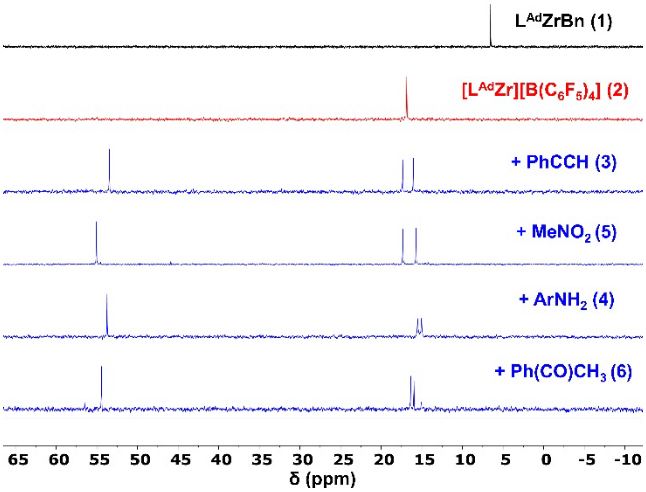

Figure 2.5. $^{31}P\{^{1}H\}$ NMR spectra illustrating the conversion of **1** (black) to **2** (red) and the subsequent 1,2-additions upon adding substrates (blue).

After addition of 1 equivalent of phenylacetylene to a solution of **2**, ^{31}P-NMR showed the complete consumption of **2** and the formation of a new, desymmetrized species consistent with two Zr-NP (~17 ppm) and one Zr-(NH)P (~ 55 ppm) (Figure 2.5). FTIR analysis of the resulting product showed both the formation of an NH band at (3293 cm^{-1}) and a Zr-acetylide band at (2077 cm^{-1}) (Figure S2.5), supporting that the acetylide C-H bond had activated across one of the Zr-NP bonds to form **3** (Scheme 2.1). Single crystal XRD on the product confirmed the assignment of **3** as the product of 1,2-addition of phenylacetylene to **2** (Figure 2.6). The Zr-NP bonds are now 1.974 Å, 2.026 Å, and 2.121 Å, with one of the Zr-NP bonds elongated significantly relative to **1**, indicating that one of the PN's has been protonated to a phosphinimine. This is further supported by the ZrNP bond angle of the elongated ZrNP bond, which has decreased to 149.36°. The Zr-C and the C-C triple bond distances are 2.210 Å and 1.242 Å , respectively. These rank as the shortest Zr-C and the longest C-C triple bond of a Zr phenylacetylide in CCSD.[24]

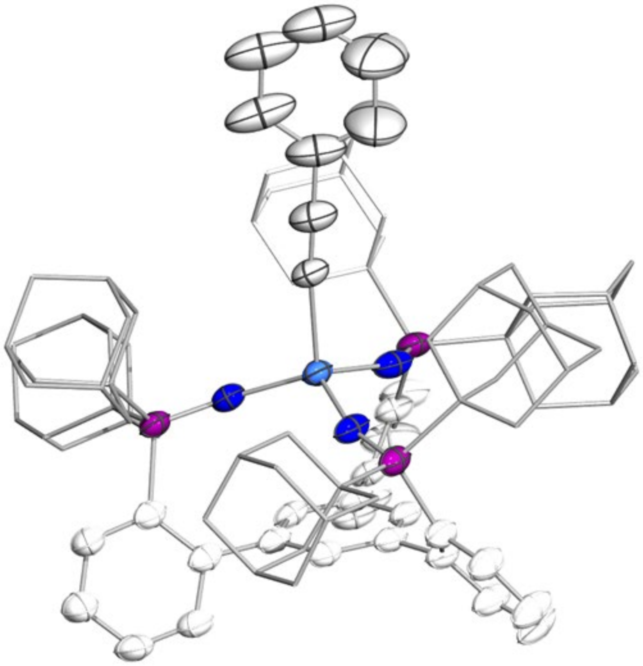

Figure 2.6. XRD structure of **3**. Thermal ellipsoids are drawn at 50% probability. *C*ounterions, solvent molecules, and C-H bonds have been removed. Portions of the ligand framework are hidden for clarity.

Addition of *p*-anisidine to a solution of **2** showed a similar desymmetrization of the ^{31}P-NMR to form **4** (Figure 2.5). FTIR indicated the formation of a broad NH band (3374 cm^{-1}) (Figure S2.6), supporting that the aniline N-H bond had activated across a Zr-NP bond. Single crystal XRD analysis of **4** confirmed the N-H activation of the aniline (Figure 2.7). Similar to **3**, one of the Zr-NP distances was significantly elongated (to 2.204 Å) concurrent with a decrease in the ZrNP bond angle (to 146.4°), indicating that there was one phosphinimine bound to the Zr.

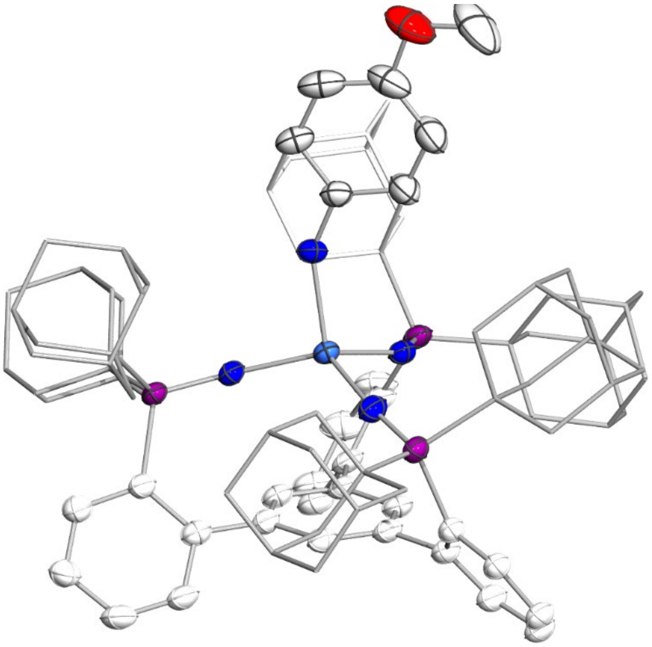

Figure 2.7. XRD Structure of **4**. Thermal ellipsoids are drawn at 50% probability. Counterions, solvent molecules, and C-H bonds have been removed. Portions of the ligand framework are hidden for clarity.

Reaction of **2** with 1 equivalent of nitromethane resulted in the complete conversion to a new species (**5**) by ^{31}P-NMR that has the indicative desymmetrization that was observed for both **3** and **4** (Figure 2.5), indicating that is had undergone a 1,2-addition. To the best of our knowledge, this is both the first observation of 1,2-addition of nitromethane at Zr and the first nitromethane adduct of Zr, although Zr nitronates have been previously characterized.[27] Deprotonated nitromethane has been observed to bind both at the carbon or oxygen.[28] ^{1}H-^{13}C HSQC was utilized to differentiate between the two binding modes (Figure S2.22); a new proton feature at 5.22 ppm derived from nitromethane correlates with a ^{13}C resonance at 104.5 ppm, which is consistent with assigning it as bound at the oxygen (Scheme 2.1).[28]

Upon the reaction of **2** with 1 equivalent of acetophenone, ^{31}P-NMR showed full conversion to a 1,2-addition product within minutes at room temperature (Figure 2.5). Just as with nitromethane, deprotonated acetophenone can be bound either at the carbon or at the oxygen.[29-31] ^{1}H-^{13}C HSQC (Figure S2.26) analysis showed an acetophenone derived peak in the ^{1}H-NMR at 4.61 ppm correlates with a ^{13}C resonance at 91.36 ppm, supporting an oxygen bound enolate structure consistent with other early metal acetophenone adducts.[29-30]

In order to ascertain whether the observed X-H bond activation was primarily pKa driven (the pKa's of activated substrates range from about 17-30[32-35]), a series of para-substituted toluenes with known pKas were reacted with **2** to check for evidence of 1,2-addition of the benzylic C-H bonds. These were chosen due to the wide and well-established pKa ranges based on the para-substituent and their essentially isosteric profile to aniline. The substituents tested (R = H, CN, COPh, and NO_2) encompassed a pKa range from 20-43[36], well within the range of the activated substrates, and none of these species showed the diagnostic changes in the ^{31}P NMR that occur upon 1,2-addition even upon extended heating (Figure S2.3), with the only noticeable change being a slight shift of the peak upon *p*-tolunitrile coordination. The lack of reactivity with toluenes more acidic than substrates that are activated indicate that the activation of substrates by **2** isn't solely pKa driven and supports that the coordination of the X group to the Zr also plays a significant role in what X-H type bonds are activated across the Zr-N bond. These results are consistent with well-precedented 1,2-RH processes which show a concerted process that is thermodynamically driven by the strength resulting M-X bond.

Group(IV) imidos have been shown to activate bonds as strong as methane via 1,2-addition[2]. The mechanism of this type of reactivity has been discussed to be a combination of σ-acidity at the metal center and π-basicity at the imido.[1] The ability of imido complexes being able to cleave stronger X-H bonds than **2** can be rationalized with this mechanistic picture. The formation of the stable, 18-electron arene complex will decrease the σ-acidity of the Zr center while the phosphinimide nitrogen is less π-basic than the formally dianionic imido ligand, as highlighted by the Zr-N distance of a **1** being longer than the typical bond metrics of an Zr-N(imido) bond.

2.3 Conclusions

In summary, a trisphosphinimide Zr platform has been prepared utilizing a sterically encumbered tridentate ligand. Upon Lewis acid abstraction of the benzyl group from precursor, a cationic Zr arene complex is formed. The reaction of this arene complex with a variety of X-H type bonds (phenylacetylenes, anilines, nitromethane, and acetophenone) resulted in the 1,2-addition of the bonds across the Zr-N bonds, as observed by a combination of NMR, FTIR, and XRD experiments. The capability of this early metal phosphinimide complex to perform 1,2-addition highlights the significant multiple bonding character of Zr-NP bonds as well as their ability to act as more than ancillary ligands in bond activation processes. This reactivity also showcases the isolobal analogy predicting the reactivity of Zr phosphinimides as PN's are isolobal to imido ligands whose ability to perform 1,2-addition on early metals has been extensively studied. While these complexes are not as capable of activating strong C-H bonds as compared to imido systems, this lessened reactivity allowed for handling in a variety of convenient solvents and conditions, and studies into further transformations enabled by this reactivity are currently underway.

2.4 Acknowledgements

This research was supported by the University of California Berkeley. We thank Dr. Heui Beom Lee for assistance with XRD and for helpful discussions. We thank Drs. Hasan Celik, Alicia Lund, and UC Berkeley's NMR facility in the College of Chemistry (CoC-NMR) for spectroscopic assistance. Instruments in the CoC-NMR are supported in part by NIH S10OD024998.

2.5 Supporting Information

General Considerations: Unless otherwise noted, all manipulations were carried out using standard Schlenk or glovebox techniques under an N_2 atmosphere. Acetonitrile (MeCN), Benzene, Diethyl ether (Et_2O), Pentane, Tetrahydrofuran (THF), and Toluene were deoxygenated by thoroughly sparging with N_2 gas followed by passing through an activated alumina column in a solvent purification system from Pure Process Technology, and were further dried over 4Å molecular sieves for 48h prior to use. Solvents were routinely tested with a THF solution of sodium benzophenone ketyl. Deuterated solvents were purchased from Cambridge Isotope Laboratories, Inc., and were distilled under N_2, degassed via freeze-pump-thaw cycles, and stored over 4Å molecular sieves prior to use. All reagents were purchased from commercial vendors and used without further purification unless otherwise stated. **$L^{Ad}H_3$**[14], Bn_4Zr[37], $[Ph_3C][B(C_6F_5)_4]$[38], and C_6D_5Br[39] were prepared according to literature procedures. Elemental analyses were performed by the Microanalytical Laboratory in the College of Chemistry at the University of California – Berkeley using a PerkinElmer 2400 Series II combustion analyzer.

Nuclear Magnetic Resonance Spectroscopy: Nuclear Magnetic Resonance (NMR) spectra were measured at Bruker AV-300, AVQ-400, NEO-500, or AV-600 spectrometers. ^1H and ^{13}C chemical shifts are reported in ppm relative to tetramethylsilane (TMS) at 0.00 ppm using residual solvent residues as internal standards. ^{31}P chemical shifts are reported in ppm relative to 85% aqueous H_3PO_4 at 0 ppm.

Infrared Spectroscopy: Solid IR measurements were obtained on a Nicolet iS20 Spectrometer as KBr pellets.

X-Ray Crystallography: XRD studies were performed at the Small Molecule X-Ray Crystallography Facility (CheXray). Crystals were mounted on a Kapton loop under Paratone oil. Data were collected on a Rigaku XtalLAB P200 (MoKα or CuKα radiation) equipped with a MicroMax-007 HF microfocus rotating anode and a Pilatus 200K hybrid pixel array detector at 100 K under a stream of N_2. Data collection, integration, and scaling were carried out using the CrysAlis^{Pro} software.[40]

Structures were solved using SHELXS and refined against F^2 on all data by full matrix least-squared with SHELXL using OLEX2 crystallographic software.[41] All non-hydrogen atoms were refined using anisotropic displacement parameters. Hydrogen atoms were placed in idealized positions and refined using a riding model.

Synthetic Procedures:

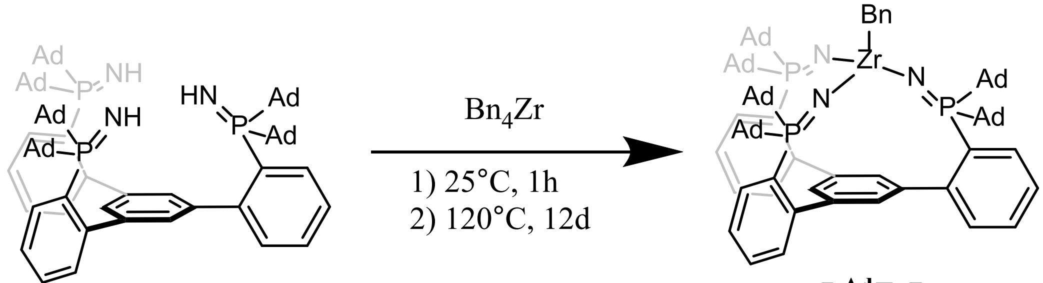

L^{Ad}ZrBn

Scheme S2.1. Synthesis of **1**

L^{Ad}ZrBn(1): In the glove box, **L^{Ad}H$_3$** (400 mg, 0.3 mmol, 1 Equiv) was loaded into a 20mL vial with Toluene (10 mL) and a stir bar. Bn$_4$Zr (144 mg, 0.3 mL, 1 Equiv) was added as a solution in Toluene (5 mL). The vial containing the Bn$_4$Zr solution was rinsed with additional toluene (2 mL). The reaction was stirred for 1h at ambient temperature and then transferred to a 50 mL Schlenk tube. The vial was rinsed with additional Toluene (5 mL). The Schlenk tube was sealed, removed from the glove box, and transferred to a preheated 120 °C oil bath. After 14 days, the reaction was cooled to ambient temperature and transferred into the glove box. The contents were transferred to a 100mL round-bottomed flask, The tube was rinsed with additional Toluene (5 mL). The volatiles were removed in vacuo and the solid residue was triturated with Pentane. The solid residue was washed with Et$_2$O (2 x 10 mL) and extracted into Benzene (40 mL). Removal of the volatiles in vacuo gave spectroscopically pure **LZrBn** as a beige powder (432 mg, 0.3 mmol, 94.6 %). Single crystals of **LZrBn** suitable for X-ray diffraction were grown from layering pentane onto a concentrated Et$_2$O solution of **LZrBn** to give colorless blocks. ^{1}H NMR (400 MHz, Benzene-*d*$_6$) δ 7.92 (s, 3H), 7.83 (t, *J* = 8.3 Hz, 3H), 7.59 (d, *J* = 7.6 Hz, 2H), 7.41 (m, 3H), 7.37 – 7.29 (m, 2H), 7.18 (m, 6H), 6.94 (t, *J* = 7.3 Hz, 1H), 3.21 (d, *J* = 10.5 Hz, 1H), 2.93 (d, *J* = 10.6 Hz, 1H), 2.54 – 2.37 (m, 36H), 2.15 – 2.06 (m, 9H), 1.97 – 1.88 (m, 18H), 1.83 – 1.74 (m, 9H), 1.67 – 1.53 (m, 18H). ^{31}P NMR (162 MHz, C$_6$D$_6$) δ 6.54. ^{13}C NMR (151 MHz, C$_6$D$_6$) δ 155.17, 150.38, 139.33, 134.04, 133.00, 131.25, 130.82, 129.11, 128.76, 128.60, 128.36, 127.03, 124.59, 119.31, 56.04, 39.76, 38.57, 37.21, 36.93, 28.99. Anal: calc. for C$_{91}$H$_{112}$N$_3$P$_3$Zr: C 76.32, H 7.88, N 2.93; found: C 74.4, H 7.78, N 2.82.

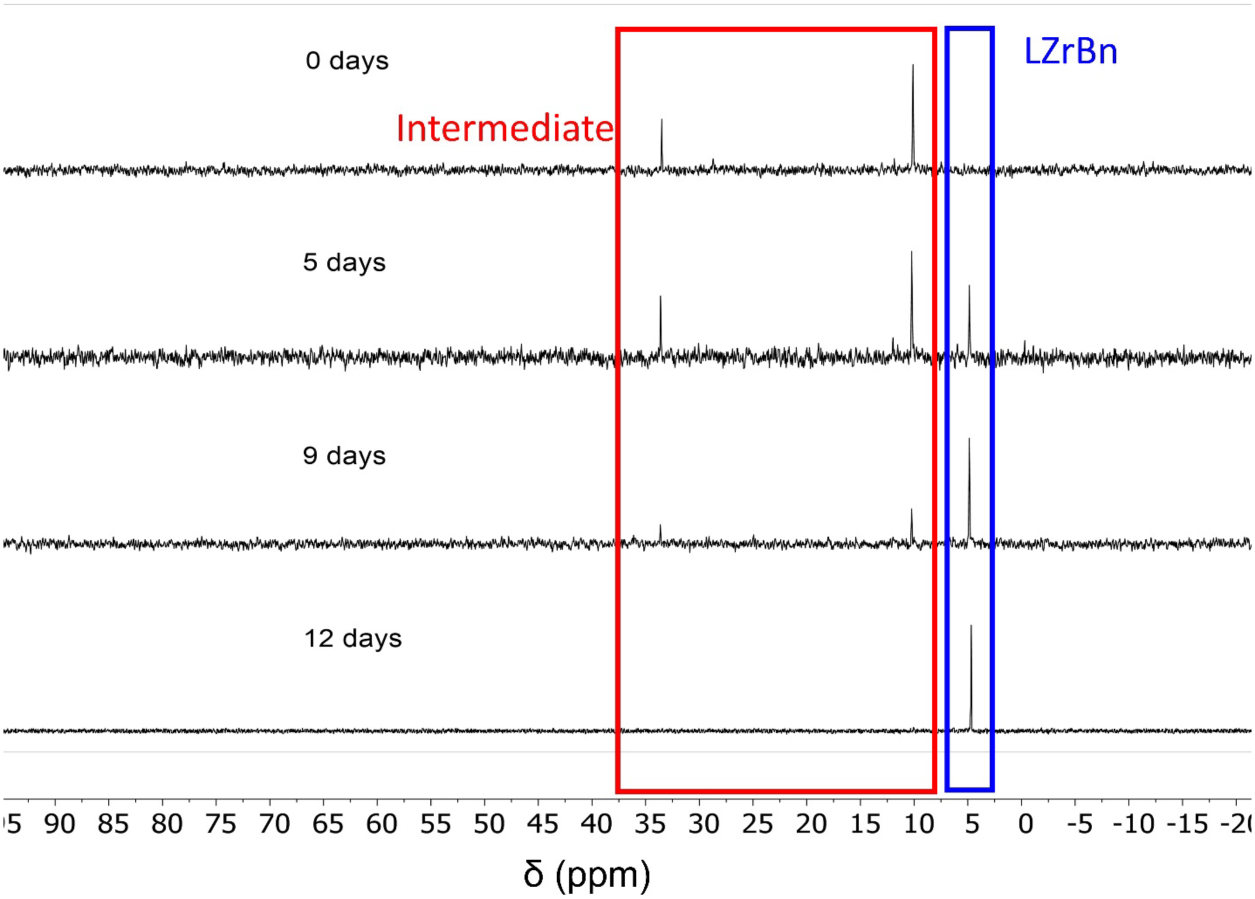

Figure S2.1. ^{31}P NMR (400 MHz, 298K) of **LZrBn** synthesis aliquots after heating at 120 °C for x days

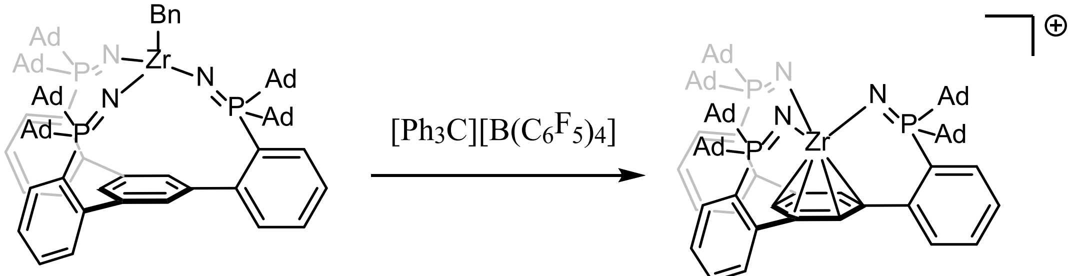

$L^{Ad}ZrBn$

$[L^{Ad}Zr]^+$

Scheme S2.2. Synthesis of **2**

$[L^{Ad}Zr]^+$(2): In the glovebox, **$L^{Ad}ZrBn$ (**15.0 mg, 10.5 μmol) was weighed out into a 4 mL crystallization vial and dissolved in C_6D_6 or C_6D_5Br (0.7 mL). $[Ph_3C][B(C_6F_5)_4]$ (1 Equiv) was added as stock solutions in C_6D_6 or C_6D_5Br. The solution was mixed with a pipette and transferred to a J-Young tube, sealed, and removed from the glovebox to be immediately analyzed. The reaction was shown to occur quantitatively by ^{31}P NMR within minutes at room temperature. ^1H NMR (600 MHz, Benzene-d_6) δ 7.98 (s, 3H), 7.53 (t, J = 8.5 Hz, 3H), 7.20 (m, 6H), 7.11 – 7.08 (m, 6H), 2.30 – 1.34 (m, 90H). ^{31}P NMR (243 MHz, C_6D_6) δ 17.31. ^{13}C NMR (151 MHz, C_6D_6) δ 147.18, 142.45, 139.00, 138.85, 137.90, 132.88, 132.57, 131.57, 131.26, 129.92, 129.34, 126.21, 124.10, 115.58, 44.88, 41.85, 39.06, 37.96, 36.38, 34.44, 28.75, 28.33.

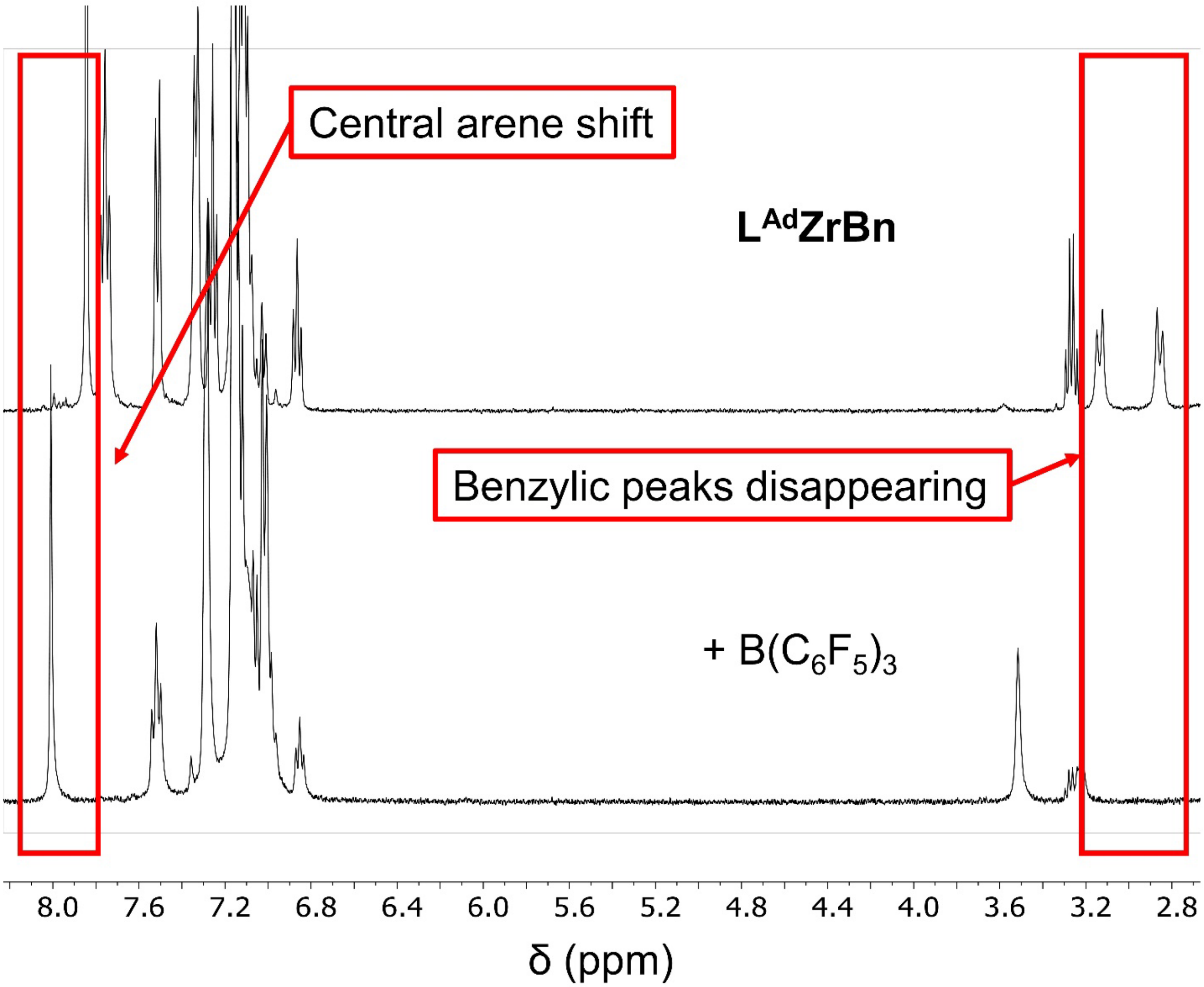

Figure S2.2. ^{1}H NMR (400 MHz, 298L) supporting formation of arene interaction in **2**.

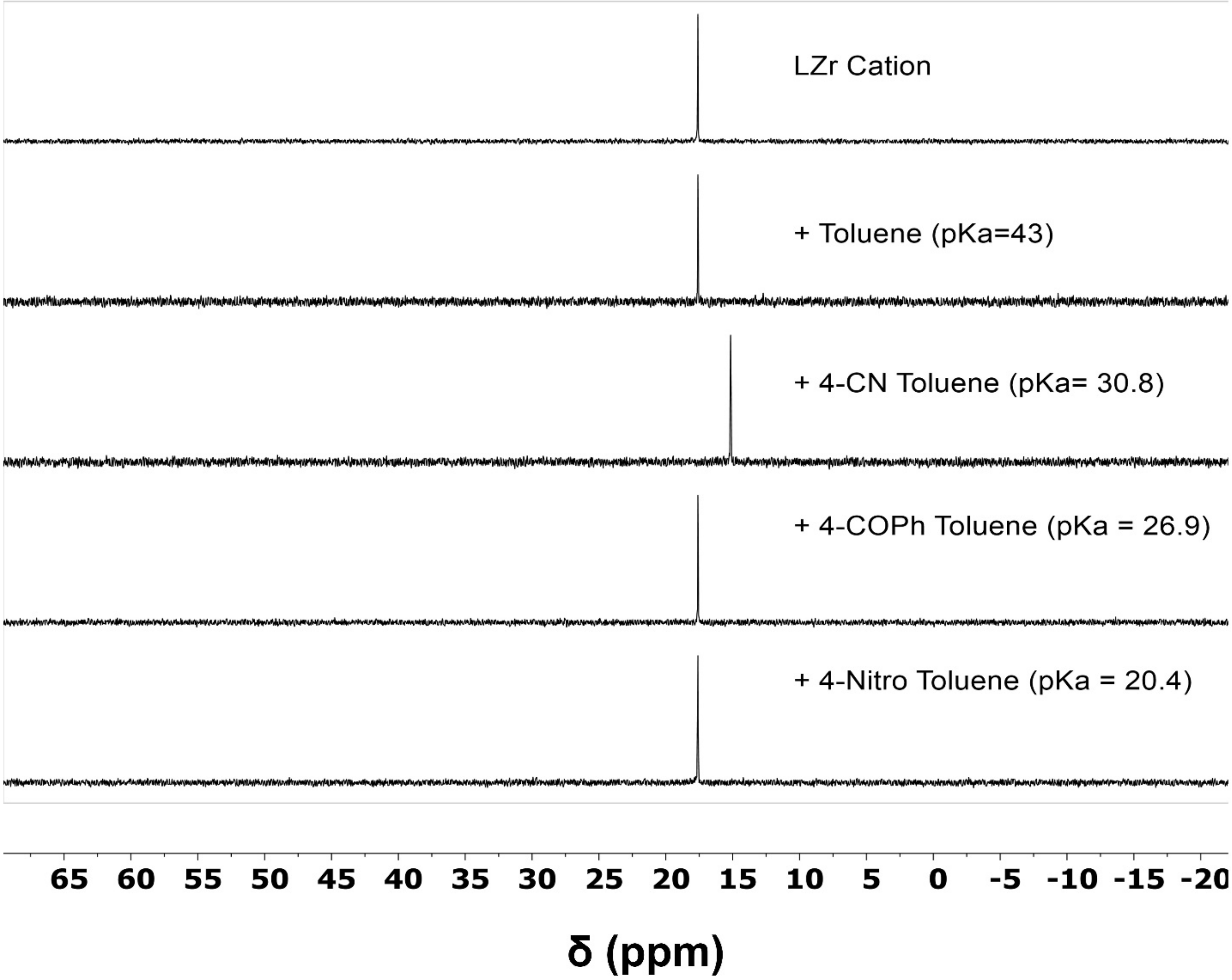

FigureS2.3. ^{31}P NMR (162 MHz, 298K) showing the lack of reactivity of **2** with toluene benzylic C-H bonds over a wide range of pKa's.[35]

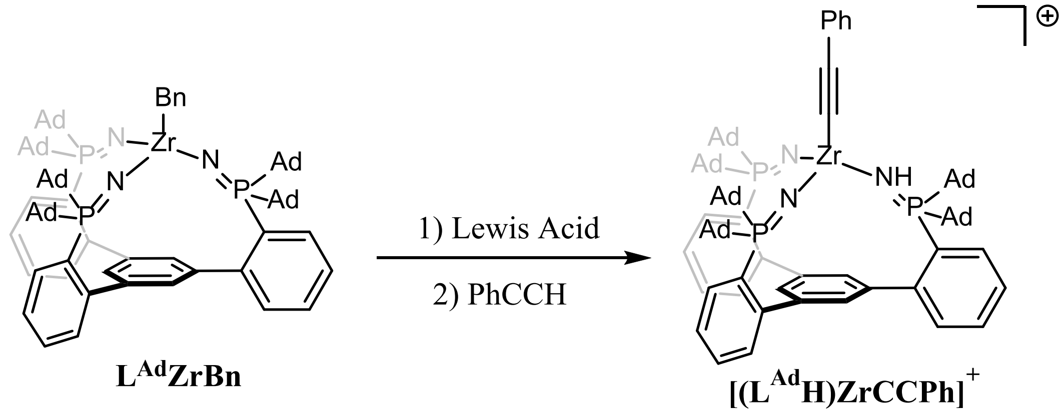

Scheme S2.3. Synthesis of **3**

[(L^{Ad}H)ZrCCPh]$^+$ (3): In the glovebox, **L^{Ad}ZrBn (**25.0 mg, 17.5 μmol) was weighed out into a 20 mL scintillation vial with a magnetic stir bar and dissolved in benzene (3 mL). $[Ph_3C][B(C_6F_5)_4]$ (1 Equiv) was added as a stock solution in benzene and the reaction was stirred for 5 minutes. Phenyl acetylene (1 Equiv) was added as a stock solution in benzene and the reaction was allowed to stir for an additional 5 minutes, by which time ^{31}P-NMR aliquots showed quantitative conversion to **[(L^{Ad}H)ZrCCPh]$^+$**. Crystals suitable for X-Ray Diffraction of **[(L^{Ad}H)ZrCCPh][B(C_6F_5)$_4$]** were grown from standing benzene after concentration to ~2 mL and filtration into a 4mL crystallization vial. ^{1}H NMR (600 MHz, Benzene-*d*$_6$) δ 7.80 (dt, *J* = 15.9, 1.7 Hz, 2H), 7.56 (m 3H), 7.52 – 7.47 (m, 2H), 7.40 – 7.38 (m, 1H), 7.26 (m, 2H), 7.20 – 7.17 (m, 4H), 7.08 (m, 6H), 2.53 – 1.27 (m, 90H). ^{31}P NMR (162 MHz, Benzene-d$_6$) δ 52.27, 15.59, 14.53.^{13}C NMR (151 MHz, C_6D_6) δ 149.70, 148.09, 144.11, 142.05, 138.62, 137.53, 136.57, 136.00, 132.02, 130.73, 129.54, 128.95, 128.43, 126.18, 126.00, 115.13, 83.55, 77.44, 39.16, 38.85, 38.12, 37.81, 37.64, 36.25, 35.88, 35.22. Anal: calc. for $C_{91}H_{112}N_3P_3Zr$: C 65.66, H 5.27, N 1.98; found: C 65.89, H 5.50, N 1.95.

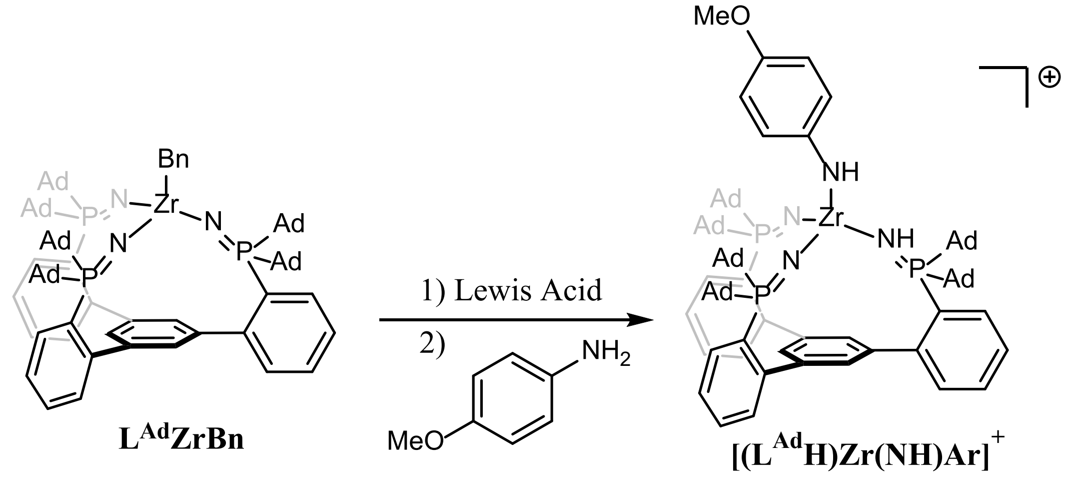

Scheme S2.4. Synthesis of **4**

[(L^{Ad}H)Zr(NH)Ar]$^+$(4): In the glovebox, **L^{Ad}ZrBn (**25.0 mg, 17.5 μmol) was weighed out into a 20 mL scintillation vial with a magnetic stir bar and dissolved in benzene (3 mL). [Ph_3C][$B(C_6F_5)_4$] (1 Equiv) was added as a stock solution in benzene and the reaction was stirred for 5 minutes. p-Methoxyaniline (1 Equiv) was added as a stock solution in benzene and the reaction was allowed to stir for an additional 5 minutes, by which time ^{31}P-NMR aliquots showed quantitative conversion to **[(L^{Ad}H)Zr(NH)Ar]$^+$**. Crystals suitable for X-Ray Diffraction of **[(L^{Ad}H)Zr(NH)Ar][$B(C_6F_5)_4$]** were grown from standing benzene after concentration to ~2 mL and filtration into a 4mL crystallization vial. ^{1}H NMR (600 MHz, Benzene-*d*$_6$) δ 7.73 (d, *J* = 24.6 Hz, 2H), 7.57 – 7.43 (m, 4H), 7.39 – 7.35 (m, 1H), 7.28 (s, 1H), 7.11 – 7.04 (m, 7H), 6.87 – 6.83 (m, 2H), 6.32 (d, *J* = 8.2 Hz, 2H), 3.36 (s, 3H), 2.62 (s, 1H), 2.40 – 1.09 (m, 90H). ^{31}P NMR (243 MHz, C_6D_6) δ 54.62, 15.99, 15.68. ^{13}C NMR (151 MHz, C_6D_6) δ 153.23, 150.12, 148.27, 144.37, 140.87, 139.00, 137.68, 129.92, 129.75, 129.34, 116.33, 115.12, 55.29, 38.63, 38.22, 36.28, 35.64, 34.44, 28.16.

Anal: calc. for $C_{91}H_{112}N_3P_3Zr$: C 64.45, H 5.36, N 2.61; found: C 62.39, H 5.40, N 2.43.

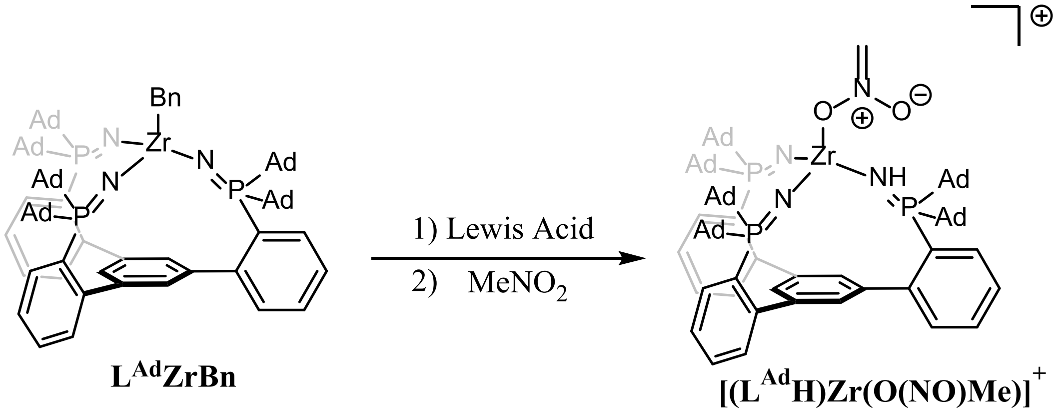

Scheme S2.5. Synthesis of **5**

[(L^{Ad}H)Zr(O(NO)CH$_2$]$^+$ (5): In the glovebox, **L^{Ad}ZrBn (**15.0 mg, 10.5 μmol) was weighed out into a 4 mL crystallization vial and dissolved in C_6D_6 or C_6D_5Br (0.7 mL). $[Ph_3C][B(C_6F_5)_4]$ (1 Equiv) was added as stock solutions in C_6D_6 or C_6D_5Br. Nitromethane (1 Equiv) was added as a stock solution in C_6D_6 or C_6D_5Br. The solution was mixed with a pipette and transferred to a J-Young tube, sealed, and removed from the glovebox to be immediately analyzed. The reaction was shown to have quantitative conversion to **[(L^{Ad}H)Zr(O(NO)CH$_2$]$^+$**by ^{31}P NMR within minutes at room temperature. ^{1}H NMR (600 MHz, Benzene-*d*$_6$) δ 7.94 (s, 1H), 7.81 (s, 1H), 7.64 – 7.46 (m, 3H), 7.41 – 7.24 (m, 4H), 7.11 – 7.05 (m, 6H), 5.24 (s, 2H), 2.40 – 1.14 (m, 90H). ^{31}P NMR (243 MHz, C_6D_6) δ 55.19, 16.98, 15.49. ^{13}C NMR (151 MHz, C_6D_6) δ 149.69, 148.17, 146.78, 138.62, 137.55, 135.96, 129.03, 128.98, 126.77, 126.21, 126.03, 125.35, 104.49, 39.02, 37.91, 36.09, 35.37, 28.68, 28.05, 27.76.

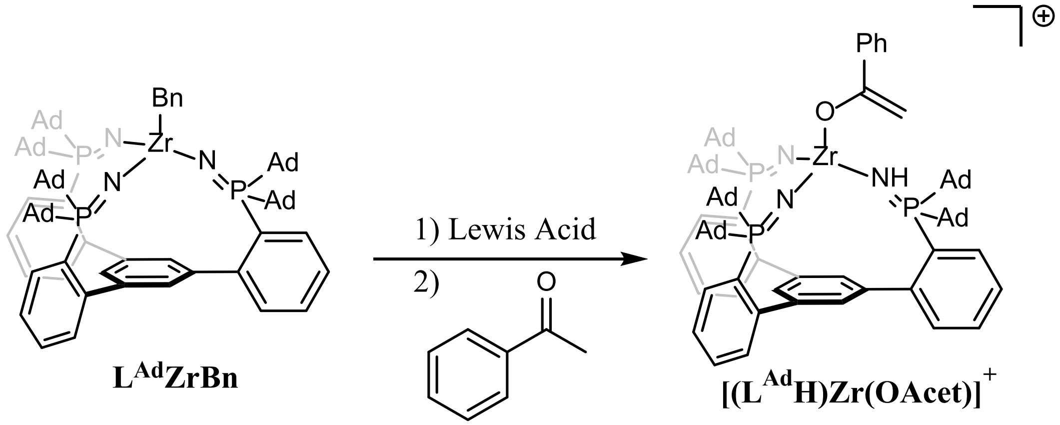

Scheme S2.6. Synthesis of **6**

[(L^{Ad}H)Zr(OAcet)]$^{+}$ (6): In the glovebox, **L^{Ad}ZrBn (**15.0 mg, 10.5 μmol) was weighed out into a 4 mL crystallization vial and dissolved in C_6D_6 or C_6D_5Br (0.7 mL). [Ph_3C][$B(C_6F_5)_4$] (1 Equiv) was added as stock solutions in C_6D_6 or C_6D_5Br. Acetophenone (1 Equiv) was added as a stock solution in C_6D_6 or C_6D_5Br. The solution was mixed with a pipette and transferred to a J-Young tube, sealed, and removed from the glovebox to be immediately analyzed. The reaction was shown to have quantitative conversion to **[(L^{Ad}H)Zr(OAcet)]$^{+}$** by ^{31}P NMR within minutes at room temperature. ^{1}H NMR (600 MHz, Benzene-*d*$_6$) δ 7.82 (d, *J* = 1.6 Hz, 1H), 7.80 (s, 1H), 7.77 – 7.74 (m, 1H), 7.65 – 7.61 (m, 2H), 7.61 – 7.51 (m, 3H), 7.48 (s, 1H), 7.15 – 7.08 (m, 9H), 4.62 (, *J* = 6.3 Hz, 2H), 2.28 – 1.29 (m, 90H).^{31}P NMR (243 MHz, C_6D_6) δ 55.25, 17.22, 16.83.^{13}C NMR (151 MHz, C_6D_6) δ 164.48, 149.66, 148.04, 141.11, 139.95, 138.62, 135.95, 134.62, 132.80, 132.13, 130.69, 129.54, 128.96, 126.29, 126.00, 115.20, 91.39, 39.41, 38.88, 38.30, 37.93, 37.65, 37.53, 36.19, 36.09, 35.89, 35.80, 35.27, 35.18, 28.50, 27.94, 27.78, 27.59.

X-Ray Crystallography

Identification code	**1**	**3**	**4**
Empirical formula	$C_{97}H_{113}N_3O_{1.5}P_3Zr$	$C_{116}H_{110}BF_{20}N_3P_3Zr$	$C_{139}H_{134}BF_{20}N_4OP_3Zr$
Formula weight	1529.03	2121.00	2451.43
Temperature/K	293(2)	293(2)	293(2)
Crystal system	monoclinic	triclinic	triclinic
Space group	C2/c	P-1	P-1
a/Å	29.2888(3)	19.2049(3)	18.8075(3)
b/Å	24.7986(2)	19.3910(3)	19.3521(3)
c/Å	24.21026(18)	19.7181(3)	19.3584(3)
α/°	90	63.620(2)	64.4279(14)
β/°	106.1472(10)	62.224(2)	64.5034(15)
γ/°	90	84.9100(10)	85.6681(12)
Volume/Å^3	16890.7(3)	5755.2(2)	5683.78(17)
Z	8	2	2
ρ_{calc}g/cm^3	1.203	1.224	1.432
μ/mm^{-1}	1.975	1.840	1.954
F(000)	6504.0	2194.0	2548.0
Crystal size/mm^3	0.2 × 0.2 × 0.15	0.3 × 0.2 × 0.2	0.25 × 0.15 × 0.1
Radiation	CuKα (λ = 1.54184)	CuKα (λ = 1.54184)	CuKα (λ = 1.54184)
2Θ range for data collection/°	6.608 to 160.438	5.61 to 158.818	5.644 to 151.798
Index ranges	-37 ≤ h ≤ 37, -27 ≤ k ≤ 31, -24 ≤ l ≤ 30	-24 ≤ h ≤ 24, -24 ≤ k ≤ 17, -25 ≤ l ≤ 24	-23 ≤ h ≤ 23, -24 ≤ k ≤ 22, -24 ≤ l ≤ 14
Reflections collected	87404	114439	92753
Independent reflections	17869 [R_{int} = 0.0496, R_{sigma} = 0.0295]	24203 [R_{int} = 0.0397, R_{sigma} = 0.0203]	22838 [R_{int} = 0.0362, R_{sigma} = 0.0260]
Data/restraints/parameters	17869/2044/953	24203/2780/1297	22838/0/1391
Goodness-of-fit on F^2	1.108	1.036	1.023
Final R indexes [I>=2σ (I)]	R_1 = 0.0745, wR_2 = 0.2048	R_1 = 0.0662, wR_2 = 0.1886	R_1 = 0.0676, wR_2 = 0.1831
Final R indexes [all data]	R_1 = 0.0812, wR_2 = 0.2110	R_1 = 0.0667, wR_2 = 0.1890	R_1 = 0.0715, wR_2 = 0.1861
Largest diff. peak/hole / e Å^{-3}	2.86/-1.76	1.67/-1.14	1.00/-1.14

Table S2.1. X-Ray Diffraction Table

Infrared Spectra

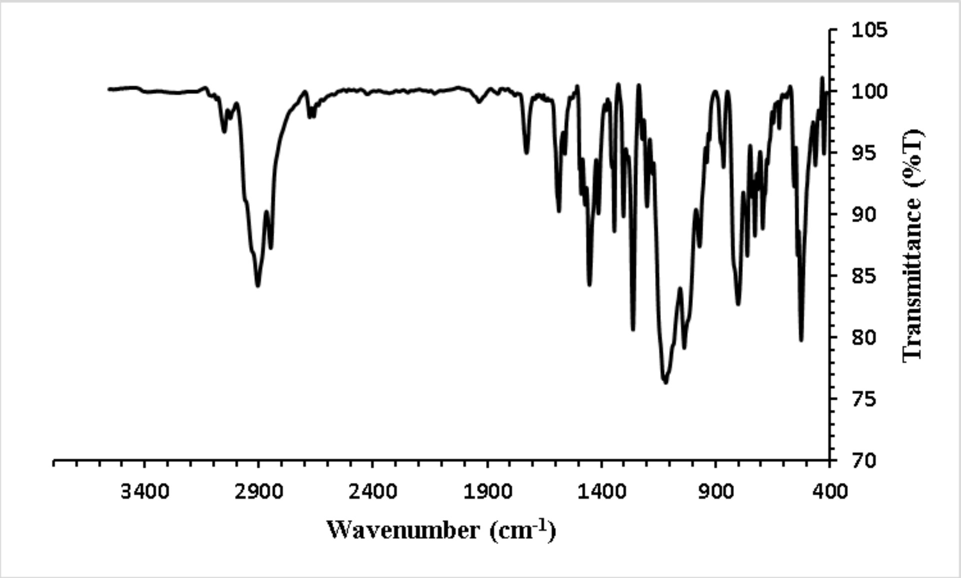

Figure S2.4. KBr-IR spectrum of **1**.

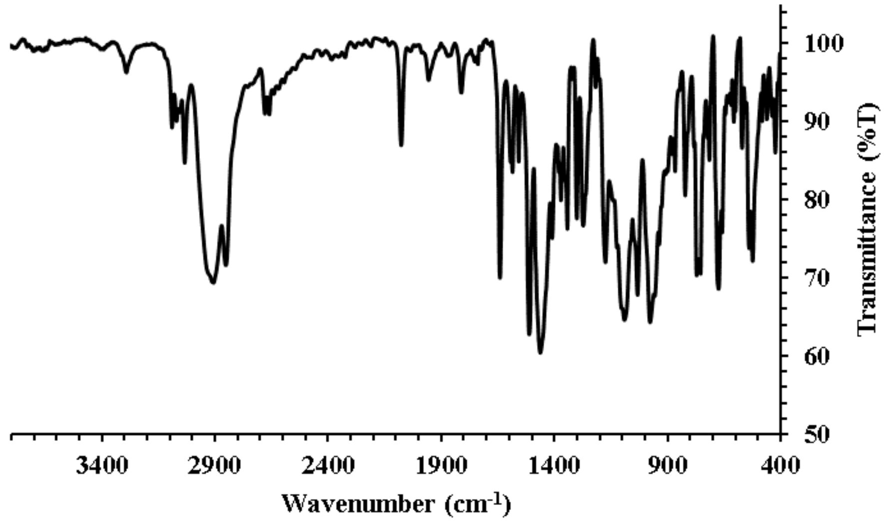

Figure S2.5. KBr-IR spectrum of **3.**

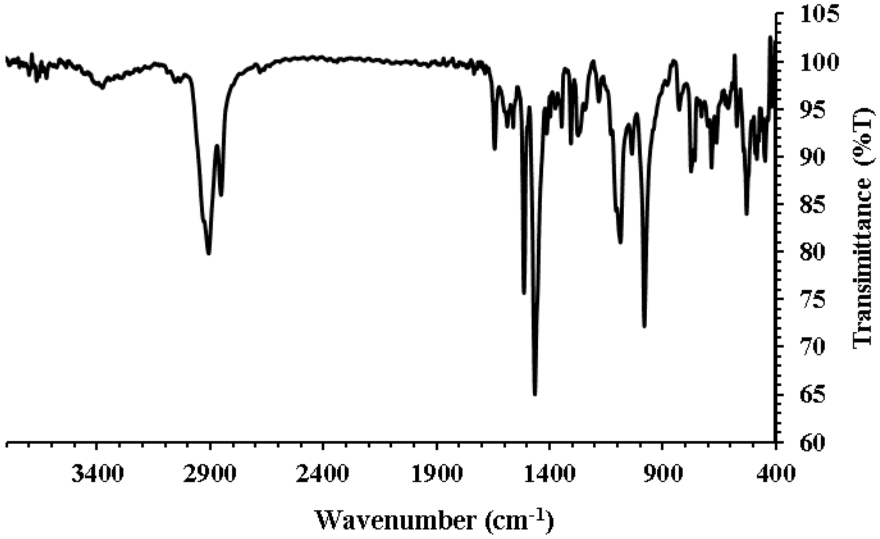

Figure S2.6. KBr-IR spectrum of **4.**

NMR Spectra

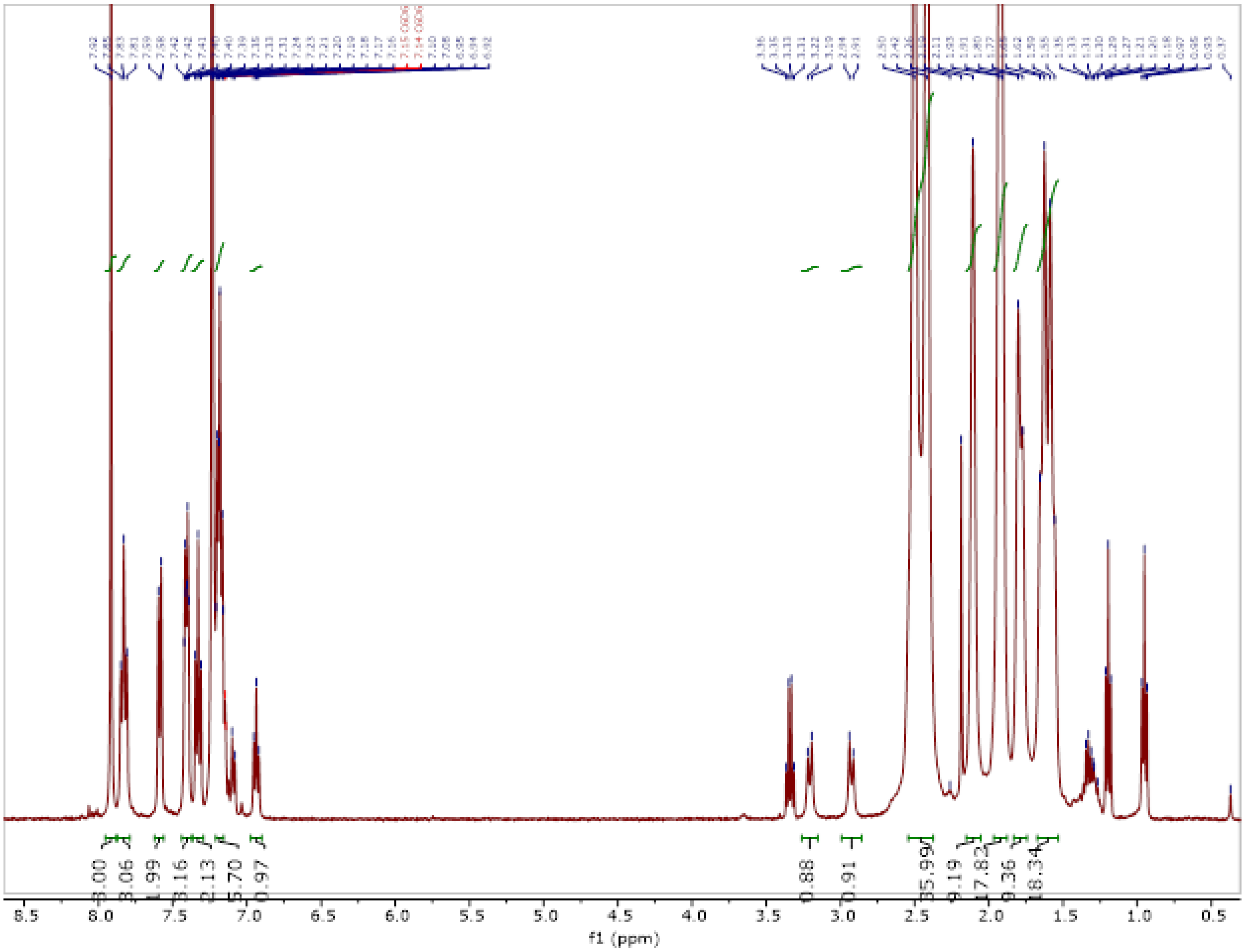

Figure S2.7. ^{1}H NMR Spectrum (400 MHz, 298K) of **LZrBn** recorded in C_6D_6

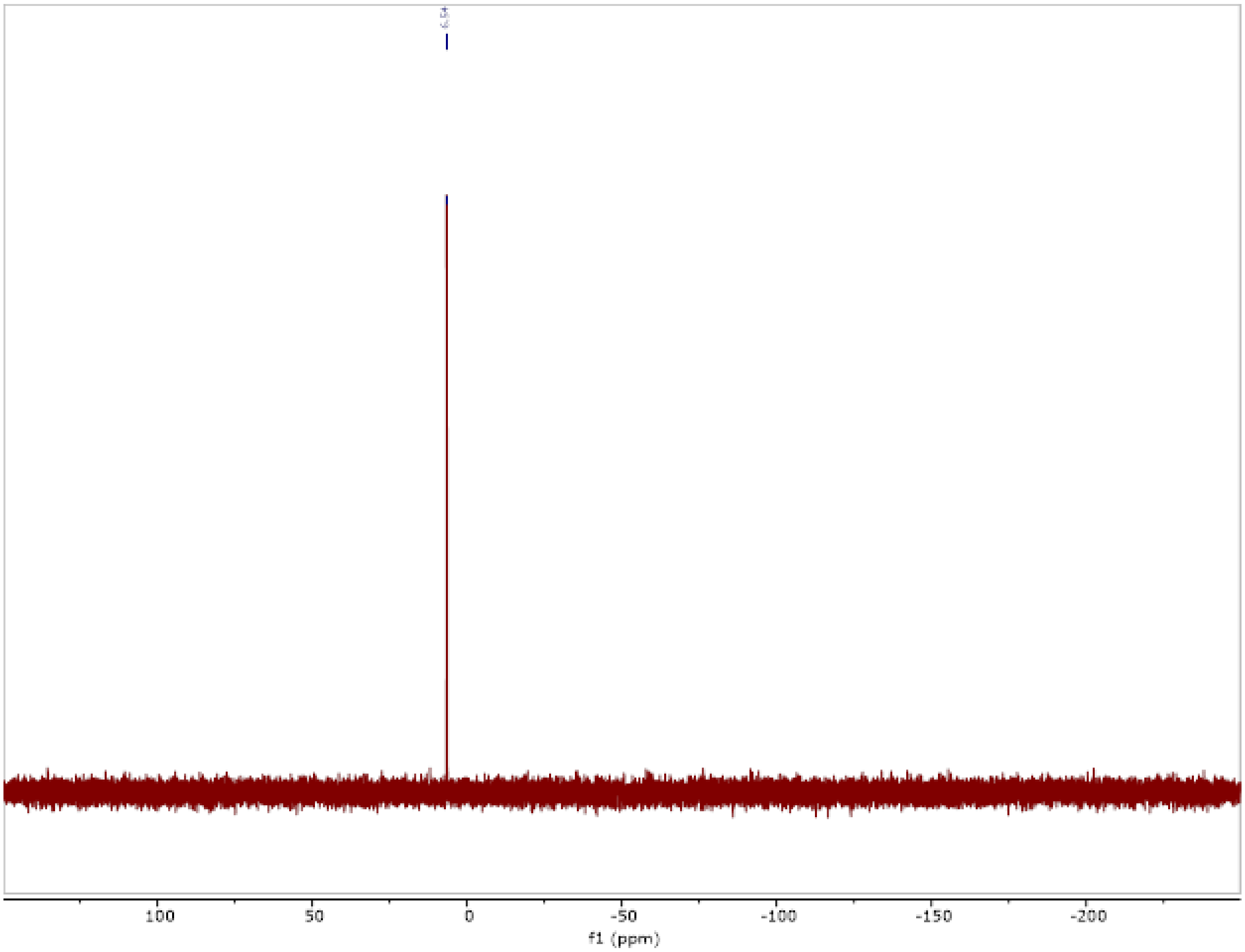

Figure S2.8. ^{31}P NMR Spectrum (162 MHz, 298K) of **LZrBn** recorded in C_6D_6

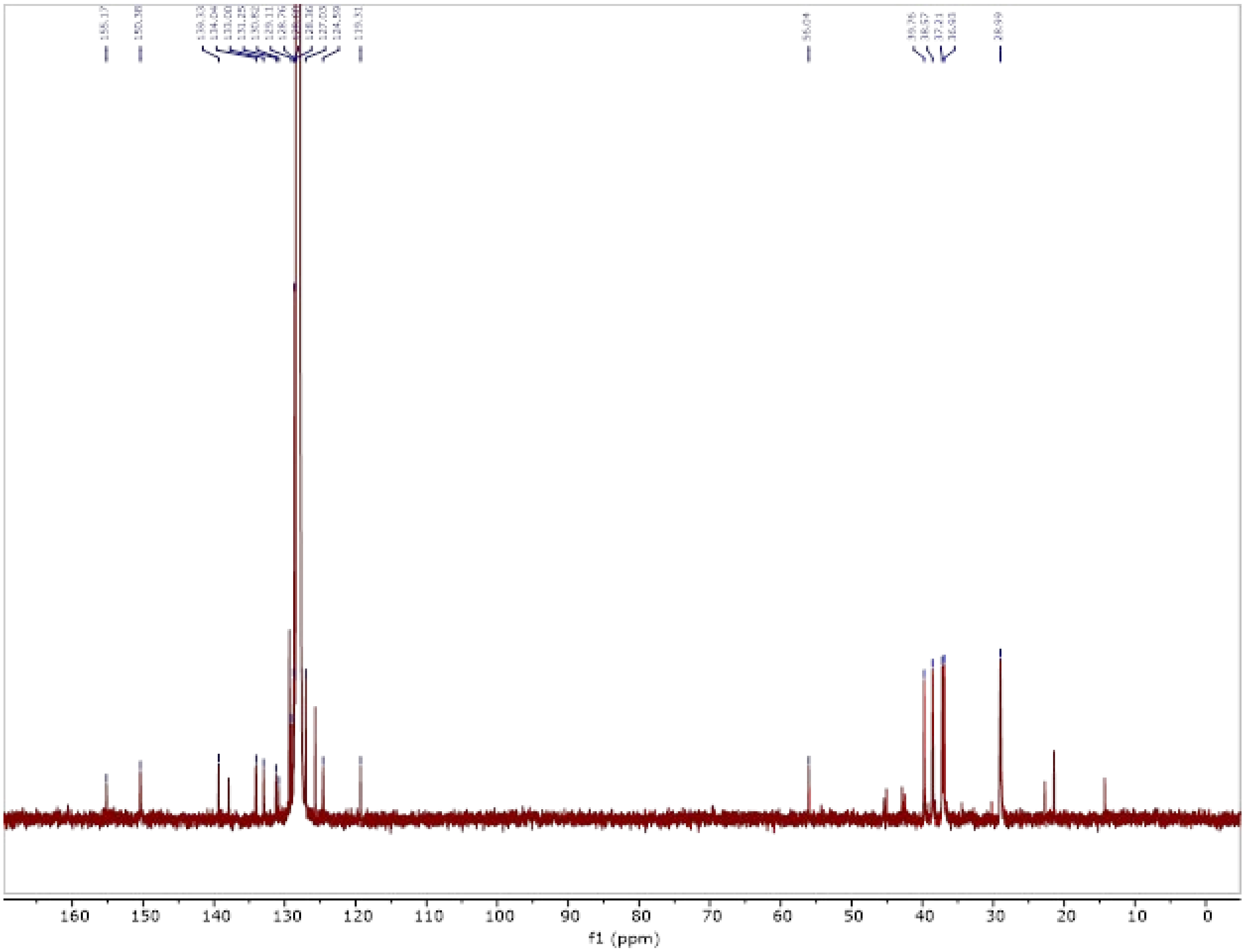

Figure S2.9. ^{13}C NMR spectrum (151 MHz, 298K) of **LZrBn** recorded in C_6D_6

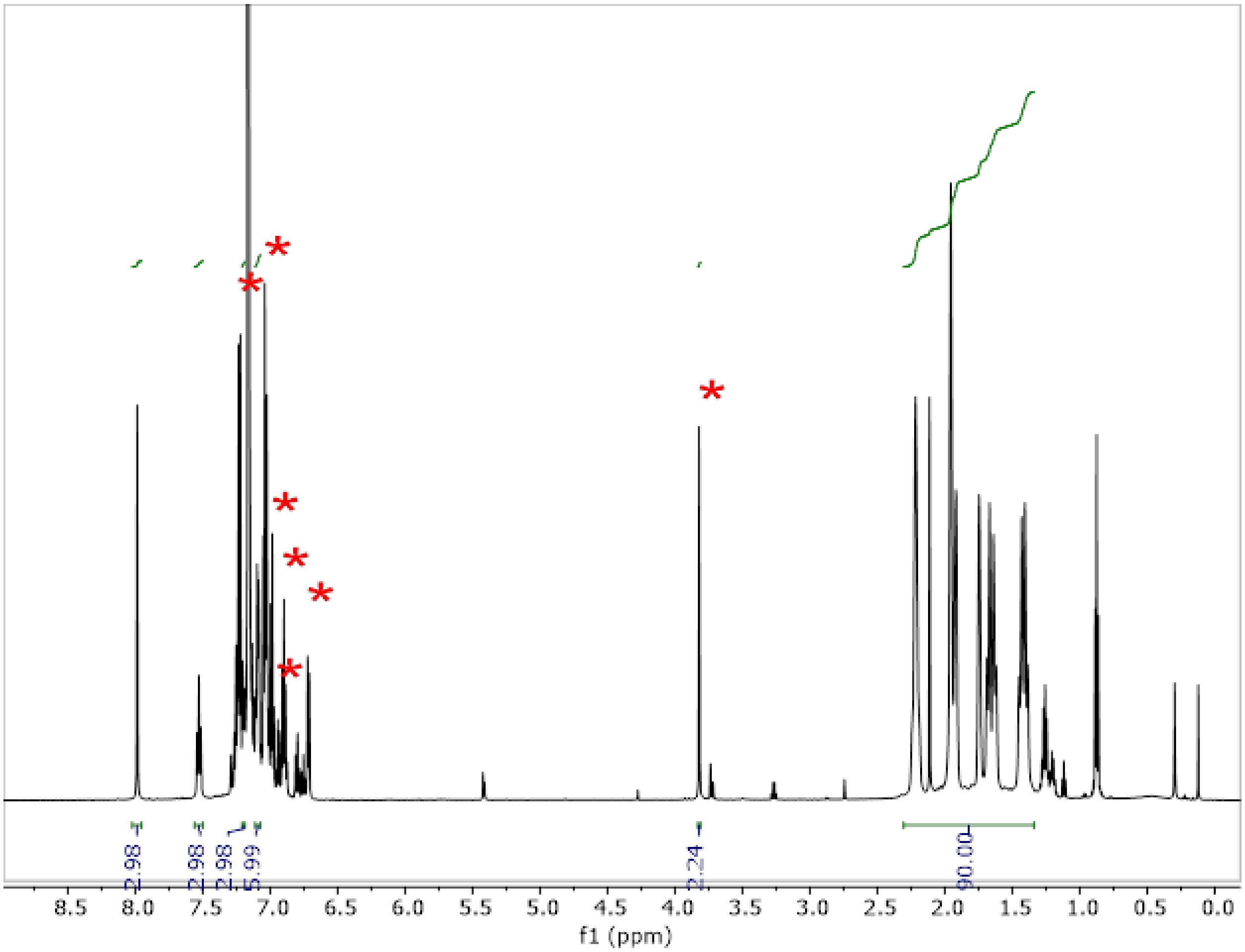

Figure S2.10. ^{1}H NMR spectrum (600 MHz, 298K) of **2** recorded in C_6D_6. Asterisks indicate peaks arising from Ph_3CBn.[42].

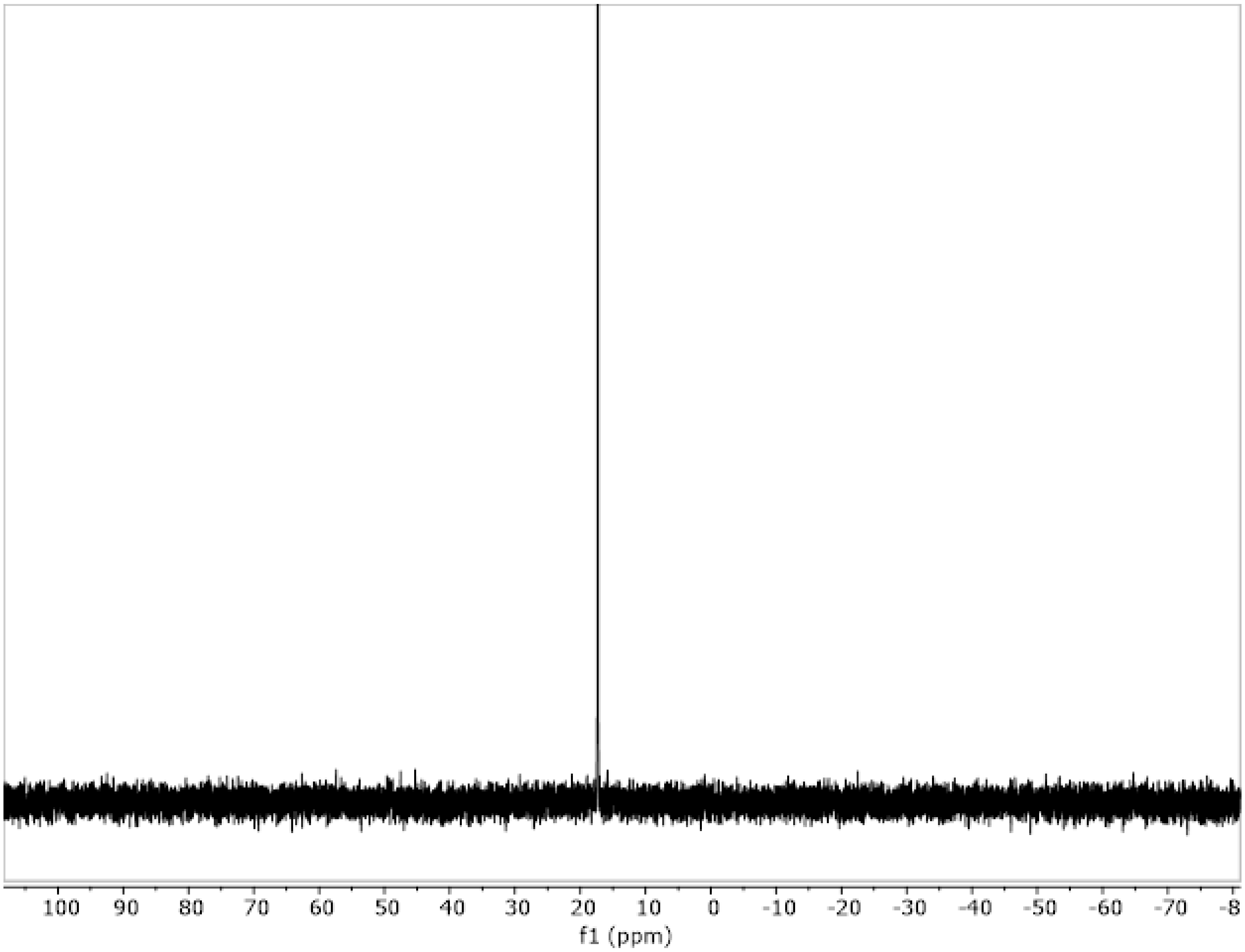

Figure S2.11. ^{31}P NMR spectrum (243 MHz, 298K) of **2** recorded in C_6D_6.

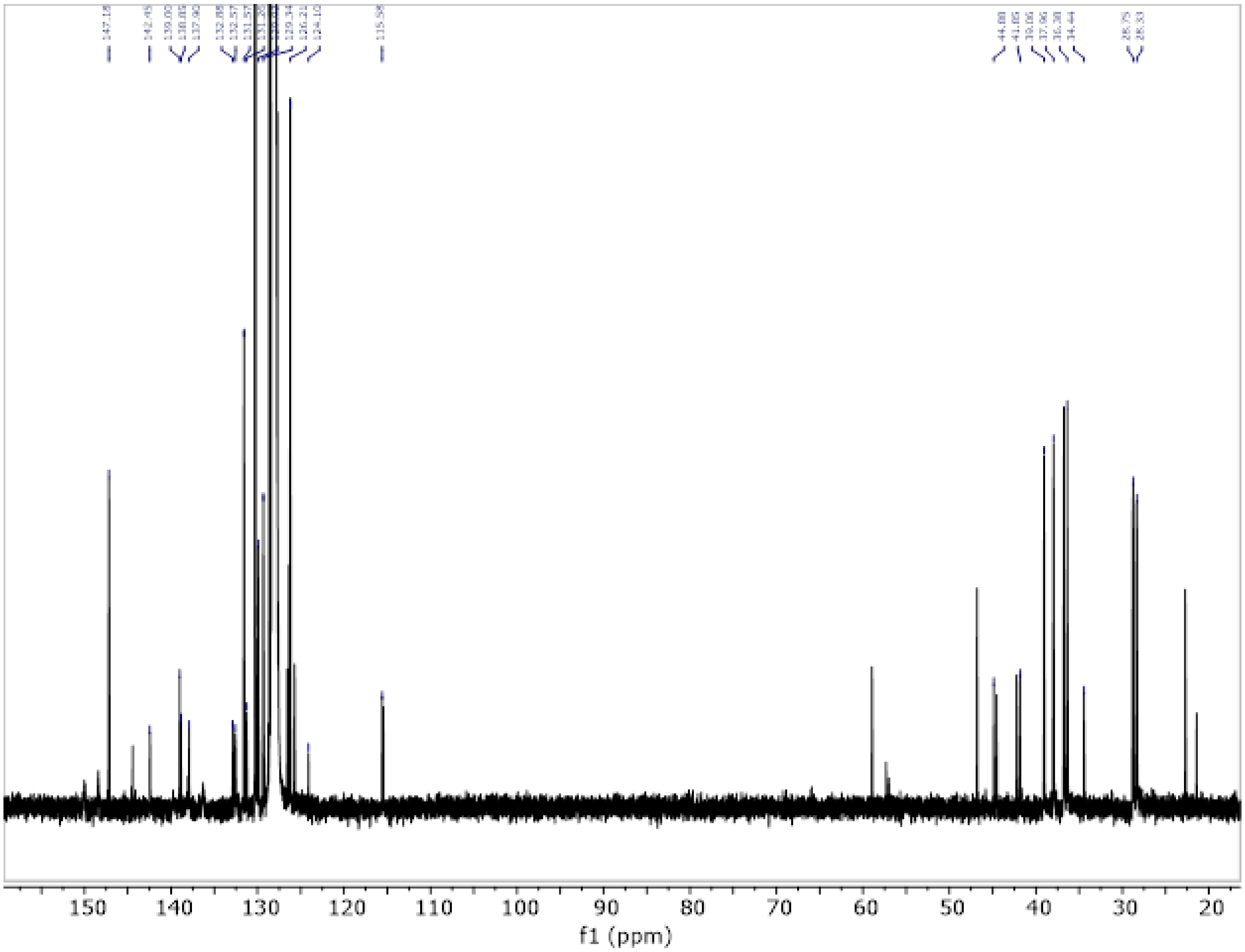

Figure S2.12. ${}^{13}C$ NMR spectrum (151 MHz, 298K) of **2** recorded in C_6D_6.

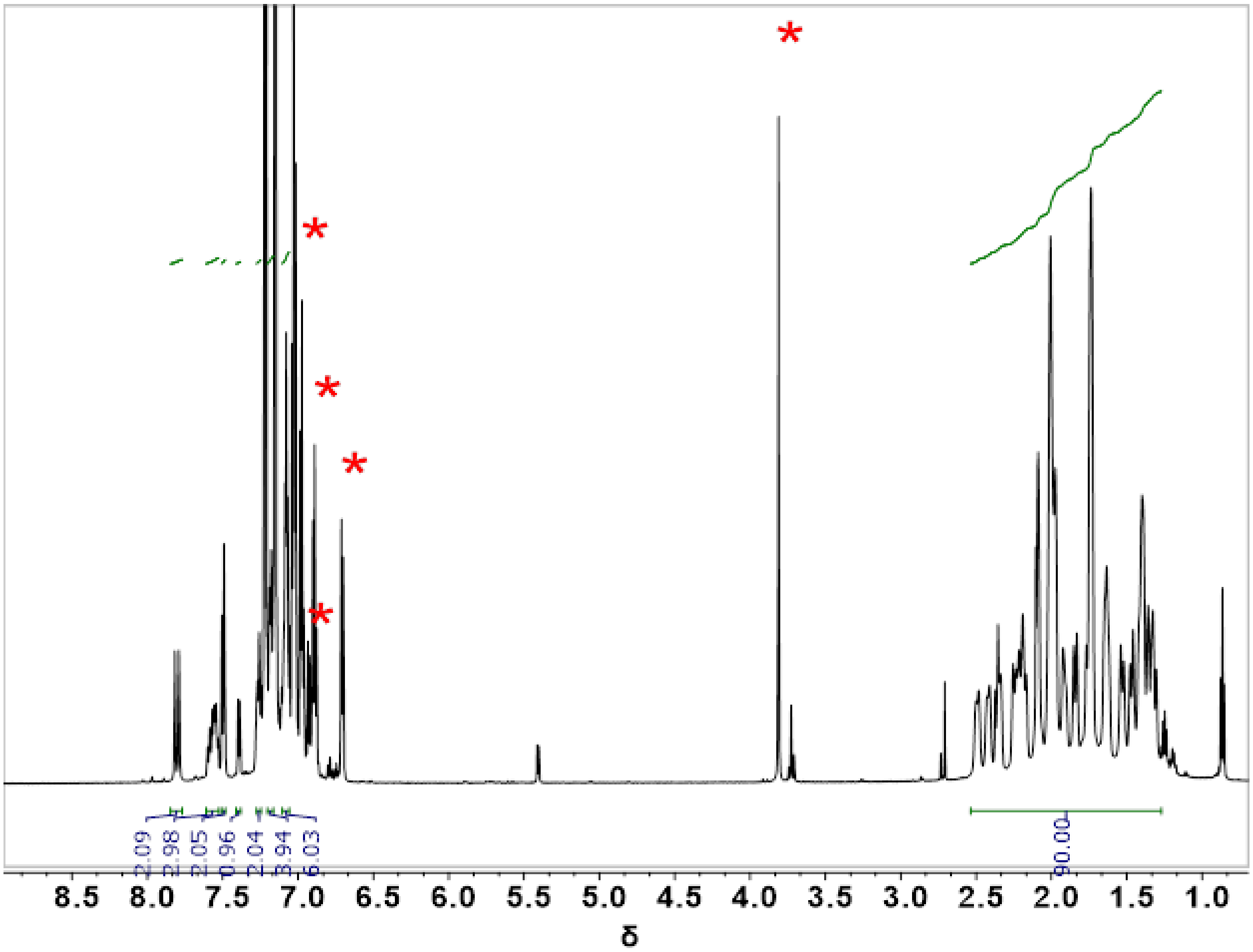

Figure S2.13. ^{1}H NMR spectrum (600 MHz, 298K) of **3** recorded in C_6D_6. Asterisks indicate peaks arising from Ph_3CBn.[42].

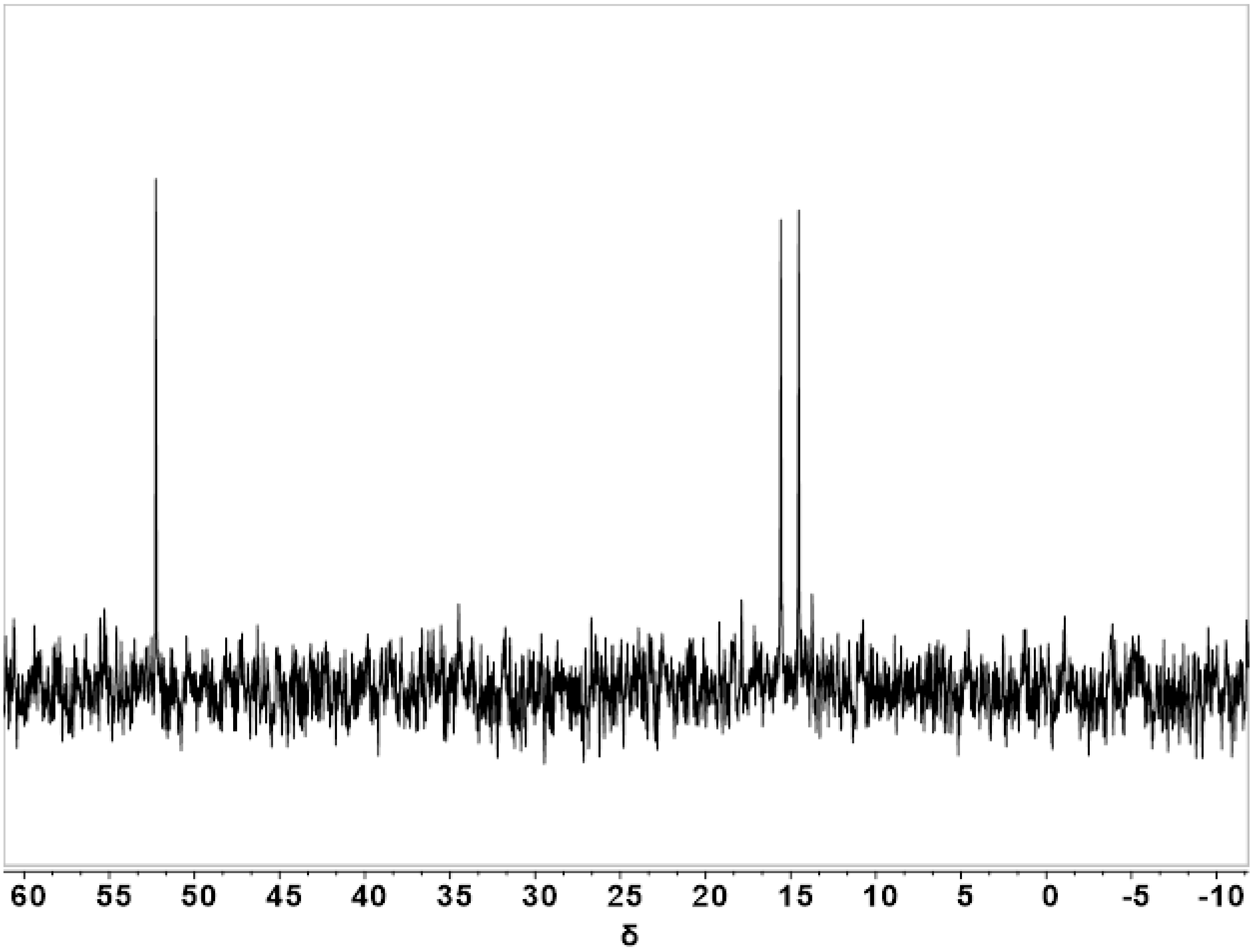

Figure S2.14. ^{31}P NMR spectrum (162 MHz, 298K) of **3** recorded in C_6D_6.

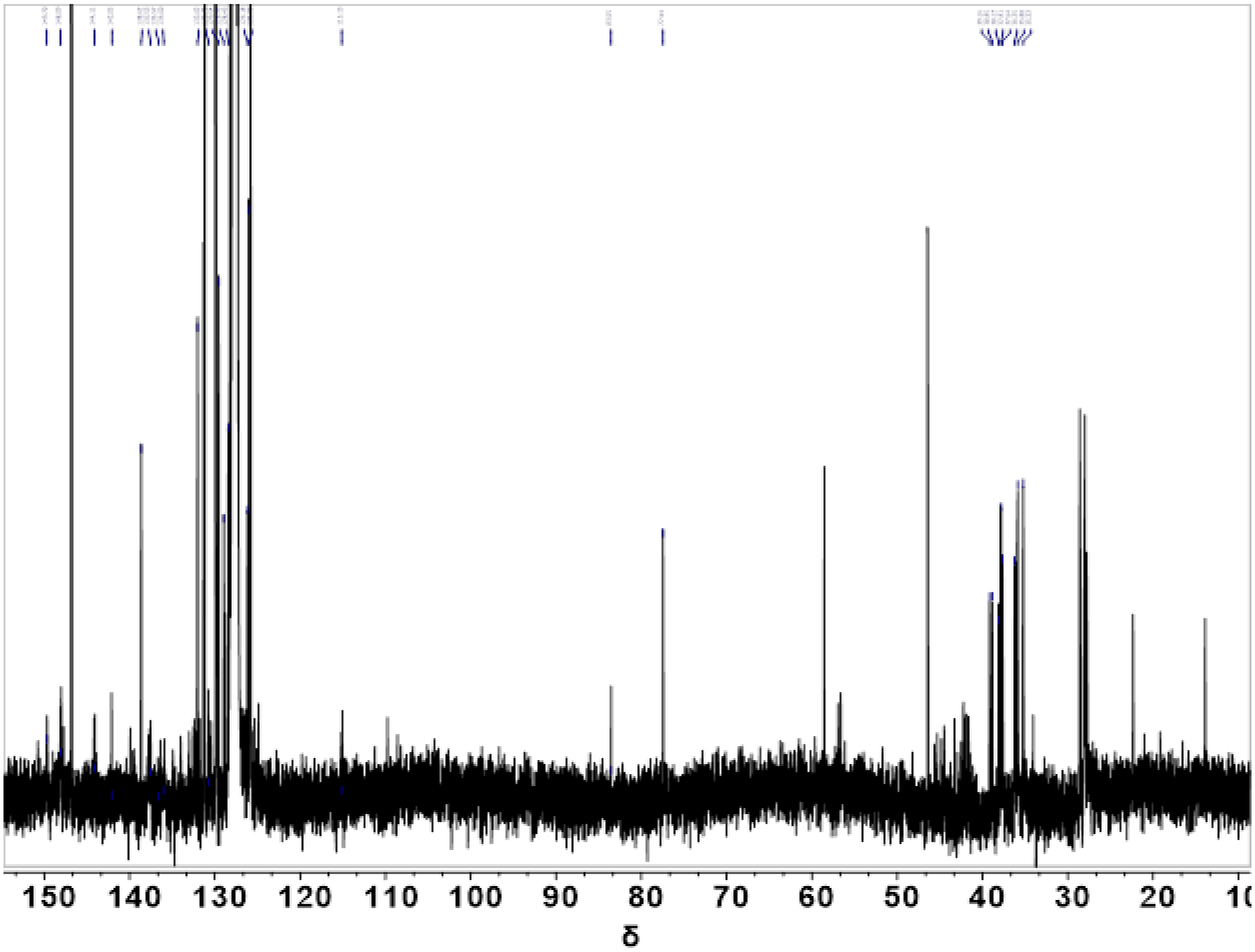

Figure S2.15. ^{13}C NMR spectrum (151 MHz, 298K) of **3** recorded in C_6D_6.

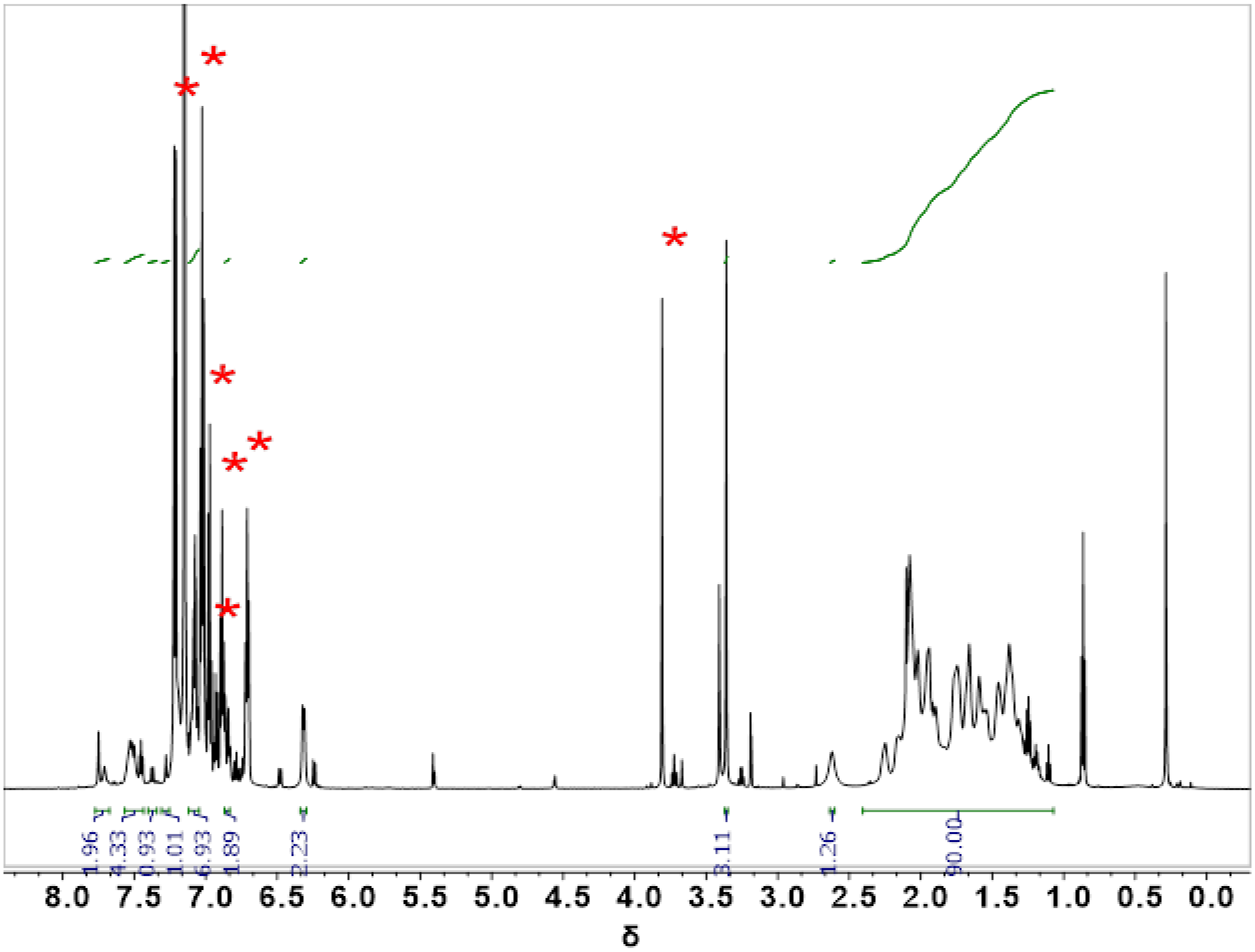

Figure S2.16. ^{1}H NMR spectrum (600 MHz, 298K) of **4** recorded in C_6D_6. Asterisks indicate peaks arising from Ph_3CBn.[42].

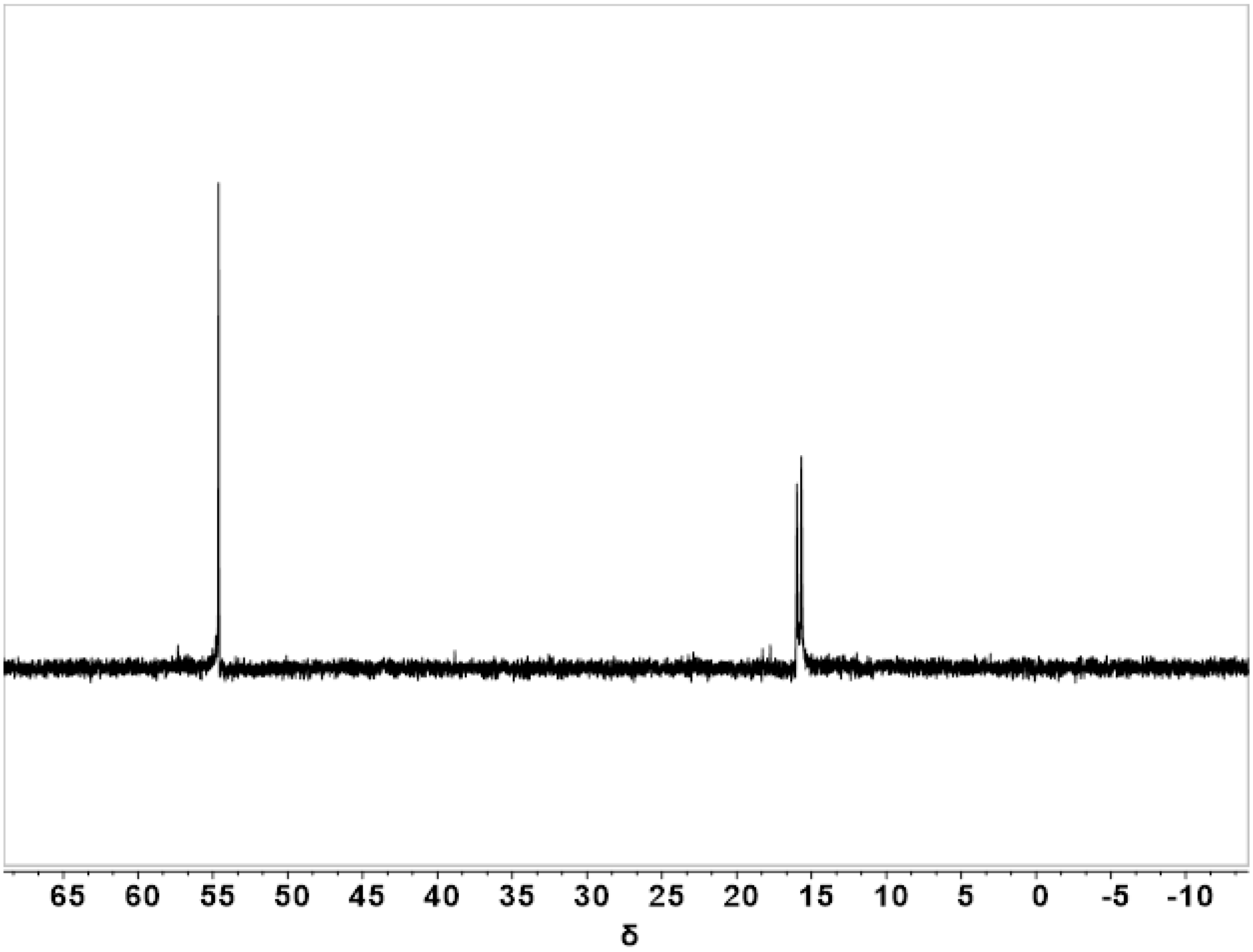

Figure S2.17. ^{31}P NMR spectrum (243 MHz, 298K) of **4** recorded in C_6D_6.

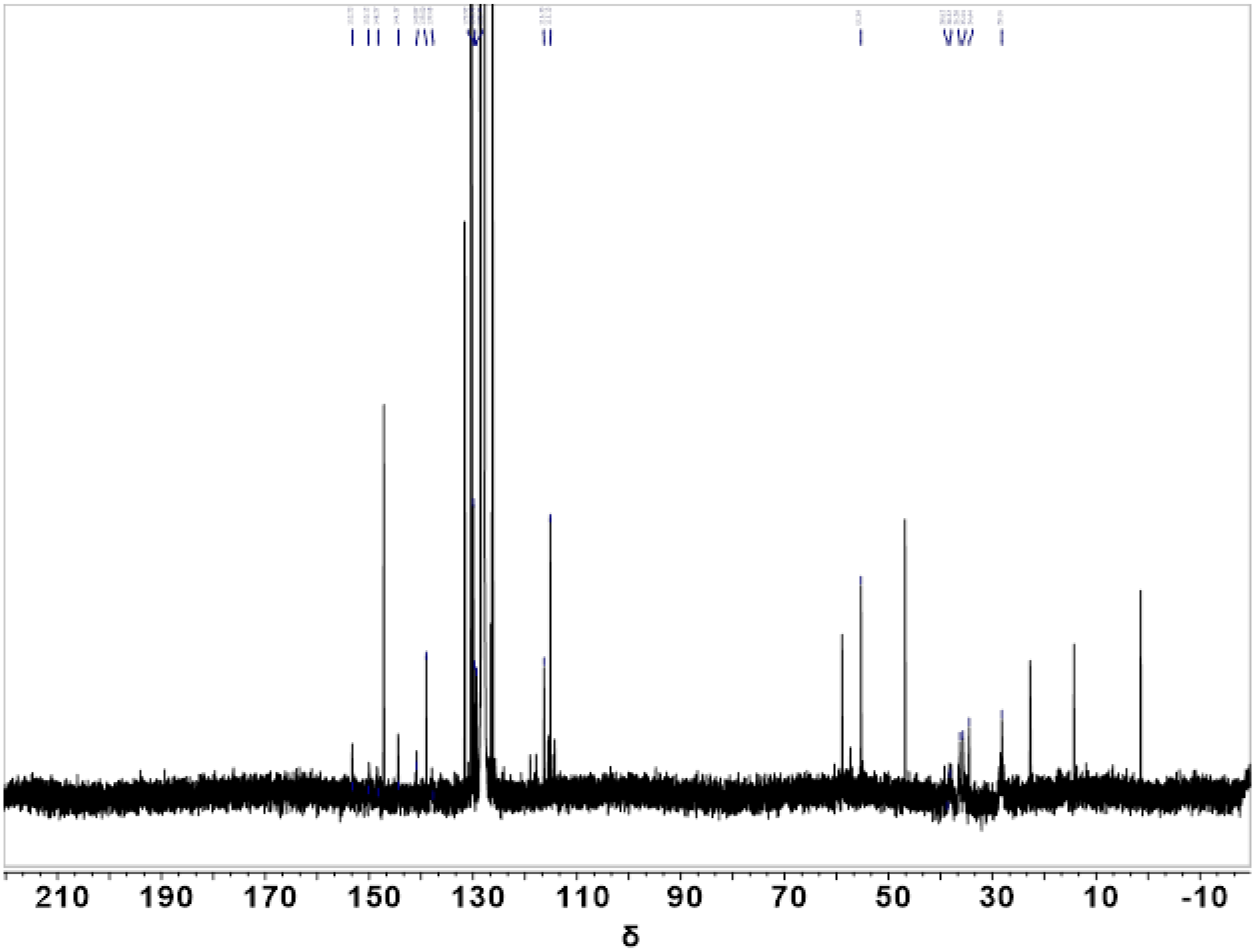

Figure S2.18. ^{13}C NMR spectrum (151 MHz, 298K) of **6** recorded in C_6D_6.

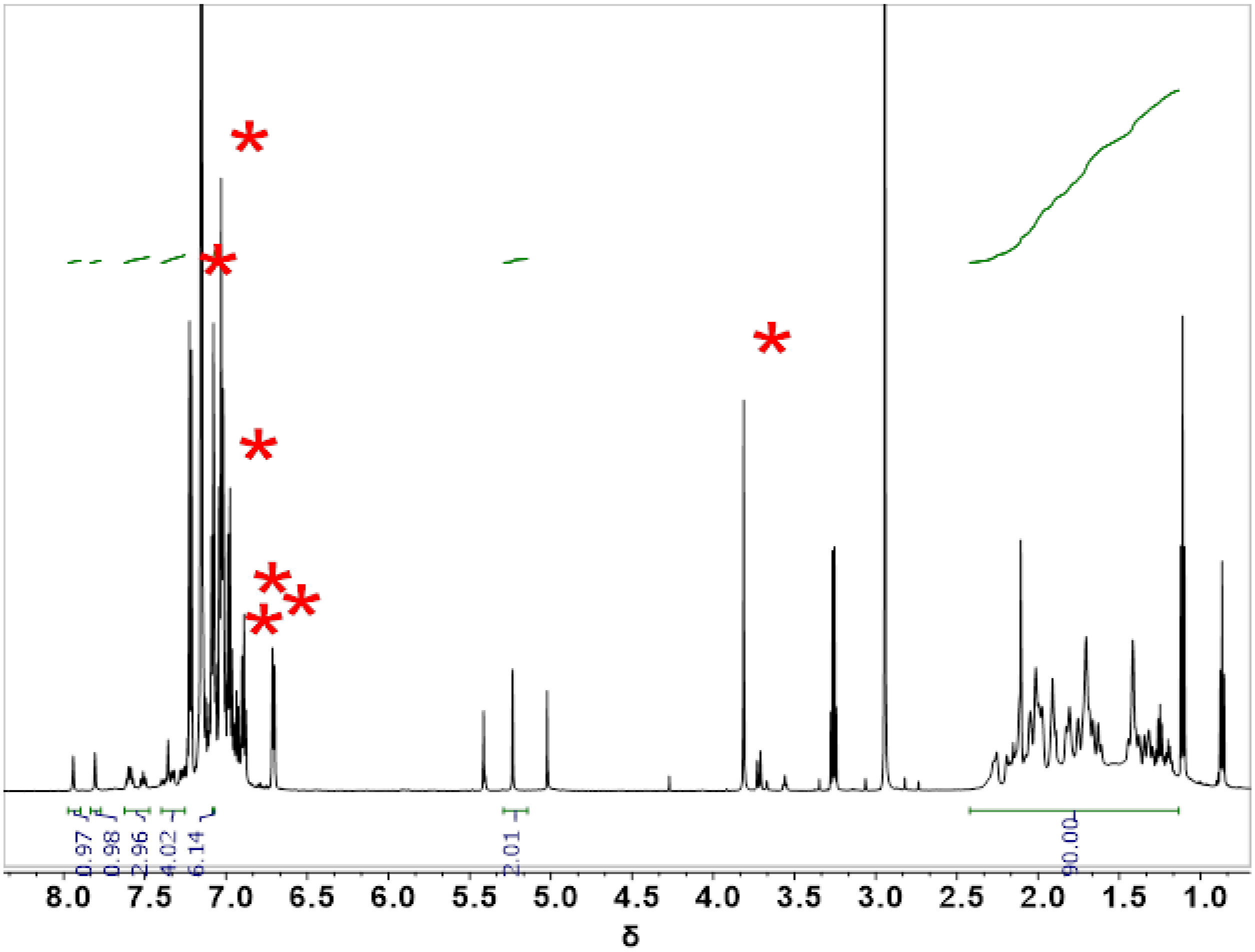

Figure S2.19. ^{1}H NMR spectrum (600 MHz, 298K) of **5** recorded in C_6D_6. Asterisks indicate peaks arising from Ph_3CBn.[42]

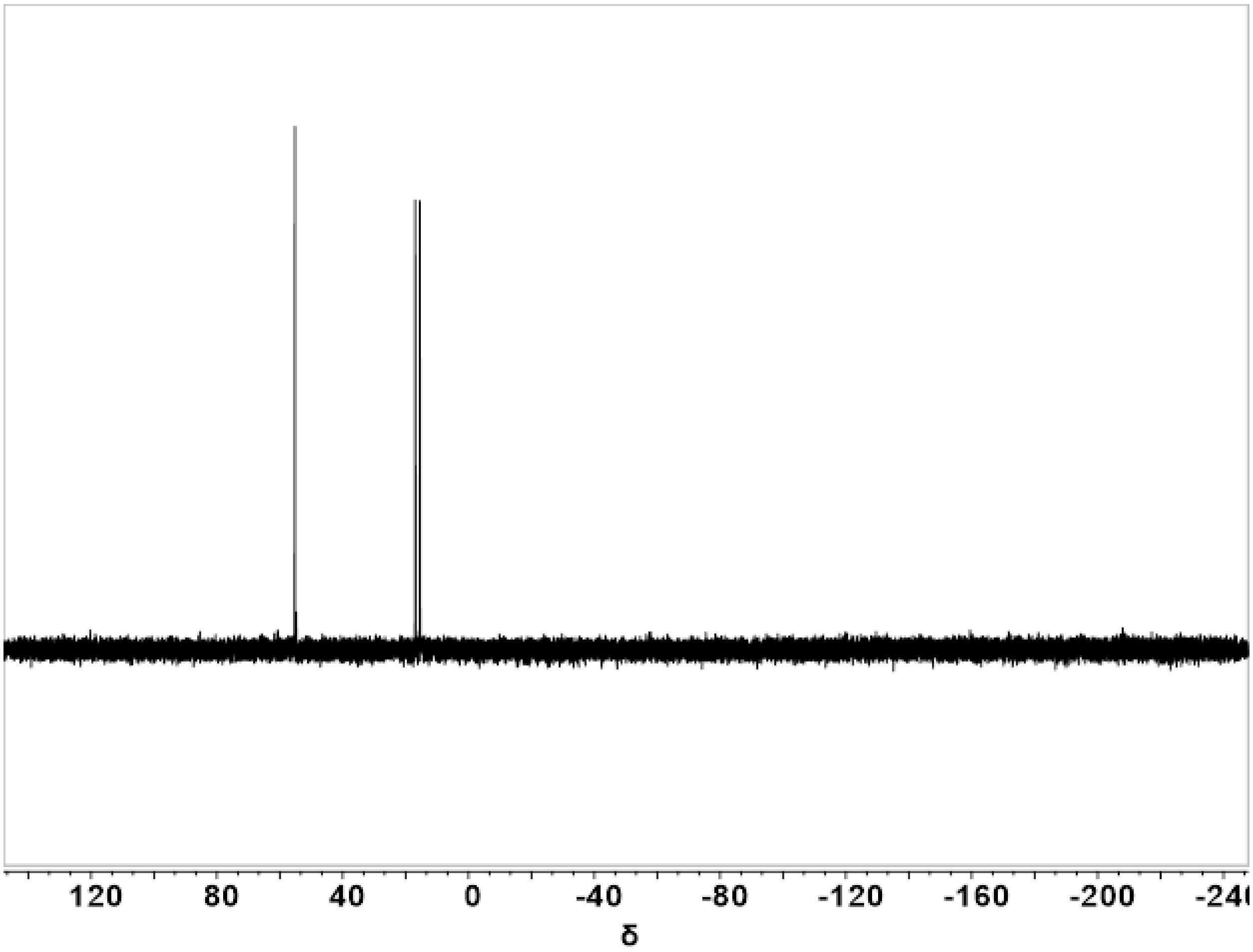

Figure S2.20. ^{31}P NMR spectrum (243 MHz, 298K) of **5** recorded in C_6D_6.

.

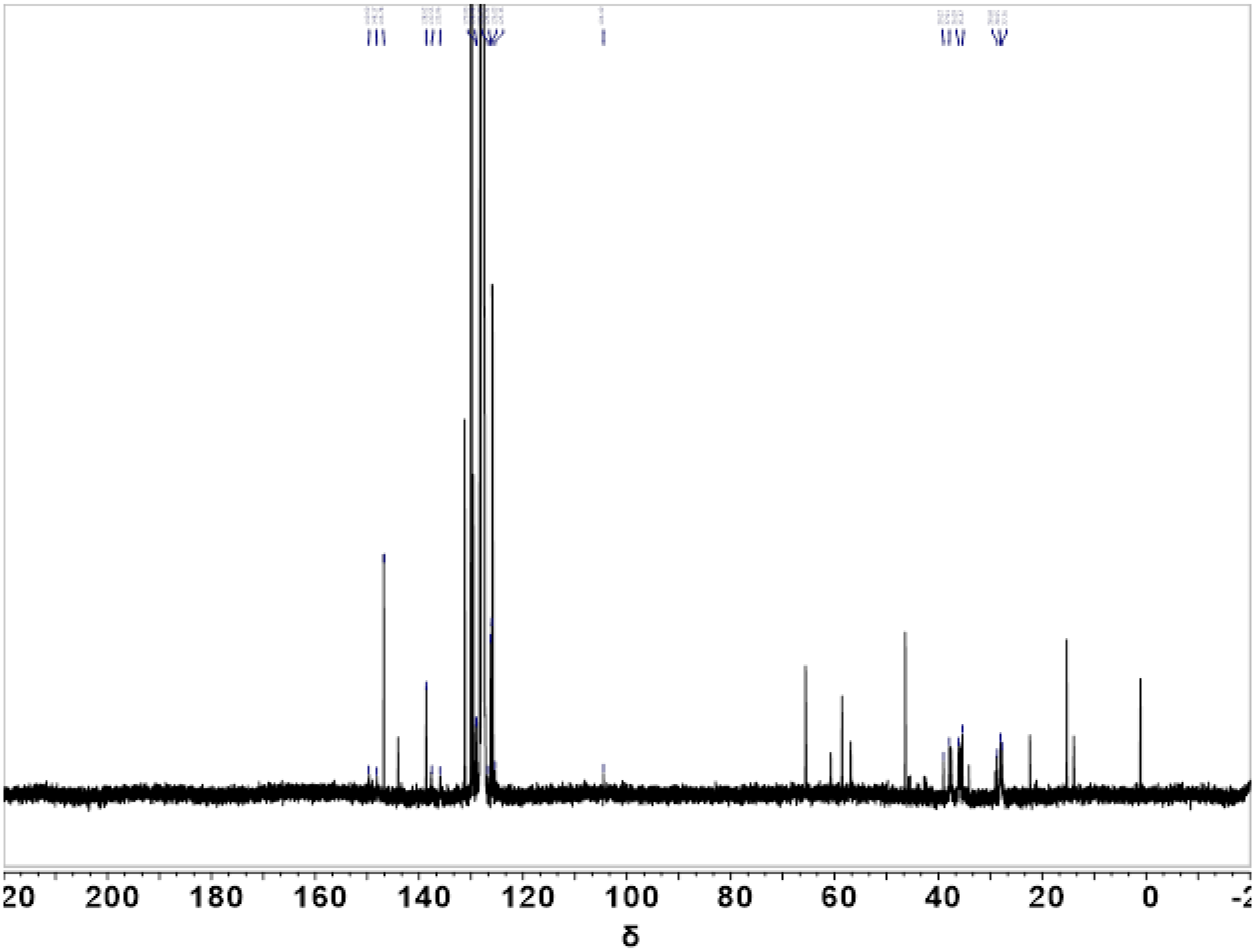

Figure S2.21. ^{13}C NMR spectrum (151 MHz, 298K) of **5** recorded in C_6D_6.

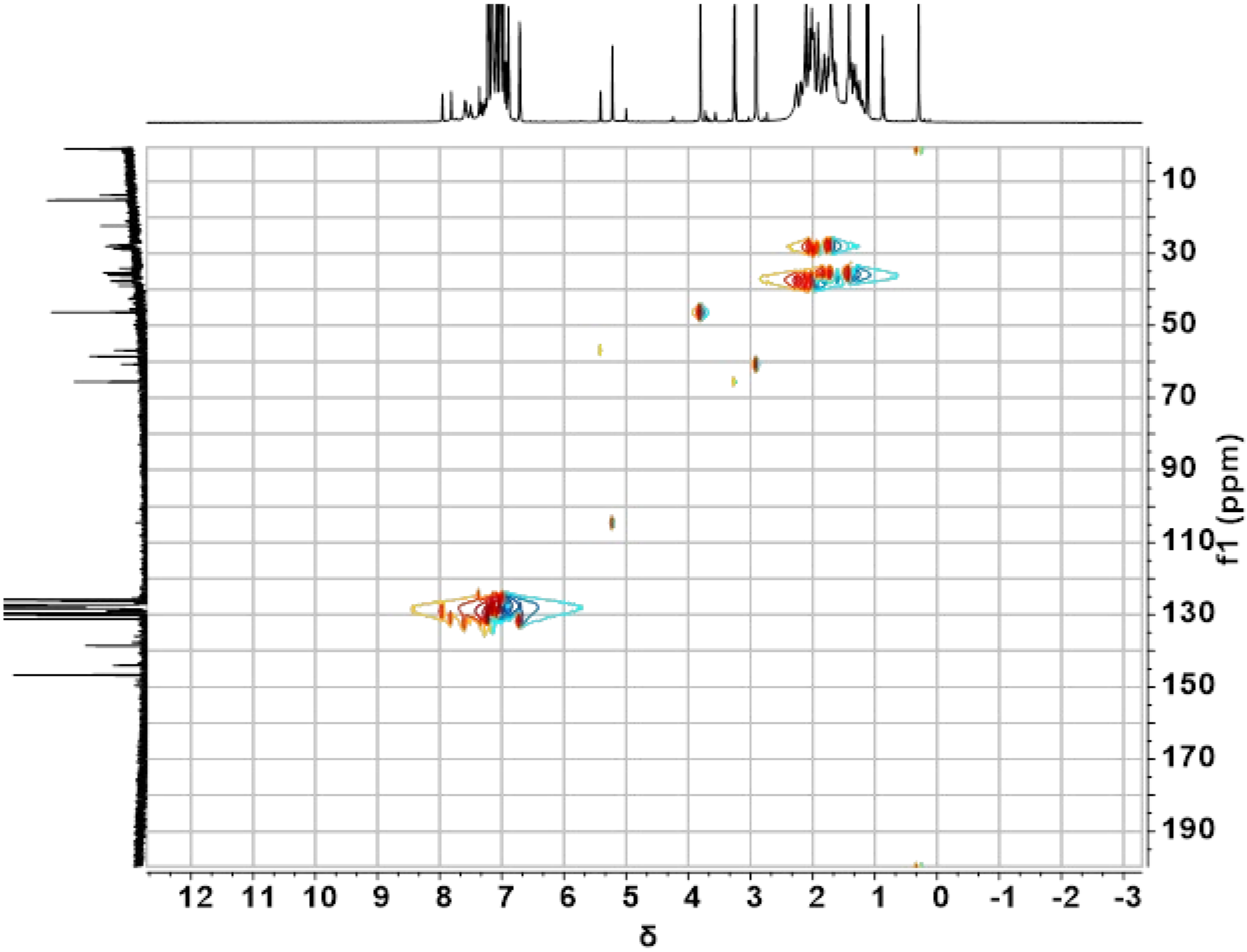

Figure S2.22. ^{1}H-^{13}C HSQC spectrum (600 MHz, 298 K) of **5** in C_6D_6

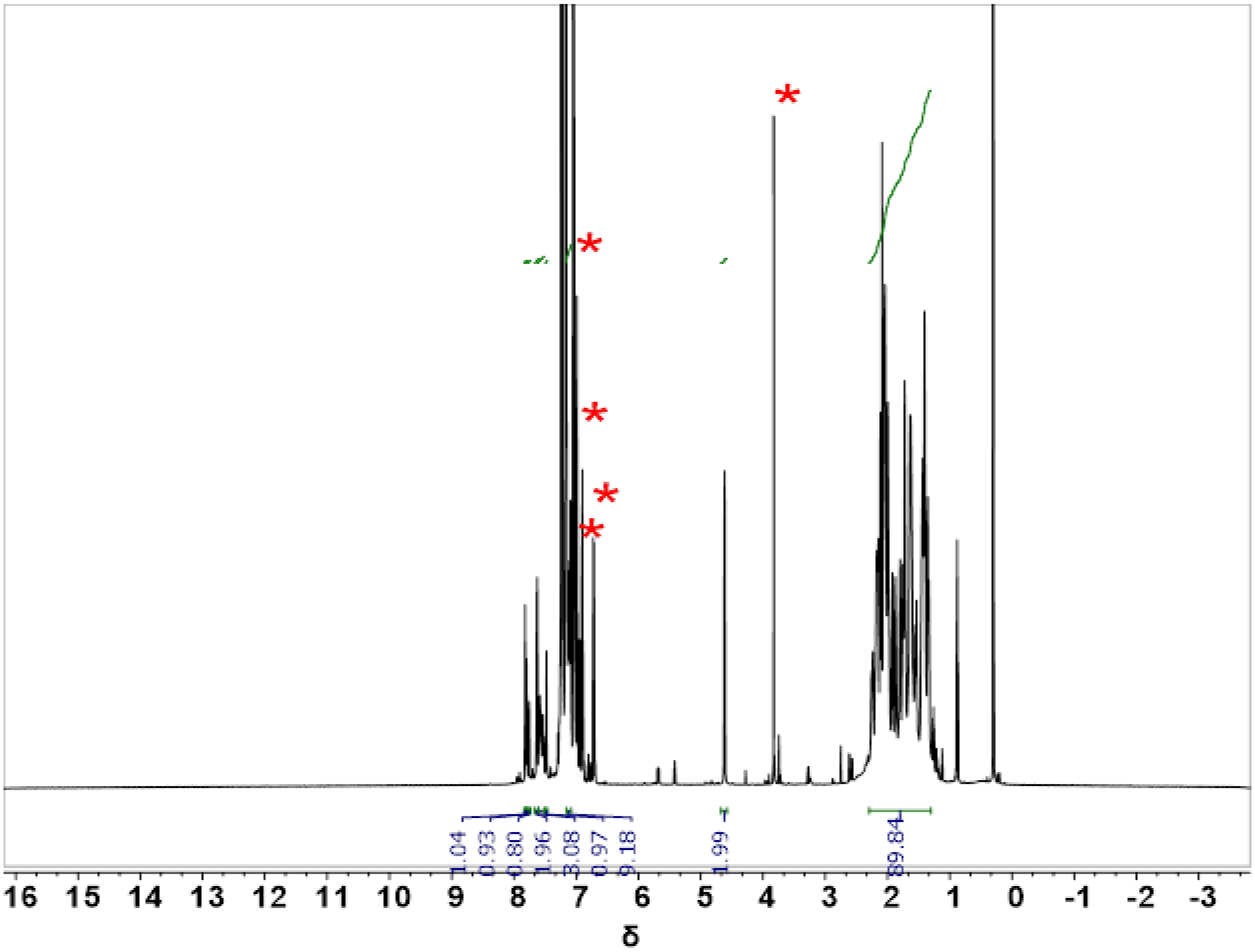

Figure S2.23. ^{1}H NMR spectrum (600 MHz, 298K) of **6** recorded in C_6D_6. Asterisks indicate peaks arising from Ph_3CBn.[42].

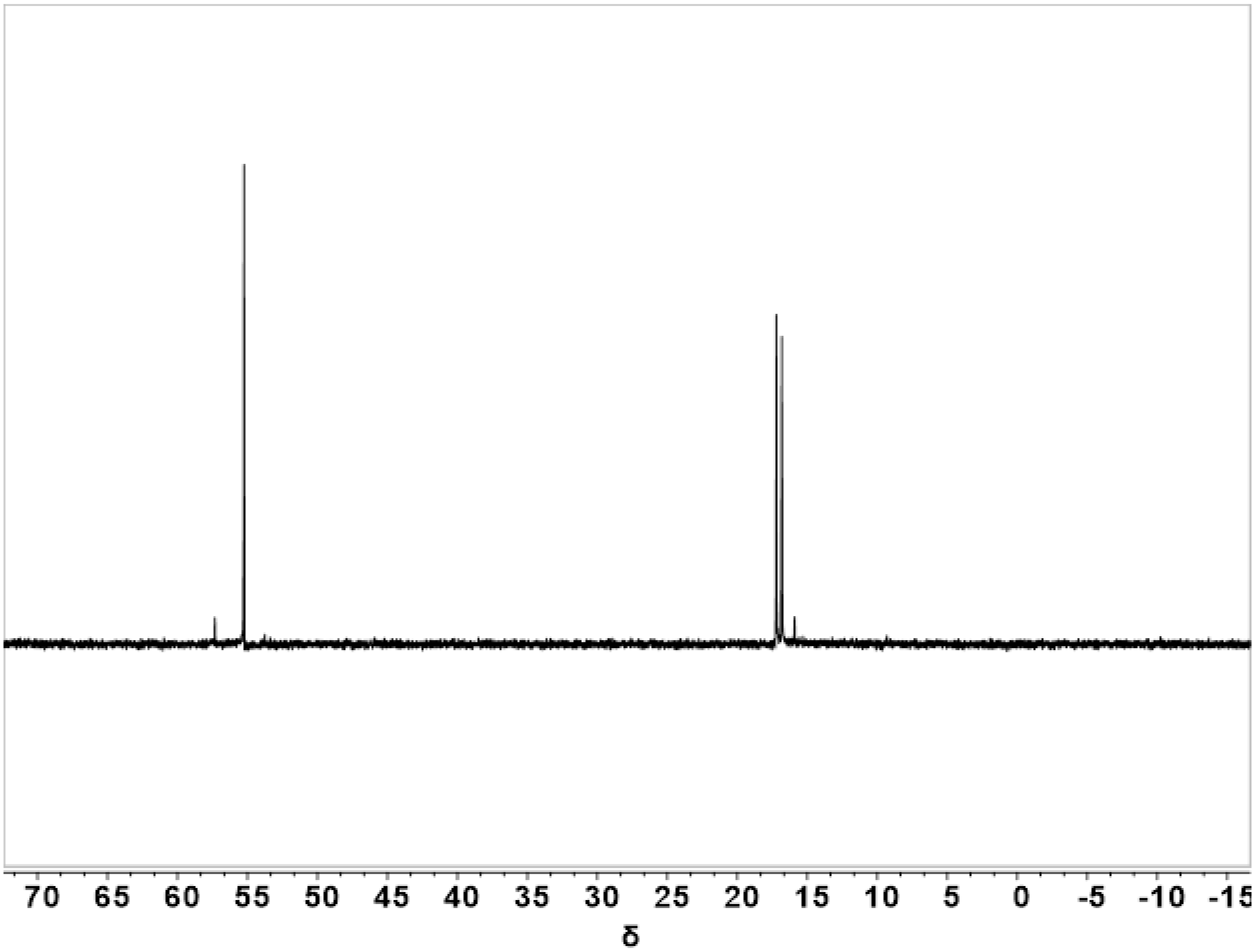

Figure S2.24. ^{31}P NMR spectrum (243 MHz, 298K) of **6** recorded in C_6D_6.

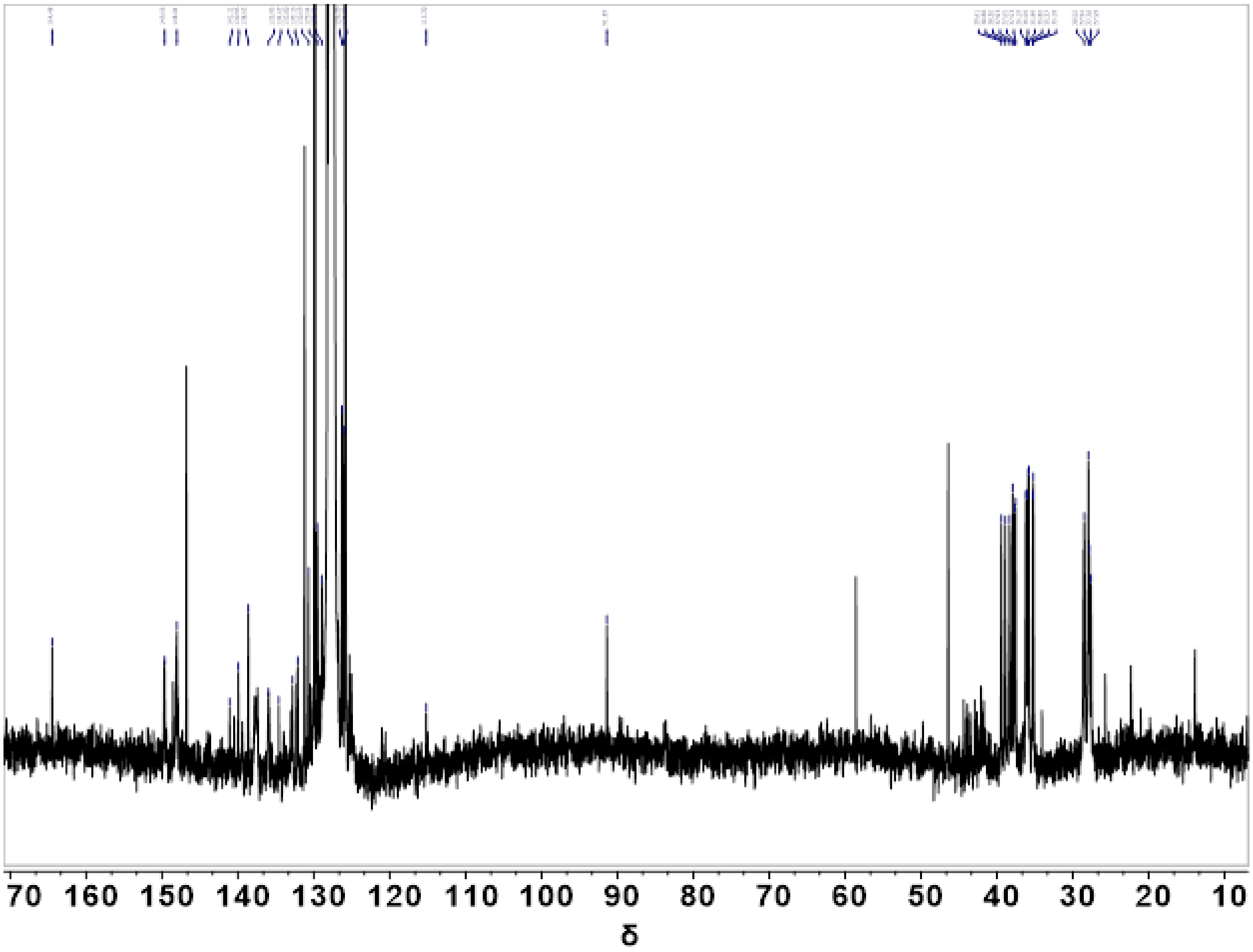

Figure S2.25. ^{13}C NMR spectrum (151 MHz, 298K) of **6** recorded in C_6D_6.

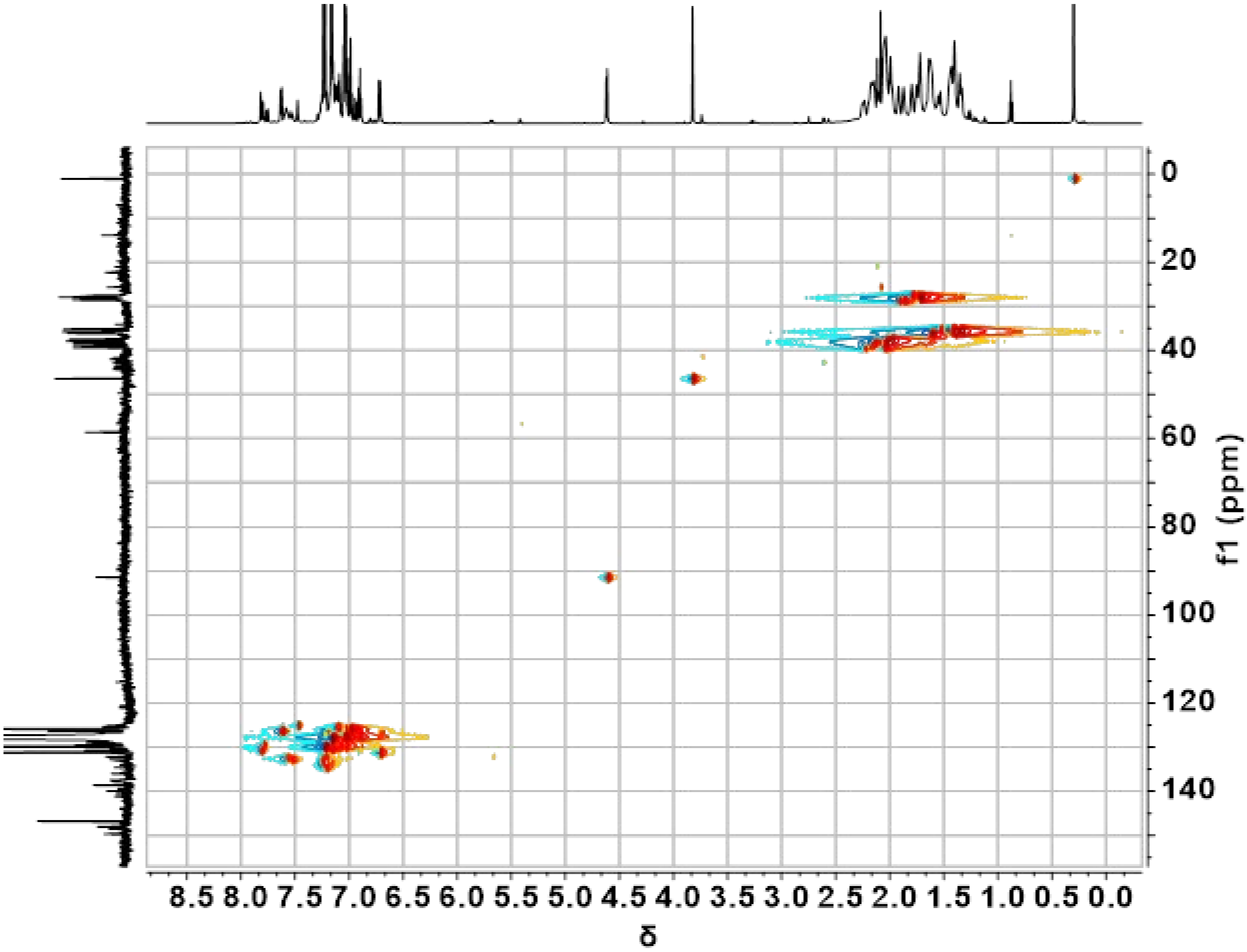

Figure S2.26. ^1H-^{13}C HSQC spectrum (600 MHz, 298 K) of **6** in C_6D_6

2.6 References

(1) Wolczanski, P. T. *Organometallics* **2018**, *37* (4), 505–516.

(2) Cummins, C. C.; Baxter, S. M.; Wolczanski, P. T. *J. Am. Chem. Soc.* **1988**, *110* (26), 8731–8733.

(3) Walsh, P. J.; Hollander, F. J.; Bergman, R. G. *J. Am. Chem. Soc.* **1988**, *110* (26), 8729–8731.

(4) Bailey, B. C.; Fan, H.; Baum, E. W.; Huffman, J. C.; Baik, M. H.; Mindiola, D. J. *J. Am. Chem. Soc.* **2005**, *127* (46), 16016–16017.

(5) Royo, P.; Sánchez-Nieves, J. *J. Organomet. Chem.* **2000**, *597* (1–2), 61–68.

(6) Zhang, S.; Tamm, M.; Nomura, K. *Organometallics* **2011**, *30* (10), 2712–2720.

(7) Cheon, J.; Rogers, D. M.; Girolami, G. S. *J. Am. Chem. Soc.* **1997**, *119* (29), 6804–6813.

(8) Andino, J. G.; Kilgore, U. J.; Pink, M.; Ozarowski, A.; Krzystek, J.; Telser, J.; Baik, M. H.; Mindiola, D. J. *Chem. Sci.* **2010**, *1* (3), 351–356.

(9) Fostvedt, J. I.; Grant, L. N.; Kriegel, B. M.; Obenhuber, A. H.; Lohrey, T. D.; Bergman, R. G.; Arnold, J. *Chem. Sci.* **2020**, *11* (42), 11613–11632.

(10) Hoffmann, R. *Angew. Chemie Int. Ed. English* **1982**, *21* (10), 711–724.

(11) Dehnicke, K.; Krieger, M.; Massa, W. *Coord. Chem. Rev.* **1999**, *182* (1), 19–65.

(12) Stephan†, D. W. *Organometallics* **2005**, *24* (11), 2548–2560.

(13) Lee, H. B.; Ciolkowski, N.; Winslow, C.; Rittle, J. *Inorg. Chem.* **2021**, *60* (16), 11830–11837.

(14) Winslow, C.; Lee, H. B.; Field, M. J.; Teat, S. J.; Rittle, J. *J. Am. Chem. Soc.* **2021**, *143* (34), 13686–13693.

(15) Aguirre Quintana, L. M.; Yang, Y.; Ramanathan, A.; Jiang, N.; Bacsa, J.; Maron, L.; La Pierre, H. S. *Chem. Commun.* **2021**, *57* (54), 6664–6667.

(16) Bai, T.; Janes, T.; Song, D. *Dalt. Trans.* **2017**, *46* (37), 12408–12412.

(17) Camacho-Bunquin, J.; Ferguson, M. J.; Stryker, J. M. *J. Am. Chem. Soc.* **2013**, *135* (15), 5537–5540.

(18) Stephan, D. W. *Adv. Organomet. Chem.* **2006**, *54*, 267–291.

(19) Vreeken, V.; Siegler, M. A.; de Bruin, B.; Reek, J. N. H.; Lutz, M.; van der Vlugt, J. I. *Angew. Chemie Int. Ed.* **2015**, *54* (24), 7055–7059.

(20) Dehnicke, K.; Weller, F. *Coord. Chem. Rev.* **1997**, *158*, 103–169.

(21) Stephan, D. W. *Organometallics* **1999**, *18* (7), 1116–1118.

(22) Gompa, T. P.; Ramanathan, A.; Rice, N. T.; La Pierre, H. S. *Dalt. Trans.* **2020**, *49* (45), 15945–15987.

(23) Guérin, F.; Stewart, J. C.; Beddie, C.; Stephan, D. W. *Organometallics* **2000**, *19* (16), 2994–3000.

(24) Groom, C. R.; Bruno, I. J.; Lightfoot, M. P.; Ward, S. C. *Acta Crystallogr.* **2016**, *B72* (2), 171–179.

(25) Shafir, A.; Arnold, J. *Organometallics* **2003**, *22* (3), 567–575.

(26) Otten, E.; Batinas, A. A.; Meetsma, A.; Hessen, B. *J. Am. Chem. Soc.* **2009**, *131* (14), 5298–5312.

(27) Diel, B. N.; Hope, H. *Inorg. Chem.* **1986**, *25* (24), 4448–4451.

(28) Zhang, X.; Emge, T. J.; Ghosh, R.; Krogh-Jespersen, K.; Goldman, A. S. *Organometallics* **2006**, *25* (5), 1303–1309.

(29) Walsh, P. J.; Hollander, F. J.; Bergman, R. G. *J. Organomet. Chem.* **1992**, *428* (1–2), 13–

47.

(30) Moore, E. J.; Straus, D. A.; Armantrout, J.; Santarsiero, B. D.; Grubbs, R. H.; Bercaw, J. E. *J. Am. Chem. Soc.* **1983**, *105* (7), 2068–2070.

(31) Veya, P.; Floriani, C.; Chiesi-Villa, A.; Rizzoli, C. *Organometallics* **1993**, *12* (12), 4899–4907.

(32) Liquori, A. M.; Dami-ani, A.; DeCoen, J. L.; Mol Biol, J.; Ajo, D.; Bossa, M.; Damiani, A.; Fidenzi, R.; Gigli, S.; Lanzi, L.; Lapic-cirella, A.; Theor Biol, J.; Matthews, W. S.; Bares, J. E.; Bartmess, J. E.; Bordwell, F. G.; Cornforth, F. J.; Drucker, G. E.; Margolin, Z.; McCallum, R. J.; McCollum, G. J.; Vanier, N. R. *J. Am. Chem. Soc.* **2002**, *97* (24), 7006–7014.

(33) Bordwell, F. G. *Acc. Chem. Res.* **2002**, *21* (12), 456–463.

(34) Taft, R. W.; Bordwell, F. G. *Acc. Chem. Res.* **2002**, *21* (12), 463–469.

(35) Bordwell, F. G.; Algrim, D. J. *J. Am. Chem. Soc.* **2002**, *110* (9), 2964–2968.

(36) Bordwell, F. G.; Algrim, D.; Vanier, N. R. *J. Org. Chem.* **2002**, *42* (10), 1817–1819.

(37) Bennett, J. L.; Wolczanski, P. T. *J. Am. Chem. Soc.* **1997**, *119* (44), 10696–10719.

(38) Sampson, J.; Choi, G.; Akhtar, M. N.; Jaseer, E. A.; Theravalappil, R.; Al-Muallem, H. A.; Agapie, T. *Organometallics* **2017**, *36* (10), 1915–1928.

(39) Ihara, E.; Young, J.; Jordan, R. F. *J. Am. Chem. Soc.* **1998**, *120* (32), 8277–8278.

(40) Whitesides, G. M.; Ehmann, W. J.; Dodge, R. P.; Schomaker, V.; Organometal, J.; Blount, J. F.; Dahl, L. F.; Hoogzand, C.; Hiibel, W.; Meriwether, S.; Leto, M. F.; Colthup, E. C.; Ken, G. W.; Zeiss, H.; Amer Chem, J. *J. Am. Chem. Soc.* **2002**, *92* (19), 5625–5640.

(41) Rigaku Oxford Diffraction. Rigaku Corporation: Oxford, U.K. 2015.

(42) Dolomanov, O. V.; Bourhis, L. J.; Gildea, R. J.; Howard, J. A. K.; Puschmann, H. *J. Appl. Crystallogr.* **2009**, *42* (2), 339–341.

(43) Abubekerov, M.; Eymann, L. Y. M.; Gianetti, T. L.; Arnold, J. *Dalt. Trans.* **2016**, *45* (37), 14581–14590.

Chapter 3

Multi-Electron Processes Mediated by a Phosphinimide Supported Chromium(II) Complex

3.1 Introduction

Enzymatic systems are capable of performing a variety of difficult multi-electron reductions such as the 4-electron reductive cleavage of dioxygen[1,2] and the reduction of dinitrogen to ammonia[3] through the use of multiple transition metal centers to activate small molecules. Influenced by the significance of these systems, synthetic chemists have sought to design reducing synthetic complexes, both mono- and multi-metallic, that are capable of mediating similar multi-electron processes.[4–8] In particular, group (VI) complexes have been shown to enable a variety of 2- and 4-electron processes[9–17] often via cooperativity between two low-valent coordinatively unsaturated metal sites.

Our research group has built a synthetic program utilizing weak-field, π-basic phosphinimide (PN) ligands to stabilize low coordinate, highly-reducing transition metal complexes in the aim of stabilizing reactive, high-valent intermediates and mediating reductive processes.[18,19] Phosphinimides are formally monoanionic ligands which have a significant resonance structure (Scheme 1) that is isolobal to -imido ligands and are capable of donating cylindrical π-density to a transition metal ion when a pseudo-linear binding geometry is adopted.[20] Our group employs a tripodal, multi-dentate phosphinimide framework to enforce such a binding angle as to maximize the electron density the transition metal ion can receive from the phosphinimide moieties.

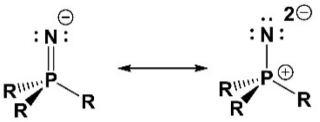

Scheme 3.4. Resonance structures of phosphinimides

Inspired by the precedent for mid-row transition metals to enable multi-electron reductive processes, we hypothesized that a multi-dentate phosphinimide chromium complex would provide an entry way into performing comparable difficult reductions. To explore this, we chose a sterically congested, hexaadamantyl framework to preclude dimerization and enforce monometallic complexes. A trigonal chromium(II) complex of this ligand was shown to mediate a variety of multi-electron reductions including the 4-electron reductions of dioxygen, aryl azides, and nitrosoarenes as well as an oxo/imido heterometathesis with a second equivalent of nitrosoarene to perform nitrene metathesis to selectively synthesize azoarenes. A structural and spectroscopic analyses of these compounds highlights the flexibility of phosphinimides in stabilizing high-valent metal complexes and showcases their ability to mediate novel oxidative processes.

3.2 Results and Discussion

While phosphinimides have been known as highly-electron donating ligands for decades[21], their application to organometallics has been mostly limited to monodentate platforms for a variety of applications including stabilizing olefin polymerization[22,23] and hydrogenation[24] catalysts as well as more recent work supporting electron-deficient lanthanide complexes[25] and chalcogenide bridged iron complexes[26]. Our group has developed synthetic methodology that gives access to rigid, multidentate phosphinimines which allow us to explore the organometallic reactivity of complexes which have multiple enforced pseudolinear P-N-M bond linkages.[18] The ligand utilized in this work features significant steric bulk on the phosphorus to enforce purely monometallic complexes and maximize the ability of the phosphinimides to donate π-electron density onto a single metal ion.

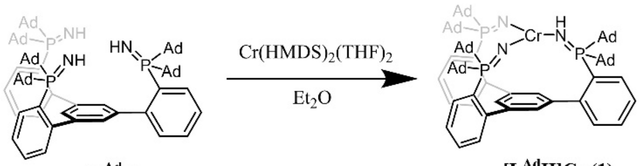

$L^{Ad}H_3$

$[L^{Ad}H]Cr$ (1)

Scheme 3.5 Synthesis of compound **1**

An electron-rich chromium(II) complex was accessed via protonolysis upon reacting the proligand **$L^{Ad}H_3$** with one equivalent of $Cr(HMDS)_2(THF)_2$ to give **1** in 88.7% net yield (Scheme 2) as the first fully characterized chromium(II) phosphinimide complex.[27] FTIR analysis indicates that one phosphinimide is still protonated and bound to the metal with an M-NH band at 3403 cm^{-1}. This was further confirmed by structural characterization via single crystal XRD. **1** crystallizes in a monoclinic cell, allowing for the differentiation between the metal phosphinimide M-N bond distances (1.9361 Å and 1.9357 Å) and the elongated metal phosphinimine M-NH distance (2.0681 Å) (Figure 3.1). Room temperature solution phase magnetic data via the Evans' method[28] support an S=2 spin state ($\mu_{eff} = 4.8\ \mu_B$). This spin state was further supported as the spin ground state by the parallel mode X-Band EPR spectrum taken at 5K which contains an intense feature at g=7.83 which can be modeled as a strongly axial S=2 state (Figure S3.4). To the best of our knowledge, this is the first instance where a chromium(II) complex has been observed by parallel mode X-Band EPR. Electrochemical analysis indicate that **1** exhibits a quasi-reversible oxidation event at -1.24 V vs Fc/Fc$^+$ in THF (Figure S3.15-S3.16), which is significantly more reducing than other neutral chromium(II) complexes.[29,30] This comparably low oxidation potential highlights the donating power of the phosphinimide ligands.

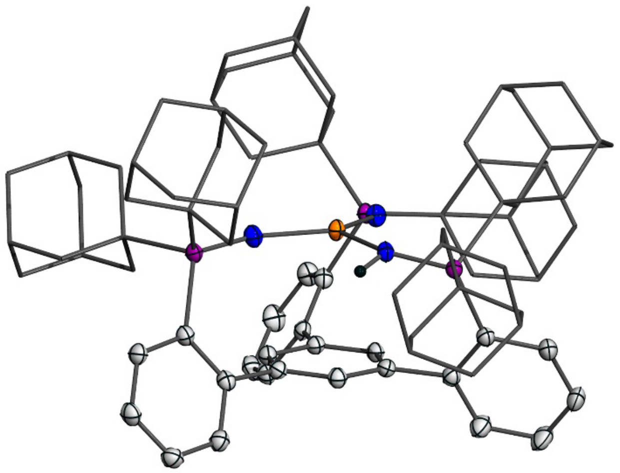

Figure 3.1. XRD structure of **1**. Thermal ellipsoids are drawn at 50% probability. Solvent molecules, disordered adamantyl substituents, and C-H bonds have been removed.

The combination of the precedent for low valent chromium dimers to split dioxygen (O_2) and the electrochemical evidence of **1** being unusually reducing lead us to explore the exposure of **1** with O_2. Exposing a -60 °C toluene solution of **1** to a 1 atm atmosphere of O_2 lead to the complete conversion of **1** to a new red species with a absorbance band at 458 nm (Figure 3.2). Slow heating of the solution indicated the chromophore was stable up to temperatures above 60 °C (Figure S3.14). ^{31}P-NMR characterization of the product that formed indicated that the product was a diamagnetic compound with C_{2v} symmetry about the metal center with two ^{31}P features consistent with two phosphinimides bound to the metal (~ 27 ppm) and one free phosphinimine at a similar resonance to that of **$L^{Ad}H_3$** (~35 ppm) (Figure 3.3). Structural characterization of the product **4** (Figure 3.5) supported the assignment of two PN's bound to chromium and one free phosphinimine. The Cr-O bond distances of 1.601 Å and 1.609 Å are consistent with the formulation of a Cr(VI) dioxo, indicating that **1** had cleaved O_2 via a 4-electron reduction to give a chromium(VI) dioxo. To the best of our knowledge, there are no previous examples of monomeric Cr(II) systems that mediate 4-electron O_2 cleavage via monometallic intermediates.[16] Isotopic labeling of **4** with $^{18}O_2$ resulted in the shift of two isotopically sensitive bands in the FTIR from 927 cm^{-1} and 904 cm^{-1} to 893 cm^{-1} and 863 cm^{-1} ($\Delta\nu$ = 34 cm^{-1} and 41 cm^{-1}), respectively (Figure 3.4). These are in close accordance with the Hooke's law predicted values which predict shifts of 40 cm^{-1} and 39 cm^{-1}, respectively, supporting the assignment of these as the asymmetric and symmetric chromium-oxo vibrations. The solid state structure of **4** also showed a significant contraction of the chromium-nitrogen bonds from an average of 1.936 Å in **1** to 1.767 Å in **4** which showcases the ability of phosphinimides to donate significant π-density into electron deficient transition metal ions and stabilize high-valent organometallic species.

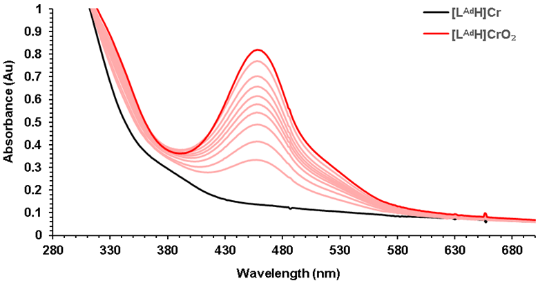

Figure 3.2. UV-Visible spectra of the reaction of **1** (black) with O_2 to produce **4** (red) at 213K. Each trace represents a 1 minute time point

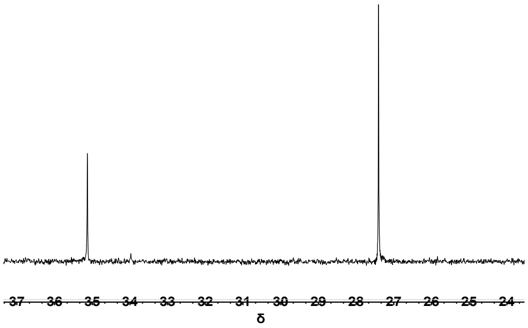

Figure 3.3. ^{31}P NMR spectrum of **4** at 298K

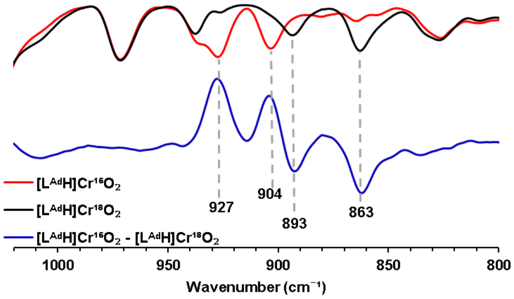

Figure 3.4. KBr-FTIR of $^{16}O_2$-**4** (red), $^{18}O_2$-**4** (black), and the difference spectrum (blue) at 298K.

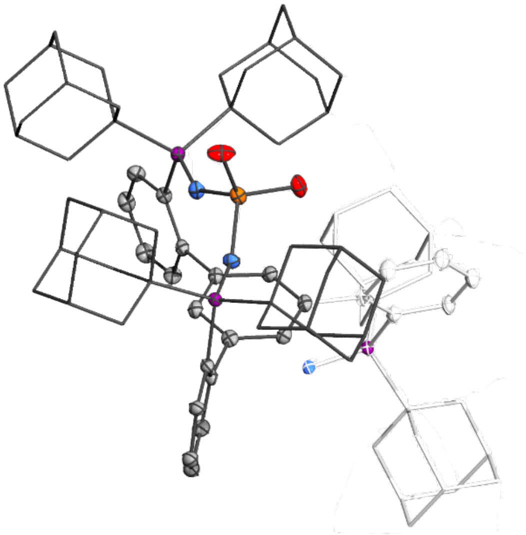

Figure 3.5. XRD structure of **4**. Thermal ellipsoids are drawn at 50% probability. Solvent molecules, disordered adamantyl substituents, and C-H bonds have been removed.

Encouraged by the ability of **1** to perform 4-electron reductions, we sought to explore its reactivity with other substrates that chromium dimers are capable of performing. The reaction of

1 with two equivalents of aryl azide (aryl = 4-methoxyphenyl) at -78 °C resulted in the solution turning red-brown with light effervescence (Scheme 3). ^{31}P-NMR characterization of the diamagnetic product **3** showed an analogous splitting pattern to **4** (Figure S3.23) indicating 2-fold symmetry about with respect to the chromium-bound phosphinimides and a similarly unbound phosphinimine. ^{1}H-NMR analysis of the product showed two inequivalent methoxy groups in a 1:1 ratio (Figure S3.21), supporting the formulation of **3** as a bis(phosphinimide) Cr(VI) bis(imido). Single crystal XRD confirmed this assignment (Figure 3.3). The solid-state structure (Figure 3.6) features two distinct imido fragments: one pseudo-linear with a bond angle of 162.2° and one more bent with a bond angle of 142.5° with Cr-N bond distances of 1.655(2) Å and 1.714(2) Å, respectively. Similar to **4**, the chromium-phosphinimide bonds significantly contract upon oxidation, shortening to an average bond distance of 1.794 Å. This marks the first occurrence of a monomeric chromium(II) species activating two equivalents of organic azides, to the best of our knowledge.

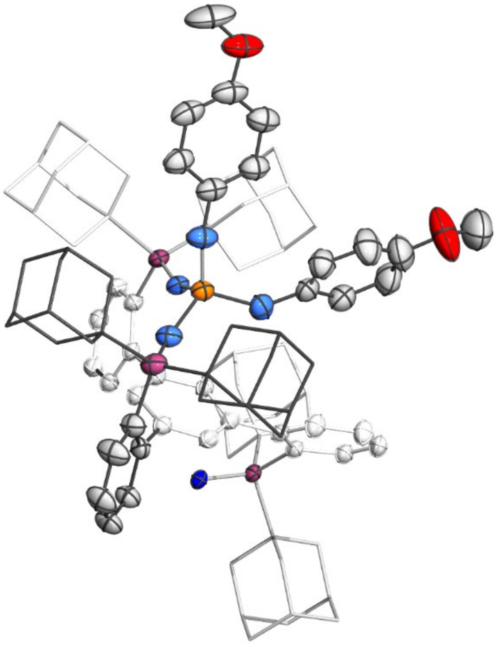

Figure 3.6. XRD structure of **3.** Thermal ellipsoids are drawn at 50% probability. Solvent molecules, disordered adamantyl substituents, and C-H bonds have been removed.

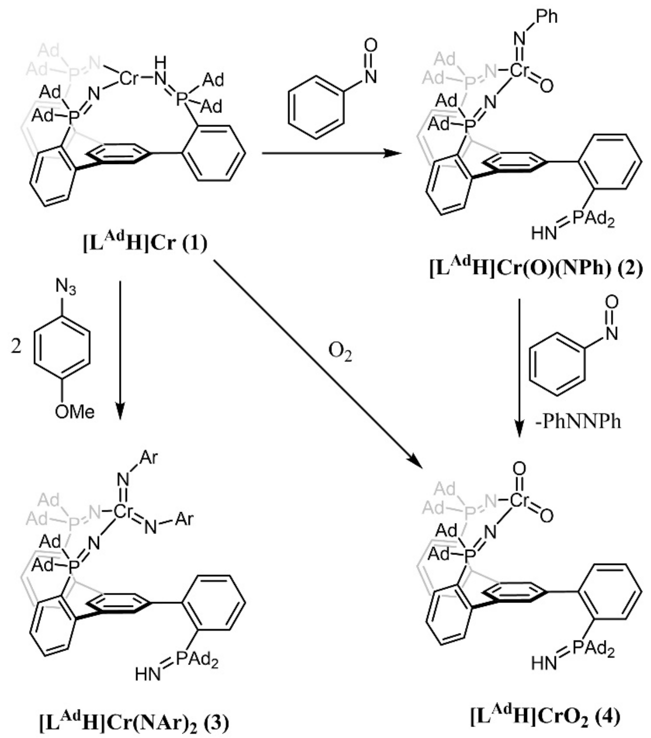

Scheme 3.6. Synthesis of complexes **2-4**

The reaction of **1** with 1 equivalent of nitrosobenzene resulted at -78 °C resulted in a rapid color change to a deep red solution. The UV-Visible spectrum of the resulting reaction indicated that there was partial formation of **4** (Figure S3.2). ^{31}P-NMR analysis confirmed the presence of **4** along with a new diamagnetic species with a similar resonances to both **3** and **4,** but with a chromium(VI)-phosphinimide resonance at an intermediate value between the bound phosphinimides in **3** and **4** (Figure S3.1). Crystallization of the mixture resulted in single crystals of both **4** and the four electron-oxidized bis(phosphinimide) chromium(VI) oxo/imido **2** (Scheme 3.3). The intractable mixture of **2** and **4** precluded the bulk characterization of **2** as multiple attempts with very careful stoichiometric control always had contaminant **4** which crystallized under identical conditions to **2**. The crystal structure of **2** (Figure 3.7) displays similar contraction of the Cr-phosphinimide bonds seen with **3** and **4** as well as Cr-O and Cr-N bond distances of 1.603(3) Å and 1.678(4) Å for the oxo and imido, respectively. This marks the first time that a chromium(II) complex has been reported to perform the 4-electron reductive cleavage of nitrosoarenes.

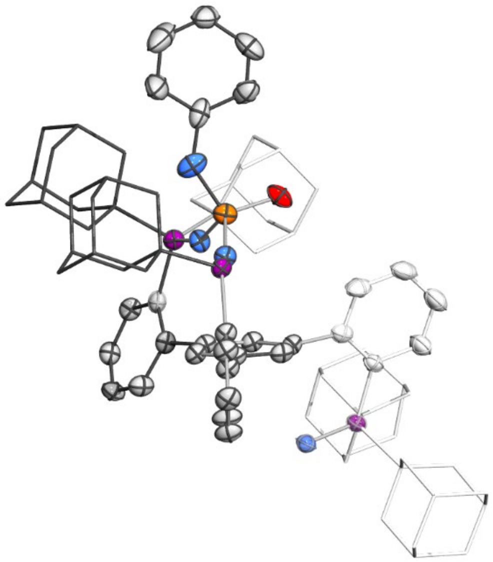

Figure 3.7. XRD Structure of **2**. Thermal ellipsoids are drawn at 50% probability. Solvent molecules, disordered adamantyl substituents, and C-H bonds have been removed.

The cycloaddition of metal-ligand multiple bonds and the multiple bonds of organic substrates has garnered great interest, particularly in the field of olefin metathesis.[31,32] Based on this precedent, various groups have studied the ability of metal-oxygen and metal-nitrogen double bonds to perform similar cycloaddition and cycloreversion processes to perform heterometathesis, which could allow for further molecular complexity using metathesis reactivity. Oxo/Imido heterometathesis (Scheme 3.4), in particular, has been observed for a variety of transition metal compounds, more commonly with early metals and 2nd and 3rd row metals as well as lanthanides.[33] Despite this, there is little precedence for chromium examples, with known examples limited to using benzaldehyde as the organic substrate.[34–36] Additionally, the only precedent for nitrosoarenes being the metathesis substrate is limited to group (IV) imidos[37–41], with no precedence for the imido formation by nitrosoarenes followed by oxo/imido metathesis with a second equivalent. The lack of literature precedent encouraged us to explore the formation of **4** with nitrosobenzene. Addition of 2 equivalents of nitrosobenzene to **1** at -78 °C resulted in the clean formation of **4** with no remaining **2** by ^{31}P-NMR. To explore the organic product of the oxo/imido metathesis, **1** was reacted with 2 equivalents of 4-fluoro-1-nitrosobenzene and tracked via ^{19}F-NMR (Figure S3.3), showing clean conversion to independently synthesized 4,4’-difluoroazobenzene (Scheme 3.3). These data support that **4** is being formed through the initial reductive cleavage of nitrosobenzene to form **3** and then subsequent oxo/imido heterometathesis, marking the first time this combined reactivity has been observed.

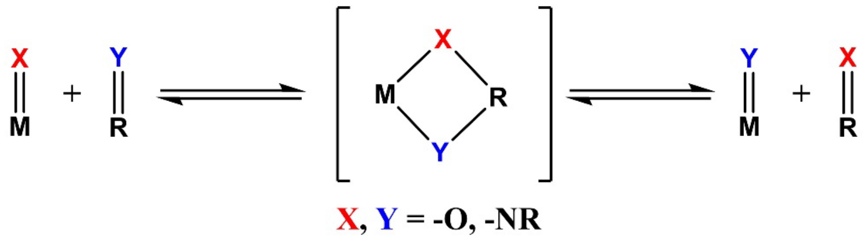

Scheme 3.4. Oxo/Imido heterometathesis reaction

.

3.3 Conclusion

In summary, a reducing chromium(II) complex supported by a sterically encumbered multi-dentate phosphinimide ligand was synthesized. The reaction of the low-coordinate complex with a variety of substrates resulted in the multi-electron reduction of the small molecule substrates, including unparalleled reactivity for monomeric chromium(II) species. The reactivity and the structural analysis of the inorganic products highlight the ability of phosphinimides to support highly reducing compounds and stabilize high-valent metal complexes through significant π-donation. This supports that transition metal complexes of multi-dentate phosphinimide platforms with significant d-electron counts are primed for the multi-electron reduction of small molecules. Additionally, the oxophilicity of the high-valent chromium center allows for unprecedented oxo/imido heterometathesis reactivity. Further studies on the ability of these complexes to abstract oxygens from organic substrates and their subsequent transformations are currently underway.

3.4 Acknowledgements

This research was supported by the University of California Berkeley. We thank Dr. Heui Beom Lee for assistance with XRD and many helpful discussions. X-ray diffraction experiments performed at beamline 12.2.1 at the Advanced Light Source at Lawrence Berkeley National Laboratory were supported by the Director, Office of Science, Office of Basic Energy Sciences, of the U.S. Department of Energy under Contract No. DE-AC02-05CH11231. We thank Prof R. David Britt and Dr. David Marchiori for access to and assistance with their EPR spectrometer (supported by NIH R35 Grant 1R35GM126961-01, to R.D.B), and Prof Christopher Chang for access to a Unisoku Cryostat. We thank Drs. Hasan Celik, Alicia Lund, and UC Berkeley's NMR facility in the College of Chemistry (CoC-NMR) for spectroscopic assistance. Instruments in the CoC-NMR are supported in part by NIH S10OD024998.

3.5 Supporting Information

General Considerations: Unless otherwise noted, all manipulations were carried out using standard Schlenk or glovebox techniques under an N_2 atmosphere. Acetonitrile (MeCN), Benzene, Diethyl ether (Et_2O), Pentane, Tetrahydrofuran (THF), and Toluene were deoxygenated by thoroughly sparging with N_2 gas followed by passing through an activated alumina column in a solvent purification system from Pure Process Technology, and were further dried over 4Å molecular sieves for 48h prior to use. Solvents were routinely tested with a THF solution of sodium benzophenone ketyl. Deuterated solvents were purchased from Cambridge Isotope Laboratories, Inc., and were distilled under N_2, degassed via freeze-pump-thaw cycles, and stored over 4Å molecular sieves prior to use. Oxygen was purchased in Ultra High Purity from Praxair and was further dried by passing through two traps immersed in a dry ice/isopropanol bath. All reagents were purchased from commercial vendors and used without further purification unless otherwise stated. **$L^{Ad}H_3$**[19], $Cr(HMDS)_2(THF)_2$[40], 4-fluoronitrosobenzene[41], and 4,4'-difluoroazobenzene[42] were prepared according to literature procedures. Elemental analyses were performed by the Microanalytical Laboratory in the College of Chemistry at the University of California – Berkeley using a PerkinElmer 2400 Series II combustion analyzer.

Nuclear Magnetic Resonance Spectroscopy: Nuclear Magnetic Resonance (NMR) spectra were measured at Bruker AV-300, AVQ-400, NEO-500, or AV-600 spectrometers. ^{1}H and ^{13}C chemical shifts are reported in ppm relative to tetramethylsilane (TMS) at 0.00 ppm using residual solvent residues as internal standards. ^{31}P chemical shifts are reported in ppm relative to 85% aqueous H_3PO_4 at 0 ppm. Solution phase magnetic measurement were performed using the Evan's method.[43]

Infrared Spectroscopy: Solid IR measurements were obtained on a Nicolet iS20 Spectrometer as KBr pellets.

X-Ray Crystallography: XRD studies were performed at the Small Molecule X-Ray Crystallography Facility (CheXray) or at beamline 12.2.1 at the Advanced Light Source at Lawrence Berkeley National Laboratory.

For studies performed at ChexRay: Crystals were mounted on a Kapton loop under Paratone oil. Data were collected on a Rigaku XtalLAB P200 (MoKα or CuKα radiation) equipped with a MicroMax-007 HF microfocus rotating anode and a Pilatus 200K hybrid pixel array detector at 100 K under a stream of N_2. Data collection, integration, and scaling were carried out using the CrysAlis^{Pro} software.[44]

For studies performed at the Advanced Light Source: Crystals were mounted on a MiTeGen loop under Paratone oil. Data were collected on a Bruker D85 three-circle diffractometer with a PHOTON II CCD area detector using silicon monochromated synchrotron radiation ($\lambda = 0.7288$ Å). Bruker APEX2 software was used for data collection. Bruker SAINT and SADABS software was utilized for data reduction and absorption correction, respectively. [45,46]

Structures were solved using SHELXS and refined against F^2 on all data by full matrix least-squared with SHELXL using OLEX2 crystallographic software.[47] All non-hydrogen atoms were refined using anisotropic displacement parameters. Hydrogen atoms were placed in idealized positions and refined using a riding model.

Electronic Paramagnetic Resonance Spectroscopy: X-band EPR spectra were obtained on a Bruker EMX spectrometer on 5 mM solutions as frozen glasses in toluene. Samples were collected at 2mW power and a temperature of 5K with modulation amplitudes of 8 Gauss. Spectra were simulated using the EasySpin[48] suite of programs in Matlab 2021.

Optical Spectroscopy: Measurements were taken on a Hewlett-Packard 8453 UV-Vis Spectrophotometer using a 1cm quartz cell sealed with a Teflon stopcock. Variable Temperature measurements were performed using a UNISOKU Unispec Cryostat.

Electrochemistry: Electrochemical measurements were carried in 0.2 M THF solutions of electrolyte ($[^{n}Bu_4N][PF_6]$). Data collection were performed on a BioLogic SP-50 Potentiostat using a freshly-polished glassy carbon electron as the working electrode and a platinum wire as the auxiliary electrode. All reported potentials are referenced to the ferrocene/ferrocenium couple (Cp_2Fe/Cp_2Fe^+).

Synthetic Procedures:

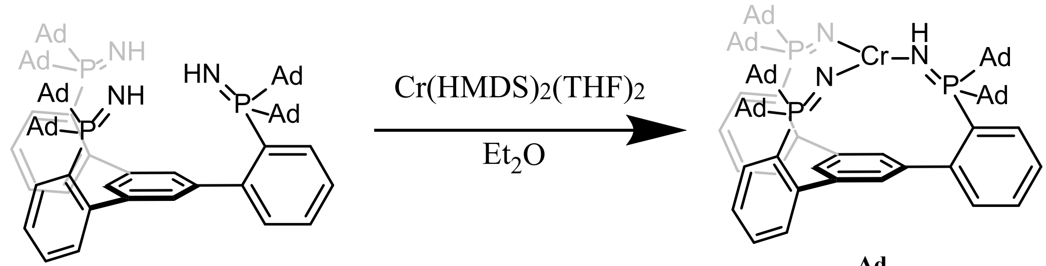

[L^{Ad}H]Cr (1)

Scheme S3.1. Synthesis of **1**

[L^{Ad}H]Cr (1) : In the glove box, a 250 mL round-bottomed flask was charged with a magnetic stir bar, **L^{Ad}H$_3$** (1.5g, 1.2 mmol, 1 Equiv), and Et$_2$O (50 mL). Cr(HMDS)$_2$(THF)$_2$ (688 mg, 1.2 mmol, 1 Equiv) was added dropwise to the flask as a solution in Et$_2$O (20 mL). The mixture was stirred for 48h resulting in a brown precipitate in a dark brown solution. The brown solid was collected on a medium frit and washed with Et$_2$O (2x20 mL) until the washings were colorless. The brown solid residue was extracted into benzene (3 x 15 mL) and the volatiles were removed to give **[L^{Ad}H]Cr** as a brown powder (1.33 g, 1.0 mmol, 85.3 %). The filtrate was concentrated and layered with pentane to obtain a second crop of **[L^{Ad}H]Cr** (53 mg, 0.03 mmol, 3.4%) to give a combined yield of 88.7 %. Single crystals of **[L^{Ad}H]Cr** suitable for X-ray diffraction were grown from layering pentane onto a concentrated Et$_2$O solution of **[L^{Ad}H]Cr** to give light brown rods. ^{1}H NMR (400 MHz, C$_6$D$_6$) δ 16.55, 13.36, 5.72. Anal: calc. for C$_{84}$H$_{106}$N$_3$P$_3$Cr: C 77.45, H 8.20, N 3.23; found: C 74.17, H 8.26, N 3.47. μ_{eff} (Benzene-*d*$_6$, 298 K, 400 MHz): 4.8 μ_B. (KBr, 298 K, cm^{-1}): 3403 ν(*N-H)*. UV-Vis (Toluene, 213K, nm {cm^{-1}M^{-1}}): 385 {1700}.

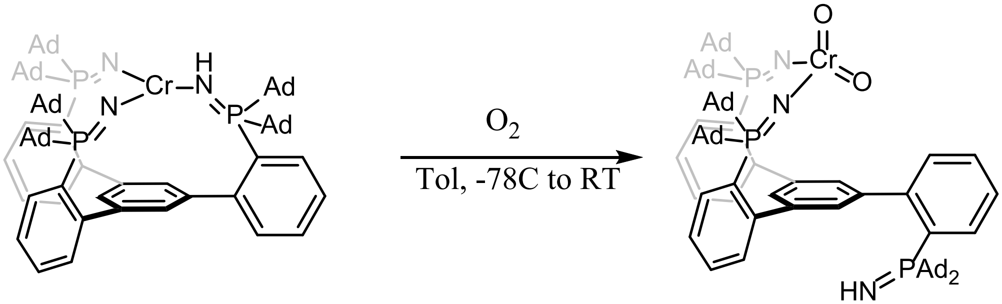

(4)
[L^{Ad}H]CrO$_2$

Scheme S3.2. Synthesis of **4**

[L^{Ad}H]CrO$_2$ (4) : In the glove box, a 50 mL Schlenk tube was charged with a Toluene (25 mL) solution of **1** (300 mg, 0.23 mmol, 1 Equiv) and a magnetic stir bar. The tube was sealed, removed from the glovebox, and cooled to -78 °C with a dry ice/isopropanol bath. The tube was partially evacuated with three quick vacuum cycles before being exposed to O_2. The reaction was allowed to warm to ambient temperature and stirred for 3h. The volatiles were removed and the Schlenk tube was transferred into the glove box. The tube was extracted with benzene (3 x 10mL), pumped down in vacuo, and washed with Et_2O (4 mL). **2** was isolated as a blood red solid (254 mg, 0.19 mmol, 82.5%). The Et_2O washings were layered with pentane (4 mL) to produce crystals suitable for XRD (22 mg, 0.02 mmol, 7.1%) to give a combined yield of 89.6%. ^{1}H NMR (400 MHz, Benzene-*d*$_6$) δ 8.46 (d, *J* = 8.0 Hz, 1H), 7.76 (d, *J* = 7.9 Hz, 2H), 7.68 (s, 1H), 7.60 (t, *J* = 8.2 Hz, 1H), 7.48 (t, *J* = 9.0 Hz, 2H), 7.36 – 7.23 (m, 3H), 7.06 (s, 5H), 2.61 – 1.40 (m, 90H), -0.51 (s, 1H). ^{13}C NMR (151 MHz, C_6D_6) δ 151.52, 150.92, 141.42, 139.31, 135.83, 134.55, 131.72, 129.88, 129.70, 125.16, 124.85, 123.37, 48.13, 47.80, 45.06, 44.76, 42.05, 41.64, 38.91, 38.49, 38.12, 37.19, 37.02, 36.84, 29.09, 28.86. ^{31}P NMR (243 MHz, C_6D_6) δ 35.13, 27.40. Anal: calc. for $C_{84}H_{106}N_3P_3CrO_2$: C 75.59, H 8.01, N 3.15; found: C 75.23, H 7.99, N 3.10. (KBr, 298 K, cm^{-1}): 904 ν(*CrOO)* , 927 ν(*CrOO)* , 3402 ν(*N-H)*. UV-Vis (Toluene, 213K, nm {cm^{-1}M^{-1}}): 458 {5200}.

[L^{Ad}H]Cr^{18}O$_2$: Prepared analogously to **2** except with 30 mg (0.023 mmol) of **1**, 2mL of Toluene, and using a J-Young tube as a reaction vessel to isolate **[L^{Ad}H]Cr^{18}O$_2$** as a blood red solid (24 mg, 0.18 mmol, 78.0 %). (KBr, 298 K, cm^{-1}): 863 ν(*CrOO)* , 893 ν(*CrOO)* , 3402 ν(*N-H)*.

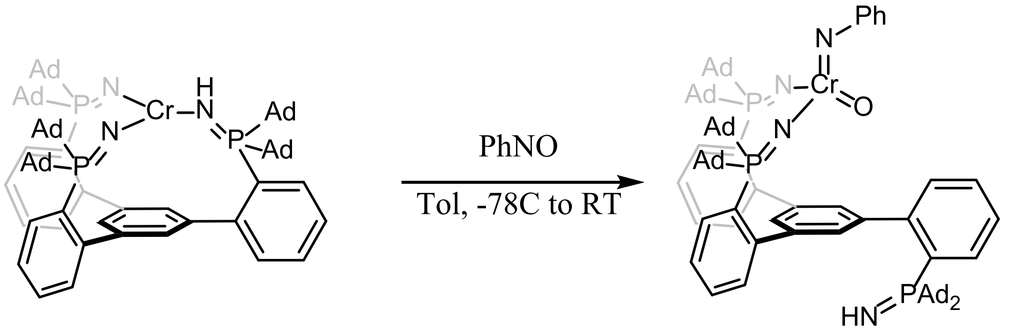

[L^{Ad}H]Cr(NPh)(O) (2)

Scheme S3.3. Synthesis of **2**

[L^{Ad}H]Cr(NPh)(O) (2) : In the glove box, a 20 mL scintillation vial was charged with **1** (100 mg, 0.076 mmol), toluene (7 mL), and a magnetic stir bar. The solution was cooled to -78 °C with a dry ice/isopropanol chilled cold well. A toluene (2 mL) solution of nitrosobenzene (8.3 mg, 0.076 mmol, 1 Equiv) was added dropwise, resulting in a color change from brown to blood red. The reaction was allowed to warm to room temperature and stirred for 3h. The volatiles were removed in vacuo, and the red residue was triturated with pentane (3 mL). The solid was washed with pentane (3 x 3mL) and then extracted into benzene (3 x 2 mL). Single crystals suitable for XRD were grown from slow evaporation of the pentane washes as a mixture of **2** and **3** crystals. ^{31}P NMR (243 MHz, C_6D_6) δ 35.11, 26.71.

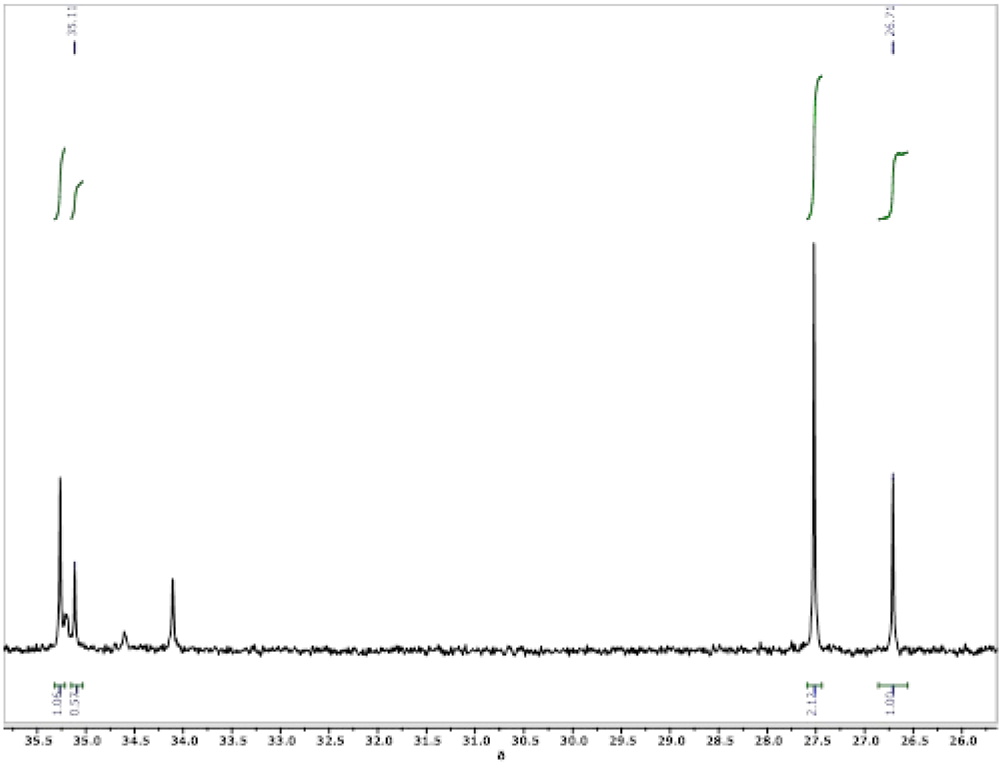

Figure S3.1. Crude ^{31}P NMR (162 MHz, 298 K) of a Mixture of **2** and **4**

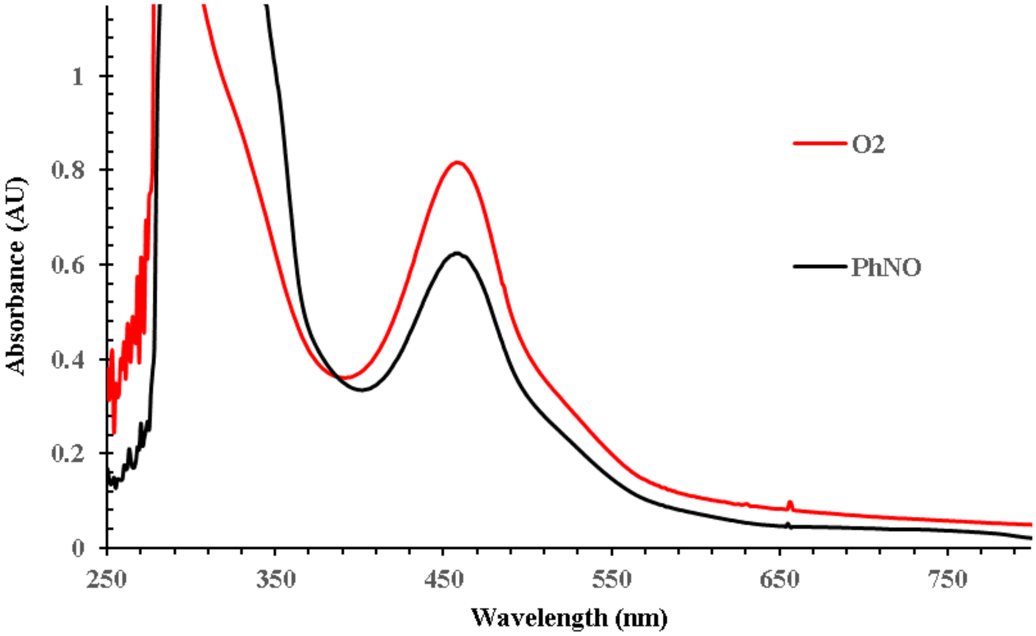

Figure S3.2. UV/Visible spectrum of **1** + 1.1 equivalents of PhNO in Toluene at 213 K

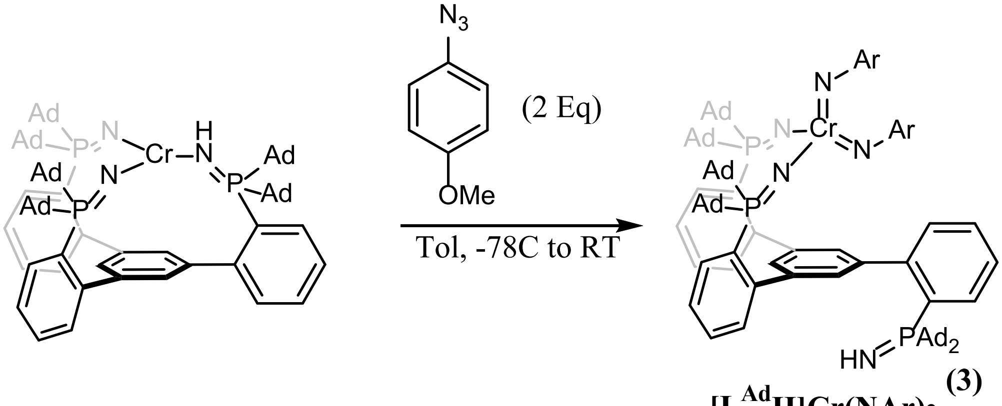

[L^{Ad}H]Cr(NAr)$_2$

Scheme S3.4. Synthesis of **3**

[L^{Ad}H]Cr(NAr)$_2$ (4) : In the glove box, a 20 mL scintillation vial was charged with **1** (100 mg, 0.076 mmol), toluene (7 mL), and a magnetic stir bar. The solution was cooled to -78 °C with a dry ice/isopropanol chilled cold well. A toluene (2 mL) solution of 4-methoxyphenylazide (23 mg, 0.152 mmol, 2 Equiv) was added dropwise, resulting in a color change from brown to dark red-brown. The reaction was allowed to warm to room temperature and stirred for 3h. The volatiles were removed in vacuo, and the residue was triturated with pentane (3 mL). The solid was washed with pentane (3 x 2mL) and then extracted into benzene (3 x 3 mL). The combined benzene fractions were concentrated and layered with pentane (12 mL) to isolate **2** as a red-brown microcrystalline solid (86 mg, 0.056 mmol, 73 %). Single crystals suitable for XRD were grown from slow evaporation of the pentane washes. ^{1}H NMR (600 MHz, Benzene-d_6) δ 8.01 – 7.96 (m, 2H), 7.81 (m, 1H), 7.69 – 7.62 (m, 3H), 7.49 – 7.44 (m, 1H), 7.38 (d, *J* = m, 2H), 7.30 (m, 2H), 7.28 – 7.22 (m, 4H), 7.14 – 7.10 (m, 4H), 6.81 – 6.77 (m, 2H), 6.71 – 6.66 (m, 2H), 3.37 (s, 3H), 3.19 (s, 3H), 2.73 – 2.64 (m, 6H), 2.41 (d, *J* = 12.7 Hz, 6H), 2.34 (t, *J* = 12.4 Hz, 12H), 2.25 (t, *J* = 12.4 Hz, 12H), 2.07 – 2.01 (m, 6H), 1.85 – 1.79 (m, 18H), 1.72 (d, *J* = 12.2 Hz, 6H), 1.59 – 1.45 (m, 24H), -0.46 (d, *J* = 3.5 Hz, 1H). ^{13}C NMR (151 MHz, C_6D_6) δ 158.42, 157.88, 156.22, 155.71, 151.96, 151.29, 141.94, 137.95, 135.28, 131.97, 131.62, 129.87, 129.82, 129.36, 129.31, 125.79, 125.13, 124.91, 124.83, 124.77, 124.65, 124.59, 113.58, 113.11, 55.00, 54.89, 46.55, 46.23, 43.71, 43.40, 42.23, 41.82, 39.27, 38.53, 38.04, 37.33, 37.20, 36.96, 29.57, 29.51, 28.98, 28.91, 28.85. ^{31}P NMR (243 MHz, Benzene-d_6) δ 34.97, 25.41. Anal: calc. for $C_{98}H_{120}N_5P_3CrO_2$: C 76.19, H 7.83, N 4.53; found: C 75.87, H 7.59, N 4.72. (KBr, 298 K, cm^{-1}): 3413 ν(*N-H)*. UV-Vis (Toluene, 298K, nm {cm^{-1}M^{-1}}): 382 {3300}.

Reaction of $[L^{Ad}H]Cr$ with 2 Equivalents of 4-fluoronitrosobenzene

Synthetic Procedure: In the glovebox, **1** (10.0 mg, 0.008 mmol) was added to a 1-dram vial with a magnetic stir bar and d^8-toluene (0.7 mL) was added. The vial was cooled to -78 °C in a dry ice/isopropanol chilled cold well. 4-fluoronitrosobenzene (0.016 mmol, 2 Equiv) was added as a stock solution in d^8-toluene. The solution was allowed to warm to ambient temperature and transferred to a J-Young tube for analysis.

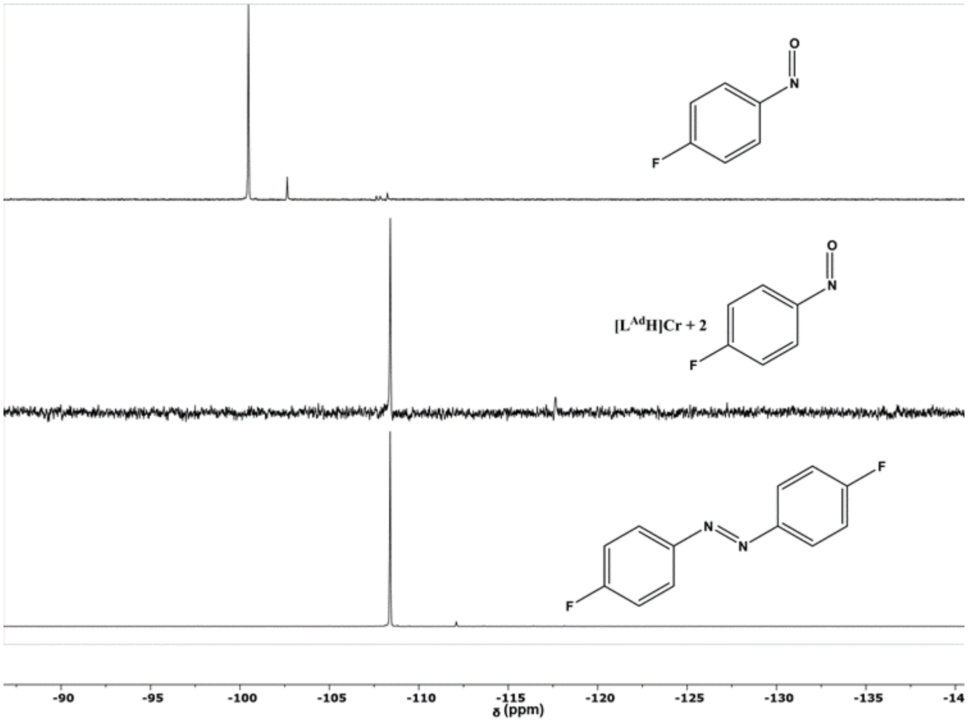

Figure S3.3. ^{19}F NMR Spectrum (400 MHz, 298K) of the reaction of $\mathbf{[L^{Ad}H]Cr}$ and 2 equivalents of 4-fluoronitrosobenzene recorded in d_8-toluene.

X-Ray Crystallography

Identification code	**1**	**2**	**3**	**4**
Empirical formula	$C_{88}H_{116}CrN_3OP_3$	$C_{88}H_{115.67}CrN_3O_3P_3$	$C_{95}H_{126}CrN_4OP_3$	$C_{98}H_{120}CrN_5O_2P_3$
Formula weight	1376.74	1408.40	1484.90	1544.89
Temperature/K	100	100	100	100
Crystal system	monoclinic	triclinic	triclinic	monoclinic
Space group	$P2_1/c$	P-1	P-1	$P2_1/c$
a/Å	10.21640(10)	15.8099(8)	15.6394(8)	25.63654(18)
b/Å	27.68330(10)	16.7046(8)	16.3015(8)	14.36215(8)
c/Å	26.95690(10)	17.2588(11)	19.3066(10)	22.45210(11)
α/°	90	75.013(3)	66.015(2)	90
β/°	96.0400(10)	63.149(2)	82.732(2)	96.5168(6)
γ/°	90	63.653(2)	63.617(2)	90
Volume/Å^3	7581.72(9)	3634.5(4)	4019.9(4)	8213.36(8)
Z	4	2	2	4
ρ_{calc}g/cm^3	1.206	1.287	1.227	1.249
μ/mm^{-1}	2.203	0.278	0.253	2.109
F(000)	2968.0	1515.0	1602.0	3312.0
Crystal size/mm^3	0.4 × 0.15 × 0.1	0.2 × 0.2 × 0.15	0.25 × 0.2 × 0.1	0.6 × 0.4 × 0.3
Radiation	CuKα (λ = 1.54184)	MoKα (λ = 0.71073)	MoKα (λ = 0.71073)	CuKα (λ = 1.54184)
2Θ range for data collection/°	6.386 to 158.16	2.652 to 56.564	2.314 to 55.97	6.94 to 158.164
Index ranges	$-12 \le h \le 10$, $-34 \le k \le 35$, $-34 \le l \le 34$	$-21 \le h \le 21$, $-22 \le k \le 22$, $-23 \le l \le 23$	$-20 \le h \le 20$, $-21 \le k \le 21$, $-25 \le l \le 25$	$-32 \le h \le 32$, $-18 \le k \le 18$, $-26 \le l \le 28$
Reflections collected	135320	118746	134753	241568
Independent reflections	16061 [R_{int} = 0.0523, R_{sigma} = 0.0253]	17046 [R_{int} = 0.1058, R_{sigma} = 0.0765]	19146 [R_{int} = 0.1064, R_{sigma} = 0.0704]	17633 [R_{int} = 0.0434, R_{sigma} = 0.0176]
Data/restraints/parameters	16061/0/871	17046/6/936	19146/201/980	17633/0/1069
Goodness-of-fit on F^2	1.073	1.088	1.112	1.031
Final R indexes [I>=2σ (I)]	R_1 = 0.0380, wR_2 = 0.1041	R_1 = 0.0885, wR_2 = 0.1908	R_1 = 0.1025, wR_2 = 0.2728	R_1 = 0.0578, wR_2 = 0.1684
Final R indexes [all data]	R_1 = 0.0395, wR_2 = 0.1054	R_1 = 0.1219, wR_2 = 0.2056	R_1 = 0.1379, wR_2 = 0.3072	R_1 = 0.0619, wR_2 = 0.1725
Largest diff. peak/hole / e Å^{-3}	0.55/-0.46	1.25/-1.05	1.52/-1.02	0.70/-1.18

Table S3.2. X-Ray Diffraction Table

EPR Spectra

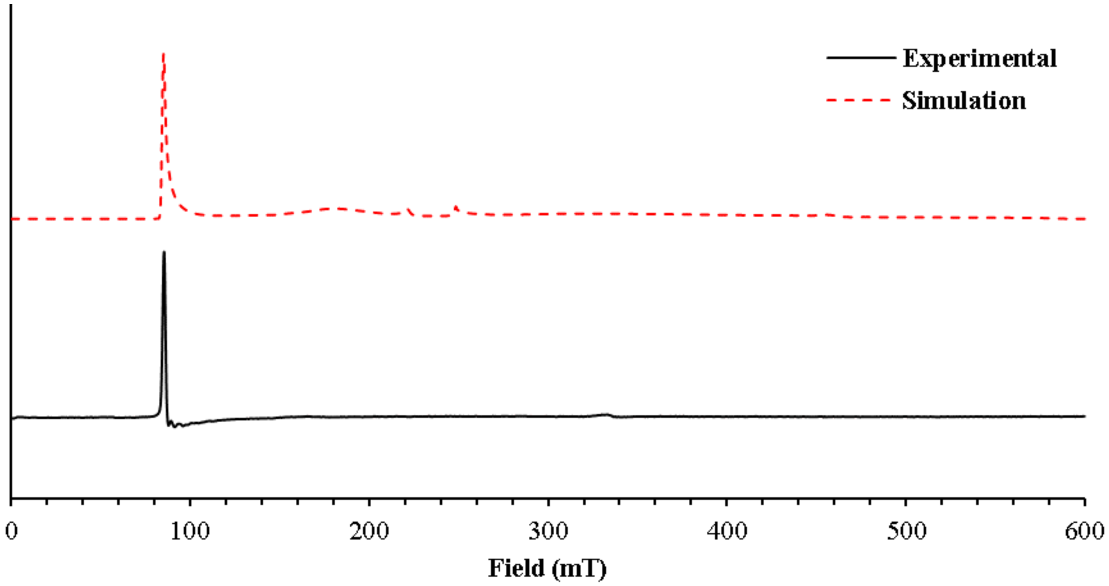

Figure S3.4. Parallel-mode X-band EPR spectrum of a toluene solution of **1** at 5 K and the S =2 (D = 0.17 cm^{-1}, E = 2.9x10^{-4} cm^{-1}, g = 2.00) simulation.

Infrared Spectra

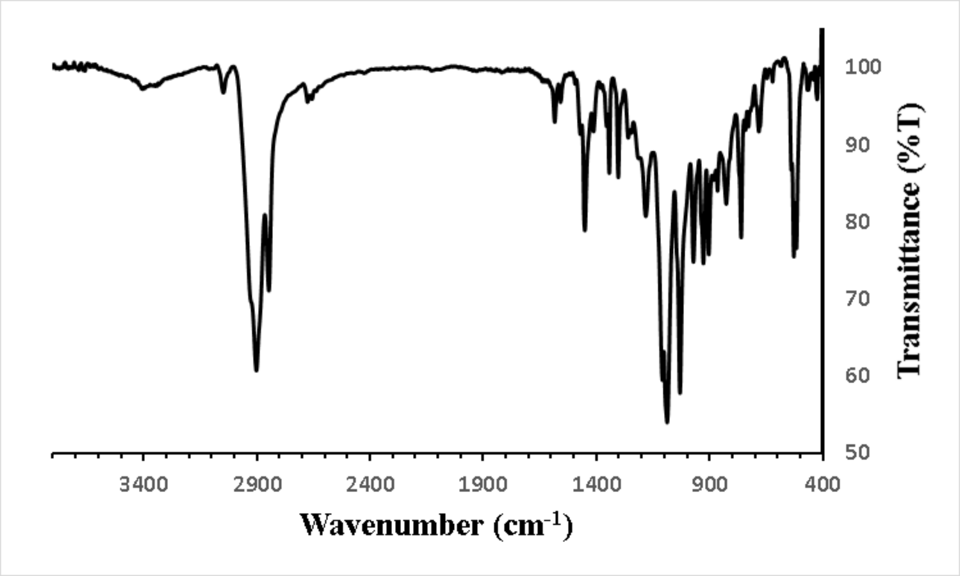

Figure S3.5. KBr-IR spectrum of **[L^{Ad}H]Cr**.

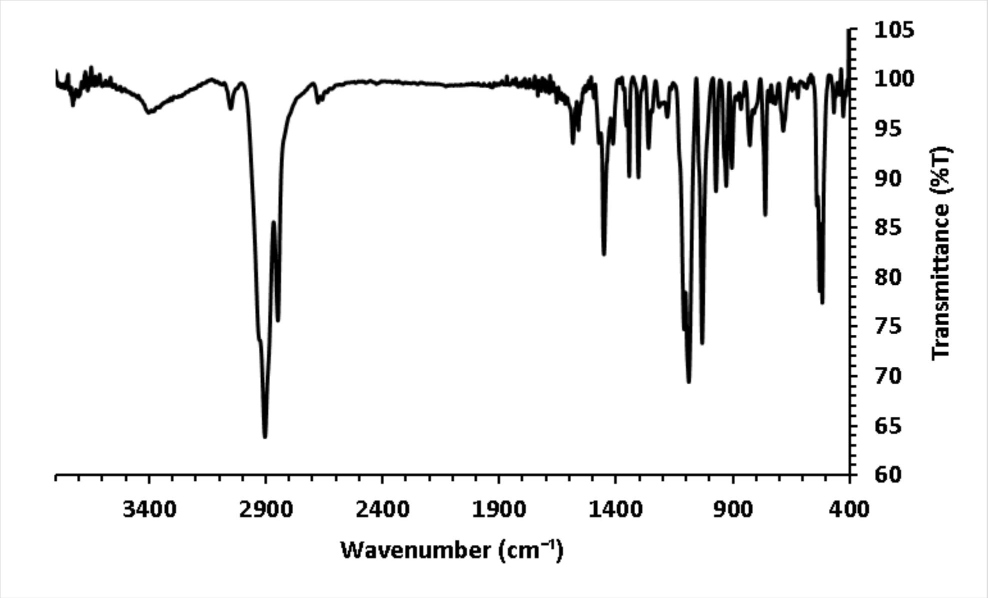

Figure S3.6. KBr-IR spectrum of **[L^{Ad}H]Cr^{16}O$_2$**

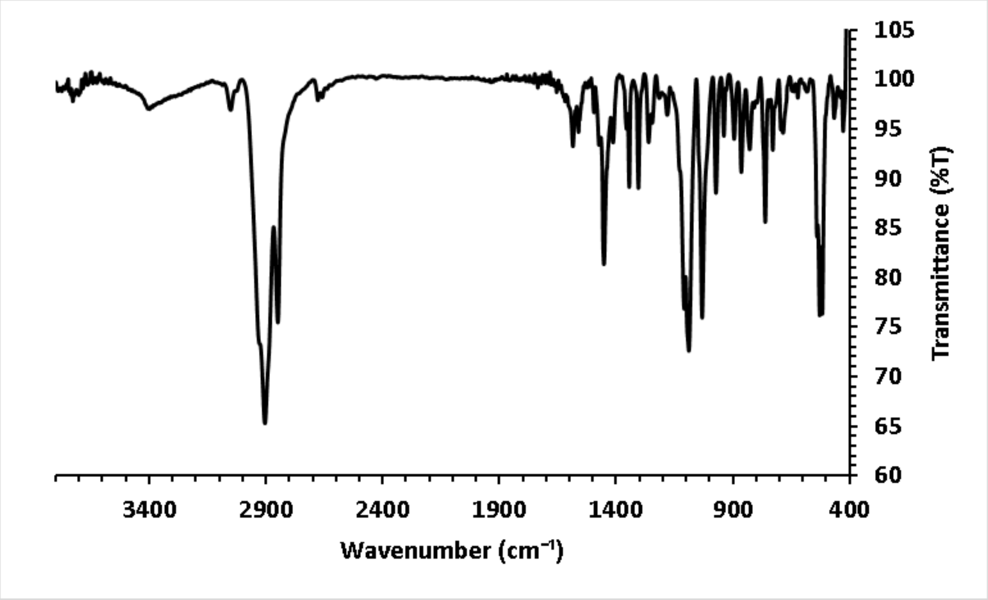

Figure S3.7. KBr-IR spectrum of **[L^{Ad}H]Cr^{18}O$_2$**

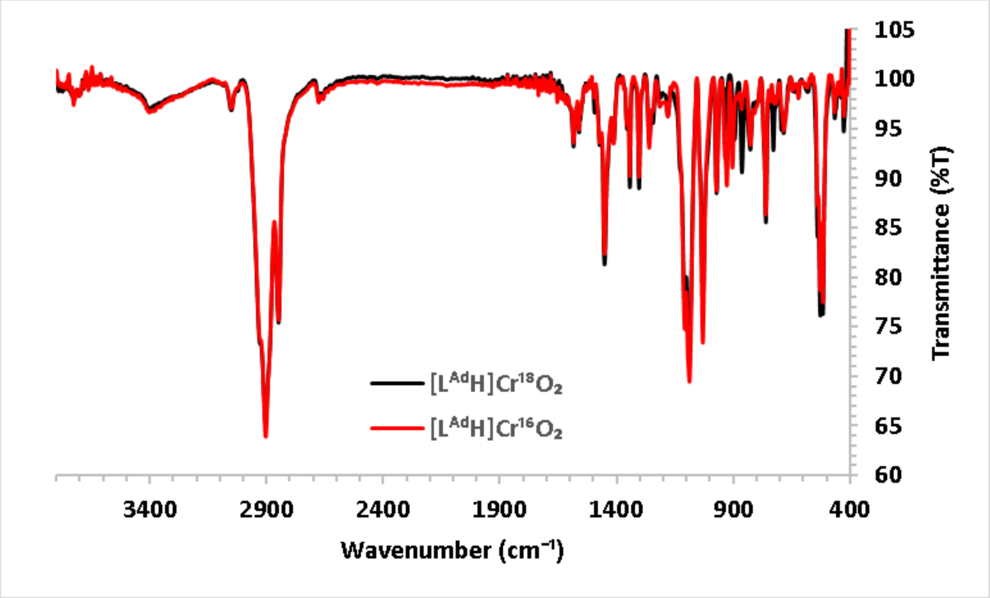

Figure S3.8. Full overlaid KBr-IR spectra of **[L^{Ad}H]Cr^{16}O$_2$** and **[L^{Ad}H]Cr^{18}O$_2$**

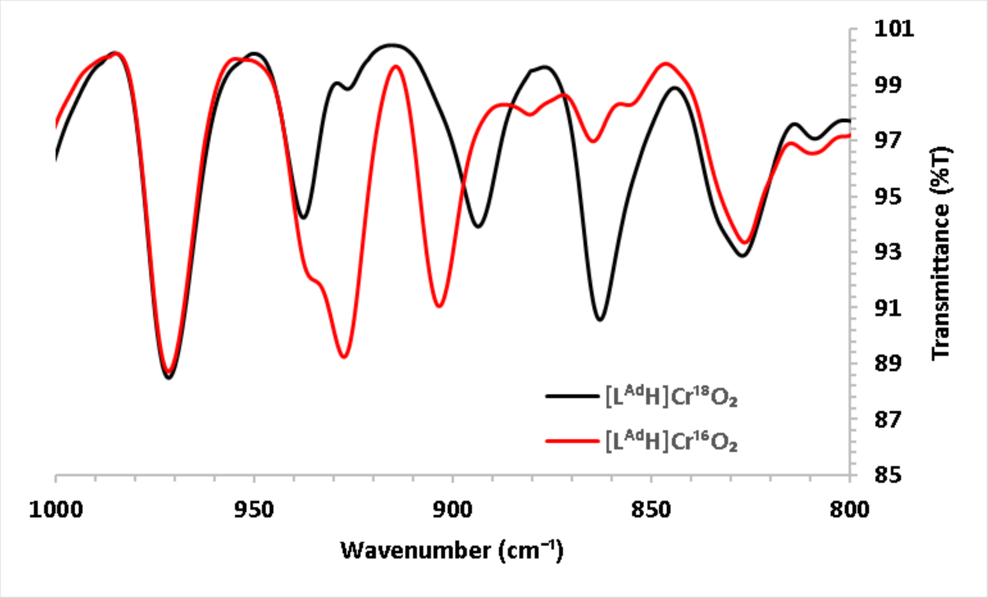

Figure S3.9. Zoomed in overlaid KBr-IR spectra of **[L^{Ad}H]Cr^{16}O$_2$** and **[L^{Ad}H]Cr^{18}O$_2$**

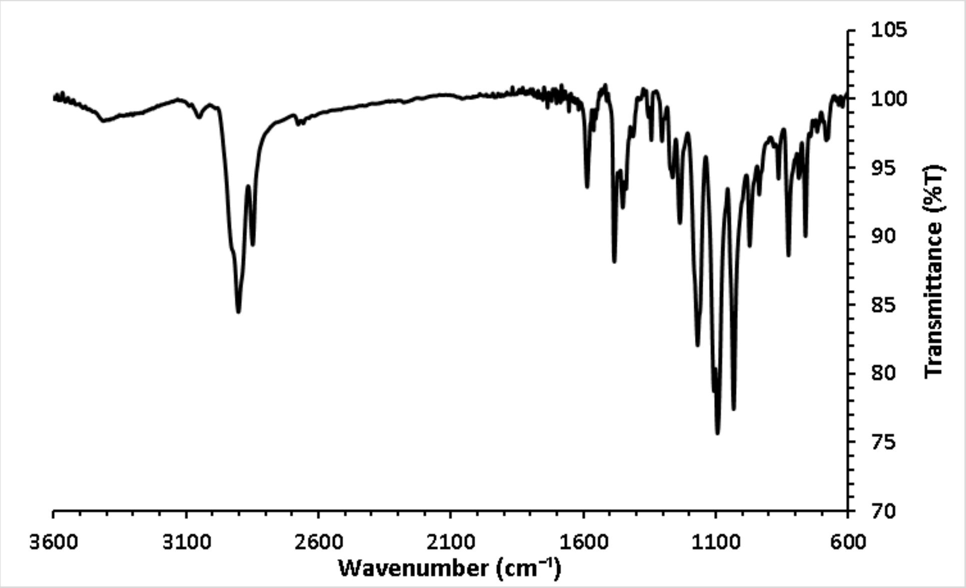

Figure S3.10. KBr-IR spectrum of **3**

UV-Visible Spectra

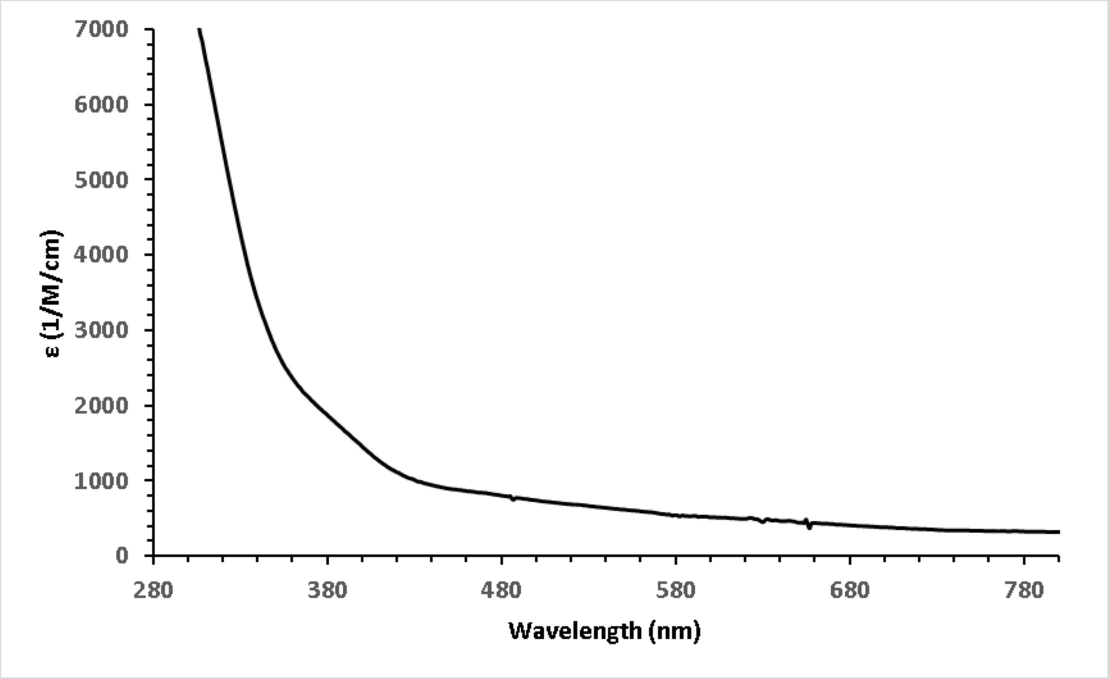

Figure S3.11. UV/Visible spectrum of **1** in Toluene at 213 K

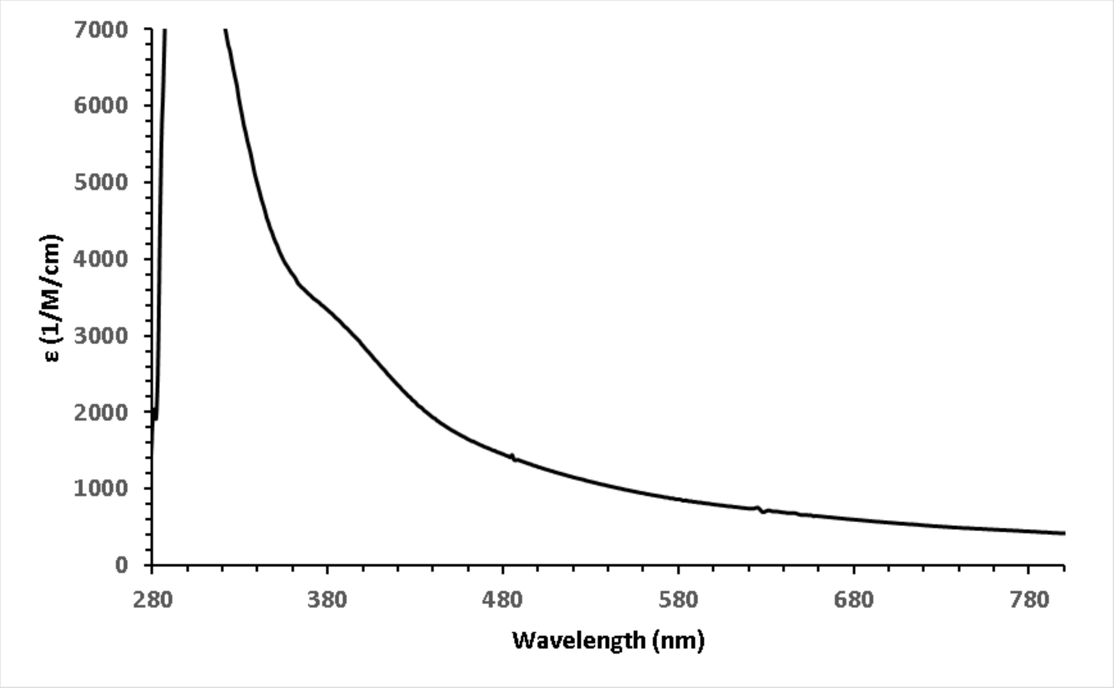

Figure S3.12. UV/Visible spectrum of **3** in Toluene at 298 K

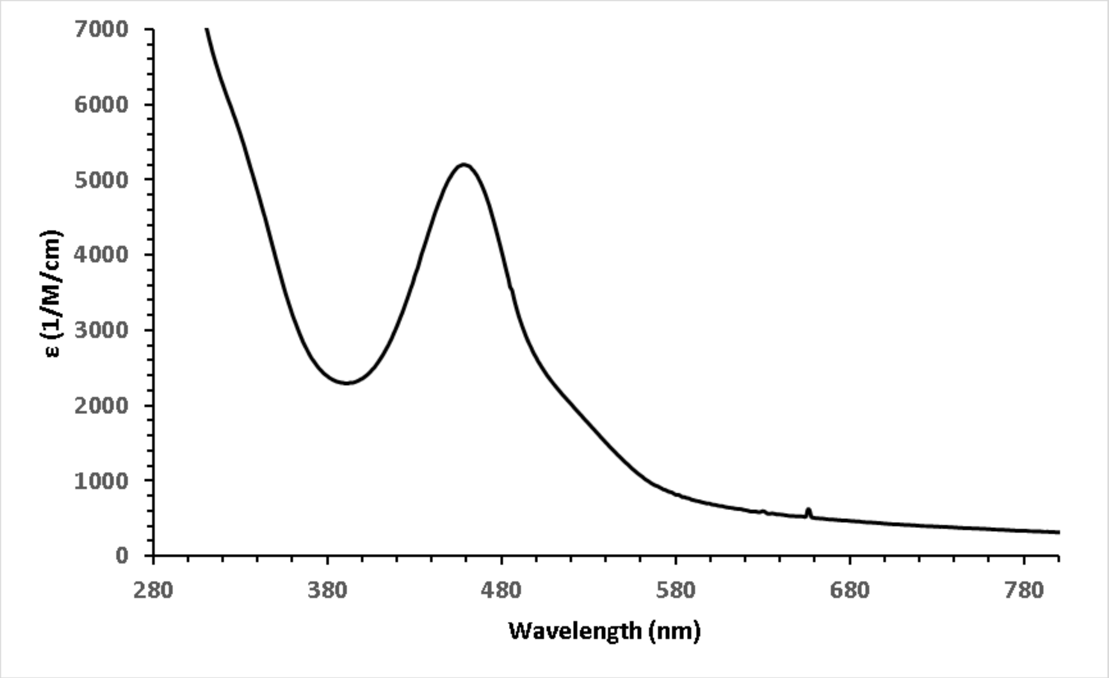

Figure S3.13. UV/Visible spectrum of **4** in Toluene at 213 K

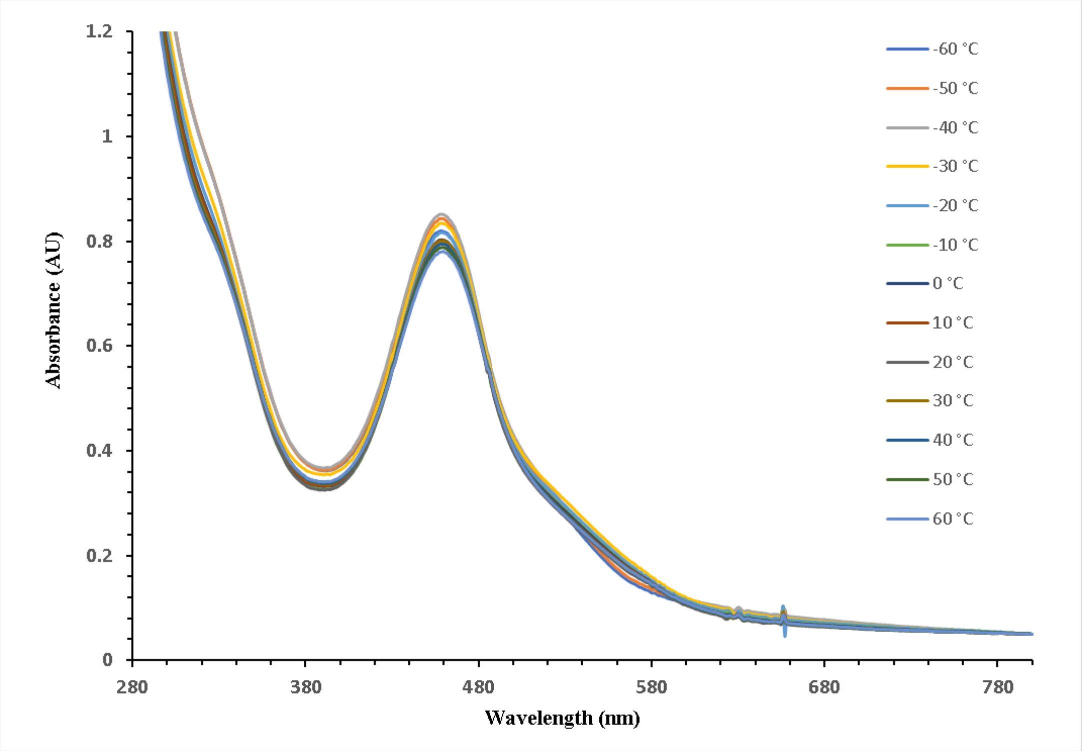

Figure S3.14. UV/Visible spectrum of **4** in toluene from 213 K to 333 K.

Electrochemistry

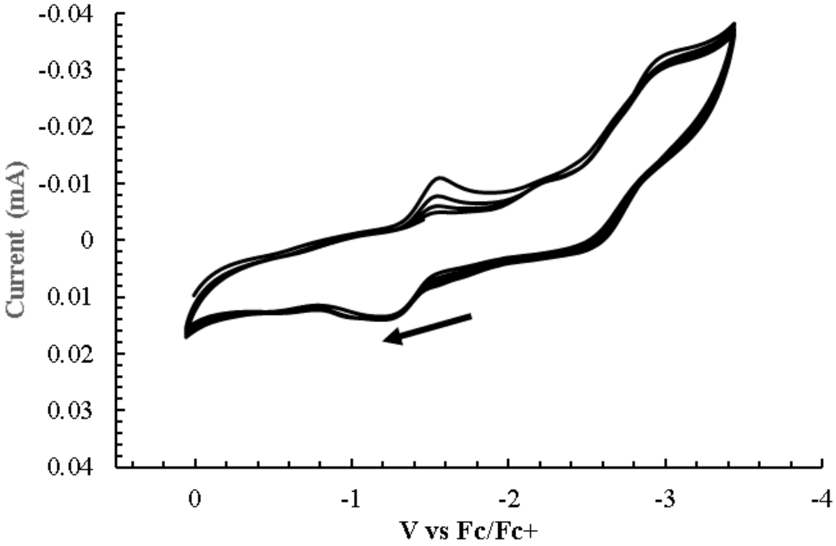

Figure S3.15. Cyclic Voltammogram of **1**, measured in 0.2 M [$^{n}Bu_4N$][PF_6]) electrolyte in THF at 298 K.

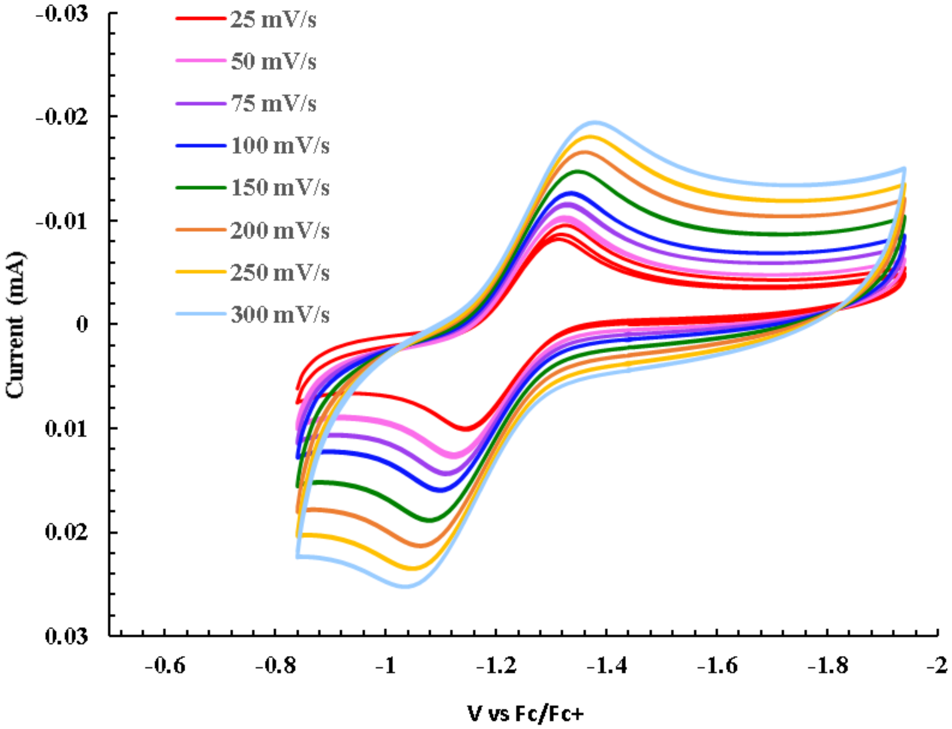

Figure S3.16. Scan rate dependence of 1st oxidation event of **1** in 0.2 M [$^{n}Bu_4N$][PF_6]) electrolyte in THF at 298 K

NMR Spectra

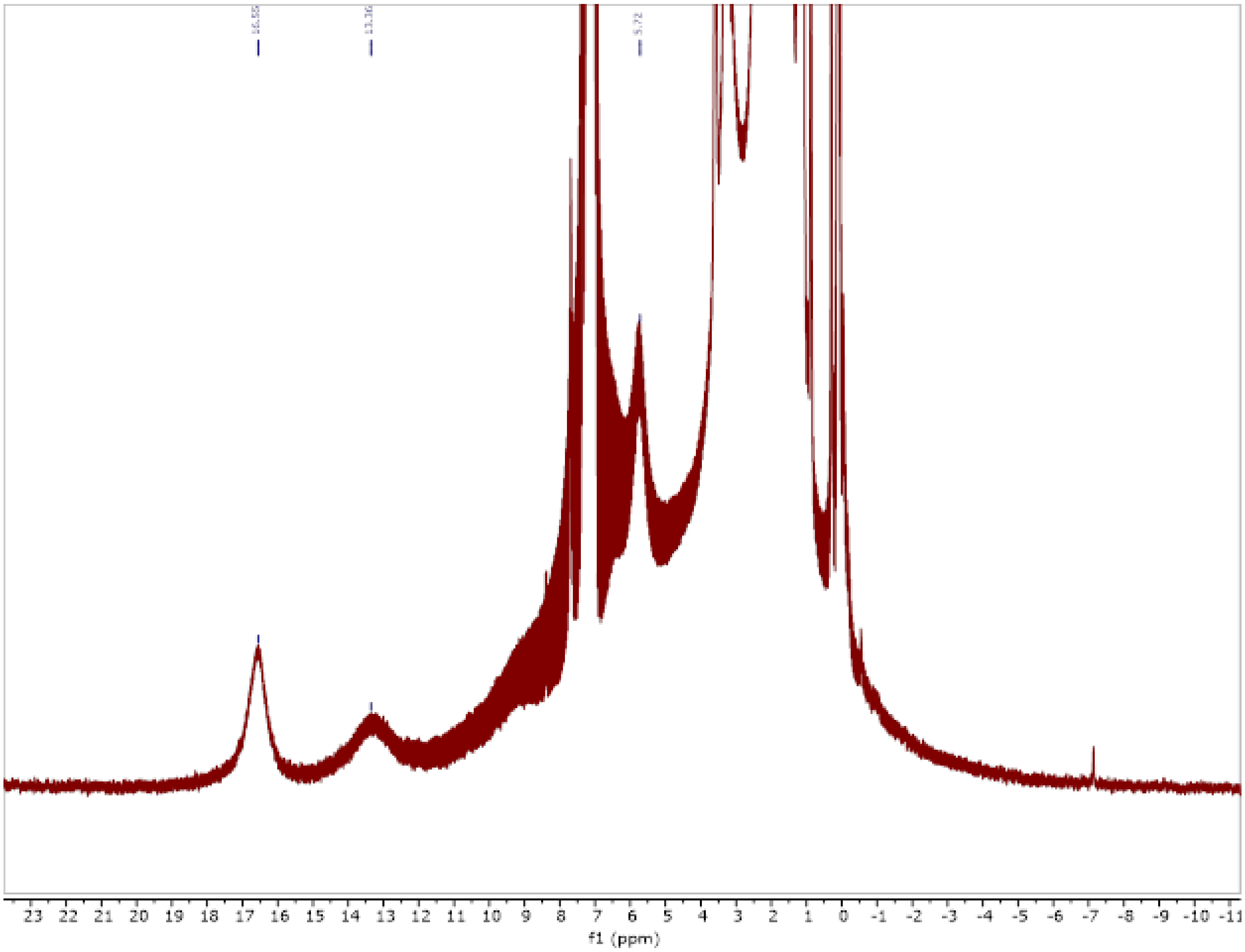

Figure S3.17. ^{1}H NMR Spectrum (400 MHz, 298K) of **[L^{Ad}H]Cr** recorded in C_6D_6

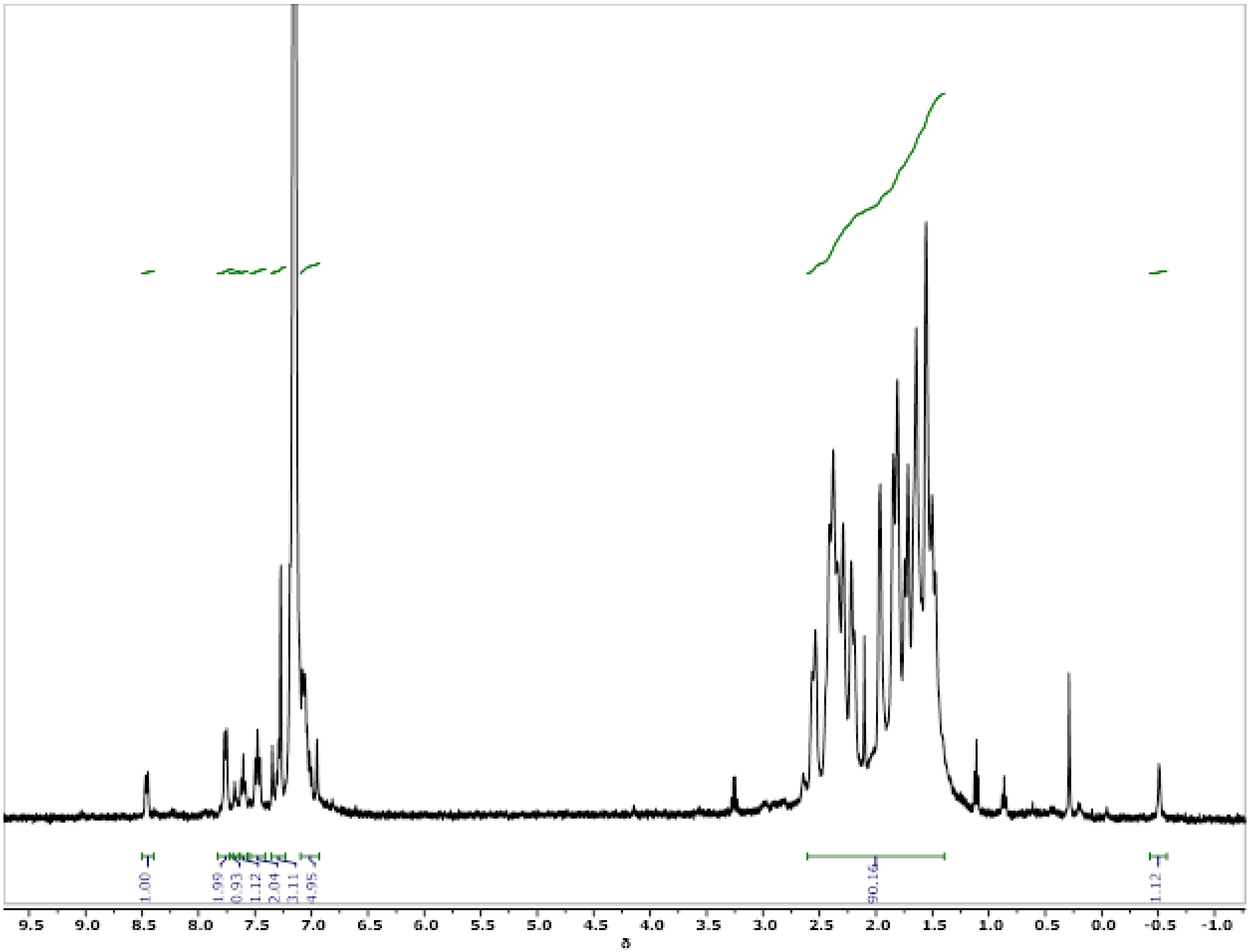

Figure S3.18. ^{1}H NMR Spectrum (400 MHz, 298K) of **[L^{Ad}H]CrO$_2$** recorded in C_6D_6

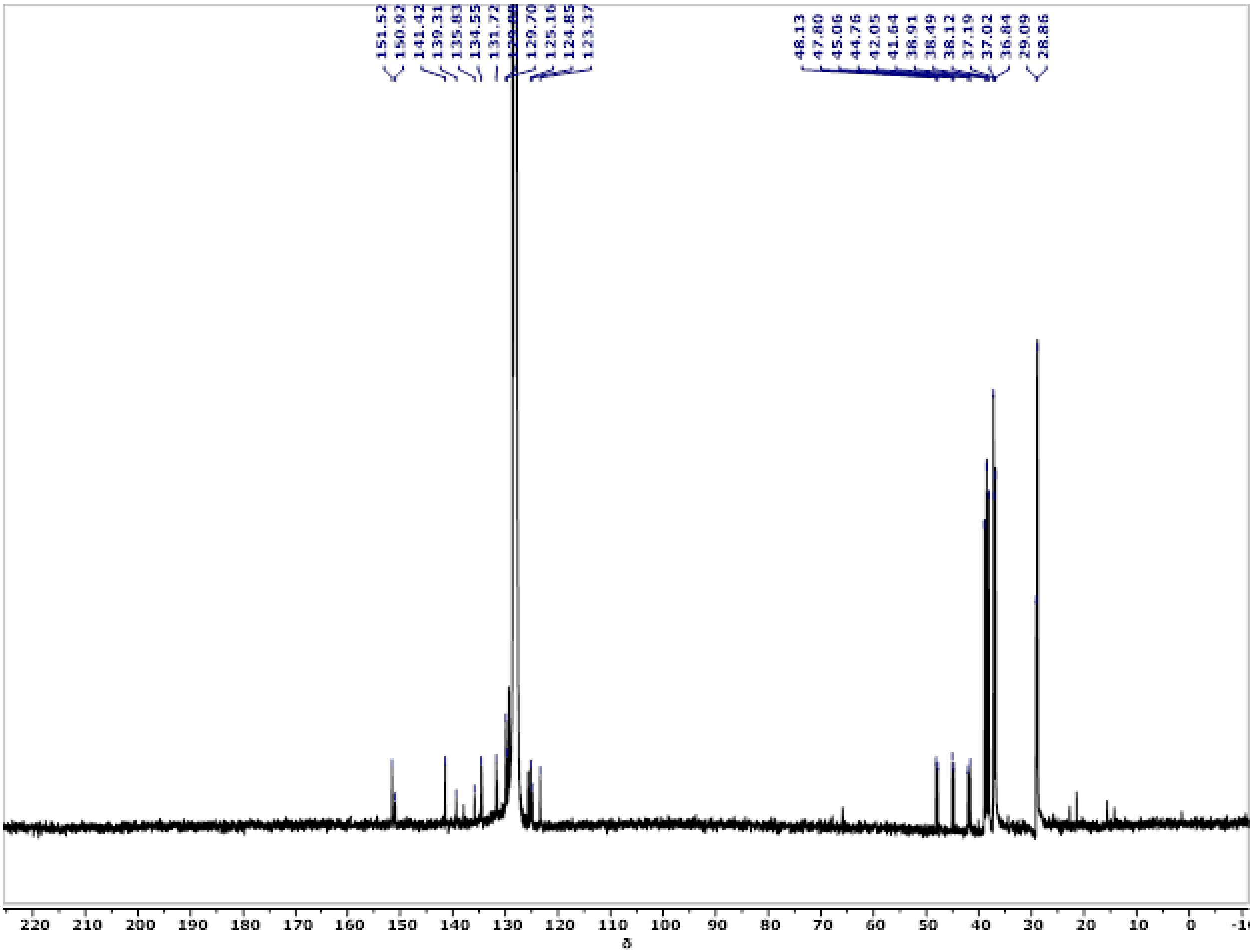

Figure S3.19. ^{13}C NMR Spectrum (151 MHz, 298K) of **[L^{Ad}H]CrO$_2$** recorded in C_6D_6

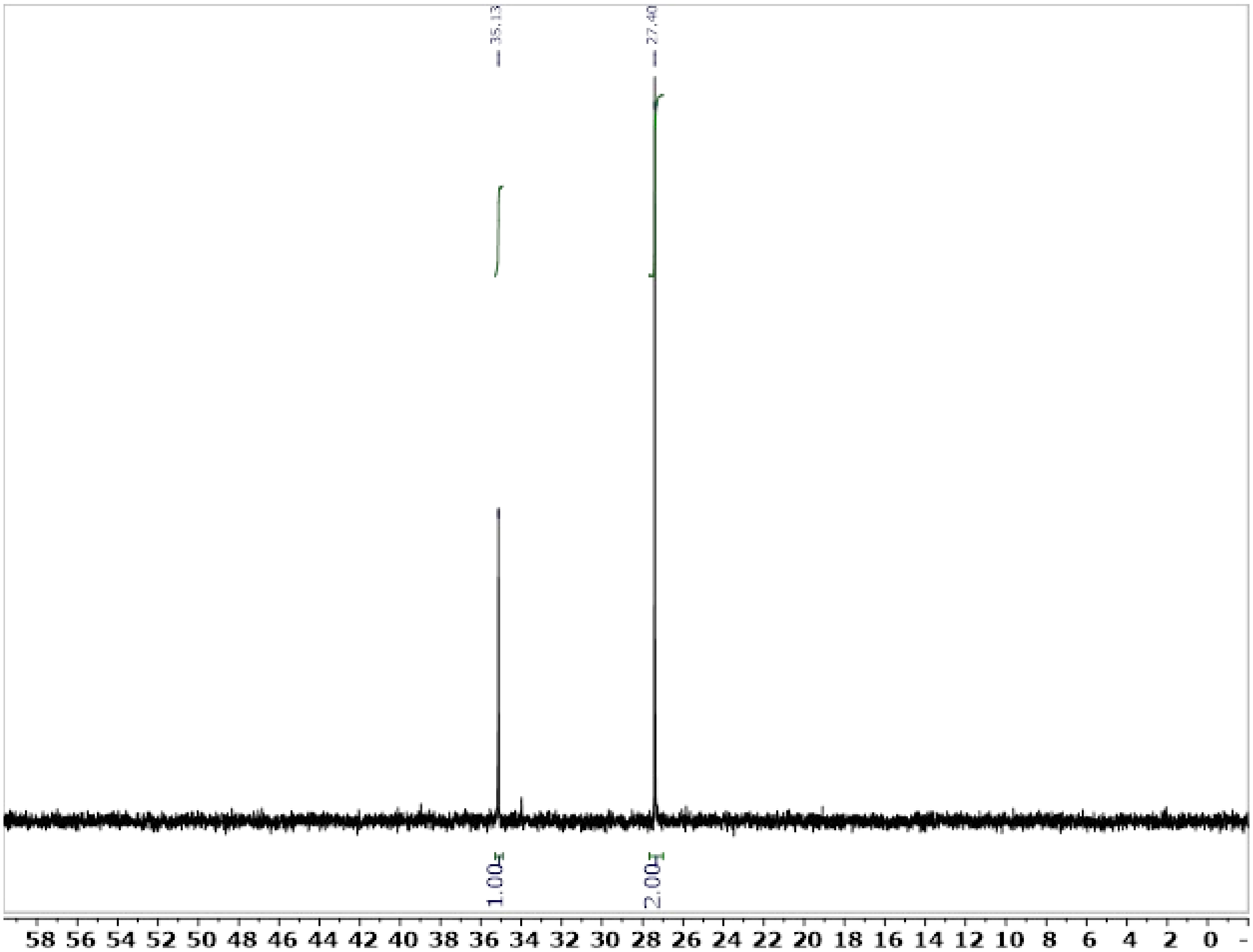

Figure S3.20.^{31}P NMR Spectrum (243 MHz, 298K) of **[L^{Ad}H]CrO$_2$** recorded in C_6D_6

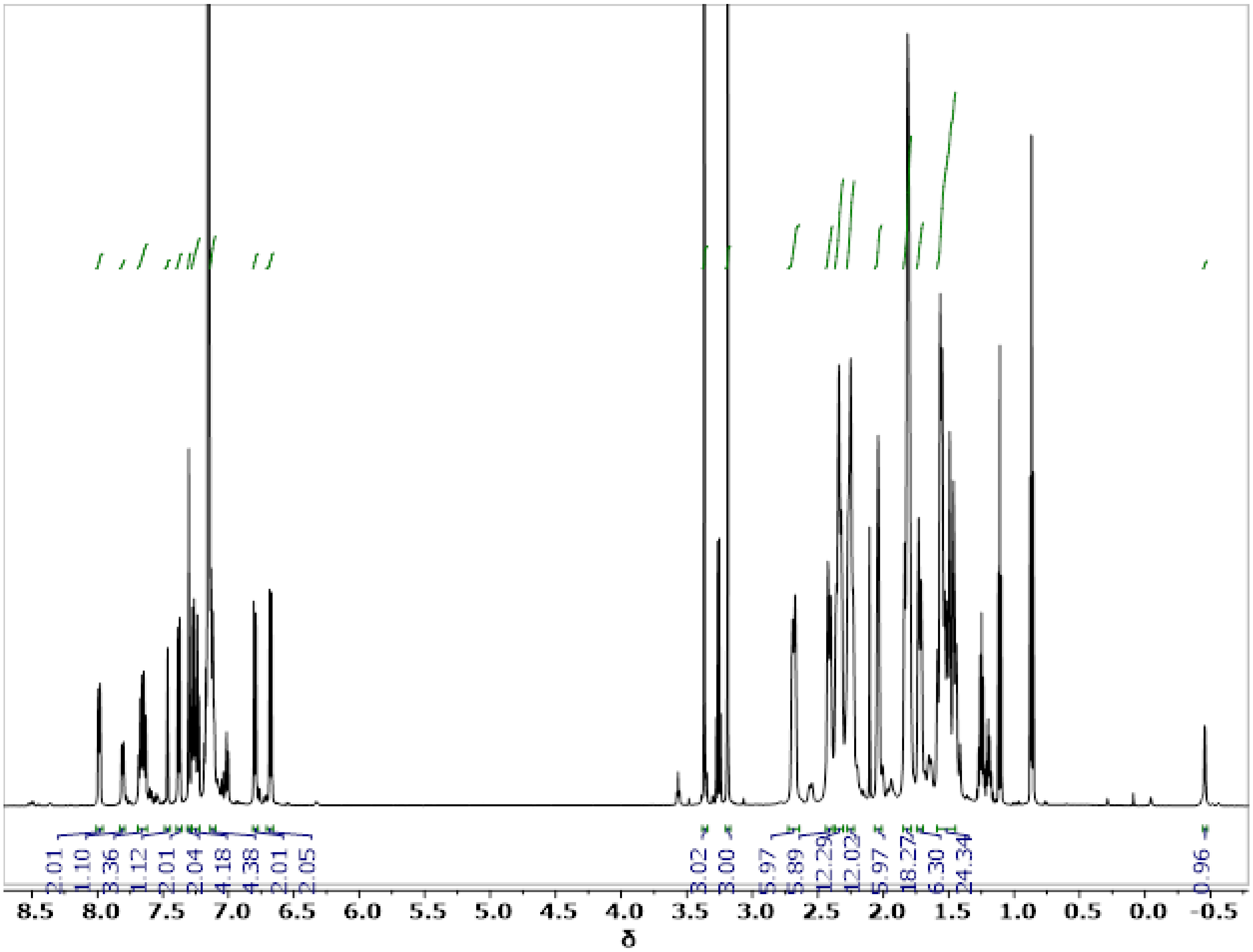

Figure S3.21. ^{1}H NMR Spectrum (600 MHz, 298K) of **3** recorded in C_6D_6

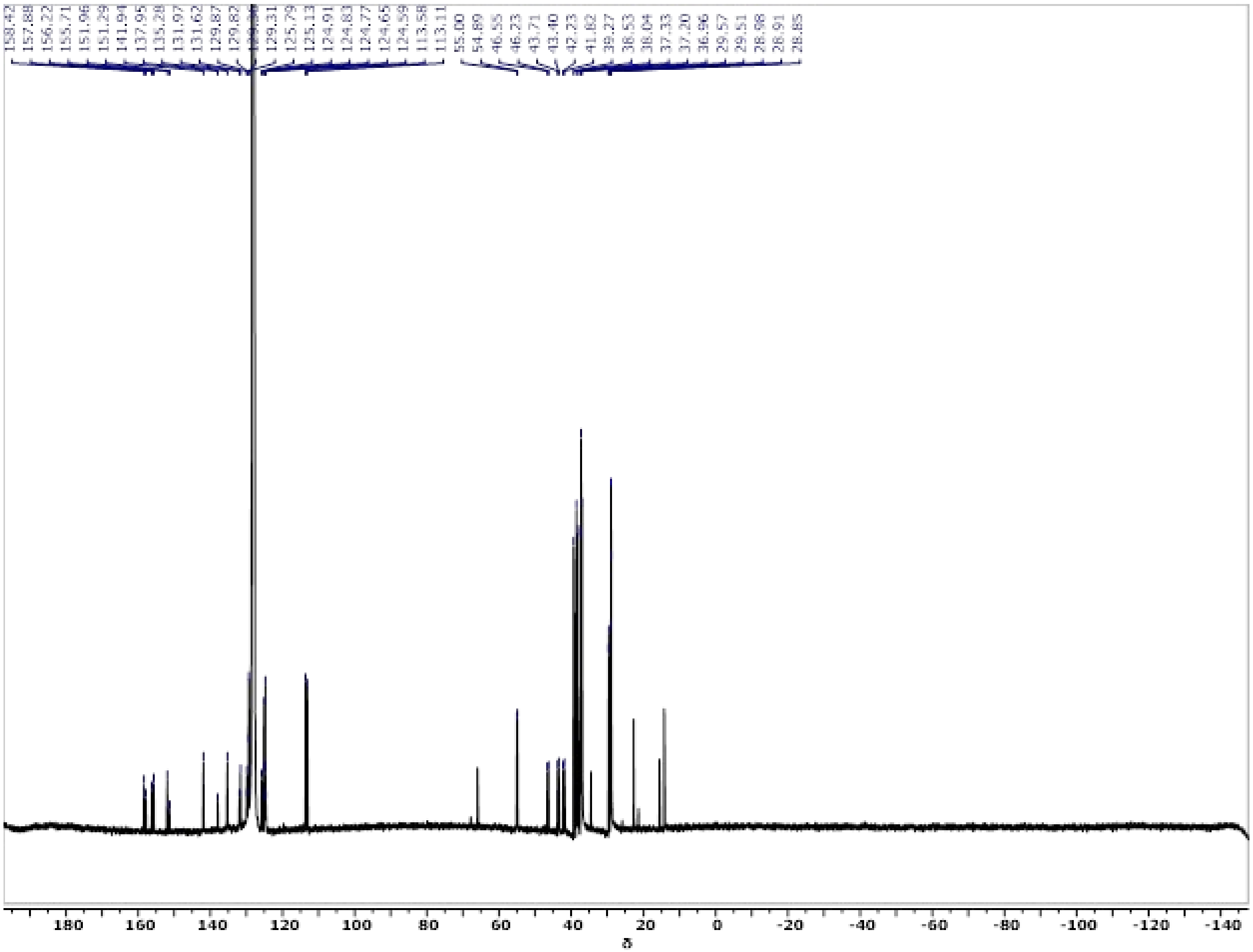

Figure S3.22. ^{13}C NMR Spectrum (151 MHz, 298K) of **3** recorded in C_6D_6

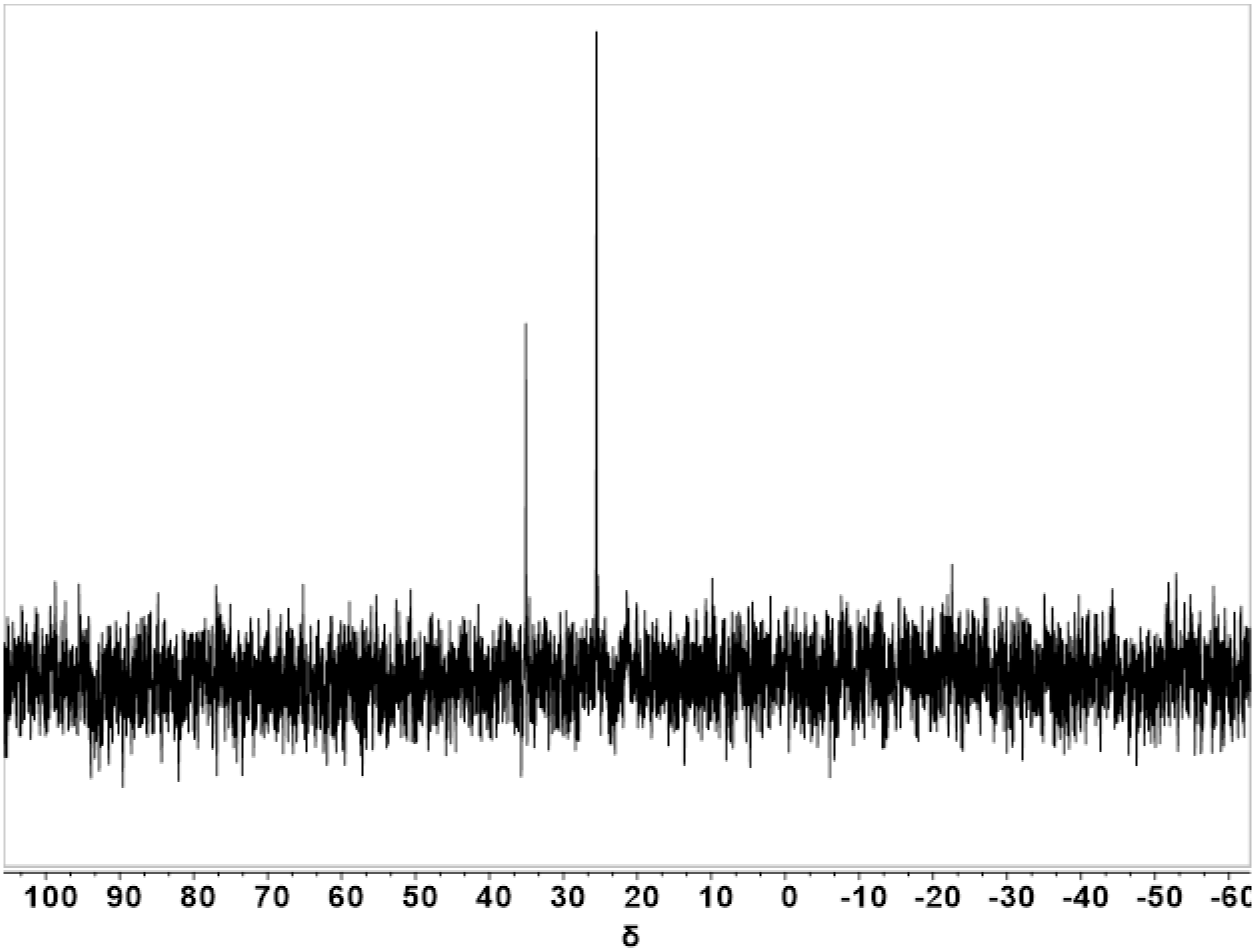

Figure S3.23. ^{31}P NMR Spectrum (162 MHz, 298K) of **3** recorded in C_6D_6

3.6 References

(1) Banerjee, R.; Jones, J. C.; Lipscomb, J. D. *Annu. Rev. Biochem.* **2019**, *88*, 409–431.

(2) Solomon, E. I.; Heppner, D. E.; Johnston, E. M.; Ginsbach, J. W.; Cirera, J.; Qayyum, M.; Kieber-Emmons, M. T.; Kjaergaard, C. H.; Hadt, R. G.; Tian, L. *Chem. Rev.* **2014**, *114* (7), 3659–3853.

(3) Hoffman, B. M.; Lukoyanov, D.; Yang, Z.-Y.; Dean, D. R.; Seefeldt, L. C. *Chem. Rev.* **2014**, *114* (8), 4041–4062.

(4) Anderson, J. S.; Rittle, J.; Peters, J. C. *Nature* **2013**, *501* (7465), 84–87.

(5) Gordon, J. B.; Vilbert, A. C.; Dimucci, I. M.; MacMillan, S. N.; Lancaster, K. M.; Moënne-Loccoz, P.; Goldberg, D. P. *J. Am. Chem. Soc.* **2019**, *141* (44), 17533–17547.

(6) Gordon, J. B.; Albert, T.; Dey, A.; Sabuncu, S.; Siegler, M. A.; Bill, E.; Moënne-Loccoz, P.; Goldberg, D. P. *J. Am. Chem. Soc.* **2021**, *143* (51), 21637–21647.

(7) Laplaza, C. E.; Cummins, C. C. *Science (80-.).* **1995**, *268* (5212), 861–863.

(8) Odom, A. L.; Cummins, C. C.; Protasiewicz, J. D. *J. Am. Chem. Soc.* **1995**, *117* (24), 6613–6614.

(9) Monillas, W. H.; Yap, G. P. A.; Theopold, K. H. *Inorganica Chim. Acta* **2011**, *369* (1), 103–119.

(10) Monillas, W. H.; Yap, G. P. A.; MacAdams, L. A.; Theopold, K. H. *J. Am. Chem. Soc.* **2007**, *129* (26), 8090–8091.

(11) Noh, S. K.; Heintz, R. A.; Haggerty, B. S.; Rheingold, A. L.; Theopold, K. H. *J. Am. Chem. Soc.* **1992**, *114* (5), 1892–1893.

(12) Ruppa, K. B. P.; Feghali, K.; Kovacs, I.; Aparna, K.; Gambarotta, S.; Yap, G. P. A.; Bensimon, C. *J. Chem. Soc. Dalt. Trans.* **1998**, No. 10, 1595–1606.

(13) Akturk, E. S.; Yap, G. P. A.; Theopold, K. H. *Angew. Chemie* **2015**, *127* (49), 15187–15190.

(14) Tsai, Y. C.; Wang, P. Y.; Chen, S. A.; Chen, J. M. *J. Am. Chem. Soc.* **2007**, *129* (26), 8066–8067.

(15) Yousif, M.; Tjapkes, D. J.; Lord, R. L.; Groysman, S. *Organometallics* **2015**, *34* (20), 5119–5128.

(16) Dai, F.; Yap, G. P. A.; Theopold, K. H. *J. Am. Chem. Soc.* **2013**, *135* (45), 16774–16776.

(17) Tahsini, L.; Kotani, H.; Lee, Y. M.; Cho, J.; Nam, W.; Karlin, K. D.; Fukuzumi, S. *Chem. – A Eur. J.* **2012**, *18* (4), 1084–1093.

(18) Lee, H. B.; Ciolkowski, N.; Winslow, C.; Rittle, J. *Inorg. Chem.* **2021**, *60* (16), 11830–11837.

(19) Winslow, C.; Lee, H. B.; Field, M. J.; Teat, S. J.; Rittle, J. *J. Am. Chem. Soc.* **2021**, *143* (34), 13686–13693.

(20) Dehnicke, K.; Krieger, M.; Massa, W. *Coord. Chem. Rev.* **1999**, *182* (1), 19–65.

(21) Dehnicke, K.; Weller, F. *Coord. Chem. Rev.* **1997**, *158*, 103–169.

(22) Stephan, D. W. *Organometallics*. American Chemical Society May 23, 2005, pp 2548–2560.

(23) Stephan, D. W. *Organometallics* **1999**, *18* (7), 1116–1118.

(24) Camacho-Bunquin, J.; Ferguson, M. J.; Stryker, J. M. *J. Am. Chem. Soc.* **2013**, *135* (15), 5537–5540.

(25) Gompa, T. P.; Ramanathan, A.; Rice, N. T.; La Pierre, H. S. *Dalt. Trans.* **2020**, *49* (45), 15945–15987.

(26) Aguirre Quintana, L. M.; Yang, Y.; Ramanathan, A.; Jiang, N.; Bacsa, J.; Maron, L.; La Pierre, H. S. *Chem. Commun.* **2021**, *57* (54), 6664–6667.

(27) Groom, C. R.; Bruno, I. J.; Lightfoot, M. P.; Ward, S. C. *Acta Crystallogr.* **2016**, *B72* (2), 171–179.

(28) Evans, D. F. *J. Chem. Soc.* **1959**, No. 0, 2003–2005.

(29) Rozenel, S. S.; Chomitz, W. A.; Arnold, J. *Organometallics* **2009**, *28* (21), 6243–6253.

(30) Cai, I. C.; Lipschutz, M. I.; Tilley, T. D. *Chem. Commun.* **2014**, *50* (86), 13062–13065.

(31) Grubbs, R. H. *Angew. Chemie Int. Ed.* **2006**, *45* (23), 3760–3765.

(32) Schrock, R. R.; Schrock, [R R; Schrock, R. R. *Angew. Chemie Int. Ed.* **2006**, *45* (23), 3748–3759.

(33) Zhizhko, P. A.; Bushkov, N. S.; Pichugov, A. V.; Zarubin, D. N. *Coord. Chem. Rev.* **2021**, *448*, 214112.

(34) Nugent, W. A. *Inorg. Chem.* **2002**, *22* (6), 965–969.

(35) Moubaraki, B.; Murray, K. S.; Nichols, P. J.; Thomson, S.; West, B. O. *Polyhedron* **1994**, *13* (3), 485–495.

(36) Danopoulos, A. A.; Wilkinson, G.; Sweet, T. K. N.; Hursthouse, M. B. *J. Chem. Soc. Dalt. Trans.* **1995**, No. 13, 2111–2123.

(37) Blum, S. A.; Bergman, R. G. *Organometallics* **2004**, *23* (17), 4003–4005.

(38) Thorman, J. L.; Keith Woo, L. *Inorg. Chem.* **2000**, *39* (6), 1301–1304.

(39) Dunn, S. C.; Hazari, N.; Cowley, A. R.; Green, J. C.; Mountford, P. *Organometallics* **2006**, *25* (7), 1755–1770.

(40) Guiducci, A. E.; Boyd, C. L.; Mountford, P. *Organometallics* **2006**, *25* (5), 1167–1187.

(41) Thorman, J. L.; Guzei, I. A.; Young, V. G.; Woo, L. K. *Inorg. Chem.* **2000**, *39* (11), 2344–2351.

(42) Frazier, B. A.; Wolczanski, P. T.; Lobkovsky, E. B. *Inorg. Chem.* **2009**, *48* (24), 11576–11585.

(43) Hauwert, N. J.; Mocking, T. A. M.; Da Costa Pereira, D.; Lion, K.; Huppelschoten, Y.; Vischer, H. F.; De Esch, I. J. P.; Wijtmans, M.; Leurs, R. *Angew. Chemie* **2019**, *131* (14), 4579–4583.

(44) Das, U. K.; Kar, S.; Ben-David, Y.; Diskin-Posner, Y.; Milstein, D. *Adv. Synth. Catal.* **2021**, *363* (15), 3744–3749.

(45) Evans, D. F. *J. Chem. Soc.* **1959**, *0* (0), 2003.

(46) Rigaku Oxford Diffraction. Rigaku Corporation: Oxford, U.K. 2015.

(47) Bruker AXS Inc.: Madison, WI 2014.

(48) Sheldrick, G. Bruker Analytical X-Ray Systems, Inc.: Madison, WI 2000.

(49) Dolomanov, O. V.; Bourhis, L. J.; Gildea, R. J.; Howard, J. A. K.; Puschmann, H. *J. Appl. Crystallogr.* **2009**, *42* (2), 339–341.

(50) Stoll, S.; Schweiger, A. *J. Magn. Reson.* **2006**, *178* (1), 42–55.

Chapter 4

Structure and Reactivity of a High-Spin, Nonheme Iron(III)- Superoxo Complex Supported by Phosphinimide Ligands

This work is based upon previously published work with permissions from all authors:

Winslow, C.; Lee, H.B.; Field, M. J.; Teat, S. J.; Rittle, J. *J. Am. Chem. Soc.* **2021**, *143* (34), 13686–13693.

4.1 Introduction

Dioxygen is the ideal chemical oxidant.[1] Enzymatic systems that effectively harness O_2, such as the large class of mononuclear nonheme iron oxygenases, are essential to myriad biological processes.[2] This particular class of enzymes catalyze an enormous range of O_2-dependent substrate oxidations that are increasingly recognized to proceed via pronounced mechanistic diversity.[3] Perhaps the only chemical events central to all of these enzymes is the coordination and activation of O_2 by the iron cofactor. Yet, discrete Fe-O_2 intermediates have proven to be highly transient or unobservable in most enzymes.[4–6] Moreover, synthetic examples of well-characterized, nonheme Fe-O_2 complexes remain scarce owing to their reactive nature.[7–9]

These enzymes have inspired numerous breakthroughs in the creation of synthetic catalysts for sustainable oxidation processes.[10–12] Molecular catalysts for selective C-H bond functionalization, alcohol oxidation and alkene epoxidation have been developed that possess structural and/or mechanistic features congruent with those of nonheme iron enzymes.[10] However, unlike the natural systems, most of these synthetic catalysts do not utilize O_2 directly and instead rely upon alternative oxidants - such as peroxides - which provide access to viable catalytic intermediates at the expense of increased cost or undesirable side reactivity.[13] Understanding and developing molecular systems that directly harness O_2 as a reagent could enable transformative advances in chemical oxidation catalysis.

We have initiated a research program that aims to develop new molecular catalysts for sustainable oxidative processes. Along these lines we have developed an electron-donating and oxidatively-resilient ligand platform featuring anionic phosphinimide donors intended to expand the reaction chemistry of Earth-abundant, first-row transition metals.[14] Herein, we show that this ligand enables the synthesis and characterization – including the XRD analysis – of a nonheme iron complex that binds O_2 in a terminal fashion. The available structural, spectroscopic, and computational data on this species corroborates a high-spin iron(III)-superoxide formulation which, in turn, is active in a diverse array of oxidation reactions, including catalytic O_2-mediated aldehyde deformylation.

4.2 Results and Discussion

Terminally-bound phosphinimides are weak-field, π-basic ligands isolobal to alkoxides.[15] They have most commonly been used to stabilize electron-deficient lanthanides and early transition metals.[16,17] In contrast, the coordination chemistry of these ligands with transition metals harboring substantial *d*-electron counts has not been intensively studied, owing in part to the propensity of phosphinimides to instead act as bridging ligands with electron-rich metal centers.[18,19] The ligand platform employed here features a rigid, sterically encumbering framework designed to preclude oligomerization and direct these ligands to a single metal ion. Scheme 1 details an abbreviated synthesis of our featured tris(phosphinimine) pro-ligand (**$L^{Ad}H_3$**) decorated with bulky 1-adamantyl substituents.

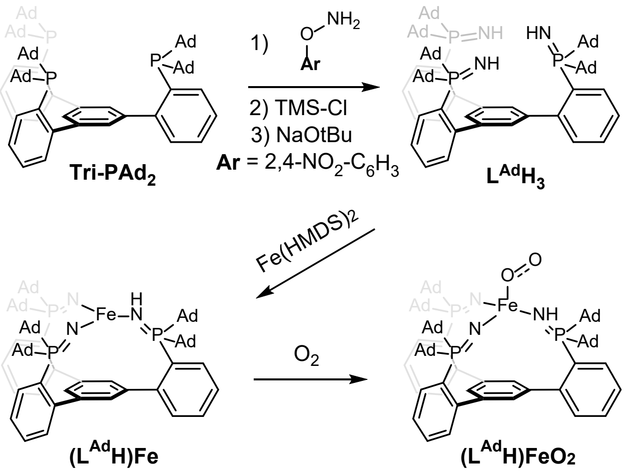

Scheme 4.7. Synthesis of the described complexes

The **L^{Ad}H$_3$** pro-ligand supports an electron-rich mononuclear Fe(II) species. The combination of Fe(HMDS)$_2$ with **L^{Ad}H$_3$** results in the protonolysis of two phosphinimines yielding neutral **(L^{Ad}H)Fe** (Scheme 4.1). The solid-state structure of **(L^{Ad}H)Fe** features a trigonal planar iron atom bound to two phosphinimides and one phosphinimine (Fig 1). Observed Fe-N bond distances coincide with the protonation state of each donor atom: the two Fe-N(phosphini*mide*) bond distances are 1.886(2) and 1.894(2) Å whereas the Fe-N(phosphini*mine*) bond distance is 2.074(2) Å. The short Fe-N(phosphinimide) bond distances can be understood by the two canonical resonance forms of phosphinimide ligands (Scheme 4.2). Considering resonance form (B), terminal phosphinimide coordination to Fe allows for Fe-N σ-bonding and multiplanar Fe-N π-bonding. Such π-donation is expected to considerably raise the energy of the *d*-orbital manifold and stabilize high-spin ground states. Solution-phase magnetic measurements of this compound are consistent with an $S = 2$ spin state ($\mu_{eff} = 4.94\ \mu_B$), as is typical for three-coordinate Fe^{II} compounds.[20,21] Electrochemical experiments indicate that **(L^{Ad}H)Fe** exhibits a quasi-reversible oxidation event at -1.35 V vs Fc/Fc$^+$ in THF electrolyte (Fig S4.17), which is significantly more reducing than related trigonal, high-spin iron(II) complexes.[22,23] We hypothesize that the unusually low oxidation potential of **(L^{Ad}H)Fe** is a testament to the π-donation presented by the terminally-bound phosphinimide ligands.

Scheme 4.8. Phosphinimide Resonance Structures

The **(L^{Ad}H)Fe** compound reacts with O$_2$ *in crystallo* to form a terminal Fe-O$_2$ complex, **(L^{Ad}H)FeO$_2$**. Yellow monoclinic crystals of **(L^{Ad}H)Fe** visibly darken to a red color upon exposure to dry O$_2$ at ambient temperature and retain strong diffraction intensity to ~0.8 Å. Subsequent XRD studies on one of these crystals at 100 K using synchrotron radiation indicate that a single O$_2$ molecule has coordinated to the Fe center (Fig 4.1) which adopts a squashed-tetrahedral geometry (THC$_{DA}$ = 0.55)[24] in **(L^{Ad}H)FeO$_2$**. Despite the low coordination geometry at Fe, the O$_2$ ligand is bound in an ordered, terminal fashion with average measured Fe-O and O-O bond distances of 1.981(3) and 1.321(5) Å, respectively, and an Fe-O-O angle of 114.8(3)^{o}. The observed O-O distance implies an activated superoxide (O$_2^{-}$) formulation (Supporting Information). Marginally shorter average Fe-N(phosphinimide) distances (1.87(2) Å) in **(L^{Ad}H)FeO$_2$** as compared to its precursor are also consistent with a more oxidized Fe center. To the best of our knowledge, this is the first crystallographically characterized, mononuclear nonheme iron-dioxygen complex obtained via addition of O$_2$ to a synthetic Fe(II) compound.[7,8] The terminal manner of O$_2$ coordination and the experimentally determined structural metrics are comparable to those computationally predicted for the Fe-O$_2$ adducts in isopenicillin N-synthase,[5] homoprotocatechuate dioxgenase,[4] and other nonheme iron oxygenases.[25–27]

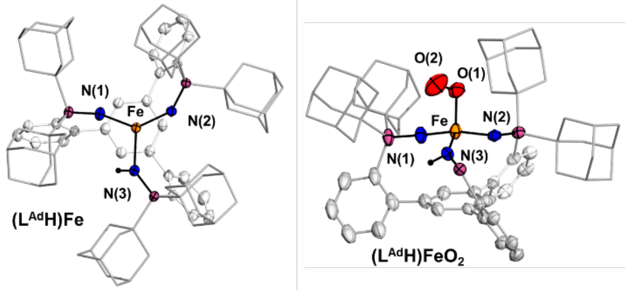

Figure 4.1. XRD structures of **(L^{Ad}H)Fe** (left) and **(L^{Ad}H)FeO$_2$** (right). Thermal ellipsoids are drawn at 50% probability. Solvent molecules, disordered adamantyl substituents, and C-H bonds have been removed. Portions of the ligand framework are hidden for clarity.

Infrared spectra were collected on KBr pellets of isolated **(L^{Ad}H)FeO$_2$** to assess the vibrational characteristics of the O$_2$-derived ligand. According to a Badger's Rule analysis (Supporting Information), the lengthened O-O distance present in **(L^{Ad}H)FeO$_2$** should correlate with a n(O-O) vibration of ~1130 cm^{-1}. A comparison of the FTIR spectra of **(L^{Ad}H)FeO$_2$** generated with ^{16}O- or ^{18}O-labelled O$_2$ reveal subtle differences in the range of 1050-1250 cm^{-1} (Fig S4.13). In contrast, the spectral features nearly overlay in the range commonly ascribed to metal-peroxo (O$_2^{2-}$) species (700-900 cm^{-}).[28] The absence of a unique, isotopically-sensitive feature in **(L^{Ad}H)FeO$_2$** can be explained by coupling of the n(O-O) vibration with the n(P=N) vibrations from the adjacent phosphinimides. High-spin iron-phosphinimide complexes commonly display intense n(P=N) modes in the range of 1050-1250 cm^{-1}.[29,30] After appropriate scaling,[31] our DFT results (*vide infra)* on **(L^{tBu}H)FeO$_2$** identify multiple vibrational modes with variable n(O-O) and n(P=N) character that span this spectral range. Upon ^{18}O-O$_2$ labelling, these studies predict an increase in spectral intensity at ~1240 and 1120 cm^{-1} with a concomitant decrease of intensity at ~1190 cm^{-1}, in modest agreement with the experimental data. Owing to the inherent complexity of this system, however, we cannot confidently assign a unique ν(O-O) vibration to **(L^{Ad}H)FeO$_2$**.

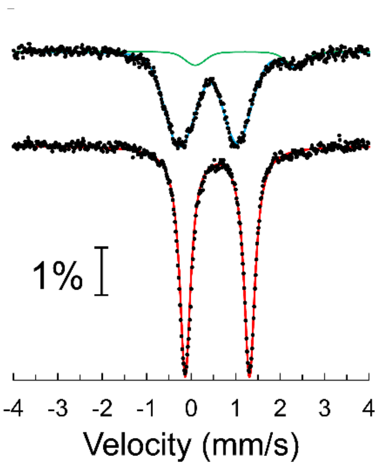

Figure 4.2. Zero-field ^{57}Fe Mössbauer spectra of **(L^{Ad}H)Fe** (bottom) and **(L^{Ad}H)FeO$_2$** (top) collected at 80 K. A 10% Fe(II) impurity (green) is observed in the **(L^{Ad}H)FeO$_2$** sample.

^{57}Fe Mössbauer measurements support a high-spin Fe(III) center in isolated **(L^{Ad}H)FeO$_2$**. The ^{57}Fe Mössbauer spectrum of polycrystalline **(L^{Ad}H)Fe** (Fig 4.2) appears as a sharp quadrupole doublet with parameters (δ = 0.59 mm/s, ΔE_Q = 1.45 mm/s) in line with those of other low-coordinate, high-spin ferrous sites.[23,32] A spectrumobtained on similarly-prepared **(L^{Ad}H)Fe** material following O_2 exposure displays a single, broad quadrupol doublet with parameters (δ = 0.37 m/ms, ΔE_Q = 1.32 mm/s) consistent with a high-spin Fe(III) center in **(L^{Ad}H)FeO$_2$**.[33] The large linewidth associated with this spectrum may be a consequence of slow electronic relaxation at 80K, as suggested by EPR measurements (*vide infra*).

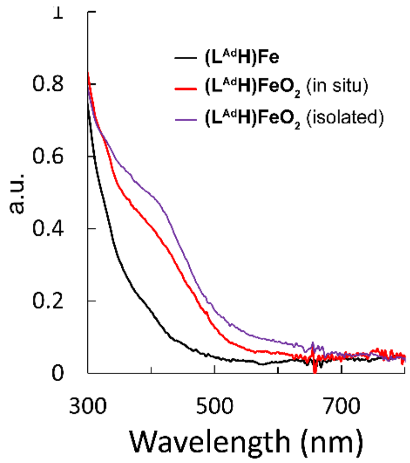

Figure 4.3. UV-visible spectra of **(L^{Ad}H)Fe** (black) and **(L^{Ad}H)FeO$_2$** generated via in situ exposure to O_2 in toluene at -80 °C (red). The purple trace is the spectrum obtained following dissolution of isolated **(L^{Ad}H)FeO$_2$** powder in N_2-saturated toluene at -80 °C.

Yellow toluene solutions of **(L^{Ad}H)Fe** rapidly develop a red color ascribed to **(L^{Ad}H)FeO$_2$** upon bubbling of dry O_2 (Fig 4.3). Dissolution of isolated, polycrystalline **(L^{Ad}H)FeO$_2$** gives rise to similar spectral features, supporting the notion that equivalent chemical species are generated upon oxygenation of **($L^{Ad}H$)Fe** either in solution or as polycrystalline material. The magnitude of the extinction coefficients at 335 and 420 nm (~9000 and 6000 M^{-1} cm^{-1}, respectively) are suggestive of LMCT bands stemming from the phosphinimides and/or the O_2-derived ligand.[14] While the ^{1}H NMR spectrum of **($L^{Ad}H$)Fe** consists of multiple sharp, paramagnetically-shifted peaks, *in situ*-generated **($L^{Ad}H$)FeO_2** is NMR-silent (Fig S4.25). Solution-phase magnetic measurements of **($L^{Ad}H$)Fe** recorded ~1 min after exposure to O_2 in C_6D_6 indicate an apparent $S = 2$ state for *in situ*-generated **($L^{Ad}H$)FeO_2** at room temperature ($\mu_{eff} = 4.9$ μ_B, Fig S4.25).

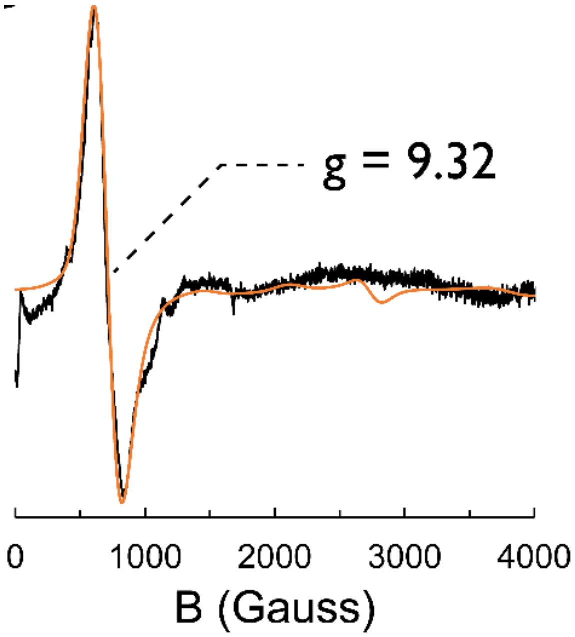

Figure 4.4. Parallel-mode X-band EPR spectrum of a toluene solution of **($L^{Ad}H$)FeO_2** at 5 K and $S_{TOT} = 2$ simulation in orange. Refer to Supporting Information for simulation parameters.

EPR studies were pursued to gain insight into the ground spin state of **($L^{Ad}H$)FeO_2**. As previously discussed in detail for other nonheme iron-dioxygen complexes,[25–27,34] the interaction of O_2 with high-spin ferrous ions can give rise to Fe-O_2 complexes with total spin states (S_{TOT}) of 1, 2 or 3. Similar total spin states can be envisioned for **($L^{Ad}H$)FeO_2**, the relative energies of which dictate the observed Boltzmann distribution at elevated temperatures. The parallel mode X-band EPR spectrum of **($L^{Ad}H$)FeO_2** at 5 K contains an intense resonance at $g = 9.32$ (Fig 4.4), similar to that observed in other synthetic[34] and enzymatic Fe-O_2 species.[4] This feature can be observed at temperatures up to 65 K and no other resonances emerge over this temperature range (Fig S4.4). This feature can be comparably simulated using $S_{TOT} = 2$ or 3 spin states attendant with rhombicity (E/D) values of 0.154 and 0.001, respectively (Fig S4.6). We favor the $S_{TOT} = 2$ simulation as **($L^{Ad}H$)FeO_2** should exhibit substantial rhombic character owing to a distorted tetrahedral Fe geometry and aspherical metal-ligand π-bonding interactions.[35] Accordingly, we assign this resonance to a transition within the $|\pm2\rangle$ doublet of an energetically well-isolated $S = 2$ ground state.[36]

DFT methods provide further insight into the electronic structure of **($L^{Ad}H$)FeO_2**. Gas-phase geometry optimizations were performed on modestly truncated **($L^{t\text{-}Bu}H$)Fe** and **($L^{t\text{-}Bu}H$)FeO_2**

using the TPSSh functional.[37] Salient metrics found for gas-phase **(L$^{t\text{-Bu}}$H)FeO$_2$** - specifically the Fe-N/O and O-O bond distances, Fe-O-O angle and local Fe geometry – closely match the experimental values found for **(L$^{\text{Ad}}$H)FeO$_2$** (Table S4.5). The natural orbitals constituting the Fe-O σ-interactions (Fig 4.5A) imply a delocalized 2-center-3-electron interaction of an Fe-d_{z^2} orbital and an O-O π^* orbital of **the O$_2$-derived ligand.** By convention, this interaction implies a formal reduction of O$_2$ to a O_2^- state. In contrast, the Fe-O π-interactions constructed from the bonding and antibonding combinations of an Fe-d_{xz} orbital and the orthogonal O-O π^* orbital exhibit non-integer electron occupancies. This situation implies a localized, antiferromagnetic interaction as the electron populations for these two orbitals sum to 2.0 electrons and the corresponding magnetic orbitals exhibit pronounced spatial overlap (Fig S4.26).[38] The magnitude of the exchange coupling constant predicted for this interaction (-58 to -136 cm^{-1})[39] corroborates a well-isolated ground spin state. Considering the three additional, singly-occupied orbitals (Fig S4.27), the electronic structure of **(L$^{t\text{-Bu}}$H)FeO$_2$** is best described as an S = 5/2 Fe(III) center antiferromagnetically coupled to an S = 1/2 O_2^- ligand.

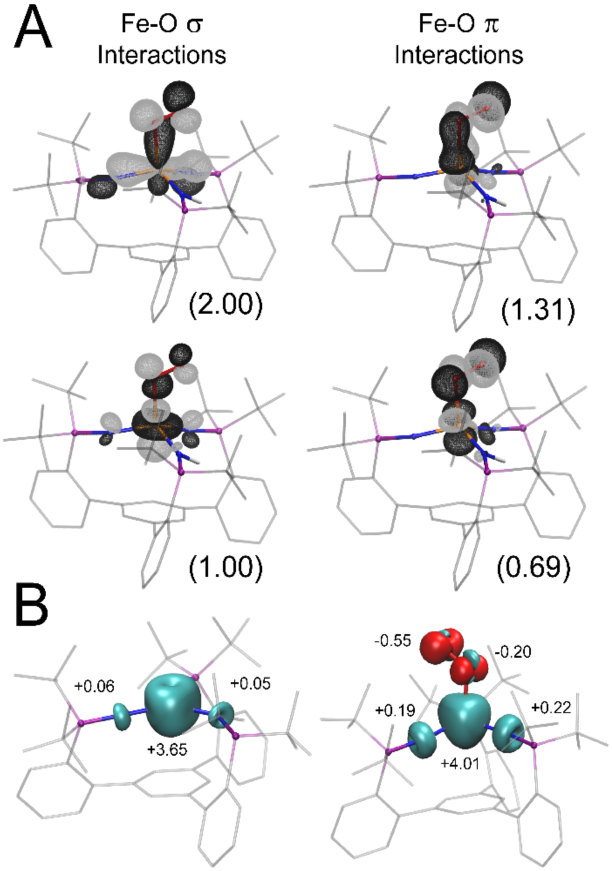

Figure 4.5. Natural orbitals of **(L$^{\text{t-Bu}}$H)FeO$_2$** constituting the Fe-O bonding interactions. Electron occupancies are denoted underneath each orbital. (B) Spin density plots of **(L$^{\text{t-Bu}}$H)Fe** (left) and **(L$^{\text{t-Bu}}$H)FeO$_2$** (right). Contour values are drawn at 0.05 and 0.01 e$^-$/Å^3 for A and B, respectively.

These computational studies also aid in rationalizing the apparent stability of **(L$^{\text{Ad}}$H)FeO$_2$**. The spin density plot for **^{5}(L$^{t\text{-Bu}}$H)Fe** (Fig 4.5B) illustrates that the Fe center bears the majority of the unpaired electron density (+3.65 electrons) with minimal spin leakage onto the two phosphinimide nitrogen atoms (+0.11 electrons total). In contrast, the spin density profile of **^{5}(L$^{t\text{-Bu}}$H)FeO$_2$** reveals substantial unpaired spin density on both the phosphinimide N-atoms (0.41 electrons total). Hence, electron density is mutually transferred from the Fe center and the supporting phosphinimides to O_2 upon its coordination. The cylindrical distribution of electron density on the N-atoms in **(L$^{t\text{-Bu}}$H)FeO$_2$** evidences Fe-N π-bonding interactions in two orthogonal planes. This situation contrasts that found for ligands commonly used to stabilize FeO_x species, such as porphyrin or amido-type (R_2N^-) donors, that are restricted to forming Fe-N π-bonds in a single orientation.[33,40,41] We hypothesize that the unique π-bonding characteristics of the **(L^{Ad}H)$^{2-}$** ligand serves to stabilize oxidized forms of bound metal ions, and in this case enables the robust coordination of O_2 to Fe.

The **(L^{Ad}H)Fe** platform engages in a range of oxidation reactions that proceed in stoichiometric and catalytic fashion. For example, **(L^{Ad}H)Fe** catalyzes the O_2-dependent conversion of 1,2-diphenylhydrazine to azobenzene (Fig 4.6A). The second order rate constants observed for azobenzene generation from ^{1}H- and ^{2}H-labeled 1,2-diphenylhydrazine implies a kinetic isotope effect of 4.9, consistent with a rate-determining hydrogen atom abstraction step that is presumably mediated by *in-situ* generated **(L^{Ad}H)FeO$_2$**. Under an O_2 atmosphere, **(L^{Ad}H)Fe** was found to quantitatively convert 1 equivalent of PPh_3 to O=PPh_3 over ~15 minutes (Fig 4.6B).[42] Isolated samples of **(L^{Ad}H)FeO$_2$** similarly react with PPh_3 under an N_2 atmosphere in benzene to afford a 74(1)% yield of O=PPh_3. The nature of the Fe-containing **(L^{Ad}H)Fe**-derived product(s) of these reactions are presently unknown and their characterization will be disclosed in a later report.

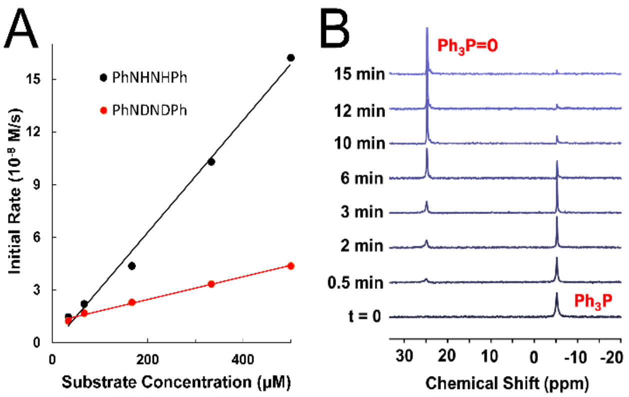

Figure 4.6. (A) Generation of azobenzene from 1,2-diphenylhydrazine (red) or d$_2$-1,2-diphenylhydrazine (blue) in the presence of **(L^{Ad}H)Fe** and 1 atm O_2 at rt. (B) ^{31}P{^{1}H} NMR spectra illustrating the rt conversion of Ph_3P to Ph_3P=O mediated by **(L^{Ad}H)Fe** under 1 atm O_2.

Finally, the **(L^{Ad}H)Fe** complex was found to catalyze C-C and C-H bond cleavage processes. Inspired by previous reports of nucleophilic metal-dioxygen species that engage in aldehyde deformylation,[7,43–48] we examined the reactivity of isolated **(L^{Ad}H)FeO$_2$** with 2-PPA. The stoichiometric combination of these compounds in benzene under an N_2 atmosphere resulted in the generation of acetophenone in 72(1)% yield. Interestingly, exposure of a 1:1 mixture of **(L^{Ad}H)Fe** and 2-PPA to 1 atm of O_2 resulted in the formation of acetophenone in >95% NMR yield. The identity of the other organic product was confirmed to be formic acid (Fig S4.2). Realizing that a full equivalent of dioxygen had been transferred to the substrate, we postulated that **(L^{Ad}H)Fe** could be regenerated upon deprotonation of the formic acid. Under ideal conditions that employ TBD as a base, 18 equiv of acetophenone were produced at 5 mol% **(L^{Ad}H)Fe** catalyst loading (Table 4.1). The direct usage of O_2 as an oxidant here is unusual,[45,48] and underscores the promising oxidation chemistry of the **(L^{Ad}H)Fe** system.

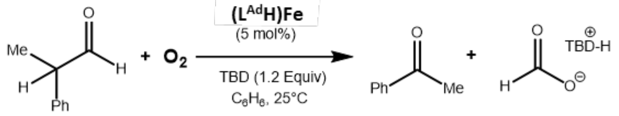

Entry	Deviation from Standard Conditions	Yield (%)[a]	TON
1	None	91	18.2
2	No HL^{Ad}Fe	<1	0
3	No base	4.8	0.9
4	No O_2	<1	0
5	NEt_3 as base	25	4.9
6	DBU as base	59	11.8
7	4°C as Temperature	88	17.9
8	Toluene as solvent, DBU as base	47	9.3

Table 4.3. (L^{Ad}H)Fe-catalyzed aldehyde deformylation [a]The yields were determined through ^{1}H NMR analysis with the aid of an internal standard – 1,3,5-$(MeO)_3C_6H_3$ (average of two experiments).

4.3 Conclusions

In summary, a nonheme Fe-O_2 complex has been prepared via exposure of O_2 to a phosphinimide-iron(II) compound. Its structural and spectroscopic features corroborate an antiferromagnetically-coupled, high-spin Fe(III)-superoxide site analogous to that predicted for many nonheme iron oxygenase enzymes. This amphoteric oxidant engages in both electrophilic O-atom transfer reactivity and nucleophilic aldehyde deformylation. These combined results demonstrate the utility in using phosphinimide ligands to simultaneously stabilize and harness reactive inorganic species. Further investigations aimed at probing the nature of the Fe-containing intermediates of these transformations are currently underway.

4.4 Acknowledgments

This research was supported by the University of California Berkeley. X-ray diffraction experiments performed at beamline 12.2.1 at the Advanced Light Source at Lawrence Berkeley National Laboratory were supported by the Director, Office of Science, Office of Basic Energy Sciences, of the U.S. Department of Energy under Contract No. DE-AC02-05CH11231. We thank Prof Michael T. Green for access to a Mössbauer spectrometer, Prof R. David Britt and Dr. David Marchiori for access to and assistance with their EPR spectrometer (supported by NIH R35 Grant 1R35GM126961-01, to R.D.B), and Prof Christopher Chang for access to a Unisoku Cryostat. We thank Drs. Hasan Celik, Alicia Lund, and UC Berkeley's NMR facility in the College of Chemistry (CoC-NMR) for spectroscopic assistance. Instruments in the CoC-NMR are supported in part by NIH S10OD024998. M.J.F. was supported by a National Sciences and Engineering Research Council of Canada (NSERC) Postgraduate Scholarship.

4.5 Supporting Information

General Considerations: Unless otherwise noted, all manipulations were carried out using standard Schlenk or glovebox techniques under an N_2 atmosphere. Acetonitrile (MeCN), Benzene, Diethyl ether (Et_2O), Pentane, Tetrahydrofuran (THF), and Toluene were deoxygenated by thoroughly sparging with N_2 gas followed by passing through an activated alumina column in a solvent purification system from Pure Process Technology, and were further dried over 4Å molecular sieves for 48h prior to use. Solvents were routinely tested with a THF solution of sodium benzophenone ketyl. Deuterated solvents were purchased from Cambridge Isotope Laboratories, Inc., and were distilled under N_2, degassed via freeze-pump-thaw cycles, and stored over 4Å molecular sieves prior to use. Oxygen was purchased in Ultra High Purity from Praxair and was further dried by passing through two traps immersed in a dry ice/isopropanol bath. All reagents were purchased from commercial vendors and used without further purification unless otherwise stated. 1,3,5-tris(2-bromophenyl)benzene[49], Di-(1-Adamantyl)Phosphine[50], O-(2,4-Dinitrophenyl)-N-hydroxyphthalimide[51], $Fe(HMDS)_2$[52], and d_2-diphenylhydrazine[53] were prepared according to literature procedures. Elemental analyses were performed by the Microanalytical Laboratory in the College of Chemistry at the University of California – Berkeley using a PerkinElmer 2400 Series II combustion analyzer.

Nuclear Magnetic Resonance Spectroscopy: Nuclear Magnetic Resonance (NMR) spectra were measured at Bruker AV-300, AVQ-400, NEO-500, or AV-600 spectrometers. ^1H and ^{13}C chemical shifts are reported in ppm relative to tetramethylsilane (TMS) at 0.00 ppm using residual solvent residues as internal standards. ^{31}P chemical shifts are reported in ppm relative to 85% aqueous H_3PO_4 at 0 ppm. Solution phase magnetic measurement were performed using the Evans' method.[54]

Infrared Spectroscopy: Solid IR measurements were obtained on a Nicolet iS20 Spectrometer as KBr pellets.

X-Ray Crystallography: XRD studies were performed at the Small Molecule X-Ray Crystallography Facility (CheXray) or at beamline 12.2.1 at the Advanced Light Source at Lawrence Berkeley National Laboratory. For studies performed at ChexRay: Crystals were mounted on a Kapton loop under Paratone oil. Data were collected on a Rigaku XtalLAB P200 (MoKα or CuKα radiation) equipped with a MicroMax-007 HF microfocus rotating anode and a Pilatus 200K hybrid pixel array detector at 100 K under a stream of N_2. Data collection, integration, and scaling were carried out using the CrysAlis^{Pro} software.[55] For studies performed at the Advanced Light Source: Crystals were mounted on a MiTeGen loop under Paratone oil. Data were collected on a Bruker D85 three-circle diffractometer with a PHOTON II CCD area detector using silicon monochromated synchrotron radiation (λ = 0.7288 Å). Bruker APEX2 software was used for data collection. Bruker SAINT and SADABS software was utilized for data reduction and absorption correction, respectively. [56,57] Structures were solved using SHELXS and refined against F^2 on all data by full matrix least-squared with SHELXL using OLEX2 crystallographic software.[58] All non-hydrogen atoms were refined using anisotropic displacement parameters. Hydrogen atoms were placed in idealized positions and refined using a riding model.

Electronic Paramagnetic Resonance Spectroscopy: X-band EPR spectra were obtained on a Bruker EMX spectrometer on 5 mM solutions as frozen glasses in toluene. Samples were collected at powers ranging from 1mW to 10mW and temperatures ranging from 5K to 65K with modulation amplitudes of 8 Gauss. Spectra were simulated using the EasySpin[59] suite of programs in Matlab 2021.

Optical Spectroscopy: Measurements were taken on a Hewlett-Packard 8453 UV-Vis Spectrophotometer using a 1cm quartz cell sealed with a Teflon stopcock. Variable Temperature measurements were performed using a UNISOKU Unispec Cryostat.

Electrochemistry: Electrochemical measurements were carried out in 0.2 M THF solutions of electrolyte ([^{n}Bu$_4$N][PF$_6$]). Data collection were performed on a BioLogic SP-50 Potentiostat using a freshly-polished glassy carbon electron as the working electrode and a platinum wire as the auxiliary electrode. All reported potentials are referenced to the ferrocene/ferrocenium couple (Fc/Fc$^+$).

^{57}Fe Mössbauer Spectroscopy: Spectra were recorder on a spectrometer from SEE Co (Edina Mn) operating in the constant acceleration mode in a transmission geometry. The sample was kept in an SVT-400 cryostat from Janis (Wilmington, MA). The quoted isomer shifts are relative to the centroid of the spectrum of a metallic foil of a-Fe at room temperature. Samples were prepared by suspending polycrystalline material in an eicosane matrix and mounted in a Delrin cup fitted with a screw-cap. Data analysis was performed using the program WMOSS (www.wmoss.org) and quadrupole doublets were fit to either Lorentzian or Voigt line shapes.

DFT Calculations: All calculations were carried out using Gaussian 09 rev. D.01.[60] Coordinates for all heavy (non-H) atoms were taken from the structures determined via X-ray crystallography. To improve the efficiency of the calculations, the adamantyl substituents were truncated to tert-butyl substituents. Gas-phase geometry optimizations and single-point and frequency calculations employed the unrestricted TPSSH functional. The 6-31g(d) basis set was employed for C and H atoms and Def2-TZVPP was used for Fe, N, P and O atoms. Successful optimization to a minimum was confirmed by the absence of imaginary frequencies in a subsequent frequency calculation. Multireference character is expected for the $S_{TOT} = 2$ state of **($L^{t\text{-}Bu}H$)FeO_2** and a broken-symmetry solution is found via quadratically convergent SCF procedures. The resultant wavefunction was found to be the most stable using the "stable=opt" command. Natural orbitals were constructed using the pop=no command. Orbitals were visualized using VMD version 1.9.4a51.[61]

Synthetic Procedures:

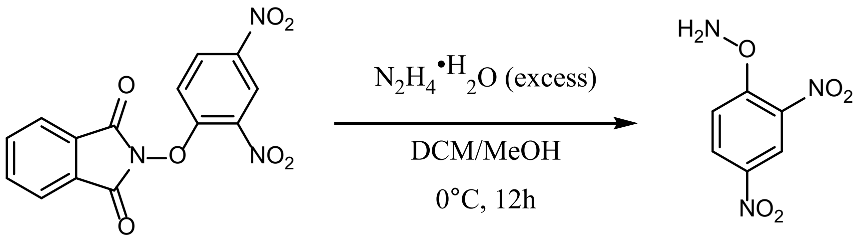

Scheme S4.1. Synthesis of O-(2,4-Dinitrophenyl)-hydroxylamine

O-(2,4-Dinitrophenyl)-hydroxylamine: Modified from a literature procedure[51]: A 3 L round-bottomed flask was charged with 60 g (182 mmol) of O-(2,4-Dinitrophenyl)-N-hydroxyphthalimide and 1.2 L of dichloromethane (DCM). The flask was cooled to 0°C with an ice bath. A solution of hydrazine monohydrate (30 mL, excess) in methanol (250 mL) was added in one portion to the colorless solution. The reaction mixture quickly turned yellow corresponding with significant precipitation. The reaction was stirred for 1h and allowed to set at 0°C for an additional 12h. Cold 1M aqueous HCl (1.5L) was added and the reaction was shaken vigorously. The suspension was filtered over a pad of celite on a course fritted glass funnel. The pad was washed with CH_3CN until the washings were colorless. The filtrate was then filtered through an additional pad of celite to remove additional precipitate. The filtrate was transferred into a separatory funnel and the organic layer was isolated. The aqueous layer was extracted once with 300mL of DCM. The combined organics were dried over Na_2SO_4, filtered, and concentrated via rotary evaporation to give 30g (151 mmol, 83% yield) of product which was used without further purification.

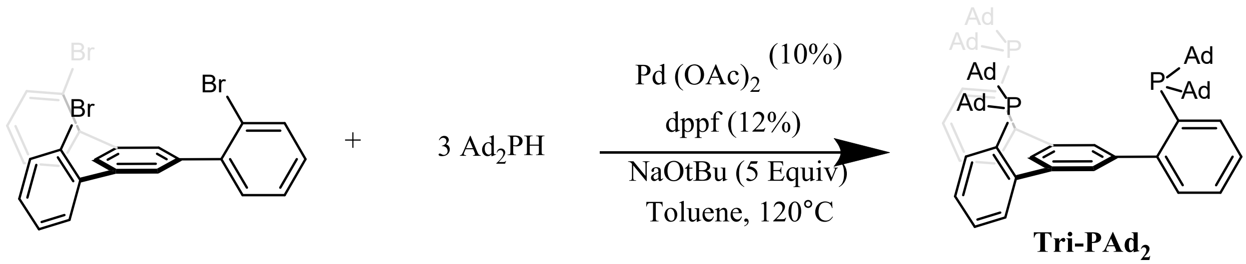

Scheme S4.2. Synthesis of **Tri-PAd$_2$**

1,3,5-tris(2-di(1-adamantyl)phenylphosphine)benzene (Tri-PAd$_2$): In the glovebox, a 500 mL Schlenk bomb with Teflon stopper and stir bar was charged with Pd(OAc)$_2$ (160 mg, 0.7 mmol, 10%), dppf (500 mg, 0.9 mmol, 12%), and 20 mL toluene. After stirring for 30 minutes at ambient temperature, the bomb was charged with 1,3,5-tris(2-bromophenyl)benzene (4.00 g, 7.4 mmol, 1 Equiv), NaOtBu (3.54 g, 36.8 mmol, 5 Equiv), and 50 mL toluene. The mixture was stirred at ambient temperature for an additional hour. The bomb was charged with di(1-Adamantyl-phosphine) (9.1 g, 30.0 mmol, 4 Equiv) and 50mL toluene. The bomb was sealed and removed from the glovebox before being placed in a preheated 120 °C oil bath. The mixture was stirred at that temperature for 7 days or until aliquots of the reaction mixture showed no further conversion to the product via monitoring by ^{31}P NMR. The mixture was cooled to room temperature and the solvents were removed in vacuo. The brown residue was dissolved in chloroform (400 mL) and washed with water (2 x 100 mL) and saturated aq. NH$_4$Cl (2 x 100 mL). The combined aqueous layers were extracted with chloroform (2 x 100 mL). The combined organics were dried over Na$_2$SO$_4$. Silica (250 g) was added to the solution and the solvents were removed via rotary evaporation and dried in vacuo until residue was a free-flowing powder. The silica adsorbed powder was dry loaded onto a silica gel column, and the compound was purified via flash column chromatography (3% to 5% Ethyl Acetate/Hexanes gradient) to give 5.8 g of the desired product as a white solid (4.8 mmol, 65% Yield). ^{1}H NMR (600 MHz, Chloroform-*d*) δ 7.91 (d, *J* = 7.7 Hz, 3H), 7.62 (m, 3H), 7.42 (t, *J* = 7.5 Hz, 3H), 7.33 (t, *J* = 7.5 Hz, 3H), 7.29 (s, 3H), 1.96 (m, 18H), 1.90 – 1.86 (m, 36H), 1.65 (s, 36H). ^{13}C NMR (151 MHz, CDCl$_3$) δ 151.32, 139.41, 135.57, 131.78, 130.85, 130.47, 127.13, 123.78, 40.97, 40.88, 36.52, 36.34, 35.99, 27.89, 27.84. ^{31}P NMR (162 MHz, CDCl$_3$) δ 20.69. HRMS (ESI, m/z): calcd for $C_{84}H_{105}P_3$ $[M+H]^+$: 1207.7429; found: 1207.7077.

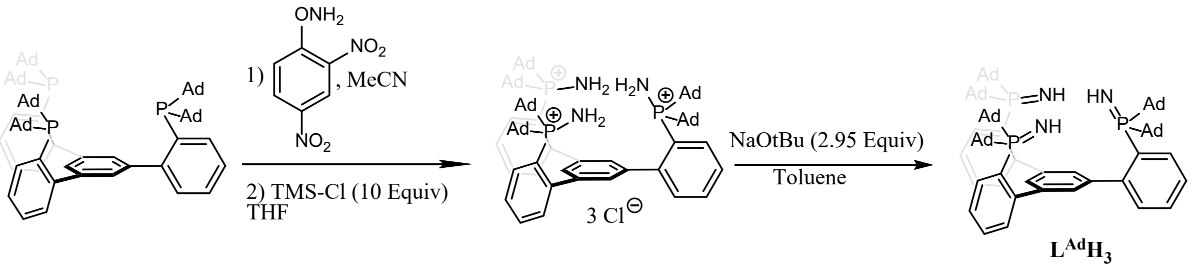

SchemeS4.3. Synthesis of $\mathbf{L^{Ad}H_3}$

$\mathbf{L^{Ad}H_3}$ **:** In the glovebox, a 250 mL round-bottomed flask was charged with a stir bar, **Tri-PAd$_2$** (4.9 g, 4.1 mmol, 1 Equiv), and 50 mL MeCN. O-(2,4-Dinitrophenyl)-hydroxylamine (2.83 g, 14.2 mmol, 3.5 Equiv) was weighed out in a 20mL Scintillation vial and added to the slurry in one portion as a solid. The scintillation vial was rinsed with 10mL MeCN which was added to the reaction. The flask was stoppered and stirred for 12h at ambient temperature. The resulting thick yellow suspension was collected on a coarse frit. The filter cake was washed successively with MeCN (50 mL), THF (20 mL), Et_2O (50 mL), and pentane (50 mL). The resulting yellow solid was dried in vacuo before being charged into a 250mL round-bottomed flask with a stir bar. The flask was charged with THF (100 mL). The yellow slurry was stirred and TMS-Cl (5.2 mL, 40.6 mmol, 10 Equiv) was added in one portion via syringe. The flask was sealed with a glass stopper and stirred for 48h at ambient temperature. The resulting white solid was collected on a medium frit, washed with THF (30mL), Et_2O (50mL), and pentane (50mL), and dried in vacuo to give the intermediate $H_6L^{Ad}Cl_3$ as a white solid (4.13g). A 250mL round-bottmed flask flask was charged with the white solid and Toluene (100 mL). NaOtBu (866mg, 9.0 mmol, 2.95 Equiv) was added to the white slurry which was stirred at ambient temperature for 24h. The mostly homogenous solution was transferred to a 250 mL Erlenmeyer flask which was heated until boiling and allowed to cool back to ambient temperature. The solution was filtered over celite. The Erlenmeyer flask and filter cake were washed with toluene (25 mL). Volatiles were removed in vacuo and the residue was triturated with pentane (10 mL) before being dried in vacuo to give 3.53 g of $\mathbf{L^{Ad}H_3}$ as an off-white solid (2.8 mmol, 69% yield over two steps). ^{1}H NMR (600 MHz, Benzene-*d*$_6$) δ 8.36 (d, *J* = 7.5 Hz, 1H), 7.70 – 7.59 (m, 7H), 7.51 (s, 1H), 7.33 (t, *J* = 7.6 Hz, 1H), 7.12 (t, *J* = 7.6 Hz, 3H), 7.04 (t, *J* = 7.5 Hz, 1H), 2.27 (s, 30H), 2.18 (m, 6H), 1.94 (s, 6H), 1.80 (m, 12H), 1.72 (m, 6H), 1.64 (m, 6H), 1.54 (m, 24H), -0.07 (s, 2H), -0.57 (s, 1H). ^{13}C NMR (151 MHz, C_6D_6) δ 150.76, 139.66, 137.60, 134.89, 134.72, 132.17, 131.90, 130.33, 129.99, 129.70, 129.50, 128.59, 128.35, 127.61, 124.99, 124.85, 42.26, 42.04, 41.87, 41.68, 41.64, 41.27, 38.53, 38.47, 37.23, 37.14, 29.14, 28.88. ^{31}P NMR (243 MHz, C_6D_6) δ 35.06, 34.02. HRMS (ESI, m/z): calcd for $C_{84}H_{105}P_3$ $[M+H)^+$: 1252.7756; found: 1252.7711.

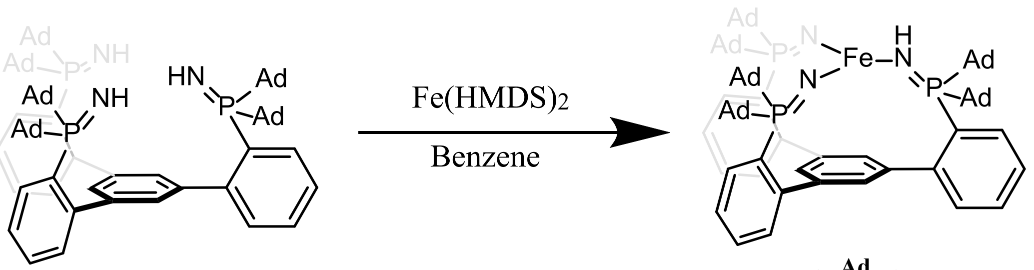

(L^{Ad}H)Fe

Scheme S4.4. Synthesis of **(L^{Ad}H)Fe**

(L^{Ad}H)Fe: In the glove box, a 250 mL round-bottomed flask was charged with a magnetic stir bar, L^{Ad}H$_3$ (1.0g, 0.8 mmol, 1 Equiv), and Et$_2$O (60 mL). Fe(HMDS)$_2$ (296.0 mg, 0.8 mmol, 1 Equiv) was added dropwise to the flask as a solution in Et$_2$O (20 mL). The mixture was stirred for 24h resulting in a beige precipitate in a brown solution. The beige solid was collected on a medium frit and washed with Et$_2$O (3x15mL) to give **(L^{Ad}H)Fe** as a beige powder (881.5 mg, 0.675 mmol, 84.5%). The filtrate was concentrated and stored at -30°C for 48h to obtain a second crop of **(L^{Ad}H)Fe** (42.5 mg, 0.03 mmol, 4.1%) to give a combined yield of 88.6%. Single crystals of **(L^{Ad}H)**Fe suitable for X-ray diffraction were grown from layering pentane onto a concentrated Et$_2$O solution of **(L^{Ad}H)Fe** to give faint yellow rods. ^{1}H NMR (400 MHz, C$_6$D$_6$) δ 47.76, 41.88, 39.83, 36.47, 27.96, 22.19, 19.33, 16.27, 15.76, 15.16, 14.33, 13.06, 9.52, 8.42, 7.94, 6.03, 5.10, 3.60, 2.99, 2.71, 1.73, 1.33, 0.96, 0.18, -2.20, -2.71, -3.25, -3.74, -9.40, -11.02, -29.16, -45.23. Anal: calc. for C$_x$H$_y$N$_3$P$_3$Fe: C 77.22, H 8.18, N 3.22; found: C 75.74, H 8.20, N 3.01. μ_{eff} (Benzene-*d*$_6$, 298 K, 400 MHz): 4.94 μ_B. (KBr, 298 K, cm^{-1}): 3344 ν(*N-H).*

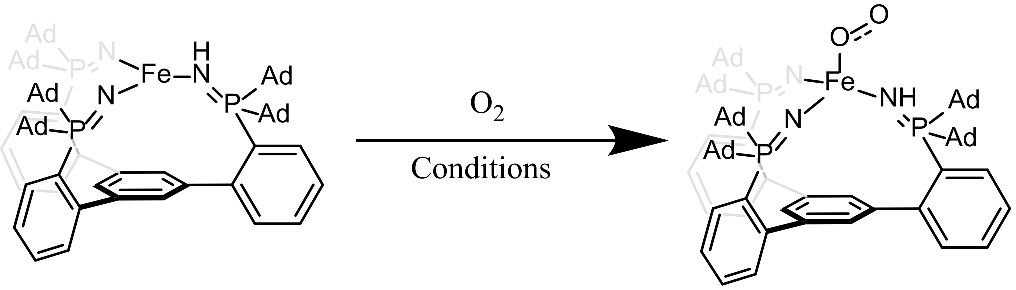

Scheme S4.5. Synthesis of **($L^{Ad}H$)FeO$_2$**

($L^{Ad}H$)FeO$_2$:

Method A: In-crystallo exposure to O$_2$

In the glove box, a 1-dram vial was charged with a suspension of crystalline **($L^{Ad}H$)Fe** in an ether/pentane mother liquor and placed into a Schlenk tube. The tube was sealed with a glass stopper after briefly applying a mild vacuum to the headspace. The tube was subsequently transferred to a gas manifold and exposed to 1 atm of dry oxygen. Following ~90 min of O$_2$ exposure, visibly red crystals were mounted onto a diffractometer.

*Method B: Exposure of **($L^{Ad}H$)Fe** powder to O$_2$*

In the glove box, a 1-dram vial was charged with **($L^{Ad}H$)Fe** as a finely ground powder and placed into a Schlenk tube. The powder was completely dried in vacuo to remove all residual solvents. The tube was sealed with a glass stopper and transferred to a gas manifold under 1 atm of dry oxygen, resulting in an instant color change from beige to red. After 60 min exposure, the oxygen atmosphere was removed in vacuo and the Schlenk tube was transferred into a glove box for further manipulations.

*Method C: Exposure of **($L^{Ad}H$)Fe** solutions to O$_2$*

In the glove box, a J-young tube or Schlenk bomb with a magnetic stir bar was charged with a solution of **($L^{Ad}H$)Fe**. The vessel was sealed, removed from the glove box, and transferred to a gas manifold under 1 atm of dry oxygen. The solution was freeze-pump-thawed once before being exposed to oxygen to give a deep red solution of an NMR silent material. Modification for EPR samples: an EPR tube was charged with a 5 mM toluene solution of **($L^{Ad}H$)Fe**, capped, and removed from the glove box before quickly being chilled in a dry ice/isopropanol bath. The tube was uncapped, and a long needle under positive pressure of O$_2$ was submerged in the solution for 10 seconds. The tube was quickly submerged in a liquid nitrogen bath to form a glass. Modification for UV-Vis: a Schlenk cuvette was charged with a 72 μM solution of **($L^{Ad}H$)Fe**, sealed, and inserted into a UNISOKU instrument precooled to -80 °C. Upon temperature equilibration, 1 mL of dry O$_2$ was slowly injected into the cuvette.

In situ-generated C_6D_6 solutions of **($L^{Ad}H$)FeO$_2$** prepared in this manner rapidly lose the paramagnetically shifted ^{1}H NMR features ascribed to **($L^{Ad}H$)Fe** within seconds. Monitoring the magnetic moment of these solution by Evans' method reveals a negligible change in frequency shift (Fig S4.25). Over longer time periods, unidentified diamagnetic impurities begin to accumulate. Due to the instability of the compound in solution, reporting an accurate magnetic moment via this method would be difficult but the negligible frequency shift is consistent with an S = 2 species at room temperature. UV-Vis (Benzene, 298K, nm {cm^{-1}M^{-1}}): 335 {9000), 420(6000).

X-Ray Crystallography

CCDC Deposition Number	2083120	2083121			
Complex	**($L^{Ad}H$)Fe**	**($L^{Ad}H$)FeO$_2$ Crystal 1**	**($L^{Ad}H$)FeO$_2$ Crystal 2**	**($L^{Ad}H$)FeO$_2$ Crystal 3**	**($L^{Ad}H$)FeO$_2$ Crystal 4**
Empirical formula	$C_{89.74}H_{119.88}FeN_3O_{1.26}P_3$	$C_{88.34}H_{116.68}FeN_3O_{2.66}P_3$	$C_{88.27}H_{116.54}FeN_3O_{2.73}P_3$	$C_{88.19}H_{116.39}FeN_3O_{2.81}P_3$	$C_{88.14}H_{116.28}FeN_3O_{2.86}P_3$
Formula weight	1409.52	1411.92	1412.05	1412.22	1412.31
Temperature/K	100.15	100.15	100(2)	100(2)	100(2)
Crystal system	monoclinic	triclinic	triclinic	triclinic	triclinic
Space group	$P2_1/c$	P-1	P-1	P-1	P-1
a/Å	10.26476(7)	11.3355(5)	11.3352(3)	11.3341(6)	11.3465(3)
b/Å	27.6986(2)	16.6638(7)	16.6840(3)	16.6808(5)	16.7224(3)
c/Å	26.69228(17)	20.5166(9)	20.4814(3)	20.4859(5)	20.4232(3)
α/°	90	91.406(2)	91.3730(10)	91.423(2)	91.1550(10)
β/°	95.5823(6)	96.994(2)	97.185(2)	97.337(3)	97.207(2)
γ/°	90	107.448(2)	107.342(2)	107.366(4)	107.487(2)
Volume/Å^3	7553.14(9)	3662.0(3)	3660.58(14)	3658.2(2)	3659.96(14)
Z	4	2	2	2	2
ρ_{calc}g/cm^3	1.24	1.28	1.281	1.282	1.282
μ/mm^{-1}	2.578	0.345	2.677	2.68	2.679
F(000)	3042	1520	1520	1520	1520
Crystal size/mm^3	0.05 × 0.05 × 0.01	0.06 × 0.05 × 0.01	0.1 × 0.05 × 0.02	0.1 × 0.05 × 0.02	0.1 × 0.05 × 0.02
Radiation	CuKα (λ = 1.54184)	synchrotron (λ = 0.7288)	CuKα (λ = 1.54184)	CuKα (λ = 1.54184)	CuKα (λ = 1.54184)
2Θ range for data collection/°	6.382 to 158.426	2.632 to 52.966	5.56 to 152.566	6.838 to 141.668	6.854 to 158.286
Index ranges	$-12 \le h \le 12, -33 \le k \le 35, -33 \le l \le 34$	$-13 \le h \le 13, -20 \le k \le 20, -25 \le l \le 25$	$-14 \le h \le 14, -20 \le k \le 20, -24 \le l \le 25$	$-13 \le h \le 13, -20 \le k \le 20, -24 \le l \le 13$	$-14 \le h \le 14, -21 \le k \le 20, -25 \le l \le 22$
Reflections collected	83129	51633	72590	45624	86040
Independent reflections	15982 [R_{int} = 0.0543, R_{sigma} = 0.0296]	14010 [R_{int} = 0.0757, R_{sigma} = 0.0756]	14998 [R_{int} = 0.1215, R_{sigma} = 0.0800]	13597 [R_{int} = 0.1110, R_{sigma} = 0.0942]	15526 [R_{int} = 0.0951, R_{sigma} = 0.0530]
Data/restraints/parameters	15982/96/962	14010/623/1106	14998/438/1106	13597/438/1106	15526/438/1106
Goodness-of-fit on F^2	1.1	1.048	1.059	1.063	1.061
Final R indexes [I>=2σ (I)]	R_1 = 0.0528, wR_2 = 0.1524	R_1 = 0.0674, wR_2 = 0.1866	R_1 = 0.0733, wR_2 = 0.1925	R_1 = 0.0861, wR_2 = 0.2318	R_1 = 0.0791, wR_2 = 0.2255
Final R indexes [all data]	R_1 = 0.0564, wR_2 = 0.1553	R_1 = 0.0981, wR_2 = 0.2100	R_1 = 0.1152, wR_2 = 0.2215	R_1 = 0.1269, wR_2 = 0.2596	R_1 = 0.1116, wR_2 = 0.2540
Largest diff. peak/hole / e Å^{-3}	0.68/-0.52	1.07/-1.14	0.69/-0.93	0.92/-0.57	0.71/-1.13

Table S4.1. X-Ray Diffraction Table

Standard Procedure for Deformylation Reactions

In the glovebox, **($L^{Ad}H$)Fe** (10.0 mg, 8 μmol) was weighed out in a scintillation vial and dissolved in benzene (3mL). 2-Phenylpropionaldehyde (25 Equiv, 0.2mmol) and DBU (30 Equiv, 0.24 mmol) were added as stock solutions in benzene. The combined solutions were transferred to a 50mL Schlenk bomb with a stir bar. The Schlenk bomb was removed from the glovebox and transferred to a gas manifold under dry oxygen. The reaction mixture was subjected to a freeze-pump-thaw cycle before being exposed to an oxygen atmosphere. The reaction mixture was stirred for 3h before being quenched with H_2O (3mL). The biphasic mixture was diluted with EtOAc (20mL) and H_2O (10 mL). The organic layer was isolated and the aqueous layer was extracted twice with EtOAc (15mL). The combined organics were dried over Na_2SO_4, filtered, and the volatiles removed under reduced pressure. The residue was taken up in a stock solution of 1,3,5-trimethoxybenzene in $CDCl_3$ as an internal standard.

Standard Procedure for Phosphine Oxygen Transfer Reactions

In the glovebox, **($L^{Ad}H$)Fe** (10.0 mg, 8 μmol) was weighed out into a 1-dram vial and dissolved in C_6D_6. Triphenylphosphine (1 Equiv, 8 μmol) was added as a stock solution in C_6D_6. The solution was transferred to a J-Young tube, sealed, and removed from the glovebox. After taking an initial NMR spectrum, the tube was attached to a gas manifold under dry oxygen, and the solution was subjected to a freeze-pump-thaw cycle before being exposed to an oxygen atmosphere. The tube was sealed and inverted twice immediately before injecting into the spectrometer.

Standard Procedure for H-Atom Transfer Reactions

In the glovebox, 40 μL of a 5.05×10^{-4} M stock solution of **($L^{Ad}H$)Fe** in benzene, 20 μL of a 10 mM solution of 1,2-diphenylhydrazine in benzene, and 2.94 mL of benzene were transferred into a Schlenk cuvette using Hamilton glass syringes. The cuvette was sealed, removed from the glovebox, and exposed to O_2 via a gas manifold under dry oxygen. The cuvette was inverted twice immediately before kinetic measurements began. The control for the kinetics of 1,2-diphenylhydrazine reactivity with oxygen was repeated with the exact procedure except replacing the 20 μL of **($L^{Ad}H$)Fe** stock solution with 20 μL of benzene.

Deformylation Reaction Control Experiments

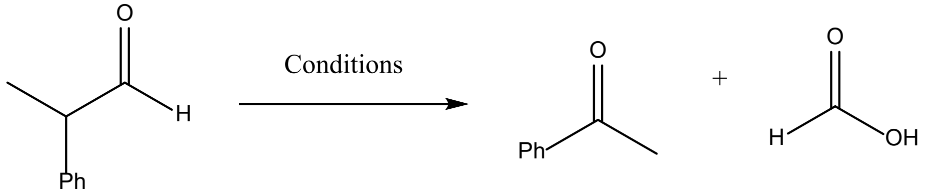

Conditions	Yield Acetophenone
Ligand + 2-PPA + O_2 (No Fe)	0
2-PPA + DBU + O_2 (No HLFe)	0
2-PPA + O_2 (No HLFe, Base)	0
HLFe + 2-PPA (no O_2)	Trace

Table S4.4. Control Experiments for Aldehyde Deformylation Reactivity

Representative NMR's for 2-PPA Deformylation:

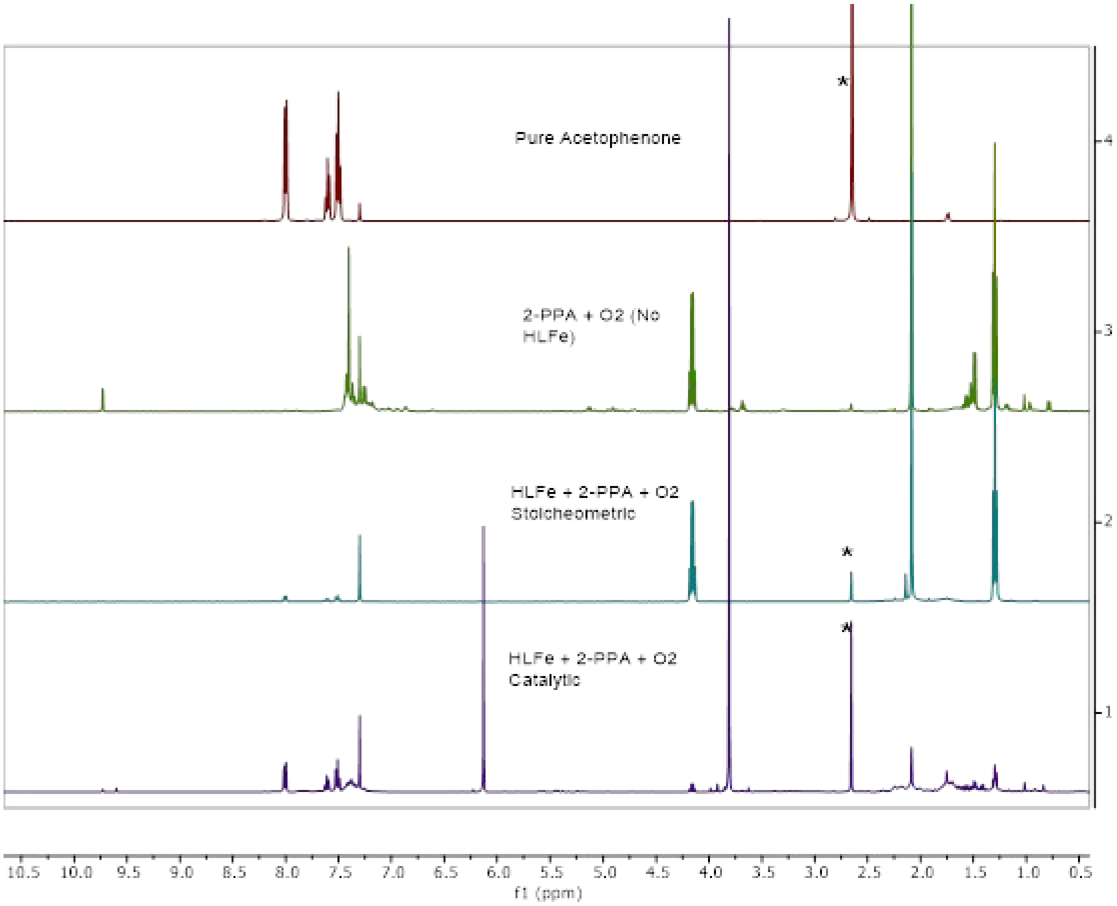

Figure S4.1. Representative ^1H NMR Spectra (400 MHz, 298 K) of 2-PPA deformylation reactions. * denotes the methyl position of acetophenone.

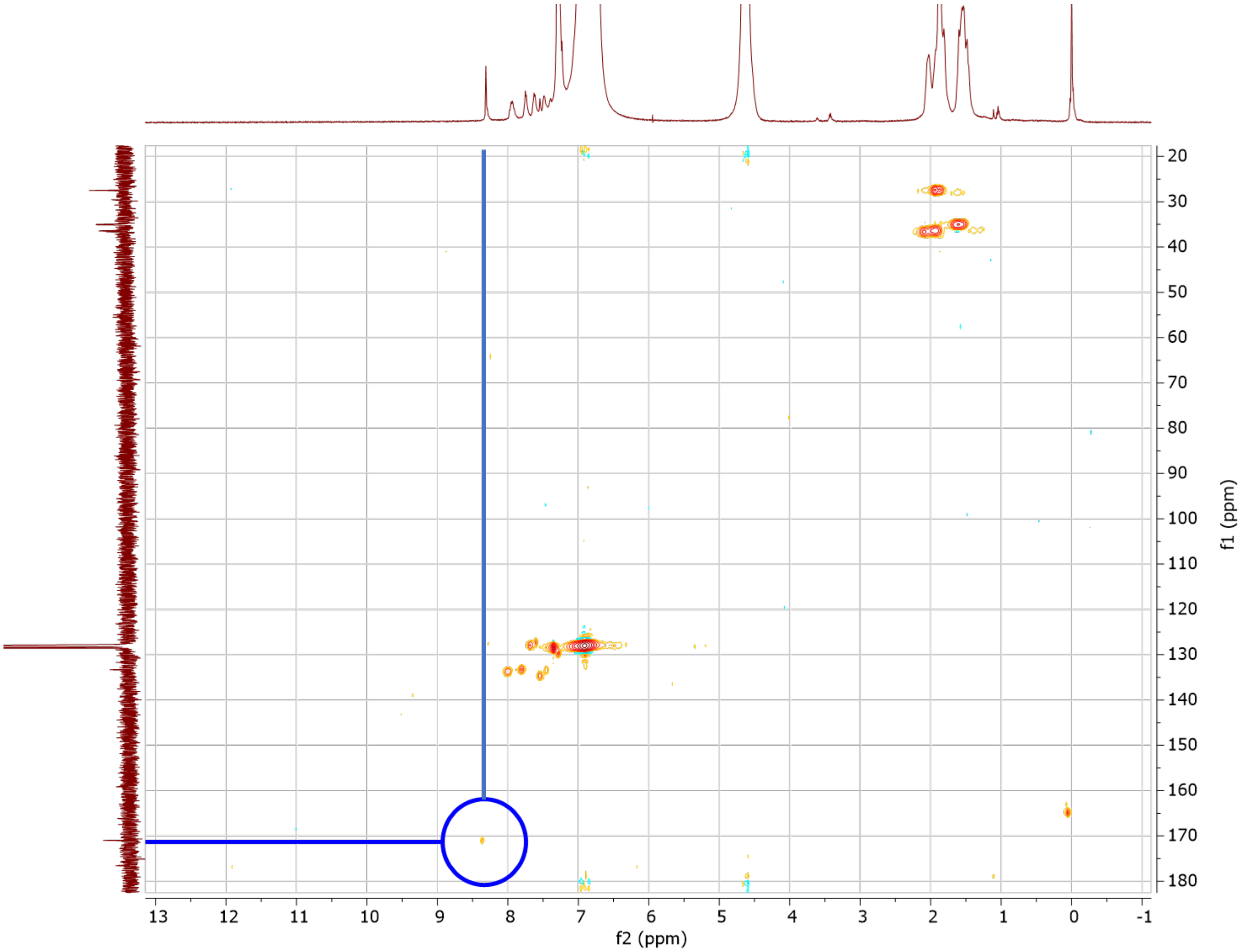

Figure S4.2. ^{1}H-^{13}C HSQC (500 MHz, 298 K) of D_2O quenched stoichiometric deformylation reaction collected in D_2O. Blue circle and lines highlight the ^{1}H and ^{13}C of formic acid, consistent with literature values[62].

EPR Spectra

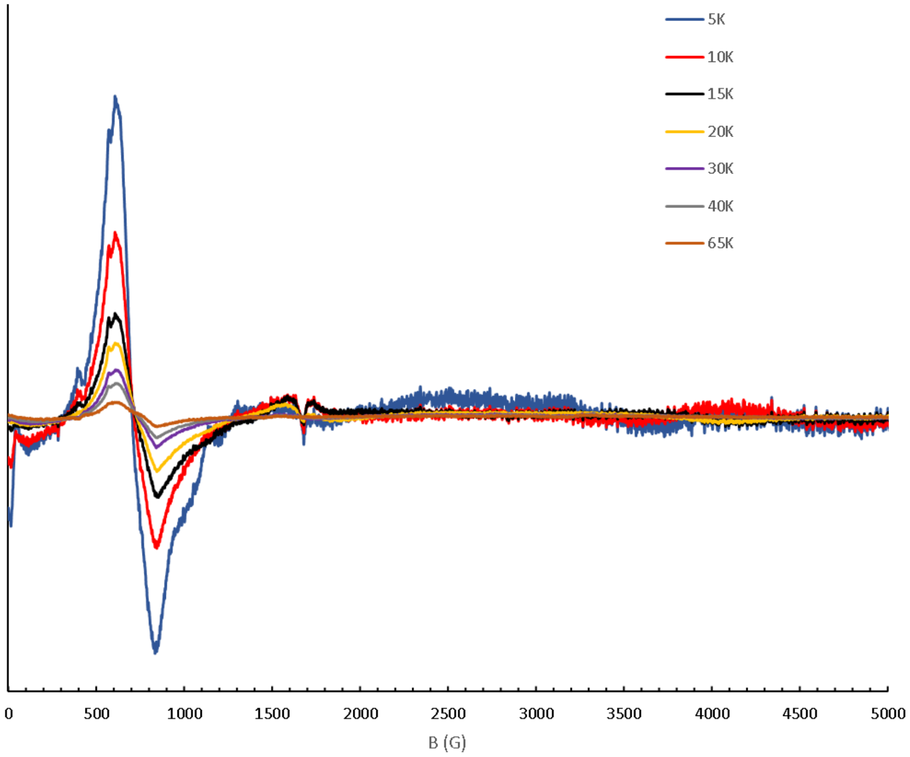

Figure S4.3. Variable temperature X-band parallel mode EPR spectra of a 5 mM toluene solution of **$(L^{Ad}H)FeO_2$** collected at 2 mW.

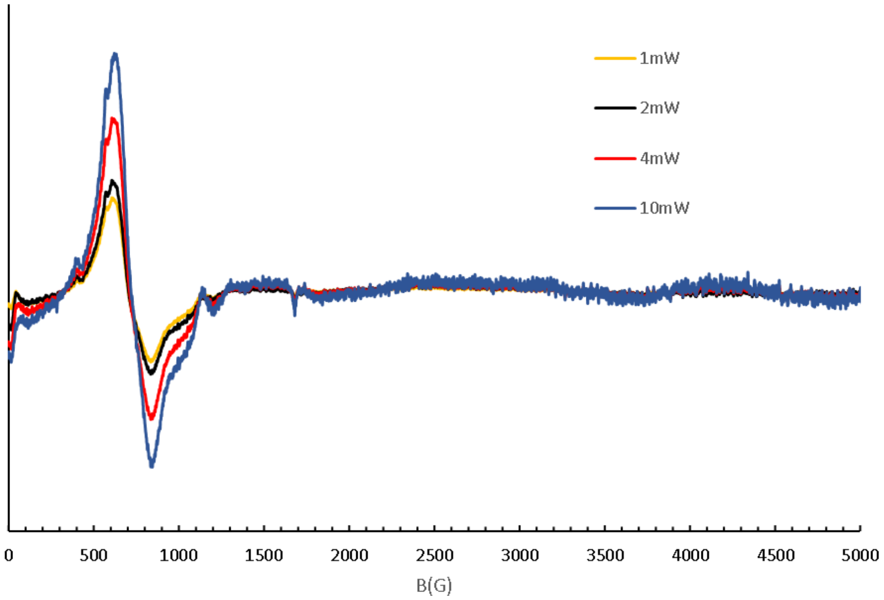

Figure S4.4. Variable temperature X-band parallel mode EPR spectra of 5 mM toluene solution of **$(L^{Ad}H)FeO_2$** collected at 5 K.

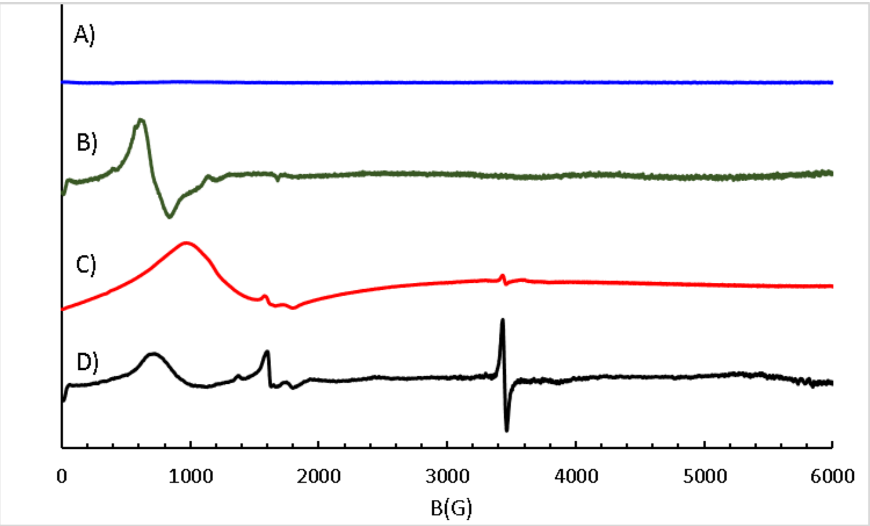

Figure S4.5. A) X-Band parallel mode EPR spectra of 5 mM toluene solution of **$(L^{Ad}H)Fe$** collected at 5 K and 2 mW; B) X-Band parallel mode EPR spectra of 5 mM toluene solution of of **$(L^{Ad}H)FeO_2$;** C) X-band perpendicular mode EPR spectra of 5 mM Toluene solution of **$(L^{Ad}H)Fe$** collected at 5 K and 2 mW; D) X-Band perpendicular mode EPR spectra of 5 mM toluene solution of **$(L^{Ad}H)FeO_2$** collected at 5 K and 2 mW. The features in (C) may arise from **$(L^{Ad}H)$**Fe. The features at ~1600 G and ~3500 G in (D) arise from unidentified radical impurities.

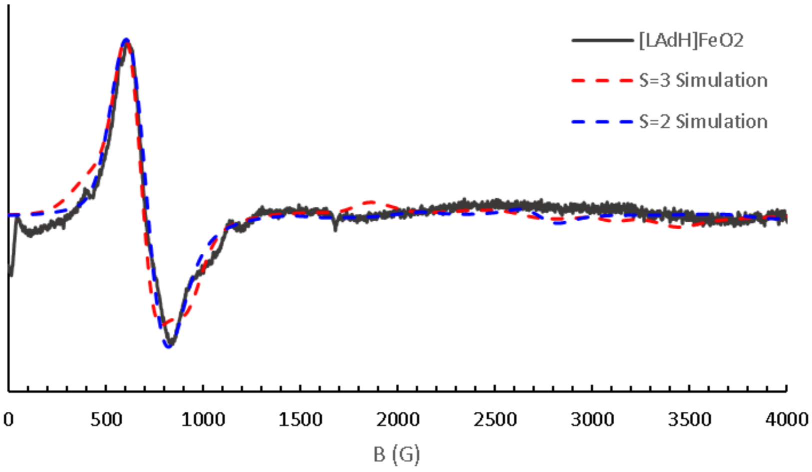

Figure S4.6. Parallel-mode X-band EPR spectra of 5 mM toluene solution of **$(L^{Ad}H)FeO_2$** collected at 5 K and 2 mW. Experimental data is plotted in grey and the simulations with S = 2 (D = 0.16 cm^{-1}, E = 0.025 cm^{-1}, E/D = 0.154, g = 2, D_{strain} = [0.022 cm^{-1}, 6.2 x 10^{-4} cm^{-1}) and S = 3 (D = 0.13 cm^{-1}, E = 1.35 x 10^{-4} cm^{-1}, E/D = 0.001, g = 2, D_{strain} = [1.4 x 10^{-4} cm^{-1}, 2.6 x 10^{-5} cm^{-1}]) are shown as colored lines.

Vibrational Spectroscopy

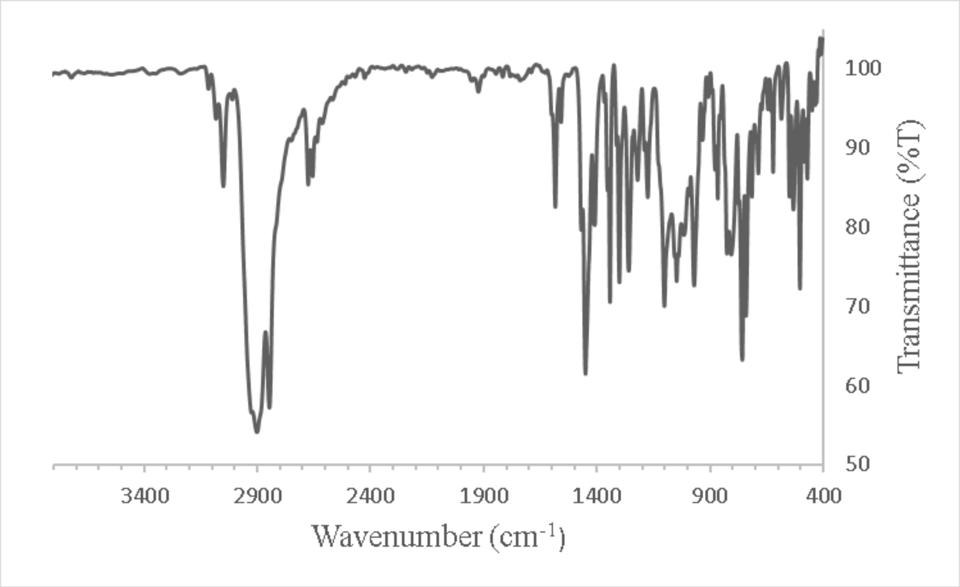

Figure S4.7. KBr-IR spectrum of **Tri-PAd$_2$.**

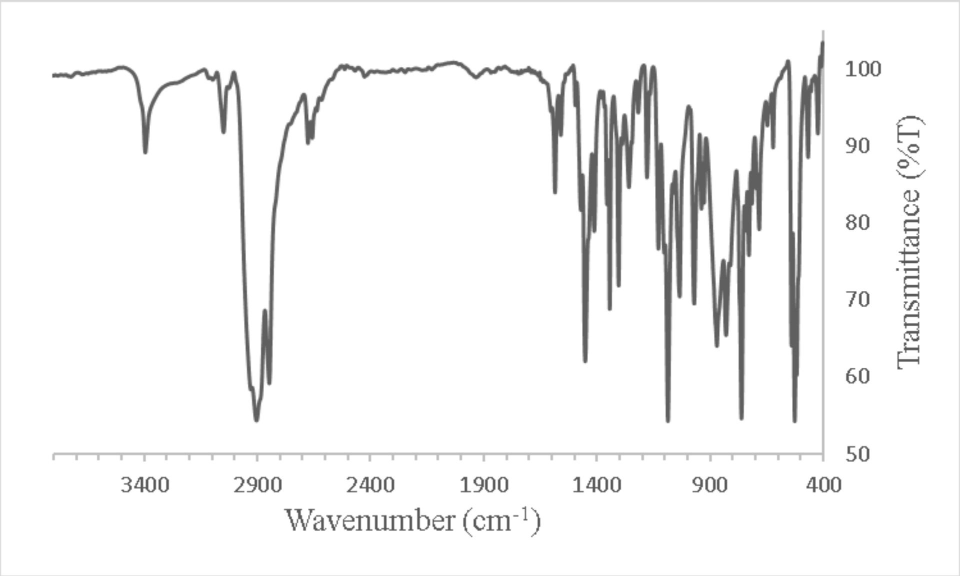

Figure S4.8. KBr-IR spectrum of **L^{Ad}H$_3$**.

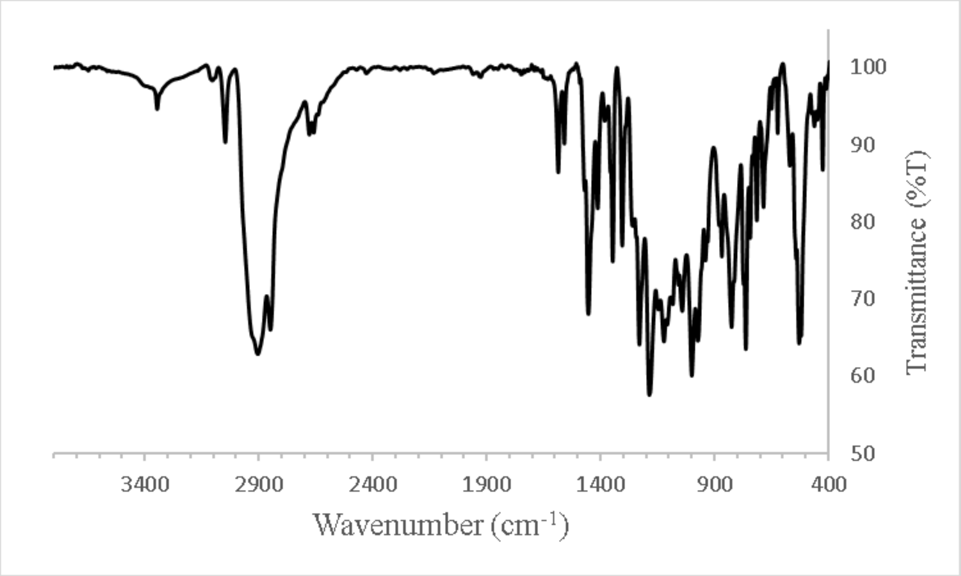

Figure S4.9. KBr-IR spectrum of **($L^{Ad}H$)Fe**.

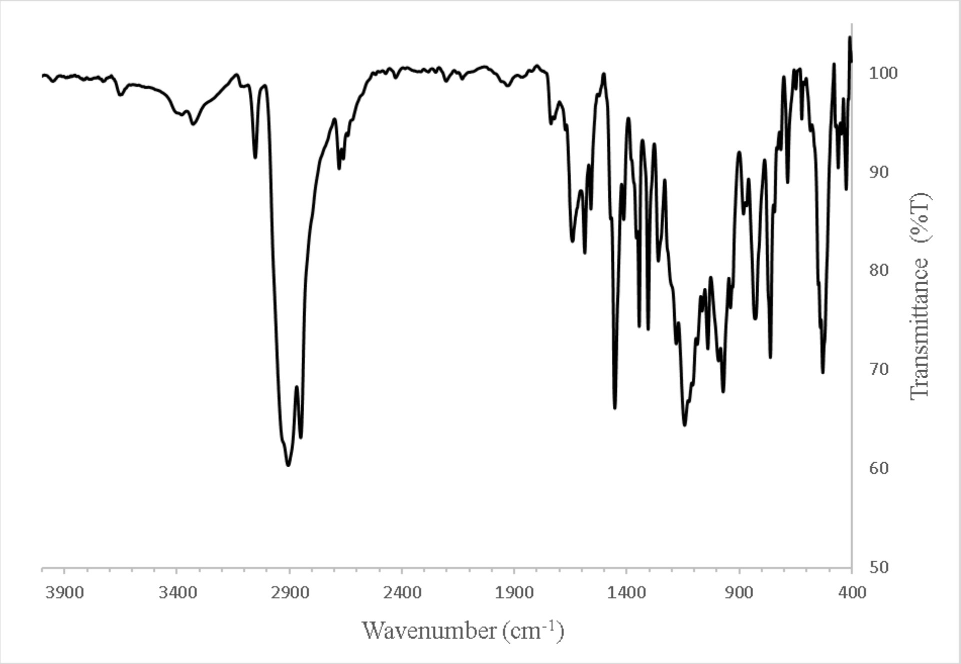

Figure S4.10. KBr-IR spectrum of **($L^{Ad}H$)FeO$_2$**.

Supplemental Discussion of the Vibrational Characteristics of ($L^{Ad}H$)FeO_2

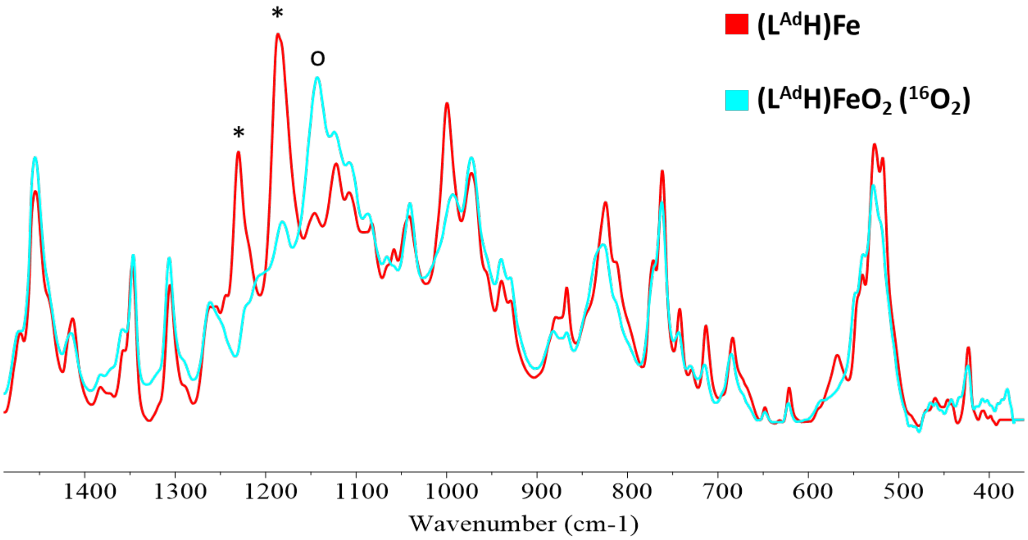

Figure S4.11: Comparison of experimental FTIR data on **($L^{Ad}H$)Fe** and ((**$L^{Ad}H$)$Fe^{16}O_2$**

The structural, spectroscopic, and computational studies on **($L^{Ad}H$)FeO_2** described in the main text collectively support an Fe(III)-superoxide formulation. As metal-superoxide complexes typically display ν(O-O) stretching frequencies in the range of 1050-1250 cm^{-1} we collected FTIR data on polycrystalline **($L^{Ad}H$)FeO_2** to assess the presence of this functional group in bulk, isolated material. The obtained spectra (Fig S4.11) contain numerous features in the aforementioned region and therefore we sought to provide a finer estimate of the ν(O-O) frequency using metrics obtained from the XRD study. Generally speaking, the vibrational characteristics and structural metrics of any isolated bond are correlated, and the usage of Badger's Rule (Eq S4.1) analyses has proven useful in understanding or predicting metrics for reactive O-O, M=O, and M-O(H) bonds,[63,64,65]

$$r_e = \frac{C_{ij}}{{\nu_e}^{2/3}} + d_{ij} \qquad \text{Eq. S4.1}$$

where r_e is the equilibrium internuclear distance, ν_e is the vibrational frequency, and C_{ij} and d_{ij} are empirical constants obtained by regression analysis. To predict the ν(O-O) vibration for **($L^{Ad}H$)FeO_2** using the measured O-O bond distance, we have performed a Badger's Rule analysis of the various oxidation states of simple O_2 derivatives and a range of synthetic η^1-M(O_2) and $\eta^{1,2}$-M(O_2)M complexes (sample size = 24) for which high-quality structural and vibrational data have been reported. The resulting correlation is presented in Fig S4.12 with the corresponding data tabulated in Table S4.4.

In the case of the simple O_2 molecules/ions (red dots), there is a strong linear correlation between the O-O bond distance and $1/\nu(\text{O-O})^{2/3}$ as expected from Eq S4.1. In contrast, the transition metal-dioxygen complexes (blue dots) exhibit a systematic deviation from this red trendline. Librational motion of O_2 ligands is well known to cause artificial shortening of O-O bond distances in XRD structures, as noted in a previous analysis of mononuclear η^2-M(O_2) complexes.[66] Additional error in the present correlation may result from the distinct physical states on which the experiments are performed: XRD studies are performed on single crystalline material whereas FTIR and Raman measurements are commonly performed on solution-phase or polycrystalline material with variable molecular contexts surrounding the $M(O_2)$ moiety that may serve to modulate the experimental metrics. Nonetheless, this collection of data points internally displays appreciable correlation between their experimental vibrational and structural metrics. It is noteworthy that all complexes assigned as containing either a O_2^- or O_2^{2-} redox state lie within the two drawn circles reflecting their experimental O-O bond metrics. Accordingly, the usage of this empirical correlation provides predictive power in discerning the redox level of the O_2-derived ligand and ascertaining unknown experimental values. For example, Tolman and coworkers have used similar analyses to predict an unknown Cu^{III}-O(H) distance using the experimentally determined ν(Cu-O) stretching frequency.[65]

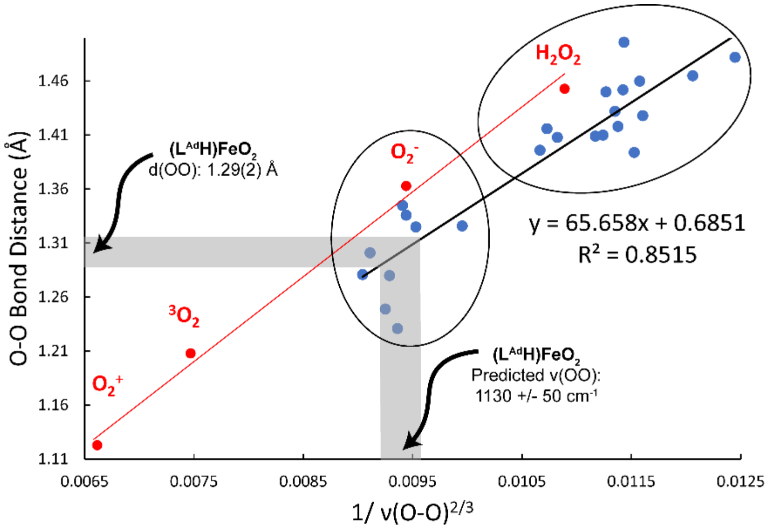

Figure S4.12. Badger's Rule plot of crystallographically and vibrationally characterized η^1-MO_2 and $\eta^{1,2}$-M-(O_2)-M species. The simple O_2-containing molecules and ions are not used in the correlation equation shown.

Owing to the unique structure of **$(L^{Ad}H)FeO_2$** we conducted single crystal XRD diffraction studies on multiple samples to confidently discuss the metrics for the $\{FeO_2\}$ unit (Table S4.3). Three XRD structures of **$(L^{Ad}H)FeO_2$** were obtained using an in-house diffractometer (Rigaku, Cu-Kα, 100 K) and exhibited resolutions limits of <0.83 Å which allowed for complete anisotropic modelling of the unit cell with minimal restraints. However, the resulting data sets displayed unexplainably large R_{int} statistics. The solid-state XRD structure and corresponding metrics described in the main text are derived from a superior data set collected using synchrotron radiation (100 K). The resultant structural model (**Crystal 1**) is nearly identical to that found in the other data sets but does not suffer from abnormal R_{int} statistics. Although we are most confident in the structural metrics reported for **Crystal 1** owing to its excellent data quality, it is noteworthy that the d(O-O) distance represents the most prominent difference between the four data sets. For the subsequent Badger's Rule analysis, we use the average d(O-O) metric from all four crystals (1.29(2) Å) to emphasize the uncertainty of this measurement (denoted as the breadth of the gray horizontal line in Fig S4.12). The Badger's Rule correlation predicts a ν(O-O) = 1130 cm^{-1} for **$(L^{Ad}H)FeO_2$** with an implied uncertainty of 50 cm^{-1} (illustrated as the breadth of the vertical gray line). If we only consider the structural metrics for **Crystal 1**, the predicted ν(O-O) = 1150 +/- 80 cm^{-1}.

	d(Fe-O) (Å)	**d(O-O) (Å)**	**<(Fe-O-O) (°)**
Crystal 1	***1.981(3)***	***1.321(5)***	***114.8(3)***
Crystal 2	1.983(3)	1.283(5)	115.6(3)
Crystal 3	1.995(4)	1.280(7)	115.6(4)
Crystal 4	1.981(4)	1.289(7)	115.1(4)
Average	1.985(5)	1.29(2)	115.3(3)

Table S4.5. Crystallographic bond metrics of four independently collected structures of **$(L^{Ad}H)FeO_2$**. The structure discussed in the main text is **Crystal 1**.

An examination of the FTIR data for **$(L^{Ad}H)FeO_2$** generated with either ^{16}O- or ^{18}O-labelled O_2 (Fig S4.13) reveals subtle differences precisely within the expected spectral range. Specifically, the ^{16}O-labelled material displays increased IR absorption at ~1140 cm^{-1} and diminished absorption at ~1080 cm^{-1} as compared to the ^{18}O-labelled material. However, the $^{16\text{-}18}\Delta$ ~ 60 cm^{-1} is smaller than the value predicted by Hooke's Law for two oxygen atoms (72 cm^{-1}). Owing to this discrepancy, we evaluated the molecular context of this particular $M(O_2)$ complex and considered the vibrational characteristics of the supporting ligand.

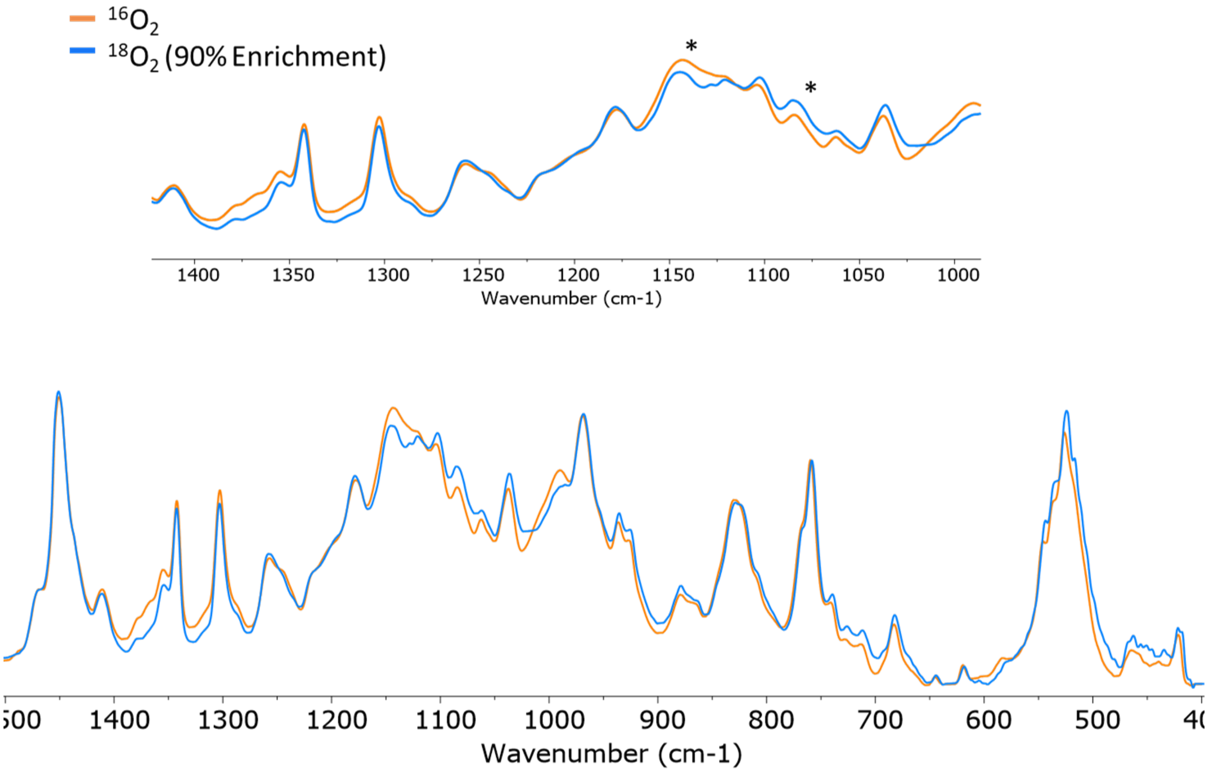

Figure S4.13. KBr-IR spectra (depicted in absorbance mode) of **(L^{Ad}H)FeO$_2$** (orange) prepared with natural abundance O_2 and with 90% ^{18}O-labeled O_2 (Blue). Asterisks highlight spectral differences that may be ascribed to isotopic variations in the O_2-derived ligand.

The phosphinimide co-ligands present in **(L^{Ad}H)FeO$_2$** complicate the assignment of a unique ν(O-O) mode owing to vibrational coupling with the iron-phosphinimide groups (R_3**P=N**-Fe). The ν(P=N) modes of terminally-bound metallo-phosphinimides occur in the range of 1050-1250 cm^{-1} and their high intensity often allows for straightforward assignment.[29] The two phosphinimide functional groups bound to iron in the **(L^{Ad}H)Fe** starting material give rise to symmetric and antisymmetric combinations of the two ν(P=N) stretching modes (Fig S11) assigned at 1231 and 1187 cm^{-1}. The high intensity of these features is comparable to that observed in other high-spin iron phosphinimide complexes.[30] In **(L^{Ad}H)FeO$_2$**, both of these features are missing and replaced by a prominent absorption at ~1140 cm^{-1} (Fig S4.11). The ν(P=N) frequency is expected to red-shift upon oxidation of the metal center.[29] Considering the discussion above, we speculate that this feature results from a combination of three, overlapping modes with variable ν(P=N) and ν(O-O) character as both sets of isolated stretching frequencies are expected in this region. This situation is reminiscent of organometallic hydrido-carbonyl complexes which commonly display coupled ν(M-H) and ν(C≡O) vibrational modes.[67] In **(L^{Ad}H)FeO$_2$**, coupling of the ν(P=N) and ν(O-O) modes is expected for a superoxide ligand, but not for a peroxide ligand owing to the disparate energy of these individual stretching frequencies.

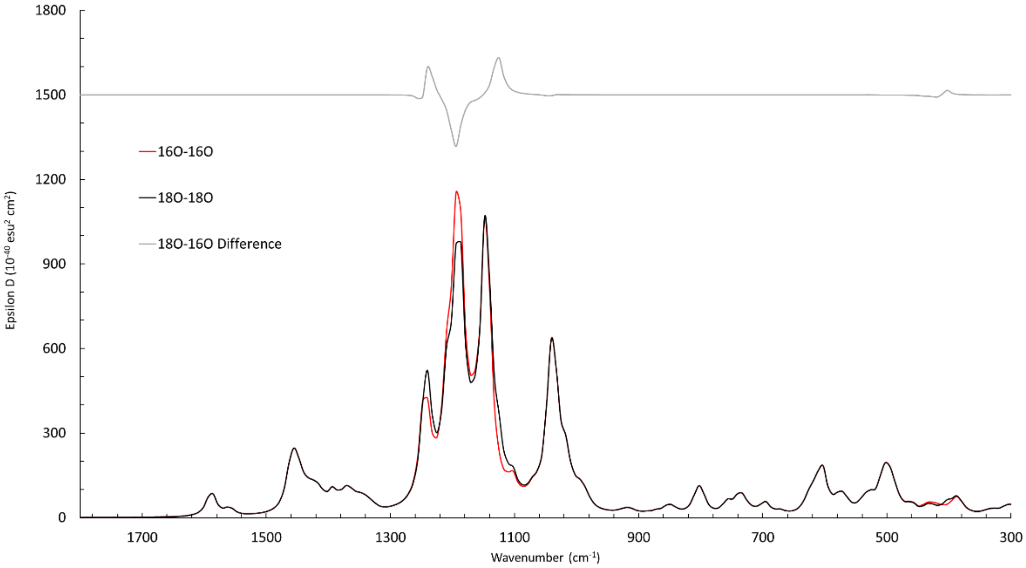

Figure S4.14. DFT-predicted infrared spectra of **(L^{tBu}H)FeO$_2$** with natural abundance O_2 (red) and with ^{18}O-labeled O_2 (black). The predicted difference spectra upon O_2 isotope exchange (gray) illustrates the consequences of vibrational coupling between the *v*(P=N) and *v*(O-O) stretching frequencies.

The gas-phase optimized geometry of truncated **(L$^{t\text{-}Bu}$H)FeO$_2$** furnishes structural metrics in excellent agreement with those found in **Crystal 1** and corroborate the prediction of vibrational coupling (Fig S4.14). For reference, the DFT-predicted d(O-O) = 1.3153 Å and the experimental distance in **Crystal 1** is 1.321(5) Å. There are three modes predicted to have variable ν(P=N) and ν(O-O) character spanning the range of 1080 - 1260cm^{-1} and this situation gives rise to non-intuitive changes in the IR response upon ^{18}O enrichment of the O_2 ligand as illustrated in the $^{18\text{-}16}O$ difference spectrum. While differences are observed in our experimental FTIR data upon isotopic substitution in **(L^{Ad}H)FeO$_2$** in the range expected for a superoxide ligand, the intense nature of isolated ν(P=N) modes and the vibrational complexity expected for this system prevents us from confidently assigning a pure ν(O-O) stretching frequency. We also note that this spectral region possesses additional vibrational modes - stemming from the six adamantyl substituents and/or the tetra-arene framework - that serve to further complicate assignment. We anticipate that that the resonant enhancement of the vibrations associated with **(L^{Ad}H)FeO$_2$** chromophore at ~400 nm via Resonance Raman spectroscopy may enable the collection of spectra free from these contributions. However, such data would not resolve the unavoidable coupling between the ν(P=N) and ν(O-O) oscillators. We have attempted Raman measurements on polycrystalline **(L^{Ad}H)Fe** and **(L^{Ad}H)FeO$_2$** with a 532 and 633 nm laser but did not observe any signals ascribable to vibrational features present in these compounds.

Compound	Experimental ν(O-O) (cm^{-1})	$1/\nu(O\text{-}O)^{2/3}$	Experimental d(O-O) (Å)	Reference
O2+	1858	0.00661662	1.123	68
O2	1549	0.007469629	1.208	68
O2-	1090	0.009441674	1.363	68
H2O2	880	0.010889591	1.453	68
(TMGtren)CuO2	1117	0.009288906	1.28	69
(14-TMC)(Cl)Cr(O2)	1104	0.009361683	1.231	42
(Tp)(Lx)Co(O2)	1150	0.009110344	1.301	70
(EtIm)(TPivPP)Fe(O2)	1163	0.009042327	1.281	71
(calix[4]arene)Mn(O2)	1124	0.009250299	1.249	72
Cu-O-O-Cu	836	0.011268406	1.45	73
	803	0.011575053	1.46	74
	818	0.011433112	1.496	75
	827	0.011350012	1.432	76
	814	0.011470536	1.368	77
Co-O-O-Co	1075	0.009529301	1.325	78
	800	0.011603972	1.428	79
	839	0.011241528	1.41	80
	824	0.011377544	1.418	81
Mn-O-O-Mn	819	0.011423804	1.452	28
Ni-O-O-Ni	1096	0.009407184	1.345	82
	720	0.012448347	1.482	83
	755	0.012060594	1.465	83
	1007	0.009953604	1.326	83
	1090	0.009441674	1.336	84
Pt-OO-Pt	808	0.011527251	1.394	85
Fe-OO-Fe	888	0.010824089	1.408	86
	908	0.010664556	1.396	87
	900	0.01072766	1.416	88

Table S4.4. Tabulated metrics for a selection of previously characterized, terminally-coordinated transition metal-O_2 compounds.

UV-Visible Spectra

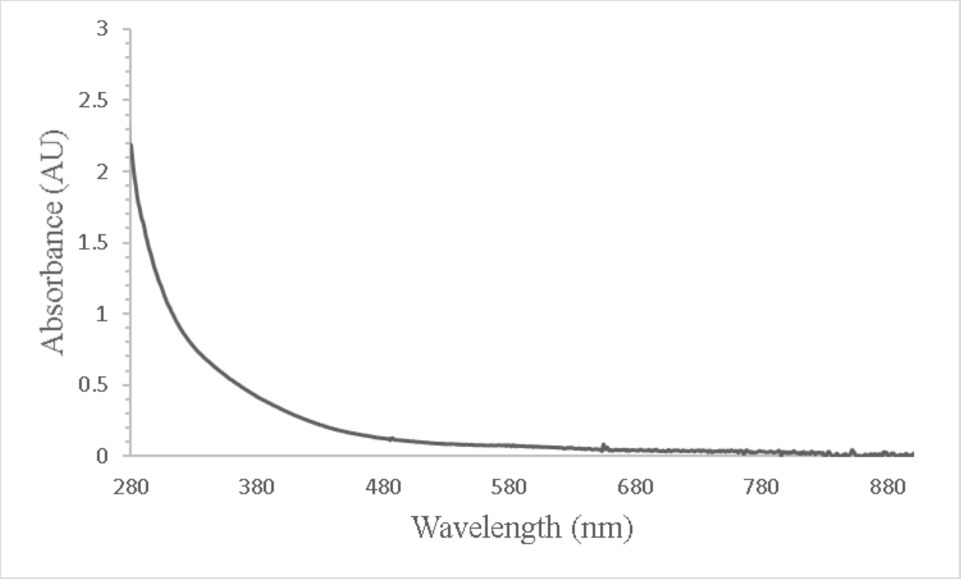

Figure S4.15. UV/Visible spectrum of **($L^{Ad}H$)Fe** in C_6H_6 at 298 K

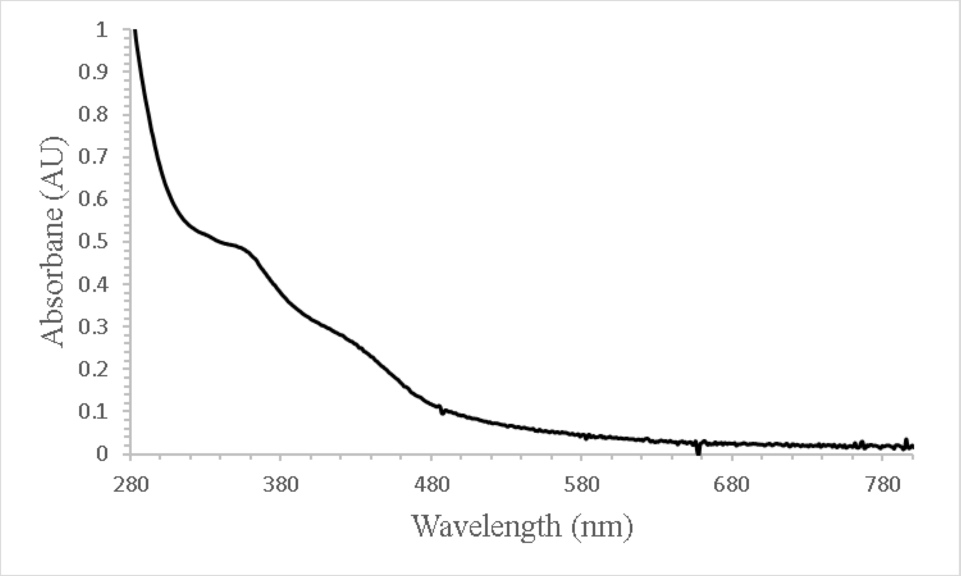

Figure S4.16. UV/Visible Spectrum of *in situ*-generated **($L^{Ad}H$)FeO_2** in C_6H_6 at 298 K

Electrochemistry

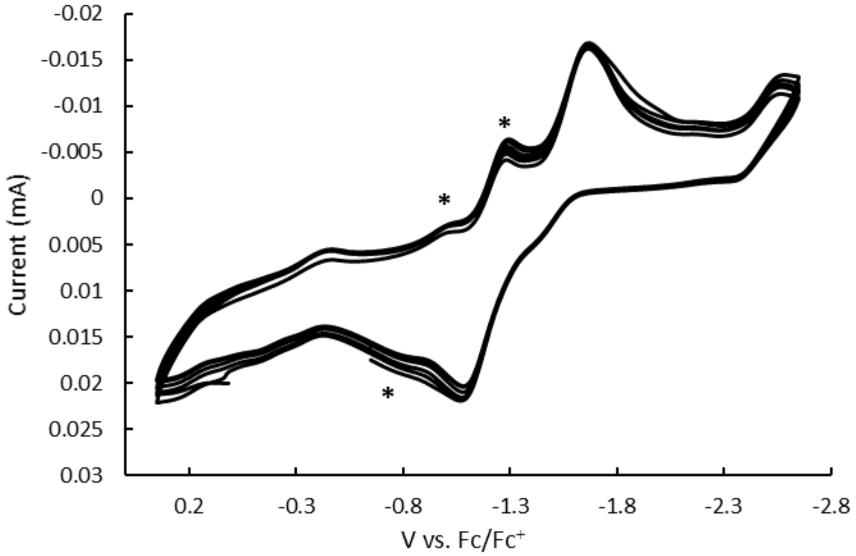

Figure S4.17. Cyclic Voltammogram of **(L^{Ad}H)Fe**, measured in 0.2 M [^{n}Bu$_4$N][PF$_6$) electrolyte in THF at 298 K. Asterisks denote unidentified impurities.

NMR Spectra

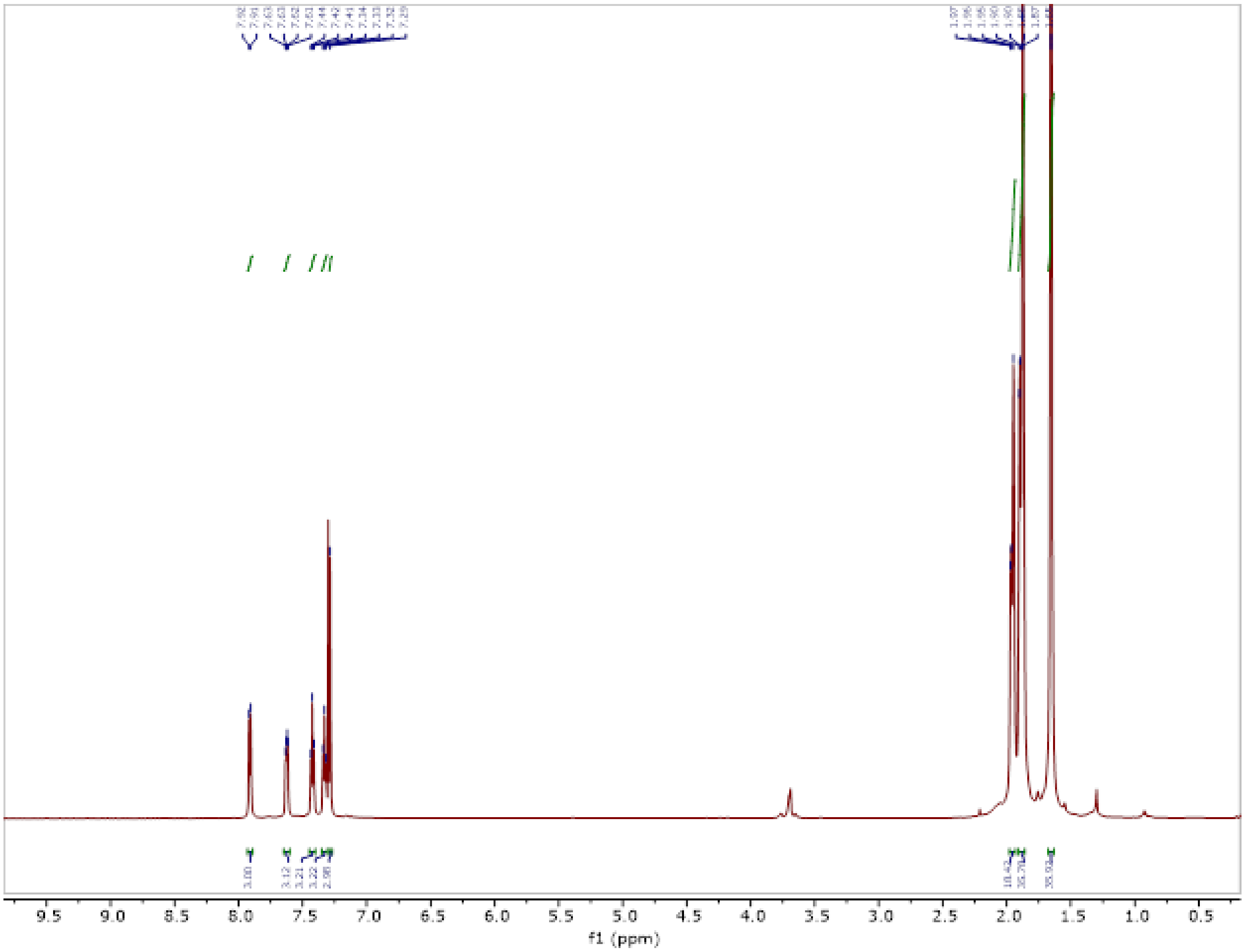

Figure S4.18. ^{1}H NMR Spectrum (600 MHz, 298 K) of **Tri-PAd$_2$** recorded in $CDCl_3$

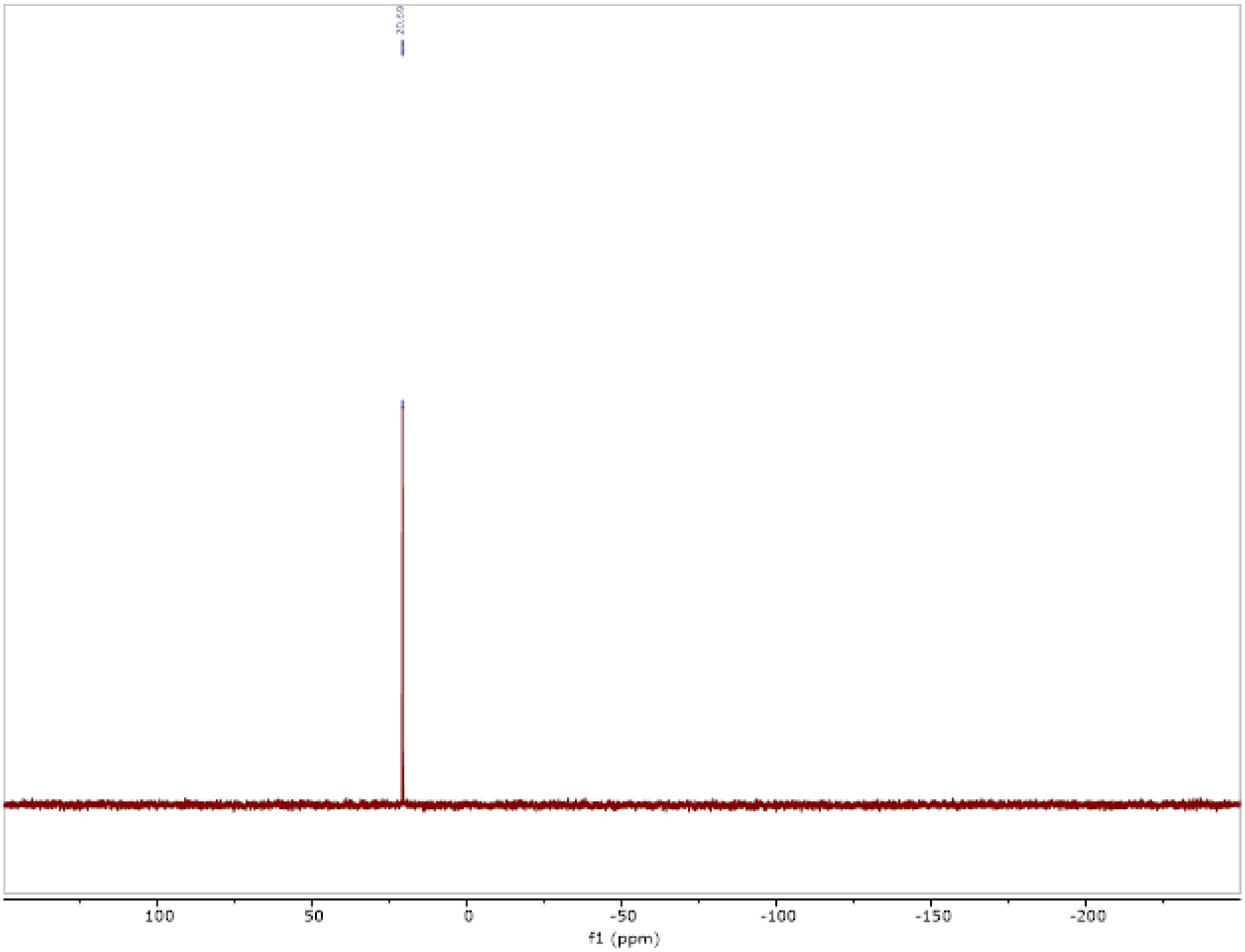

Figure S4.19. ^{31}P NMR Spectrum (162 MHz, 298 K) of **Tri-PAd$_2$** recorded in CDCl$_3$

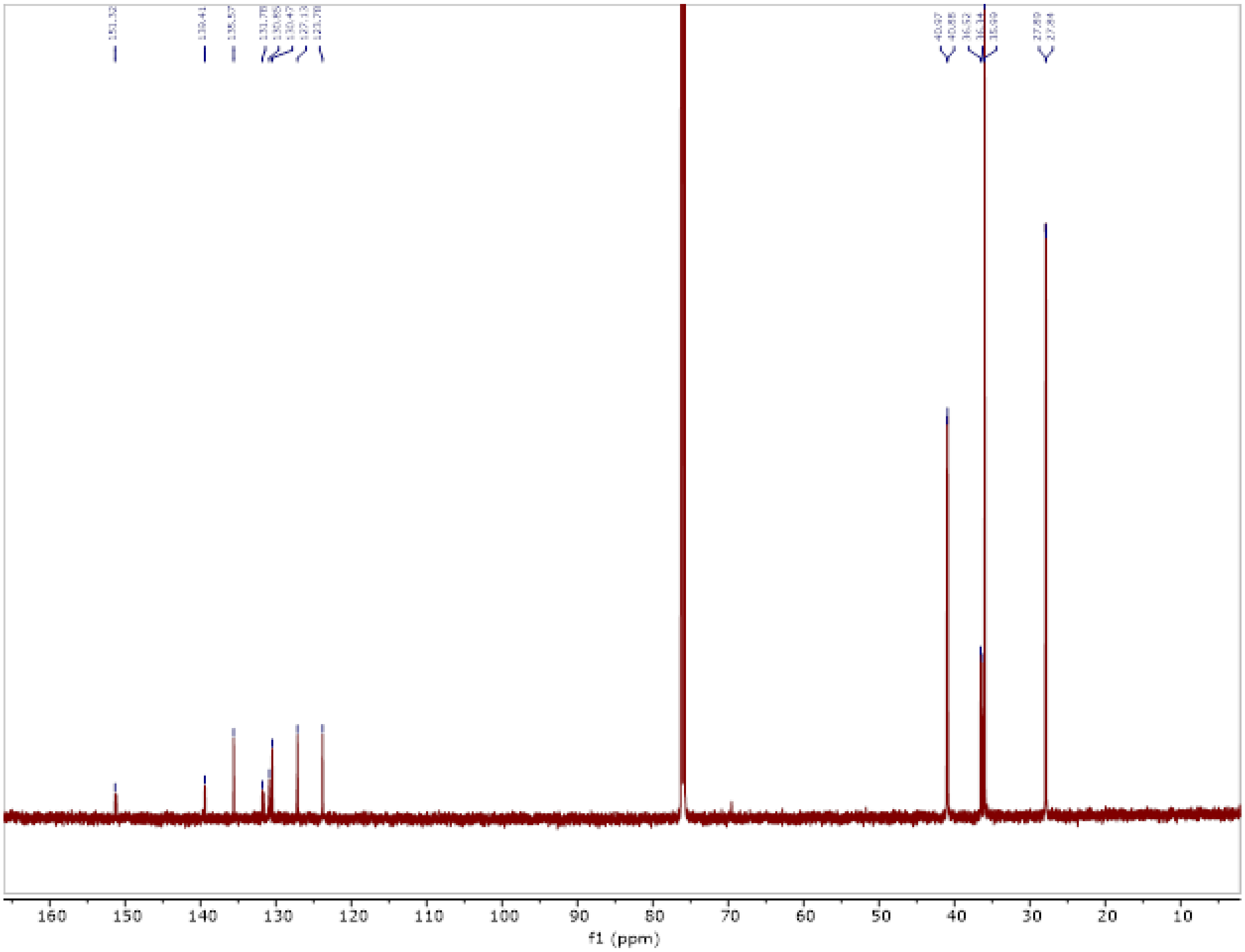

Figure S4.20. ^{13}C NMR spectrum (151 MHz, 298 K) of **Tri-PAd$_2$** recorded in $CDCl_3$

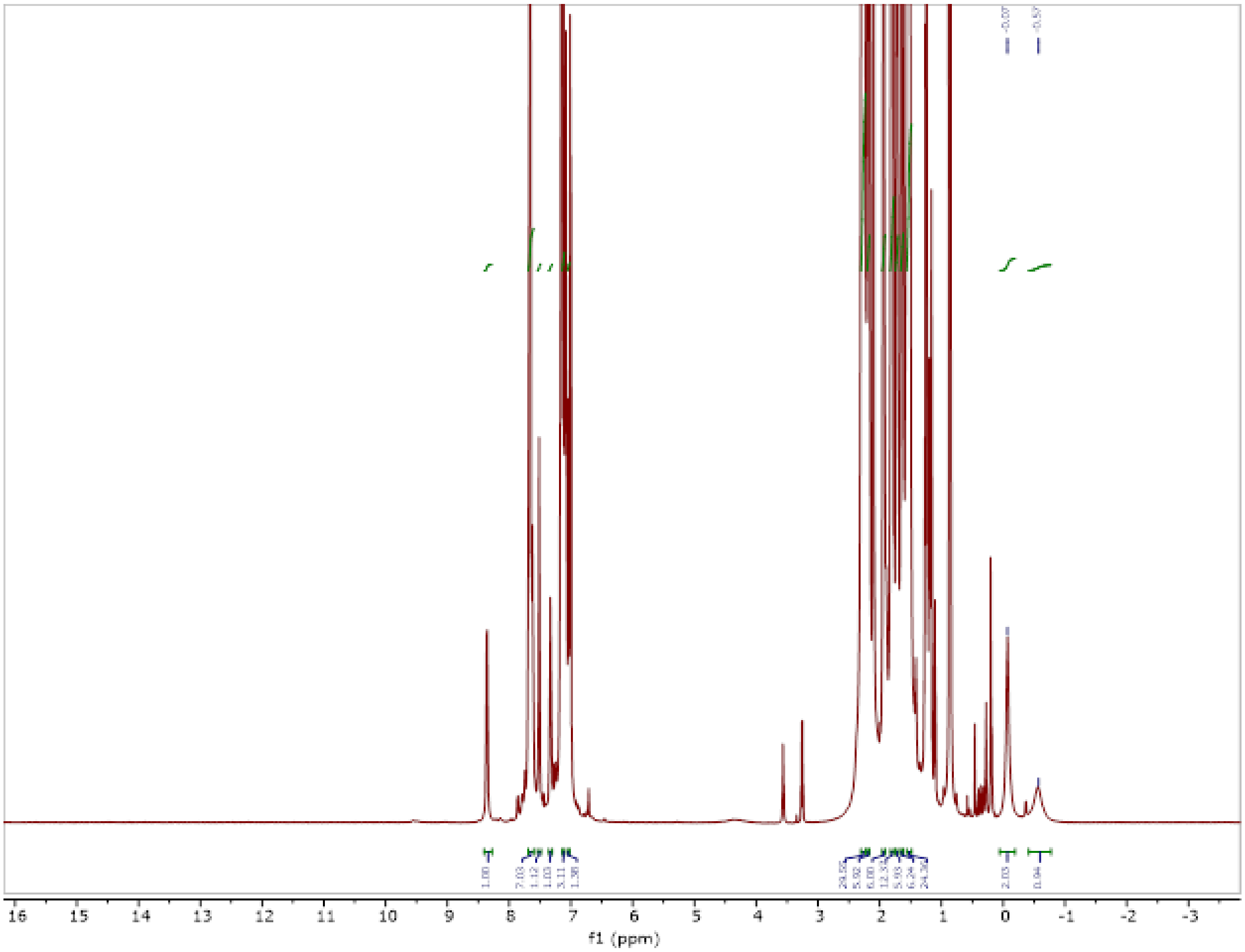

Figure S4.21. ^{1}H NMR Spectrum (600 MHz, 298 K) of $\mathbf{L^{Ad}H_3}$ recorded in C_6D_6

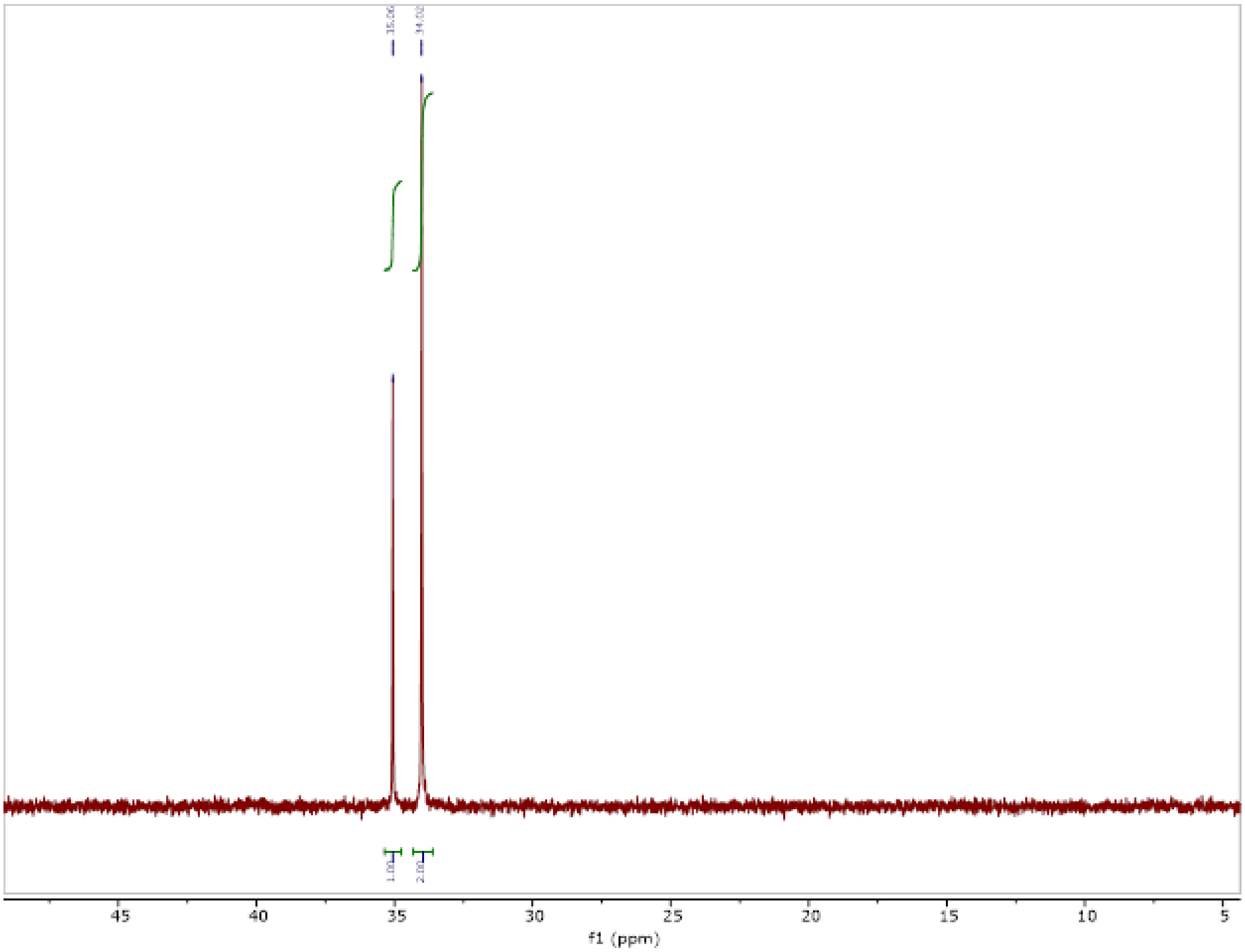

Figure S4.22. ^{31}P NMR Spectrum (243 MHz, 298 K) of $\mathbf{L^{Ad}H_3}$ recorded in C_6D_6

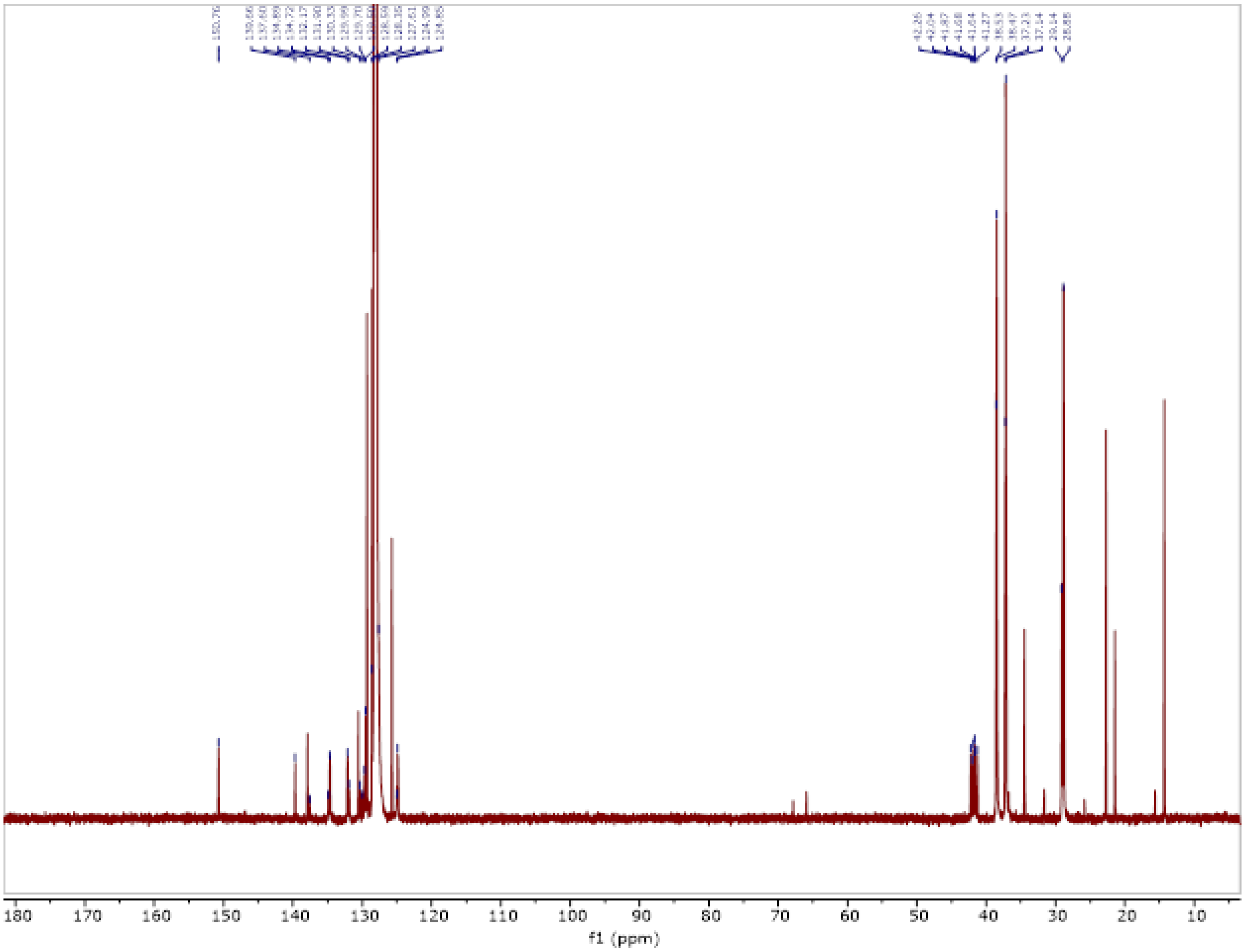

Figure S4.23. ^{13}C NMR Spectrum (151 MHz, 298 K) of **L^{Ad}H$_3$** recorded in C_6D_6

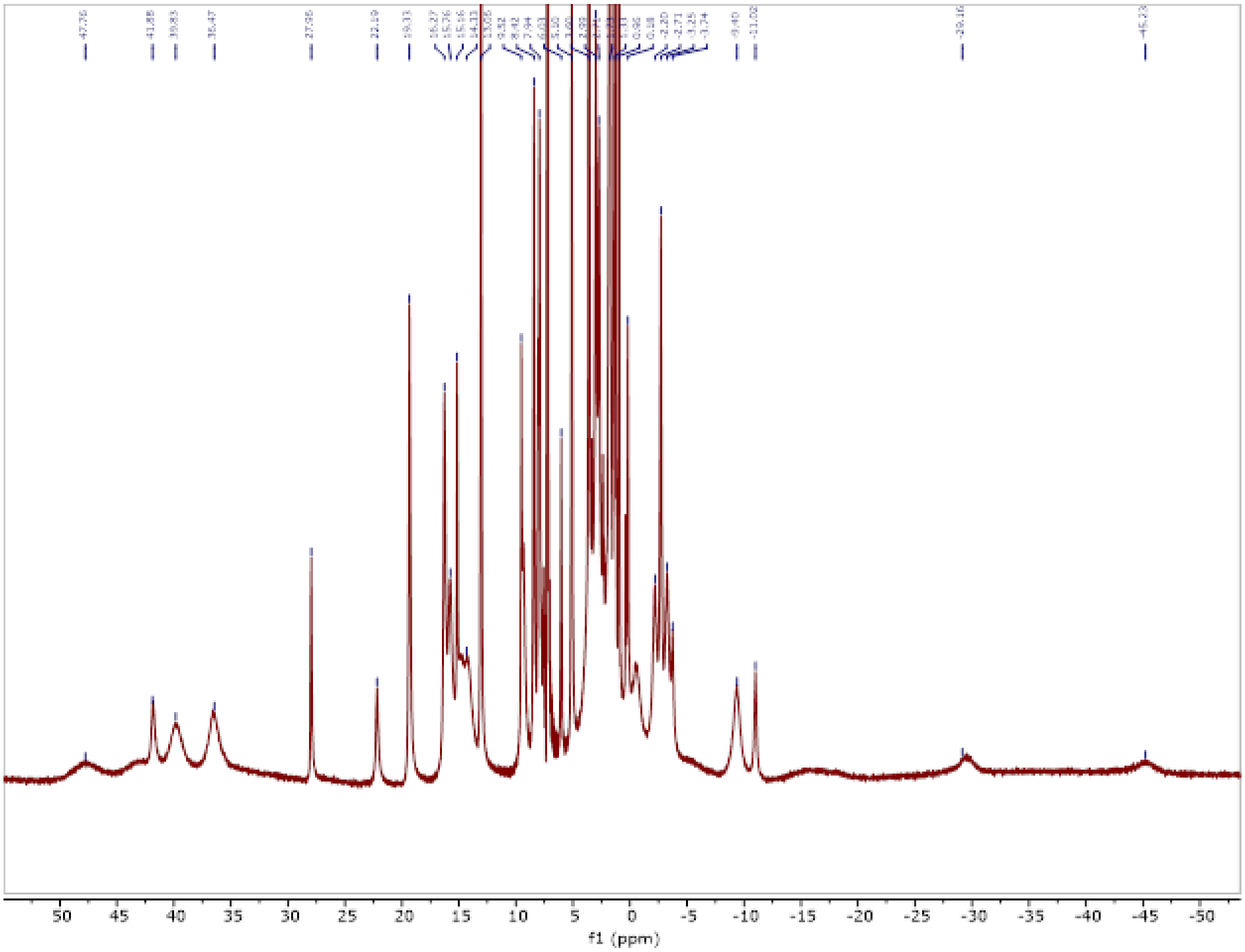

Figure S4.24. ^{1}H NMR (400 MHz, 298 K) of **(L^{Ad}H)Fe** recorded in C_6D_6

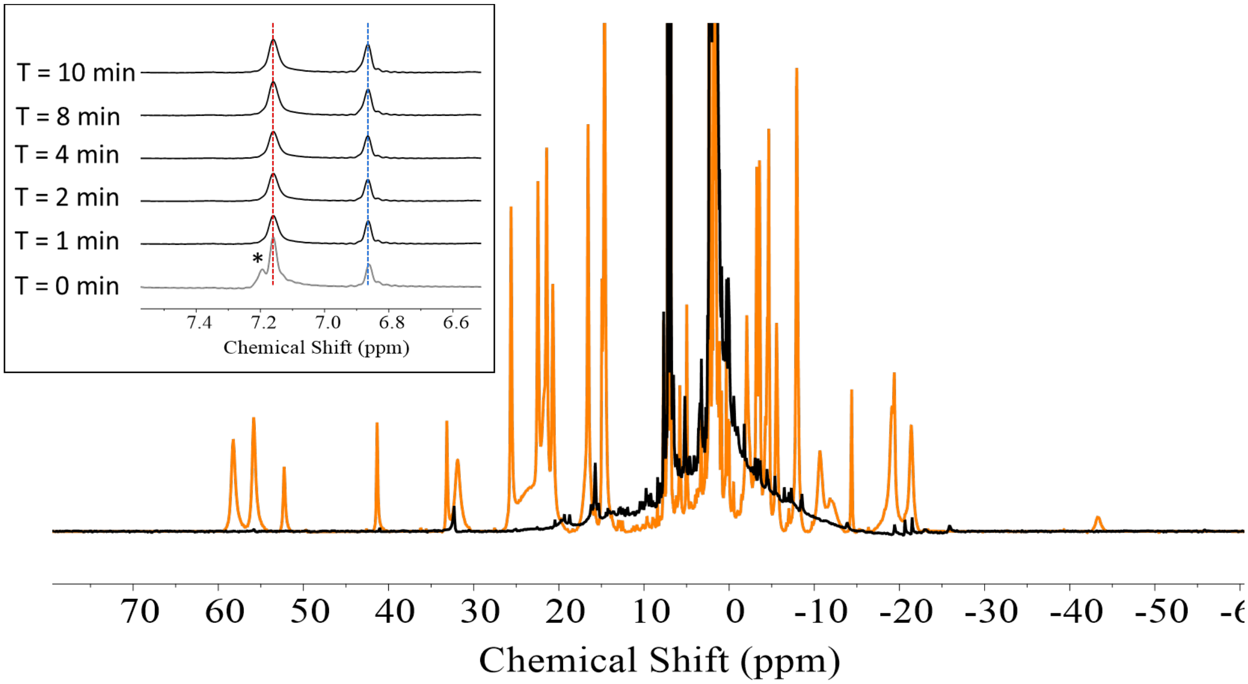

Figure S4.25. ^{1}H NMR (400 MHz, 298 K) of **(L^{Ad}H)Fe** (orange trace) and **(L^{Ad}H)Fe** ca. 1 minute after exposure to 1 atm O_2 (black trace). Oxygenation results in the rapid loss of sharp paramagnetic features ascribed to **(L^{Ad}H)Fe** with concomitant generation of a small number of minor, irreproducibly produced features ascribed to impurities. (Inset) Time course of C_6D_5H resonances present in the NMR tube containing **(L^{Ad}H)Fe** (left) and capillary insert (right) prior to, and following O_2 exposure. Dashed lines are a guide to illustrate that the solution phase magnetic moment does not appreciable change up to 10 minutes following oxygenation. The asterisk corresponds to a resonance ascribed to **(L^{Ad}H)Fe**.

Density Functional Theory

Gas-phase Optimized Geometry: $(L^{t\text{-}Bu}H)Fe$ Spin = 2 Charge = 0

Fe	0.11951700	-0.12770800	-0.96140600
P	-2.81180200	-1.80466900	-0.64222200
P	3.09551800	-1.35183000	-0.58747900
P	-0.28635400	3.34020300	-0.58163200
N	-0.69571100	1.82069300	-0.84043300
N	1.98942700	-0.30180100	-0.84687300
N	-1.42069100	-1.18799300	-0.86081300
C	-3.54170300	-1.52782700	1.05659300
C	0.43862200	3.74006400	1.07080200
C	3.01505500	-2.25793300	1.04827600
C	2.03910300	-2.02080700	2.05491200
C	1.03138100	3.71096900	-1.87205800
C	1.26111600	0.39741100	2.04269500
H	2.29334900	0.72570700	2.00702500
C	5.04373400	0.13587600	-1.91962900
H	5.29641400	-0.61246600	-2.67930100
H	4.16017100	0.68729000	-2.25541600
C	-4.09753700	-1.03433000	-1.85023200
C	-4.88259700	-1.89347600	1.28720300
H	-5.44019900	-2.38190400	0.49569100
C	0.96904700	-0.97550200	2.02316900
C	4.80421100	-0.50979900	-0.53894200
C	3.93260800	-3.30472600	1.26832200
H	4.68044000	-3.51665500	0.51392800
C	-2.78571600	-3.69885000	-0.82389000
C	-1.41569300	-0.44093400	2.06504700
C	4.68046800	0.60964700	0.51551100
H	3.83946700	1.26968900	0.29203700
H	4.54135100	0.19210100	1.52046900
C	3.05817200	-2.73953200	-1.91487800
C	2.37592500	3.17803100	-1.33147800
H	2.71504600	3.73751500	-0.45349400
H	2.30928600	2.11153700	-1.08251500
C	0.61843300	2.79649800	2.11859200
C	0.23731300	1.35046500	2.07252000
C	-5.53816200	-1.63907500	2.49269300
H	-6.57395300	-1.94209700	2.62237800
C	-0.37014200	-1.37786500	2.05874900
H	-0.60615900	-2.43577800	2.03995800
C	3.91728500	-4.10109800	2.41338200
H	4.64923300	-4.89582400	2.53219400
C	-1.10002800	0.92175600	2.11693300

H	-1.90227800	1.65452700	2.16104500
C	-4.55920300	0.30853700	-1.24796900
H	-3.69649600	0.91404400	-0.94912100
H	-5.20659400	0.17562100	-0.37538800
C	-3.52438600	-0.61598600	3.31864200
H	-2.97626500	-0.12065500	4.11652100
C	-2.84611000	-0.87974900	2.11291900
C	0.68583300	2.92475500	-3.15897400
H	0.67780900	1.84734800	-2.98017900
H	-0.28223600	3.21187900	-3.57941000
C	1.18391900	5.19884800	-2.24784500
H	0.27867600	5.60778900	-2.70806600
H	1.46851700	5.83244700	-1.40242600
C	-5.34277600	-1.85212400	-2.24502400
H	-5.08078200	-2.77896700	-2.76500200
H	-5.98840700	-2.10119500	-1.39675300
C	2.95014800	-3.86917300	3.39064400
H	2.91206200	-4.47642500	4.29121900
C	-4.07455300	-4.48650200	-0.52165300
H	-4.91833800	-4.20241200	-1.15600800
H	-4.37425200	-4.38388700	0.52628800
C	6.03401800	-1.35784400	-0.15914900
H	5.97517900	-1.72048800	0.87180000
H	6.19114000	-2.21324100	-0.82212300
C	2.62445100	-2.05924800	-3.23345000
H	1.69557700	-1.49879400	-3.09952600
H	3.38378100	-1.36753400	-3.61259200
C	-1.82468900	4.43372100	-0.71386800
C	-4.85311900	-0.98704000	3.51801700
H	-5.34280200	-0.77348500	4.46453900
C	-2.43115600	4.24928800	-2.12215200
H	-1.83219500	4.74813900	-2.89164800
H	-2.52506300	3.19137400	-2.38530100
C	0.91494100	5.05326500	1.26802300
H	0.80926300	5.78325700	0.47443700
C	-3.31311300	-0.71760400	-3.14381500
H	-2.42922800	-0.11313500	-2.92534400
H	-2.97863800	-1.62538000	-3.65608100
C	-1.71021900	-4.19078800	0.16679600
H	-0.76061100	-3.67377700	0.01017400
H	-2.02916500	-4.03501500	1.20483000
C	-1.64444900	5.93916500	-0.43057500
H	-1.38055600	6.12920000	0.61390300
H	-0.89897500	6.41303300	-1.07472300
C	1.25860900	3.21999900	3.29992000
H	1.39222900	2.48920000	4.09279100

C	4.34262200	-3.53804400	-2.20740600
H	5.15195900	-2.89789200	-2.57321500
H	4.70856800	-4.10666100	-1.34695300
C	1.93595900	-3.71425000	-1.50281200
H	2.20740100	-4.31216800	-0.62660300
H	1.01119100	-3.16983000	-1.28082100
C	-2.82644700	3.89684300	0.33516500
H	-3.12469900	2.86262300	0.14008100
H	-2.41974600	3.96320500	1.35069700
C	-2.30745000	-4.01350100	-2.25662600
H	-3.08620400	-3.81424400	-3.00145800
H	-1.42252400	-3.42127800	-2.51072300
C	2.02888900	-2.84162600	3.20099500
H	1.27631000	-2.64592500	3.96088100
C	1.53966100	5.45300700	2.44806100
H	1.89191500	6.47508700	2.55555800
C	1.71228200	4.52525300	3.47566500
H	2.19812100	4.81218700	4.40424700
H	-1.52043900	1.53093400	-0.31386100
H	4.12455000	-4.26809300	-3.00013900
H	2.46615200	-2.83751100	-3.99350200
H	1.73134100	-4.40306000	-2.33466300
H	-5.11924400	0.87348900	-2.00660100
H	-3.97185000	-0.16533100	-3.82981100
H	-5.94827200	-1.25262200	-2.94039700
H	-3.43179600	4.70074300	-2.13801000
H	-3.73542200	4.51109600	0.29728600
H	-2.60493700	6.43665700	-0.62058700
H	-2.04695600	-5.07879000	-2.32847800
H	-1.55287000	-5.26907000	0.02400000
H	-3.87884900	-5.55365100	-0.69994600
H	6.92821900	-0.72199100	-0.23065600
H	5.88891500	0.83571300	-1.85318300
H	5.60511100	1.20418400	0.52575900
H	3.13124500	3.29555100	-2.12023300
H	1.46086800	3.14845700	-3.90408400
H	1.98977800	5.27515900	-2.98895300

Gas-phase Optimized Geometry: $(L^{t\text{-}Bu}H)FeO_2$ Spin = 2 Charge = 0

Fe	0.14880000	0.05928200	-1.25289100
P	-2.19589000	-2.57838900	-0.46494100
P	3.39665500	-0.48271400	-0.53602500
P	-1.26902600	3.05899800	-0.47350900
N	-1.45213800	-1.18457400	-0.69593100
H	-1.95724600	-0.41713000	-0.24522800
N	1.86800000	-0.48856800	-0.80571900

O	0.20330400	-0.20607100	-3.20617100
N	-0.59967800	1.68578000	-0.73793600
C	3.86731000	-0.00388900	1.19593600
C	2.92240000	0.19769900	2.23421500
C	-2.02589900	-3.26913000	1.24176500
C	4.13153400	-2.22535400	-0.71888900
C	4.29812300	0.74955300	-1.68944600
C	-2.64547600	-4.50306700	1.53011600
H	-3.26008100	-4.98202600	0.77756600
C	0.81319700	-1.21265700	2.14059000
H	1.42017600	-2.11133200	2.12044100
C	-1.23141800	-2.66458600	2.25351800
C	-4.05162000	-2.33179900	-0.75828000
C	5.62146200	-2.42988800	-0.37948800
H	6.29901400	-1.84466300	-1.00581500
H	5.83286600	-2.20506100	0.67071400
C	-4.89299500	-3.60738800	-0.96232200
H	-4.55531200	-4.19062000	-1.82418700
H	-4.91658000	-4.25342400	-0.07989500
C	3.86293300	-2.69201800	-2.16501000
H	2.83079900	-2.48686900	-2.46537500
H	4.53298700	-2.20285500	-2.88069400
C	1.43422500	0.04630700	2.12661800
C	3.38296400	0.60591100	3.50165000
H	2.64767800	0.75898300	4.28748600
C	0.63856200	1.19487900	2.16518900
H	1.11385400	2.16911300	2.17514600
C	3.32590400	-3.11135900	0.25290400
H	3.55480500	-2.86096100	1.29591300
H	2.25327900	-2.99409700	0.09191500
C	-1.39915000	-3.81500600	-1.61693100
C	-0.58084500	-1.32061000	2.16410500
C	-2.82248100	3.28752800	-1.57181300
C	-4.23158300	-1.44303200	-2.01172800
H	-3.58162600	-0.56605800	-2.00119400
H	-4.02668100	-1.99247600	-2.93357600
C	0.11465500	-3.72997700	-1.33189100
H	0.51371000	-2.72381300	-1.48169600
H	0.33647300	-4.04744100	-0.30676400
C	5.66908400	0.60909100	2.75446500
H	6.72936200	0.76500500	2.93498600
C	-2.48055600	-5.15190500	2.75304700
H	-2.97768600	-6.10084200	2.93380100
C	4.73510000	0.80981600	3.77067300
H	5.05213100	1.12330000	4.76178300
C	5.22785200	0.21106700	1.49272300

H	5.96642400	0.07546500	0.71116200
C	-1.66376400	-4.57682100	3.72714200
H	-1.51091600	-5.07102300	4.68268600
C	-4.60544800	-1.57460400	0.47048700
H	-4.52212900	-2.16535700	1.38855400
H	-4.09972600	-0.61576000	0.62813600
C	4.14472100	2.15373600	-1.07218900
H	4.75207100	2.28270800	-0.17035200
H	3.10014500	2.35230000	-0.81784500
C	5.78522100	0.50284900	-2.01138700
H	6.43572100	0.51003700	-1.13139300
H	5.93975800	-0.43565500	-2.55261900
C	-1.05597100	-3.34935100	3.47115000
H	-0.43985700	-2.88019900	4.23334400
C	-1.35973800	-0.15352400	2.22032100
H	-2.44197000	-0.23260700	2.28777500
C	-1.87716000	3.26854700	1.27331800
C	-1.81961400	-5.28671600	-1.42370200
H	-1.50506700	-5.68098300	-0.45318700
H	-2.89439800	-5.45385400	-1.54234900
C	-1.61224800	2.33442500	2.30781800
C	-0.76102400	1.10993900	2.17966500
C	3.52933300	0.73437900	-3.03043400
H	3.59861100	-0.23111800	-3.54028300
H	2.46987200	0.95743900	-2.89513500
C	-1.67567400	-3.40014200	-3.07843700
H	-1.49078300	-2.33780300	-3.25333000
H	-2.70177600	-3.64233000	-3.37793800
C	-0.05621900	4.50328000	-0.70380900
C	-2.69244500	4.37519200	1.58302600
H	-2.91766900	5.10040700	0.80963400
C	-2.18250800	2.54178500	3.57868100
H	-1.96910000	1.81615000	4.35952700
C	1.11203600	4.20390700	0.25675400
H	0.80533200	4.33023600	1.30224800
H	1.48155600	3.18498400	0.12323100
O	-0.93083200	-0.10958500	-3.86520800
C	-3.97297700	2.50622200	-0.90407200
H	-3.65032400	1.49797500	-0.62246700
H	-4.35047100	3.00739000	-0.00706600
C	0.46207700	4.45152700	-2.15572900
H	-0.29220400	4.79986500	-2.87000000
H	0.76021400	3.43593000	-2.43491000
C	-3.24150400	4.57400200	2.84997200
H	-3.86502800	5.44351600	3.04043300
C	-3.30493600	4.71853200	-1.88299600

H	-2.56120800	5.28399800	-2.45322300
H	-3.57917100	5.29862600	-0.99645300
C	-2.98758200	3.64439000	3.85842000
H	-3.40729900	3.77536500	4.85228600
C	-2.49771700	2.61216100	-2.92130400
H	-2.18148100	1.57374100	-2.80478400
H	-1.70365200	3.13736200	-3.46145200
C	-0.55354100	5.92493500	-0.37686100
H	-1.38478000	6.25277100	-1.00550400
H	-0.84889000	6.01831000	0.67314400
H	4.04007000	-3.77433700	-2.23627600
H	3.59619300	-4.16438700	0.09274700
H	5.86554300	-3.48973200	-0.54041000
H	3.96987100	1.49618400	-3.68912300
H	4.46183200	2.90552600	-1.80800400
H	6.13017000	1.31364700	-2.66834500
H	-3.40038100	2.63819000	-3.54852800
H	-4.80257000	2.40691100	-1.61718000
H	-4.20546200	4.64788200	-2.50917600
H	0.27737900	6.62468800	-0.54424800
H	1.33672700	5.10932400	-2.25231300
H	1.93295400	4.90702500	0.06071100
H	0.63292000	-4.41526100	-2.01535300
H	-1.00208500	-3.97353700	-3.72821300
H	-1.31164700	-5.87539300	-2.19830000
H	-5.92854200	-3.30189600	-1.16271800
H	-5.27681800	-1.10825300	-2.04615200
H	-5.66743600	-1.35716900	0.29883800

Metric	**Experimental (XRD)**	**Optimized (DFT, TPSSh)**
Fe-O	1.981(3)	1.972
Fe-N(1)	1.894(3)	1.863
Fe-N(2)	2.042(3)	2.102
Fe-N(3)	1.853(3)	1.859
O-O	1.321(5)	1.315
Fe-O-O	114.8(3)	117.56
THC$_{DA}$	0.55	0.65

Table S4.5. Comparison of bonding metric obtained from XRD studies of **(L^{Ad}H)FeO$_2$** and computational studies on **(L$^{t\text{-}Bu}$H)FeO$_2$**.

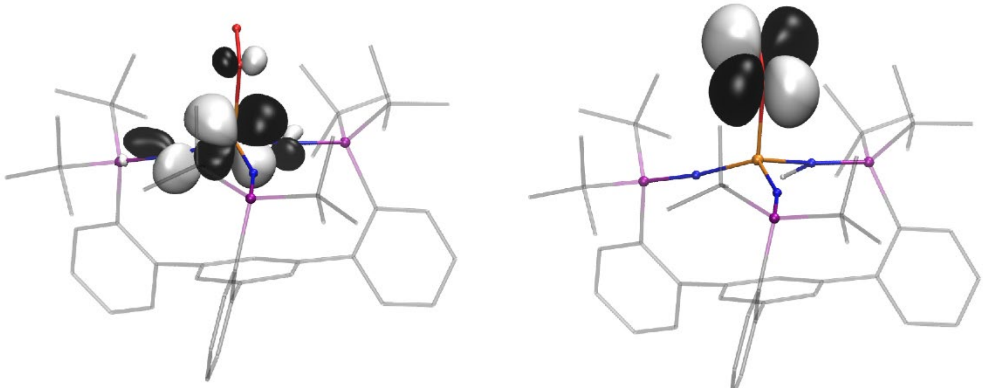

Figure S4.26. Magnetic orbitals of $^5(L^{t\text{-}Bu}H)FeO_2$ obtained from linear combinations of the two natural orbitals containing non-integer electron occupancies. The spatial overlap at the α -O atom is expected to favor antiferromagnetic coupling. Orbitals are drawn at a contour of 0.05 electrons per cubic Angstrom.

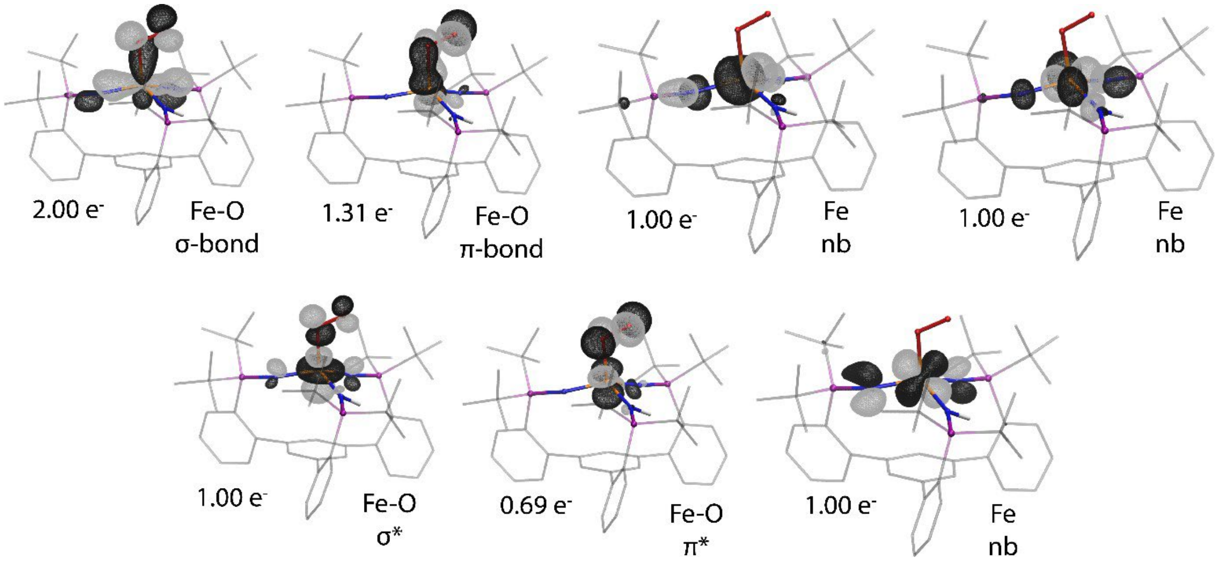

Figure S4.27. Natural orbitals, their electron occupancies and corresponding bonding assignment. Orbitals are drawn at a contour of 0.05 electrons per cubic Angstrom.

4.6 References

(1) Shi, Z.; Zhang, C.; Tang, C.; Jiao, N. *Chem. Soc. Rev.* **2012**, *41* (8), 3381–3430.

(2) Costas, M.; Mehn, M. P.; Jensen, M. P.; Que, L. *Chem. Rev.* **2004**, *104* (2), 939–986.

(3) Peck, S. C.; van der Donk, W. A. *J. Biol. Inorg. Chem.* **2017**, *22* (2–3), 381–394.

(4) Mbughuni, M. M.; Chakrabarti, M.; Hayden, J. A.; Bominaar, E. L.; Hendrich, M. P.; Münck, E.; Lipscomb, J. D. *Proc. Natl. Acad. Sci. U. S. A.* **2010**, *107* (39), 16788–16793.

(5) Tamanaha, E.; Zhang, B.; Guo, Y.; Chang, W. C.; Barr, E. W.; Xing, G.; St Clair, J.; Ye, S.; Neese, F.; Bollinger, J. M.; Krebs, C. *J. Am. Chem. Soc.* **2016**, *138* (28), 8862–8874.

(6) Karlsson, A.; Parales, J. V.; Parales, R. E.; Gibson, D. T.; Eklund, H.; Ramaswamy, S. *Science (80-.).* **2003**, *299* (5609), 1039–1042.

(7) Hong, S.; Sutherlin, K. D.; Park, J.; Kwon, E.; Siegler, M. A.; Solomon, E. I.; Nam, W. *Nat. Commun.* **2014**, *5* (1), 1–7.

(8) Chiang, C. W.; Kleespies, S. T.; Stout, H. D.; Meier, K. K.; Li, P. Y.; Bominaar, E. L.; Que, L.; Münck, E.; Lee, W. Z. *J. Am. Chem. Soc.* **2014**, *136* (31), 10846–10849.

(9) Blakely, M. N.; Dedushko, M. A.; Yan Poon, P. C.; Villar-Acevedo, G.; Kovacs, J. A. *J. Am. Chem. Soc.* **2019**, *141* (5), 1867–1870.

(10) Oloo, W. N.; Que, L. *Acc. Chem. Res.* **2015**, *48* (9), 2612–2621.

(11) Collins, T. J. *Acc. Chem. Res.* **2002**, *35* (9), 782–790.

(12) M. Christina White; Abigail G. Doyle, and; Jacobsen*, E. N. *J. Am. Chem. Soc.* **2001**, *123* (29), 7194–7195.

(13) Chen, M. S.; White, M. C. *Science (80-.).* **2010**, *327* (5965), 533–571.

(14) Lee, H. B.; Ciolkowski, N.; Winslow, C.; Rittle, J. *Inorg. Chem.* **2021**, *60* (16), 11830–11837.

(15) Dehnicke, K.; Krieger, M.; Massa, W. *Coord. Chem. Rev.* **1999**, *182* (1), 19–65.

(16) Stephan, D. W. *Organometallics* **1999**, *18* (7), 1116–1118.

(17) Rice, N. T.; Popov, I. A.; Russo, D. R.; Bacsa, J.; Batista, E. R.; Yang, P.; Telser, J.; La Pierre, H. S. *J. Am. Chem. Soc.* **2019**, *141* (33), 13222–13233.

(18) Scepaniak, J. J.; Harris, T. D.; Vogel, C. S.; Sutter, J.; Meyer, K.; Smith, J. M. *J. Am. Chem. Soc.* **2011**, *133* (11), 3824–3827.

(19) Camacho-Bunquin, J.; Ferguson, M. J.; Stryker, J. M. *J. Am. Chem. Soc.* **2013**, *135* (15), 5537–5540.

(20) Eckert, N. A.; Smith, J. M.; Lachicotte, R. J.; Holland, P. L. *Inorg. Chem.* **2004**, *43* (10), 3306–3321.

(21) Maddock, L. C. H.; Cadenbach, T.; Kennedy, A. R.; Borilovic, I.; Aromí, G.; Hevia, E. *Inorg. Chem.* **2015**, *54* (18), 9201–9210.

(22) Margraf, G.; Schödel, F.; Sänger, I.; Bolte, M.; Wagner, M.; Lerner, H. W. *Zeitschrift fur Naturforsch. - Sect. B J. Chem. Sci.* **2012**, *67* (6), 549–556.

(23) Sazama, G. T.; Betley, T. A. *Inorg. Chem.* **2010**, *49* (5), 2512–2524.

(24) Höpfl, H. *J. Organomet. Chem.* **1999**, *581* (1–2), 129–149.

(25) Kumar, D.; Thiel, W.; De Visser, S. P. *J. Am. Chem. Soc.* **2011**, *133* (11), 3869–3882.

(26) Bassan, A.; Borowski, T.; Siegbahn, P. E. M. *Dalt. Trans.* **2004**, No. 20, 3153–3162.

(27) Ye, S.; Riplinger, C.; Hansen, A.; Krebs, C.; Bollinger, J. M.; Neese, F. *Chem. - A Eur. J.* **2012**, *18* (21), 6555–6567.

(28) Coggins, M. K.; Sun, X.; Kwak, Y.; Solomon, E. I.; Rybak-Akimova, E.; Kovacs, J. A. *J. Am. Chem. Soc.* **2013**, *135* (15), 5631–5640.

(29) Dehnicke, K.; Strähle, J. *Polyhedron* **1989**, *8* (6), 707–726.
(30) Creutz, S. E.; Peters, J. C. *Inorg. Chem.* **2016**, *55* (8), 3894–3906.
(31) Alecu, I. M.; Zheng, J.; Zhao, Y.; Truhlar, D. G. *J. Chem. Theory Comput.* **2010**, *6* (9), 2872–2887.
(32) MacDonnell, F.; Ruhlandt-Senge, K.; Ellison, J. J.; Holm, R. H.; Power, P. P. *Inorg. Chem.* **1995**, *34* (7), 1815–1822.
(33) MacBeth, C. E.; Golombek, A. P.; Young, J.; Yang, C.; Kuczera, K.; Hendrich, M. P.; Borovik, A. S. *Science (80-.).* **2000**, *289* (5481), 938–941.
(34) Stout, H. D.; Kleespies, S. T.; Chiang, C. W.; Lee, W. Z.; Que, L.; Münck, E.; Bominaar, E. L. *Inorg. Chem.* **2016**, *55* (11), 5215–5226.
(35) Sazama, G. T.; Betley, T. A. *Inorg. Chem.* **2014**, *53* (1), 269–281.
(36) Kostka, K. L.; Fox, B. G.; Collins, T. J.; Münck, E.; Hendrich, M. P.; Rickard, C. E. F.; Wright, L. J. *J. Am. Chem. Soc.* **1993**, *115* (15), 6746–6757.
(37) Jensen, K. P. *Inorg. Chem.* **2008**, *47* (22), 10357–10365.
(38) Woertink, J. S.; Tian, L.; Maiti, D.; Lucas, H. R.; Himes, R. A.; Karlin, K. D.; Neese, F.; Würtele, C.; Holthausen, M. C.; Bill, E.; Sundermeyer, J.; Schindler, S.; Solomon, E. I. *Inorg. Chem.* **2010**, *49* (20), 9450–9459.
(39) Tomson, N. C.; Crimmin, M. R.; Petrenko, T.; Rosebrugh, L. E.; Sproules, S.; Christopher Boyd, W.; Bergman, R. G.; Debeer, S.; Dean Toste, F.; Wieghardt, K. *J. Am. Chem. Soc.* **2011**, *133* (46), 18785–18801.
(40) Schappacher, M.; Weiss, R.; Montiel-Montoya, R.; Trautwein, A.; Tabard, A. *J. Am. Chem. Soc.* **1985**, *107* (12), 3736–3738.
(41) De Oliveira, F. T.; Chanda, A.; Banerjee, D.; Shan, X.; Mondal, S.; Que, L.; Bominaar, E. L.; Münck, E.; Collins, T. J. *Science (80-.).* **2007**, *315* (5813), 835–838.
(42) Cho, J.; Woo, J.; Nam, W. *J. Am. Chem. Soc.* **2012**, *134* (27), 11112–11115.
(43) Wertz, D. L.; Valentine, J. S. In *Metal-Oxo and Metal-Peroxo Species in Catalytic Oxidations*; Meunier, B., Ed.; Springer Berlin Heidelberg: Berlin, Heidelberg, 2000; pp 37–60.
(44) Shokri, A.; Que, L. *J. Am. Chem. Soc.* **2015**, *137* (24), 7686–7691.
(45) Annaraj, J.; Suh, Y.; Seo, M. S.; Kim, S. O.; Nam, W. *Chem. Commun.* **2005**, No. 36, 4529–4531.
(46) Lin, Y. H.; Kutin, Y.; Van Gastel, M.; Bill, E.; Schnegg, A.; Ye, S.; Lee, W. Z. *J. Am. Chem. Soc.* **2020**, *142* (23), 10255–10260.
(47) Cho, J.; Sarangi, R.; Annaraj, J.; Kim, S. Y.; Kubo, M.; Ogura, T.; Solomon, E. I.; Nam, W. *Nat. Chem.* **2009**, *1* (7), 568–572.
(48) Corcos, A. R.; Villanueva, O.; Walroth, R. C.; Sharma, S. K.; Bacsa, J.; Lancaster, K. M.; MacBeth, C. E.; Berry, J. F. *J. Am. Chem. Soc.* **2016**, *138* (6), 1796–1799.
(49) Hillenbrand, J.; Leutzsch, M.; Yiannakas, E.; Gordon, C. P.; Wille, C.; Nöthling, N.; Copéret, C.; Fürstner, A. *J. Am. Chem. Soc.* **2020**, *142* (25), 11279–11294.
(50) Goerlich, J. R.; Schmutzler, R. *Phosphorus. Sulfur. Silicon Relat. Elem.* **1995**, *102* (1–4), 211–215.
(51) Legault, C.; Charette, A. B. *J. Org. Chem.* **2003**, *68* (18), 7119–7122.
(52) Broere, D. L. J.; Čorić, I.; Brosnahan, A.; Holland, P. L. *Inorg. Chem.* **2017**, *56* (6), 3140–3143.
(53) Sadique, A. R.; Gregory, E. A.; Brennessel, W. W.; Holland, P. L. *J. Am. Chem. Soc.* **2007**, *129* (26), 8112–8121.

(54) Evans, D. F. *J. Chem. Soc.* **1959**, *0* (0), 2003.
(55) Rigaku Oxford Diffraction. Rigaku Corporation: Oxford, U.K. 2015.
(56) Bruker AXS Inc.: Madison, WI 2014.
(57) Sheldrick, G. Bruker Analytical X-Ray Systems, Inc.: Madison, WI 2000.
(58) Dolomanov, O. V.; Bourhis, L. J.; Gildea, R. J.; Howard, J. A. K.; Puschmann, H. *J. Appl. Crystallogr.* **2009**, *42* (2), 339–341.
(59) Stoll, S.; Schweiger, A. *J. Magn. Reson.* **2006**, *178* (1), 42–55.
(60) Frisch, M. J.; Trucks, G. W.; Schlegel, H. B.; Scuseria, G. E.; Robb, M. A.; Cheeseman, J. R.; Scalmani, G.; Barone, V.; Mennucci, B.; Petersson, G. A.; Nakatsuji, H.; Caricato, M.; Li, X.; Hratchian, H. P.; Izmaylov, A. F.; Bloino, J.; Zheng, G.; Sonnenberg, J. L.; Hada, M.; Ehara, M.; Toyota, K.; Fukuda, R.; Hasegawa, J.; Ishida, M.; Nakajima, T.; Honda, Y.; Kitao, O.; Nakai, H.; Vreven, T.; J. A. Montgomery, J.; Peralta, J. E.; Ogliaro, F.; Bearpark, M.; Heyd, J. J.; Brothers, E.; Kudin, K. N.; Staroverov, V. N.; Keith, T.; Kobayashi, R.; Normand, J.; Raghavachari, K.; Rendell, A.; Burant, J. C.; Iyengar, S. S.; Tomasi, J.; Cossi, M.; Rega, N.; Millam, J. M.; Klene, M.; Knox, J. E.; Cross, J. B.; Bakken, V.; Adamo, C.; Jaramillo, J.; Gomperts, R.; Stratmann, R. E.; Yazyev, O.; Austin, A. J.; Cammi, R.; Pomelli, C.; Ochterski, J. W.; Martin, R. L.; Morokuma, K.; Zakrzewski, V. G.; Voth, G. A.; Salvador, P.; Dannenberg, J. J.; Dapprich, S.; Daniels, A. D.; Farkas, O.; Foresman, J. B.; Ortiz, J. V; Cioslowski, J.; Fox, D. J. Gaussion Inc.: Wallingford CT 2013.
(61) Humphrey, W.; Dalke, A.; Schulten, K. *J. Mol. Graph.* **1996**, *14* (1), 33–38.
(62) Babij, N. R.; McCusker, E. O.; Whiteker, G. T.; Canturk, B.; Choy, N.; Creemer, L. C.; Amicis, C. V. D.; Hewlett, N. M.; Johnson, P. L.; Knobelsdorf, J. A.; Li, F.; Lorsbach, B. A.; Nugent, B. M.; Ryan, S. J.; Smith, M. R.; Yang, Q. *Org. Process Res. Dev.* **2016**, *20* (3), 661–667.
(63) Cramer, C. J.; Tolman, W. B. *Acc. Chem. Res.* **2007**, *40* (7), 601–608.
(64) Green, M. T. *J. Am. Chem. Soc.* **2006**, *128* (6), 1902–1906.
(65) Spaeth, A. D.; Gagnon, N. L.; Dhar, D.; Yee, G. M.; Tolman, W. B. *J. Am. Chem. Soc.* **2017**, *139* (12), 4477–4485.
(66) Cramer, C. J.; Tolman, W. B.; Theopold, K. H.; Rheingold, A. L. *Proc. Natl. Acad. Sci.* **2003**, *100* (7), 3635 LP – 3640.
(67) Fernández-Terán, R.; Ruf, J.; Hamm, P. *Inorg. Chem.* **2020**, *59* (11), 7721–7726.
(68) Cramer, C. J.; Tolman, W. B. In *Accounts of Chemical Research*; American Chemical Society, 2007; Vol. 40, pp 601–608.
(69) Würtele, C.; Gaoutchenova, E.; Harms, K.; Holthausen, M. C.; Sundermeyer, J.; Schindler, S. *Angew. Chemie - Int. Ed.* **2006**, *45* (23), 3867–3869.
(70) Oddon, F.; Chiba, Y.; Nakazawa, J.; Ohta, T.; Ogura, T.; Hikichi, S. *Angew. Chemie - Int. Ed.* **2015**, *54* (25), 7336–7339.
(71) Li, J.; Noll, B. C.; Oliver, A. G.; Schulz, C. E.; Scheidt, W. R. *J. Am. Chem. Soc.* **2013**, *135* (41), 15627–15641.
(72) Liu, L.-L.; Li, H.-X.; Wan, L.-M.; Ren, Z.-G.; Wang, H.-F.; Lang, J.-P. *Chem. Commun.* **2011**, *47* (39), 11146–11148.
(73) Komiyama, K.; Furutachi, H.; Nagatomo, S.; Hashimoto, A.; Hayashi, H.; Fujinami, S.; Suzuki, M.; Kitagawa, T. *Bull. Chem. Soc. Jpn.* **2004**, *77* (1), 59–72.
(74) Kindermann, N.; Bill, E.; Dechert, S.; Demeshko, S.; Reijerse, E. J.; Meyer, F. *Angew. Chemie Int. Ed.* **2015**, *54* (6), 1738–1743.

(75) Hoppe, T.; Schaub, S.; Becker, J.; Würtele, C.; Schindler, S. *Angew. Chemie Int. Ed.* **2013**, *52* (3), 870–873.

(76) Jacobson, R. R.; Tyeklar, Z.; Farooq, A.; Karlin, K. D.; Liu, S.; Zubieta, J. *J. Am. Chem. Soc.* **1988**, *110* (11), 3690–3692.

(77) Würtele, C.; Sander, O.; Lutz, V.; Waitz, T.; Tuczek, F.; Schindler, S. *J. Am. Chem. Soc.* **2009**, *131* (22), 7544–7545.

(78) Schmidt, S.; Heinemann, F. W.; Grohmann, A. *Eur. J. Inorg. Chem.* **2000**, *2000* (7), 1657–1667.

(79) Nurdin, L.; Spasyuk, D. M.; Fairburn, L.; Piers, W. E.; Maron, L. *J. Am. Chem. Soc.* **2018**, *140* (47), 16094–16105.

(80) Gavrilova, A. L.; Qin, C. J.; Sommer, R. D.; Rheingold, A. L.; Bosnich, B. *J. Am. Chem. Soc.* **2002**, *124* (8), 1714–1722.

(81) Ramprasad, D.; Gilicinski, A. G.; Markley, T. J.; Pez, G. P. *Inorg. Chem.* **1994**, *33* (13), 2841–2847.

(82) Shiren, K.; Ogo, S.; Fujinami, S.; Hayashi, H.; Suzuki, M.; Uehara, A.; Watanabe, Y.; Moro-oka, Y. *J. Am. Chem. Soc.* **2000**, *122* (2), 254–262.

(83) Duan, P.-C.; Manz, D.-H.; Dechert, S.; Demeshko, S.; Meyer, F. *J. Am. Chem. Soc.* **2018**, *140* (14), 4929–4939.

(84) Cho, J.; Furutachi, H.; Fujinami, S.; Tosha, T.; Ohtsu, H.; Ikeda, O.; Suzuki, A.; Nomura, M.; Uruga, T.; Tanida, H.; Kawai, T.; Tanaka, K.; Kitagawa, T.; Suzuki, M. *Inorg. Chem.* **2006**, *45* (7), 2873–2885.

(85) Davies, M. S.; Hambley, T. W. *Inorg. Chem.* **1998**, *37* (21), 5408–5409.

(86) Kim, K.; Lippard, S. J. *J. Am. Chem. Soc.* **1996**, *118* (20), 4914–4915.

(87) Zhang, X.; Furutachi, H.; Fujinami, S.; Nagatomo, S.; Maeda, Y.; Watanabe, Y.; Kitagawa, T.; Suzuki, M. *J. Am. Chem. Soc.* **2005**, *127* (3), 826–827.

(88) Dong, Y.; Yan, S.; Young Jr., V. G.; Que Jr., L. *Angew. Chemie Int. Ed. English* **1996**, *35* (6), 618–620.